Magnéto-transport dans les nanorubans de graphène

Rebeca Ribeiro

▶ **To cite this version:**

Rebeca Ribeiro. Magnéto-transport dans les nanorubans de graphène. Materials Science [cond-mat.mtrl-sci]. Université Paul Sabatier - Toulouse III, 2013. English. NNT : . tel-00905585

HAL Id: tel-00905585
https://theses.hal.science/tel-00905585

Submitted on 18 Nov 2013

HAL is a multi-disciplinary open access archive for the deposit and dissemination of scientific research documents, whether they are published or not. The documents may come from teaching and research institutions in France or abroad, or from public or private research centers.

L'archive ouverte pluridisciplinaire **HAL**, est destinée au dépôt et à la diffusion de documents scientifiques de niveau recherche, publiés ou non, émanant des établissements d'enseignement et de recherche français ou étrangers, des laboratoires publics ou privés.

Université de Toulouse

THÈSE

En vue de l'obtention du

DOCTORAT DE L'UNIVERSITÉ DE TOULOUSE

Délivré par : *l'Université Toulouse 3 Paul Sabatier (UT3 Paul Sabatier)*

Présentée et soutenue le *11 juillet 2013* **par :**

REBECA RIBEIRO

Magnéto-transport dans les nanorubans de graphène

JURY

ERIK DUJARDIN	DR- CEMES-Toulouse	Président du Jury- Examinateur
BENJAMIN SACEPE	CR - Institut NEEL	Examinateur
ENRIQUE DIEZ	Professeur - Université de Salamanca	Rapporteur
BENOÎT JOUAULT	DR - Université de Montpellier	Rapporteur
BERTRAND RAQUET	Professeur- INSA-Toulouse	Directeur de Thèse
JEAN-MARC BROTO	Professeur - Université de Toulouse	Directeur de Thèse

---

École doctorale et spécialité :
SDM : Physique - COR 02
Unité de Recherche :
Laboratoire National des Champs Magnétiques Intenses (UPR 3228)
Directeur(s) de Thèse :
Jean-Marc BROTO et *Bertrand RAQUET*
Rapporteurs :
Enrique DIEZ et *Benoît JOUAULT*

Acknowledgment

This PhD thesis started on September 2nd, 2009 and finished on July 11th, 2013 in the *Laboratoire National des Champs Magnétique Intenses de Toulouse*, as the begining of my carrer as a researcher and a new adventure. Rapidly it became one of the best and hardest experiences of my life. Here, I would like to thank to the people that, in one way or another, were part of this important and unforgettable moment of my life:

First of all, I would like to thanks to *Fundación Gran Mariscal de Ayacucho*, for the economical and moral support that they gave to me and to many of the Venezuelan studying abroad. As well I would like to thanks the Venezuelan goverment for the opportunity that they give to people like me to have a public education.

I would like to thank my thesis director Bertrand Raquet and the members of the jury: Benoit Jouault, Enrique Diez, Benjamin Sacepe and Erik Dujardin for their work in the evaluation of this work. Thanks to all the people that work at the LNCMI-Toulouse for an extraordinary work and all the help that they gave me during my PhD.

L'equipe Nano: Bertrand, a great thesis director who I appreciate a lot and who taught me a lot of things not just related to physics but also about myself. GRACIAS, sin ti esto no hubiese sido posible.

Walter and Michel, thanks for everything. Thanks Walter for your organization (quelque fois extrême) and needs to go further and make things better. Michel, I appreciate a lot the way you always want to understand better the physics behind the experimental results and your passion for physics.

Jean-Marie, I have no words to thank you for your help with my integration to the French culture (même quand tu es pas le meilleur exposant), you were an amazing colleague but specially a wonderful friend. Fabrice, now it's your time, I know you will make a great work.

I would like to specially thank to Ludo, Jérôme, Oliver Portugal, Severine and Françoise, Geert Rikken (5 bonjour et une blage de fromage de chevre), Paul Frings, Bertrand Griffe, Loic, the people at the workshop, Nicola Bruyant, Marc Nardone and Azis people that gave every day their best to help in the development of my thesis.

Thanks to *L'equipe FFC et l'equipe Paulina et Duncan*, for all the materials, equipment, help, knowlegde, PhD students, postdocs, patience and for the good moments (inside and outside the lab). Duncan: for the "nasty questions", since they were very helpful. Cyril et Batiste: un grand merci pour tout le soutiens, pour le bières et les sourires. Merci Cyril pour partager ton vision de la recherche avec moi et pour me montrer que peut-être on est pas tout seul dans notre avis.

Also, I would like thank the *TEAM (and more) at LAAS* for their work and support during the development of the processes neccesary for sample's fabrication. Franck, Emmanuelle, Jean-Batiste, George, Laurent and Sebastien, la techno est

pas facile mais avec vous c'etait bcp plus sympa! I would like to specially thanks to Franck Carcenac, more than a engeneer, always full of wisdom, hope and happiness. You taught me the most important lessons of my PhD: Be happy is the most important thing, the rest doesn't matter. I'm very greatful (agradecida, obrigada) for everything.

People from other labs that also make a big contribution to this thesis, Dominique Coquillard (LCC-Montpellier), Stephane Roche (Barcelone), Alessandro Cresti (Grenoble), Michel Viret (CEA-Saclay), Olivier Couturaud (CEMES Toulouse), Miguel Rubio-Roy (CEMES-Toulouse), Francesco (Pavia), Vittorio (Pavia), Carsten (Dresden-Bristol) and Benjamin Lassagne (LPCNO-Toulouse) merci, grazie, gràcies, danke.

Specially I would like to thank to *"les thésards et Xavier"*: Vladimir, c'était un plaisir de partager ce temps avec toi, Vika et la belle Clementina, vous êtes une très belle famille! Stephane, On a finis !!!!!! The light at the end of the tunnel is here!!!

Sven et Gernot, j'ai pas les mots pour vous remercié la bonne ambiance, les sorties ensemble et BCP plus (Marion et Aude aussi) !!!! Xav, ça me fait du mal de te dire au revoir mais comme tu viens à Paris bientôt ça va aller, ça va me manquer que tu fasses la tête tous les matins et que tu ramène Timothée de temps en temps au labo, tu nous invite à ta soutenance? Fabrice (Fabricito), bon courage, c'est pas facile mais il faut finir !!! Je sais que tu va t'en sortir !!! Mais il faut arrêter avec les pommes de terre avec l'Alu. Haolian: Good luck ! there is still a lot of work in this subject, so, go for it ! Agathe, il faut pas être trop BMV (trop isolée) c'est toujours mieux d'aller manger avec les gens des autres groups et profite pour changer la tête. Anais, je sais que cet dificile mais c'est bientôt finis. Asha and Anatole: Excellent! I hope to see you both soon in Paris !!!

Jérôme, Paul, Winnie et Chris Baker: Des incroyables journées au bureau. Paul, merci pour ta patience, ton bon espirit et ton beau sourire tous les jours. Jérôme, merci pour tes conseils, pour ton regarde critique qu'aide bcp, pas seulement a moi sinon a tout le labo en général, sans toi je ne sais pas a quoi ça ressemblerait le labo. Chris Baker, merci pour les wafers, on s'a en servi de tes mails pour faire des blagues et pour tenir le contact avec Paul quand il est parti aux states.

Los latinoamericanos

La poh, el tripack (German, Majo y Kungfu), Lucia, Laia (bueno casi latinoamericana), el cuchi (oui, toi aussi), Reina, Camila, Hender, Eileen, Jordan y Alex (tula pa' los panas) y José: No tengo palabras para agradecer el apoyo, las risas, las salidas para "levantar la moral", las empanadas, los asados, los viajes, los conciertos, las reuniones, las cervezas, los regaños, las preocupaciones, las llamadas (las quedadas) y en general todas las veces que estuvieron ahí para mi en estos cuatro años. Han sido la familia que necesitaba en Francia y serán siempre la familia que aunque este lejos se recuerda y se tiene ganas de volver a ver.

Finalmente y no por eso menos importante a mi familia por el apoyo durante todos estos años. Al Dr. Ismardo Bonalde, por ser mi apoyo académico y moral, al Dr. Medina por ser siempre mi punto de referencia (yo quiero ser como Medina cuando sea grande), a Nelson por haberme apoyado para venir aqui y a David por

estar ahí, apoyarme en todo y en todas las maneras posibles y ser siempre más de lo que yo podia pedir.

Esta tesis esta dedicada a mi familia: Dora Palau, Zoraida Palau, Maria Palau, Nino Ferreras, Salvador Palau, Carvi Ferreras Palau y Antonio Ferreras Palau, Jose Ribeiro, Simon y Rodrigo. Por el aporte genetico, educacional, el apoyo incondicional y los buenos momentos.

"La vie n'est facile pour aucun de nous.
Mais quoi, il faut avoir de la persévérance,
et surtout de la confiance en soi.
Il faut croire que l'on est doué pour quelque chose,
et que cette chose il faut l'atteindre coûte que coûte."
Marie Curie

Contents

Introduction

The current and future advances in electronic applications require size reduction and performance improvement. These two subjects are not trivial and suppose a central issue in the conception of new devices, since the limits of Si transistors become imminent.

In the quest of new technologies, the carbon based electronics have become promising. Of especial interest, graphene, has attracted a lot of attention in the last years because of its high electronic mobility (more than 200,000 cm^2V^{-1} s^{-1}), its high maximum current density ($\sim$ 2 mA/μm) and its mechanical flexibility. However, the major inconvenient for future graphene applications in logic-electronics is its semimetallicity i.e. the absence of energy gap to guaranty a large enough ON/OFF current ratio.

In the search of a best way to engineer an energy gap, the electronic confinement seems the more reliable approach. If we consider the simple picture of a particle in a box, when an electron is confined in one dimension, the hard-wall conditions impose a quantization of the transverse k-vector. This quantization leads to the onset of a 1D electronic band structure and the opening of an energy gap between the highest valence band and the lowest conducting band. The same mechanism occurs for graphene, when it is cut into nanoribbons. Except that, here, the electronic confinement is also dependent on the edge symmetry, e.g. zigzag or armchair, that drive the boundary conditions of the electronic wave function. This results into a specific 1D electronic band structure depending on the edge configurations. For zigzag graphene nanoribbons (GNRs), localized states at the edges induce a flat energy band at zero energy. At higher energy, a perfectly conducting subband, robust to disorder, is expected to develop and the valley degeneracy is preserved like in graphene. In case of armchair GNRs, a direct energy gap, of the order of $[0.2-1.5]\text{eV}/W(nm)$ (being W, the width of the ribbon), develops and the different 1D subbands are fully valley degeneracy lifted.

Obviously, the edge configuration offer a new degree of freedom to adjust the electrostatic properties of the GNR, in strong analogy with the rolling vector in carbon nanotubes.

Unfortunately, the current methods to design a nanoribbon do not allow an accurate control of the edge symmetry. Most of them introduce a high degree of edge disorder, this induces a drastic reduction of the carrier mobility and the formation of a transport gap in the vicinity of the charge neutrality point. At the very end, the cut standing electronic properties of the mother material, graphene, are not anymore present in confined structures and the specificities of the edge symmetry only remains at a stage of theoretical predictions. This calls for additional experimental efforts to optimize the graphene nanoribbons quality and to develop original techniques to get some signatures of the GNR band structure even when a reasonable degree of disorder is present in the device. Indeed, a suitable way to

study the intrinsic band structure is the magneto-transport experiment in the high magnetic field regime. For some of the electrons, close to the edges, the trajectories are not closed orbits but skipping orbits, forming new conducting channels much less sensitive to the disorder. In the same time, the electronic band structure gradually evolves to a Landau spectrum with some reminiscence of the electronic confinement that dominates at zero magnetic field. A measurement of the electronic transport in such a regime would reveal the strength of the electronic confinement.

In this thesis, we propose the study of graphene nanoribbons in pulse high magnetic field (up to 55 T) to unveil their electronic properties which are partly hidden by the presence of disorder.

This manuscript is divided in two parts. In the first one (the first three chapters), we review the major concepts of the electronic transport properties of graphene and graphene nanoribbons. We mainly focus on the size reduction effects on the band structure, the impact of the disorder and the influence of a large magnetic field. In this part, we also present the experimental state of art on these subjects.

The second part (from chapter four to seven) is dedicated to the presentation of the works done during this thesis, from the sample fabrications to the experimental magneto-transport results. We first start by presenting the experimental developments from the samples fabrications (lithographically patterned GNRs and derived from unzipping carbon nanotubes by calcilation and sonication) to the main measurement techniques used in this work.

The heart of this work relies on magneto-transport experiments performed on monolayer GNR made by e-beam lithography. We observe the signature of an electronic confinement through anomalous Shubnikov-de Haas oscillations and a new Landau spectrum which may be related to the presence of armchair edges on the GNRs.

In case of bilayer GNRs, we observe some signatures of Landau states through quantum oscillations in the magneto-resistance as a consequence of the onset of Landau states. However, the quantized regime is not reached. Some anomalies in the Landau spectrum are observed, possibly related to the electronic confinement.

Finally, we present a study of quantum interferences in GNRs. We evidence the effects of temperature and bias voltages as sources of decoherence and we provide evidence of ergodicity in bilayer GNRs. As an additional part, we shortly present a preliminary study of graphene under THz radiations. A good agreement between the photoresponse fluctuations and the second order conductance fluctuations shows the possibility to use THz radiations to probe non-linear quantum phenomena.

Chapter 1

Electronic Structure and Transport in Pristine Graphene Nanoribbons

Contents

In the present chapter, we review the electronic structure and transport properties of 2D graphene and graphene nanoribbons. We focus on the modifications of the electronic band structure of graphene when electrons are confined in one dimension.

Graphene is an allotropic form of carbon, defined as a single atomic layer of carbon atoms arranged in hexagonal structure (honeycomb lattice). Its crystalline structure, Fig. 1.1, can be seen as two interpenetrating triangular sublattices: the center of one sublattice (red) is at the center of the triangle defined by the other sublattice (green). It has then, two carbon atoms per unit cell, designated A and B (red and green in Fig. 1.1), and it is invariant under 120° rotation around any lattice site. The external electronic structure on atom is formed by one s and three p orbitals. Two in-plane p orbitals and the s orbital hybridize themselves to form sp^2 molecular orbitals that are tied up in graphene's strong covalent bonding and do not contribute to its conductivity. The remaining p orbital, perpendicular to the molecular plane, is odd under inversion in the plane and hybridizes to form π (valence) and π^* (conduction) bands.

Since early 40's, graphene has been extensively studied in theory as the base of graphite (3D material made of stacked graphene planes that are binded by van

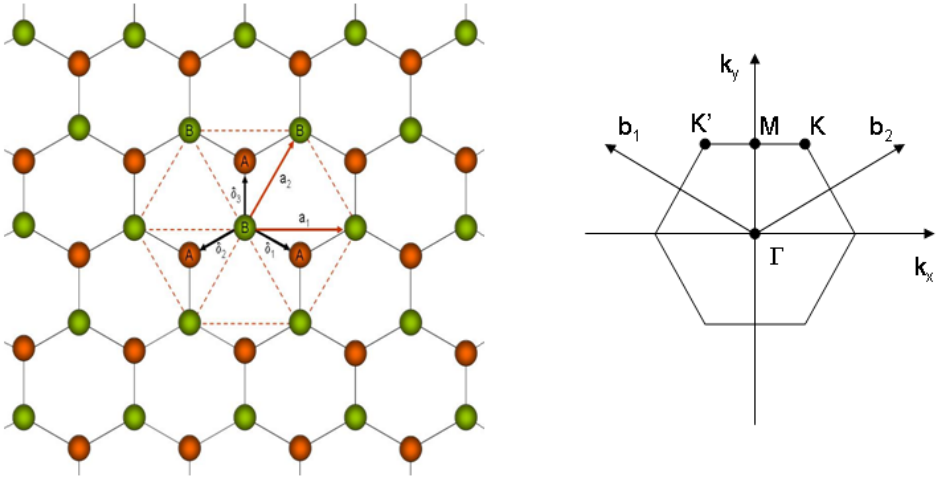

Figure 1.1: **Left**, Graphene crystal structure, red atoms represent sublattice A and green ones, sublattice B. $\delta_{1,2,3}$ are the nearest neighbor vectors and, $\mathbf{a}_{1,2,3}$ the second nearest neighbors. **Right**, first Brillouin zone; $\mathbf{b}_{1,2}$ are the reciprocal lattice vectors.

der Waals forces), while, at this time, the idea of a perfect 2D atomic structure was not realistic. The electronic structure of graphene was presented for the first time in 1947 in the pioneering work of [Wallace 1947]. It was not till 2004 that gated graphene was finally obtained [Novoselov 2004] and since then, a tremendous number of theoretical and experimental works have been focus on main electronic, mechanical and chemical properties of this material (more than 25000 published articles).

1.1 Graphene Electronic Structure and Transport

1.1.1 Graphene Monolayer

An electron moving in 2D graphene honeycomb lattice unveils unique properties due to the two equivalent lattice sites (A and B, Fig. 1.1) which give rise to the "chirality" in the graphene carrier dynamics.

The tight-binding Hamiltonian for electrons in graphene, considering that electrons can hop to both nearest- and next-nearest-neighbor atoms, has the form (using unit such that $\hbar = 1$):

$$H = -t \sum_{\langle i,j\rangle,\sigma} (a^{\dagger}_{\sigma,i} b_{\sigma,j} + H.c.) - t' \sum_{\langle\langle i,j\rangle\rangle,\sigma} (a^{\dagger}_{\sigma,i} a_{\sigma,j} + b^{\dagger}_{\sigma,i} b_{\sigma,j} + H.c.), \tag{1.1}$$

where $a_{i,\sigma}$ ($a^{\dagger}_{i,\sigma}$) annihilates (creates) an electron with spin σ on site $\mathbf{R}_i$ on sublattice A (an equivalent definition is used for sublattice B), $t(\sim 2.8eV)$ is the nearest-neighbor hopping energy (hopping between different sublattices, represented by $\delta_{1,2,3}$

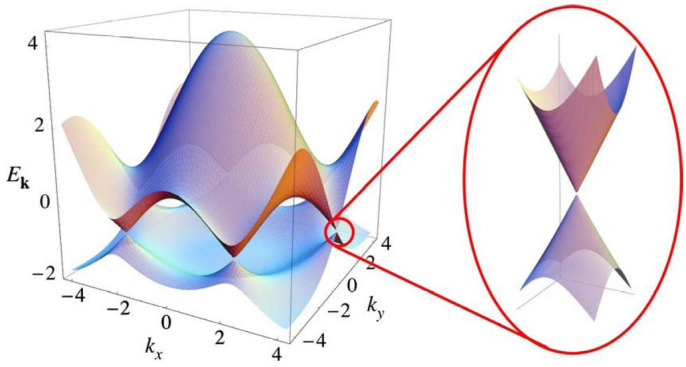

Figure 1.2: Graphene energy spectrum (in units of t) calculated from eqs. (1.2) and (1.3), using $t = 2.7$ eV and $t' = -0.2t$. **Zoom**, energy band close to the Dirac point. Adapted from [Castro-Neto 2009].

in Fig. 1.1), and t' is the next-nearest-neighbor hopping energy (hopping in the same sublattice, represented by $\mathbf{a}_{1,2,3}$ in Fig. 1.1)[1]. The energy bands derived from this Hamiltonian have the form [Wallace 1947]:

$$E_{\pm}(\mathbf{k}) = \pm\sqrt{3 + f(\mathbf{k})} - t' f(\mathbf{k}), \tag{1.2}$$

with

$$f(\mathbf{k}) = 2\cos(\sqrt{3}k_y a) + 4\cos\left(\frac{\sqrt{3}}{2}k_y a\right)\cos\left(\frac{3}{2}k_x a\right), \tag{1.3}$$

where the plus and minus signs, in eq. (1.2), apply to the conduction (upper, π^*) and valence (lower, π) bands, respectively, and $a = 0.142$ nm is the carbon-carbon distance. For $t' = 0$, the energy spectrum is symmetric around zero energy and for finite values of t', the electron-hole symmetry is broken, as seen in Fig. 1.2.

The conduction and valence bands touch each other at six points. These are the $\mathbf{K}$ and $\mathbf{K}'$ points of the Brillouin zone (Fig. 1.1) which are non-equivalents, meaning that they can not be connected by a reciprocal lattice vector. The existence of these two Dirac points gives rise to the valley degeneracy ($g_v = 2$) of graphene. If the band structure is expanded around them, we find the almost universally used graphene band dispersion[2] (for $t' = 0$):

$$E_{\pm}(\mathbf{q}) \approx \pm v_F|\mathbf{q}| + O[(q/K)^2], \tag{1.4}$$

where $\mathbf{q}$ is the momentum measured relatively to the Dirac Point and v_F is the Fermi velocity, given by $v_F = 3ta/2 \simeq 10^6$ m/s. This equation reveals the linear energy-momentum relationship with the conductance and valence band intersecting at $q = 0$, with no energy gap.

[1] The value of t' is not well known but tight-binding fit to cyclotron experiments finds $t' \sim 0.1eV$ [Castro-Neto 2009].

[2] as $\mathbf{k} = \mathbf{K} + \mathbf{q}$, with $|\mathbf{q}| \ll |\mathbf{K}|$ [Wallace 1947].

Taking the Hamiltonian, eq. (1.1), with $t' = 0$ and the Fourier transform of the electron operators and after some algebra (for more details see [Castro-Neto 2009]) one remarks that the two-component of the electronic wave-function close to the **K** point, obeys the 2D Dirac equation:

$$-iv_F\boldsymbol{\sigma}\cdot\nabla\psi(\mathbf{r}) = E\psi(\mathbf{r}), \tag{1.5}$$

where $\boldsymbol{\sigma} = (\sigma_x, \sigma_y)$ is the usual vector of the Pauli matrices (in 2D) and $\psi(\mathbf{r})$ is a 2D spinor wave-function. The eq. (1.5) corresponds to the effective low energy Dirac Hamiltonian:

$$\mathcal{H} = v_F \begin{pmatrix} 0 & q_x - iq_y \\ q_x + iq_y & 0 \end{pmatrix} = v_F\boldsymbol{\sigma}\cdot\mathbf{q}\,. \tag{1.6}$$

This is the equation for massless chiral Dirac Fermions in 2D. The spinor here refers to the graphene pseudospin.

The graphene's pseudospin has its origin in the existence of two equivalent, but independent, sub-lattices A and B. This leads to the presence of a novel chirality in graphene dynamics, where the two linear branches of graphene energy dispersion become independent of each other, indicating the appearance of a pseudospin quantum number analogous to electron spin (but completely independent of real spin). Thus graphene carriers have a pseudospin index in addition to the spin and orbital index.

The momentum space pseudo-spinor eigenfunctions for eq. (1.5) can be written as:

$$\psi(\mathbf{q}, K) = \frac{1}{\sqrt{2}}\begin{pmatrix} e^{-i\theta_q/2} \\ \pm e^{i\theta_q/2} \end{pmatrix}, \qquad \psi(\mathbf{q}, K') = \frac{1}{\sqrt{2}}\begin{pmatrix} e^{i\theta_q/2} \\ \pm e^{-i\theta_q/2} \end{pmatrix}, \tag{1.7}$$

where the $+/-$ signs corresponds, again, to the conduction/valence band with $E_\pm(q) = \pm v_F q$ and θ_q is the angle in momentum space given by:

$$\theta_q = \arctan\left(\frac{q_x}{q_y}\right). \tag{1.8}$$

Note that the wave functions at **K** and **K′** are related by time-reversal symmetry: if the origin of coordinates in momentum space is set in the M point of the Brillouin zone (Fig. 1.1), time reversal becomes equivalent to a reflection along k_y axis, that is $(k_x, k_y) \to (-k_x, k_y)$. Also, note that if the phase θ is rotated by 2π, the wave function changes its sign indicating a phase of π (in the literature, this is commonly called the Berry's phase). This π phase change under rotation is characteristic of spinors. In fact, the wave function is a two-component spinor.

A relevant quantity to characterize the eigenfunction is its helicity. It is defined as the projection of the momentum operator along the (pseudo)spin direction, σ. The form of the quantum-mechanical operator for the helicity, $\hat{h}$, is [Castro-Neto 2009]:

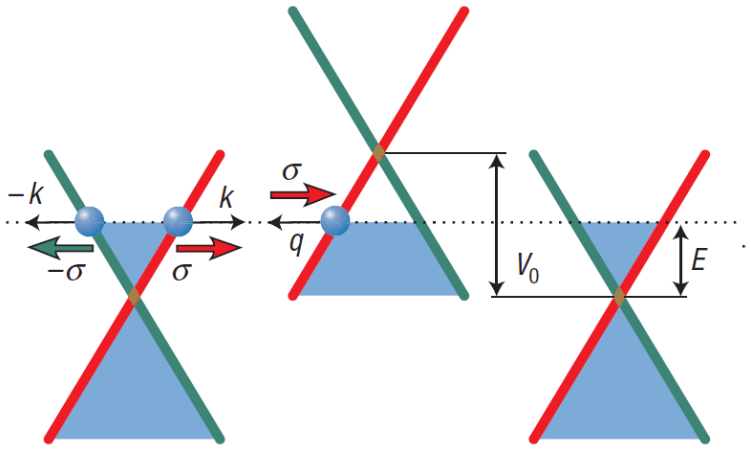

Figure 1.3: Graphene energy dispersion at the Dirac point. Red arrows represent electron's pseudospin, σ. When σ and the momentum, $\mathbf{p}$, are in the same (opposite) direction the helicity is positive (negative). Adapted from [Peres 2010].

$$\hat{h} = \frac{1}{2}\boldsymbol{\sigma} \cdot \frac{\mathbf{p}}{|\mathbf{p}|}\,. \tag{1.9}$$

From the definition of $\hat{h}$, we see that the states $\psi(r, K)$ and $\psi(r, K')$ are also eigenstates of $\hat{h}$

$$\hat{h}\psi(r, K) = \pm\frac{1}{2}\psi(r, K)\,, \tag{1.10}$$

and equivalently for $\psi(r, K')$, with the reversed sign. Consequently, electrons (holes) have positive (negative) helicity for the valley $\mathbf{K}$ and the opposite for valley $\mathbf{K'}$ (Fig. 1.3). Equation (1.10) implies that σ has its eigenvalues either in the direction of ($\Uparrow$) or against ($\Downarrow$) the momentum $\mathbf{p}$. This means that the states of the system close to the Dirac point have well defined chirality or helicity. Note that chirality is not defined with regard to the real spin of the electron but to a pseudospin variable associated with the two components of the wave function. The helicity values are good quantum numbers as long as the Hamiltonian is valid. Hence, it holds only as an asymptotic property, which is well defined close to the Dirac points. At larger energies or in presence of a finite t', it stops to be a good quantum number [Castro-Neto 2009].

The electronic linear dispersion and the chirality of carrier's wave function give to graphene its remarkable characteristic concerning electronic transport and are the responsible for the unique properties of this material as the Klein tunneling (Fig. 1.3). In the presence of long-range potential fluctuations, carriers move across charge puddles. As chirality is a conserved quantity when the Fermi energy cuts the potential barrier, carriers are converted from an electron to a hole (or from a hole to an electron). This requires a forward moving electron hitting the potential barrier at a normal angle to be scattered as backward moving hole (inter-band tunneling).

The real electron continues to move in the same direction. Backscattering is then suppressed because of the perfect charge transmission [Mucciolo 2010].

1.1.2 Graphene Bilayer

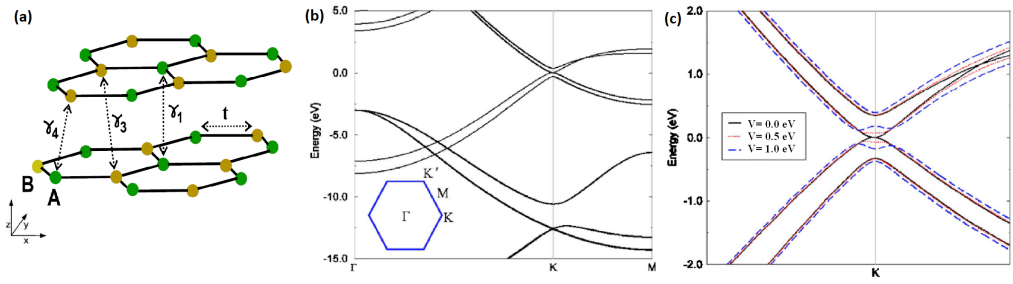

Figure 1.4: **(a)** Bilayer graphene crystal structure in presence of Bernal stacking, t, γ_1, γ_3 and γ_4, represent the intra and inter-layer hopping energies. **(b)** Graphene bilayer band structure in absence of an external electric field. Inset: first Brillouin zone. **(c)** Graphene bilayer band structure near the **K** point for an applied electric field perpendicular to the layers. Adapted from [Min 2007].

The case of graphene bilayer is interesting since it is intermediate between graphene monolayer and bulk graphite. The tight-binding description relies on a specific stacking of the two layers. Graphene bilayer can be described as the simplest generalization of graphite, with the so-called A-B (or Bernal) stacking of the two layers, which is the 3D most common graphitic stacking. It consists of two graphene layers where half of the atoms are above and below the empty centers of the hexagonal rings, Fig. 1.4 (a). The tight-binding Hamiltonian is written as [Castro-Neto 2009]:

$$H = -t\sum_{\langle i,j\rangle}(a^{\dagger}_{m,i,\sigma}b_{m,j,\sigma} + H.c) - \gamma_1\sum_{j,\sigma}(a^{\dagger}_{1,j,\sigma}a_{2,j,\sigma} + H.c) \\ - \gamma_4\sum_{j\sigma}(a^{\dagger}_{1,j,\sigma}b_{2,j,\sigma} + a^{\dagger}_{2,j,\sigma}b_{1,j,\sigma} + H.c) - \gamma_3\sum_{j,\sigma}(b^{\dagger}_{1,j,\sigma}b_{2,j,\sigma} + H.c) \quad (1.11)$$

where $a^{\dagger}_{m,i,\sigma}$ ($b_{m,j,\sigma}$) creates (annihilates) an electron with spin σ on sublattice A (B), in plane $m = 1, 2$ at site $\mathbf{R}_i$. For the hopping parameter, the same nomenclature as for graphite is used, Fig. 1.4 (a): t is the in-plane hopping energy, γ_1 is the hopping energy between atom A_1 and A_2, γ_4 is the hopping energy between atom A_1 (A_2) and atom B_2 (B_1), and γ_3 connects B_1 and B_2.

In the continuum limit, by expanding the momentum close to the **K** point in the Brillouin zone, the Hamiltonian reads [Castro-Neto 2009]:

$$\mathcal{H} = \sum_{\mathbf{k}} \Psi^{\dagger}_{\mathbf{k}} \cdot \mathcal{H}_K \cdot \Psi_{\mathbf{k}} \quad (1.12)$$

where, if we ignore γ_4,

$$\mathcal{H}_K \equiv \begin{pmatrix} -V & v_F k & 0 & 3\gamma_3 a k^* \\ v_F k^* & -V & \gamma_1 & 0 \\ 0 & \gamma_1 & V & v_F k \\ 3\gamma_3 a k & 0 & v_F k^* & V \end{pmatrix}, \tag{1.13}$$

here, $k = k_x + ik_y$ is a complex number, V is the half of the shift in electrochemical potential between the two layers (this term will appear if a potential bias is applied between the layers e.g. by an applied electric field perpendicular to the layers) and

$$\Psi^\dagger_{\mathbf{k}} = (b_1^\dagger(\mathbf{k}), a_1^\dagger(\mathbf{k}), a_2^\dagger(\mathbf{k}), b_2^\dagger(\mathbf{k})) \tag{1.14}$$

is a four-component spinor. If $V = 0$ and $\gamma_3, v_F k \ll \gamma_1$, it is possible to eliminate the high-energy state pertubatively and write an effective Hamiltonian:

$$\mathcal{H}_K \equiv \begin{pmatrix} 0 & \frac{v_F^2 k^2}{\gamma_1} + 3\gamma_3 a k^* \\ \frac{v_F^2 (k^*)^2}{\gamma_1} + 3\gamma_3 a k & 0 \end{pmatrix}. \tag{1.15}$$

For $\gamma_3 = 0$, this equation gives two parabolic bands $\boldsymbol{\varepsilon}_{\pm,\mathbf{k}} \approx \pm v_F^2 k^2 / t_\perp$ (with $t_\perp$ the effective interlayer hopping energy), which touch at $\boldsymbol{\varepsilon} = 0$, Fig. 1.4 (b)-(c). The electronic spectrum is electron-hole symmetric and it has two additional bands that start at $\pm t_\perp$. Within this approximation, graphene bilayer is metallic, with a constant density of states. The term γ_3 changes qualitatively the spectrum at low energies since it introduces a trigonal distortion or warping, of the bands. The electron-hole symmetry is preserved but, instead of two bands touching at $k = 0$ we obtain three sets of Dirac-like linear bands.

The term V, in eq. (1.13), breaks the equivalence of the two layers, or alternatively, the inversion symmetry. In this case, the dispersion relation becomes:

$$\boldsymbol{\varepsilon}^2_{\pm,\mathbf{k}} = V^2 + v_F^2 k^2 + t_\perp^2/2 \pm \sqrt{4V^2 v_F^2 k^2 + t^2 v_F^2 k^2 + t_\perp^4/4}\,, \tag{1.16}$$

giving rise to the opening of an energy gap close to, but not directly at, the **K** point, Fig. 1.4 (c). For small momenta, and $V \ll t$, the energy of the conduction band can be expanded as:

$$\varepsilon_k \approx V - 2V v_F^2 k^2 / t_\perp + v_F^4 k^4 / 2t_\perp^2 V\,. \tag{1.17}$$

The energy dispersion for the valence band can be obtained replacing $\boldsymbol{\varepsilon}_{\mathbf{k}}$ by $-\boldsymbol{\varepsilon}_{\mathbf{k}}$. Thus, graphene bilayer has an energy gap at $k^2 \approx 2V^2/v_F^2$. Note, therefore, that the energy gap in the biased bilayer system depends on the applied bias and hence can be measured experimentally.

The electronic transport measurements in double gated graphene bilayer show the opening of an energy gap. In Fig. 1.5 (a), we see a very sharp increase of the resistance at the charge-neutrality point with increasing the electric field applied

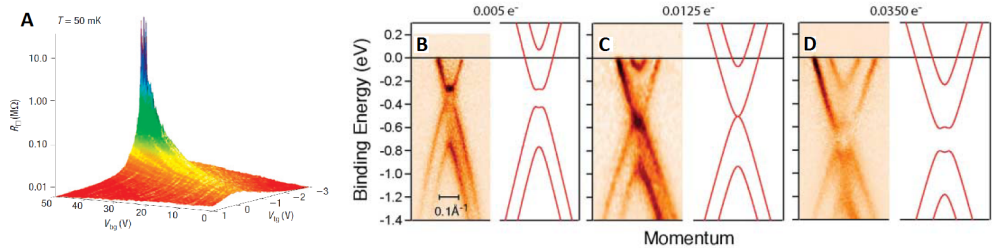

Figure 1.5: **(a)** Gate-induced insulating state in a bilayer graphene device. Three-dimensional plot of the square resistance as a function of both top- and back-gate voltages (V_{tg} and V_{bg}, respectively) at $T = 50$ mK, showing a sharp rise of the charge-neutrality peak with the electric field. Adapted from [Oostinga 2008]. From **(b)** to **(d)**: Evolution of the energy gap by changing the doping level by potassium adsorption in synthesized bilayer graphene on a SiC substrate. Experimentally deduced and theoretical bands (solid lines). **(a)** For an as-prepared graphene bilayer, **(b)** and **(c)** with progressive adsorption of potassium. Adapted from [Ohta 2006].

perpendicular to the layer. The double-gate device configuration allows a simultaneous and independent control of the charge density in the layers. A transition from a zero-gap semiconductor to an insulator is achieved, by disymmetrizing the two layers by the double gate voltage.

The difference in electrochemical potential between the two layers can also be induced by doping, as seen in angle-resolved photo-emission spectroscopy (ARPES) on a chemically doped graphene bilayer [Ohta 2006]. In Fig. 1.5 (b)-(d), we observe the variation in the apparent energy gap at the **K** point: first finite (b) in the as prepared samples due to charge accumulation on the graphene layer close to the interface with SiC, then closes (c) by a small amount of potassium absorption and then open (d) by the increase of doping. This gap variation is also reproduced by tight-binding calculations (red lines in Fig. 1.5) and it is attributed to the variations on the relative potential of the two layers due to the different levels of doping [Ohta 2006].

1.1.3 Electronic Transport in Graphene

The conductivity in defect-free graphene is studied using the ballistic approach (where the mean free path is larger than the distance between electrodes $l_e \gg L$) of Landauer conduction expression (for more details of the origin of the Landauer formula see below)

$$\sigma = \frac{L}{W} \times \frac{g_s g_v e^2}{h} \sum_{n=0}^{\infty} T_n \,, \tag{1.18}$$

where L and W are the length and the width of the conducting channel, respectively, $g_{s(v)} = 2$ is the spin (valley) degeneracy factor and $2e^2/h \approx 77.48\ \mu$S is the quantum of conductance, G_0. The sum holds for all the accessible 1D subbands.

The expression (1.18) is the so-called *Landauer formula*, it represents the ballistic approach of the conductance when the mean free path is larger than the distance between electrodes ($l_e \gg L$).

We consider a source-graphene-drain system as a n-p-n or n-n-n junction where the leads are heavily electron doped and while the graphene sheet may be electron doped, hole doped or pinned at the Dirac point with zero doping [Katsnelson 2006b]. For graphene, the transmission at an angle normal to the junction barrier is always perfect, although there could be some reflection at other angles (Klein tunneling). At the Dirac point, using the non-interacting Dirac equation and the appropriate boundary conditions, the transmission probability of a mode n is given by [Das Sarma 2010]:

$$T_{\mathrm{n}} = \left| \frac{1}{\cosh(q_{\mathrm{n}} L)} \right|^2 , \tag{1.19}$$

where $q_{\mathrm{n}} = \pi(\mathrm{n} + 1/2)/W$ is the transversal momentum. Considering the Landauer formula, eq. (1.18), we obtain:

$$\sigma = \frac{4e^2}{h} \sum_{n=0}^{\infty} \frac{L}{W \cosh^2[\pi(n+1/2)L/W]} \xrightarrow{W \gg L} \frac{4e^2}{\pi h} . \tag{1.20}$$

At zero energy, for $W \gg L$, an and in the ballistic regime, we obtain a non zero universal value of the conductivity. This has been evidenced by [F. Miao 2007]. They found that, at high aspect ratio ($W/L \gg 1$), the conductivity at the charge neutrality point (CNP) for a graphene monolayer saturates at $\sim 4e^2/\pi h$ (Fig. 1.6). It is important to remark that this "universal value" does not hold for samples of large areas ($A > 3\mu m^2$), inset Fig. 1.6.

Similar calculations in graphene bilayer, when the trigonal warping is absent [Katsnelson 2006a, Cserti 2007], show a minimum of conductivity always 2 times larger than the monolayer case, while, in presence of the trigonal warping, it becomes 6 times larger, independently of the strength of the warping [Cserti 2007].

We now calculate the conductivity as a function of the carrier density in the ballistic regime. We assume transparent electrodes and the total number of occupied transverse modes is defined by $N = W k_F/\pi$ with $k_F = \sqrt{4\pi n/g_s g_v}$. From eq. (1.18), we deduce the following expression of the conductivity:

$$\sigma = \frac{g_s g_v e^2}{h} N = \frac{g_s g_v e^2}{h} \frac{W k_F}{\pi} \propto \sqrt{n} . \tag{1.21}$$

The sub-linear dependence of the conductivity with the carrier density has been observed experimentally on suspended graphene samples after electrical annealing, Fig. 1.6 (b). It goes along with a very long electronic mean free path of the order of 1 μm and an extremely large electronic mobility in the range of 170 000 $\mathrm{cm}^2\ \mathrm{V}^{-1}\ \mathrm{s}^{-1}$. The non-zero minimum of conductivity at zero energy (i.e. for vanishing charge carriers concentration) and the huge mobility obtained on clean devices constitute some of the remarkable electronic properties of graphene.

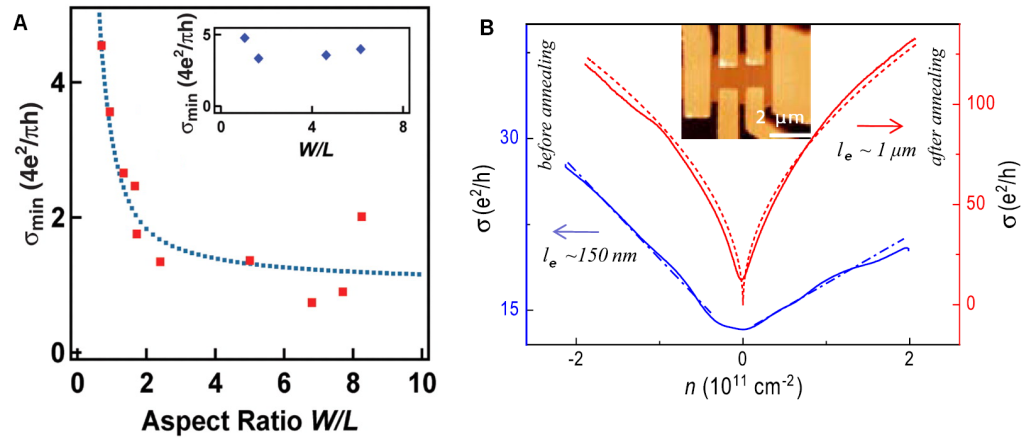

Figure 1.6: **(a)**, σ_{min} (in units of $4e^2/\pi h$) versus the device aspect ratio W/L. Red squares are experimental results in small monolayer devices. The dotted line is calculated from eq. (1.20). Inset: same measurement for large monolayer devices (blue diamonds). Adapted from [F. Miao 2007]. **(b)**, Conductance of a suspended graphene sample before (blue) and after (red) electrical annealing as a function of the carrier density, measurement performed at 40 K. Inset: AFM image of the suspended device. Adapted from [Bolotin 2008].

1.2 Graphene Nanoribbons Electronic Structure and Transport

Graphene nanoribbons (GNRs) result from the cutting of a graphene sheet into stripes with parallel edges and with width sizes in the nanometric scale. In Fig. 1.7, we illustrate the possible edge symmetries: zigzag (b), armchair (c) and a mix of armchair and zigzag (d).

The lateral size reduction is responsible for the electronic confinement. If we go back to basic considerations, the straightforward consequence of an electronic confinement along a given direction, let us say y, is to introduce hard-wall boundary conditions, also called Dirichlet conditions, on the electronic wave functions. Following the simplest picture of an electron in a box, the electronic wave functions along Oy are defined by $\phi(y)_n \propto \sin(k_n y)$ with quantized allowed wave vectors $k_n = n\pi/W$. Here, W is the width of the confinement and n, an integer.

If we consider a confinement along the y direction of a graphene sheet with zigzag edges, Fig. 1.8 (a), the energy spectrum is modified by the quantization of the transverse momentum and we obtain a set of 1D dispersive subbands defined by $E \approx \hbar v_F \sqrt{k_y^2 + (n\pi/W)^2}$. This new band structure can be seen as projections of the 2D graphene band structure along the k_y axis (blue lines Fig. 1.8 (b)).

Close to the CNP, on each projection,the two valleys at **K** and **K′** are preserved (Fig. 1.8 (c)-right). However, the projections alone do not allow to account for the flat bands at zero energy (localized states) deduced from tight-binding simulations.

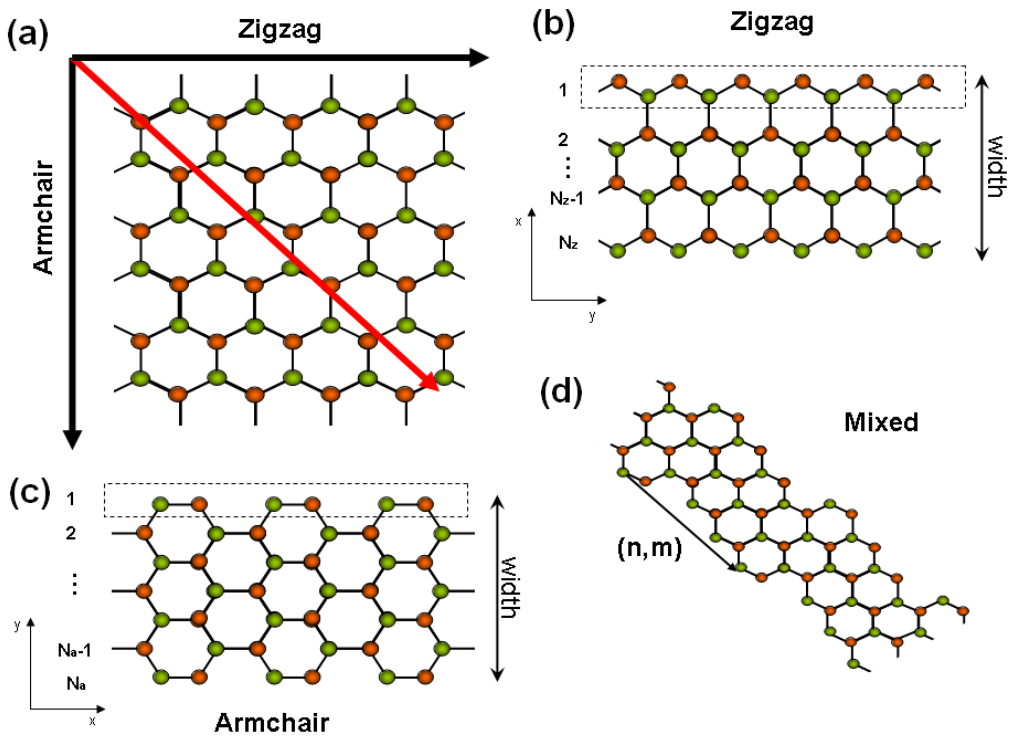

Figure 1.7: **(a)**, graphene monolayer. **(b)**, zigzag GNR. **(c)**, armchair GNR. **(d)**, GNR with mixed edges characterized by the edge vector (3,1).

This means that a deeper study of the band structure is needed.

Now,for armchair edges with a confinement along the x direction (Fig. 1.8 (a)), the energy spectrum is approached by $E \approx \hbar v_F \sqrt{k_x^2 + (n\pi/W)^2}$. The new band structure corresponds to projections of the 2D graphene band structure along the k_x direction (Fig. 1.8 (b)). In this direction, the $\mathbf{K}$ and $\mathbf{K'}$ points are superimposed at the center of the Brillouin zone. The tight-binding calculation (summarized after) will give evidence of the admixing of the two valley in the armchair configuration (Fig. 1.8 (d)-right).

For GNRs, the minimum energy separation between the 1D sub-bands is expected to be $hv_F/2W \approx 1.9$ eV$/W(nm)$. This value is also the largest expected energy gap between the highest 1D hole subband and the lowest electron subband, that develops when the allowed k_n-vectors do not match with the $\mathbf{K}$ and $\mathbf{K'}$ points.

At this stage, a comparison with the electronic confinement in a carbon nanotube, a roll-up graphene layer, is instructive. Indeed, in case of a tubular geometry, the boundary conditions are fixed by periodicity of the electronic wave functions along the circumference (C_h). This yields to $k_{\mathrm{n,CNT}} = 2\pi n/C_h = 2 \times k_{\mathrm{n,GNR}}$ when we identify the ribbon width and the CNT circumference. This very rough approach demonstrates that CNT is certainly a better candidate to achieve an ultimate confinement. The situation is even more obvious if one considers the extreme experimental conditions to realize a defect free 1-3 nm wide GNR.

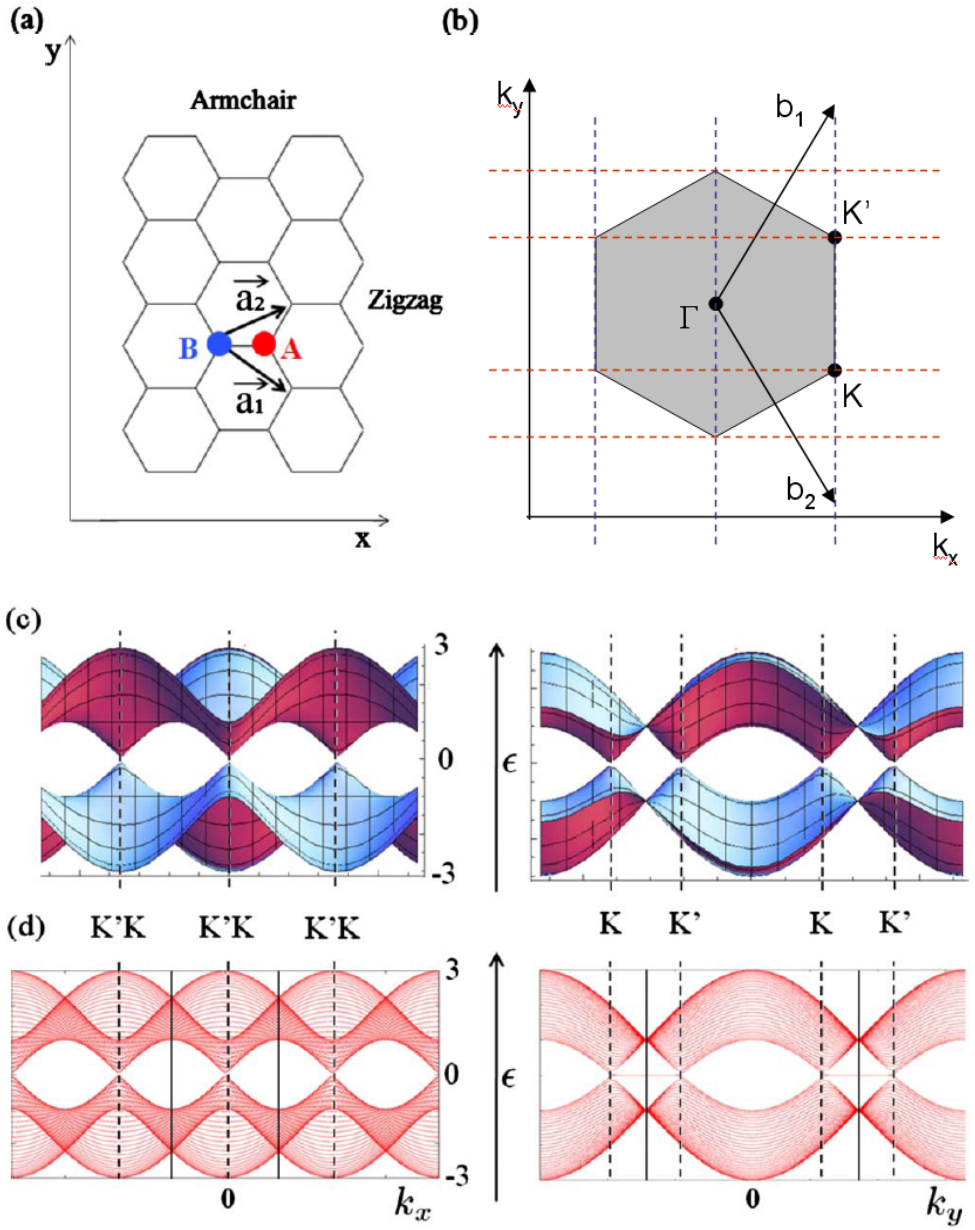

Figure 1.8: **(a)** Graphene crystalline structure with armchair (along x axis) and zigzag (along the y axis) edges. **(b)** First Brillouin zone for graphene with projections along k_x (red dashed lines) and k_y (blue dashed lines) corresponding to armchair and zigzag confinement, respectively. **(c)** Projections of the 2D band structure of graphene along the k_x (left) and k_y (right) axis. **(d)** GNRs energy band structure for armchair (left) and zigzag (right) edges. Adapted from [Delplace 2010].

In the next sections, we study more deeply the electronic structure and transport properties of GNRs, considering the atomic configuration at the edges and the resulting boundary conditions for zigzag and armchair GNR.

1.2.1 Zigzag graphene nanoribbons

The crystallographic structure of a zigzag graphene nanoribbon (zGNRs) is illustrated in Fig. 1.7 (b). The atoms at each edge of the zGNRs, monolayer or bilayer, belong to different sublattices: A (red) on top edge and B (green) on the bottom edge.

The zGNR width can be described in term of the number of zigzag chains between edges, N_z, as: $W_z = (N_z - 1)3a/2$. As we said before, the electronic band structure of a zGNR can not be fully derived from a straightforward projection of the band structure of 2D graphene. Tight-binding simulations have been performed to deduce its band structure [Deretzis 2011, A. Cresti 2008] with localized states that develop at zero energy (Fig. 1.9). These states are not related to the electronic confinement. They have been already evidenced on finite graphite segments with zigzag terminations [Fujita 1996].

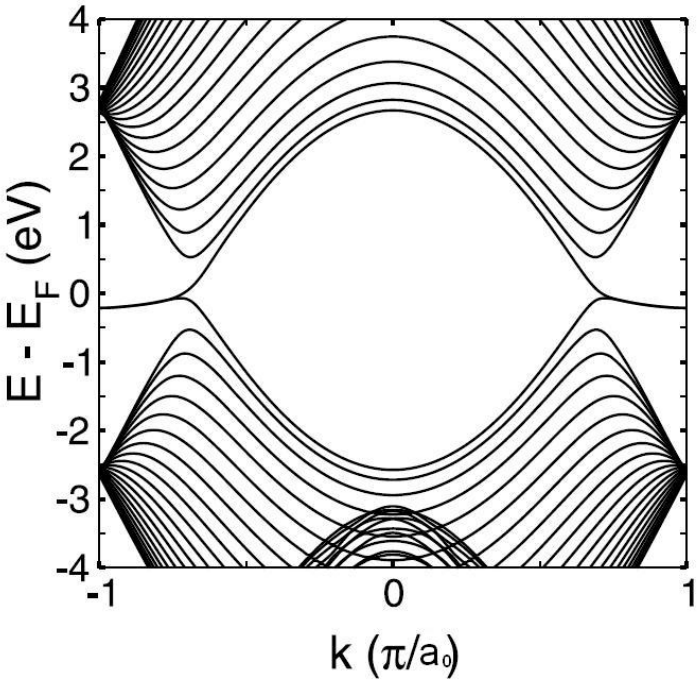

Figure 1.9: Energy dispersion of a monolayer 22-zGNR within the extended Hückel theory. Adapted from [Deretzis 2011].

We study the zGNRs band structure through the Dirac Hamiltonian around the **K** and **K′** points, which reads in momentum space [Castro-Neto 2009, Brey 2006]:

$$\mathcal{H}_{K(K')} = v_F \begin{pmatrix} 0 & p_x \mp ip_y \\ p_x \pm ip_y & 0 \end{pmatrix} = v_F \boldsymbol{\sigma} \cdot \mathbf{q}\,. \tag{1.22}$$

The wave function, in real space, for sublattice A (B) is given by:

$$\Psi_{A(B)}(\mathbf{r}) = e^{i\mathbf{K}\cdot\mathbf{r}}\psi_{A(B)}(\mathbf{r}) + e^{i\mathbf{K}'\cdot\mathbf{r}}\psi'_{A(B)}(\mathbf{r}) \tag{1.23}$$

where $\psi_{A(B)}$ is the component of the spinor wave function of the Hamiltonian around the $\mathbf{K}$ point and $\psi'_{A(B)}$ around the $\mathbf{K}'$ point. GNR's edges are parallel to the y axis and the translational symmetry guarantees that the spinor wave function is written as:

$$\psi(\mathbf{r}) = e^{ik_y y}\begin{pmatrix}\phi_A(x)\\ \phi_B(x)\end{pmatrix}. \tag{1.24}$$

For zigzag edges, atoms at each edge of the ribbon belong to different sublattices, this determines the boundary conditions, the wave function for the sublattices A and B will vanish just in one edge of the system:

$$\Psi_A(x=0) = 0, \qquad \Psi_B(x=W) = 0\,, \tag{1.25}$$

these boundary conditions are satisfied for any x by the choice

$$\phi_A(0) = \phi'_A(0) = \phi_B(W) = \phi'_B(W) = 0\,. \tag{1.26}$$

After some algebra (for more details about the calculations see [Castro-Neto 2009, Brey 2006]), we deduce the transcendental equation for the allowed z-vectors perpendicular to the ribbon:

$$e^{-2zW} = \frac{k_y - z}{k_y + z}\,, \tag{1.27}$$

where $z = \sqrt{k_y^2 - \varepsilon^2}$ can be real or imaginary. Remarkably, the z-vectors and the longitudinal k_y-vectors are coupled. The transcendental equation has real solutions for z, these solutions correspond to edge states and are the electronic states in the almost flat bands of the zigzag ribbons, Fig. 1.9. This flat band gives to zGNRs its metallic behavior. In addition, it is also possible to find pure imaginary solutions of the form $z = ik_n$, leading to:

$$k_y = \frac{k_n}{\tan(k_n W)}\,. \tag{1.28}$$

This solution corresponds to the confined modes in the ribbon. For each solution k_n, there are two confined states with energies $\hat{\varepsilon} = \pm\sqrt{k_n^2 + k_y^2}$ and wave functions defined by:

$$\begin{pmatrix}\phi_A\\ \phi_B\end{pmatrix} = \left\{\begin{array}{c}\sin(k_n x)\\ \pm\frac{i}{\hat{\varepsilon}}[-k_n\cos(k_n x) + k_x\sin(k_n x)]\end{array}\right\}. \tag{1.29}$$

Here, the index n indicates the number of nodes of the confined wave functions. We can examine more closely the transition from confined to extended states in the zGNRs by having a look of the charge density in a semi-infinite graphene flake with zigzag edges. In Fig. 1.10 A-D, a schematic representation of the wave function is proposed. These ones are completely localized at the edge sites when $k = \pi$

which corresponds in the band structure, Fig. 1.9, with the places where upper valence band and lower conduction band touch each other forming a partially flat degenerated band with zero energy.

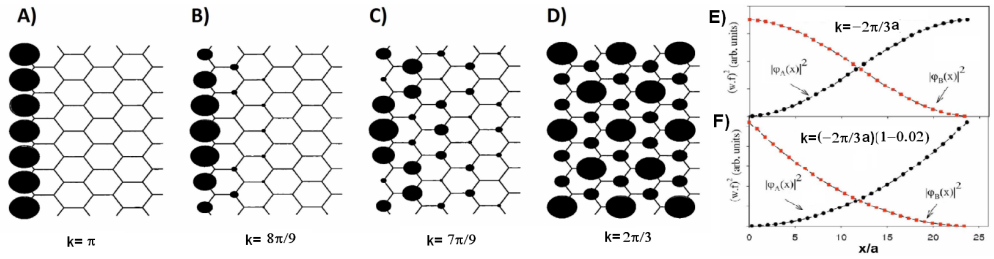

Figure 1.10: Edge states. From **A** to **D** schematic figures of the real part of the analytic solutions for the edges states in semi-infinite graphite, when **A** $k = \pi$, **B** $k = 8\pi/9$, **C** $k = 7\pi/9$ and **D** $k = 2\pi/3$ (from [Nakada 1996]). **E** and **F**: Wave functions for states close to zero energy for zigzag nanoribbons. Adapted from [Brey 2006].

Localized states start gradually to penetrate into the inner sites as k deviates from π, reaching the extended state, where the Dirac points of 2D graphene are projected, at $k = \pm 2\pi/3$. In Fig. 1.10 E - F, the squared wave function for the lowest energy states of a zGNR has been presented (Fig. 1.10-E, correspond to $k = -2\pi/3a$ and F corresponds to $k = -(1 - 0.02) \times 2\pi/3a$). We see that the only difference with the edge state in a semi-infinite graphene flake is that due to the finite width of the ribbon, the wave functions of each sublattice overlap. This overlap generates a small bent in the zero energy band.

The edge states have been evidenced by sub-nanometer-resolved STM (Scanning Tunneling Microscope) and STS (Scanning Tunneling Spectroscopy) [Tao 2011]. Fig. 1.11 A, shows the atomically-resolved edge region of a monolayer GNR allowing an experimental determination of GNR's chirality (here (8,1), a mixed edge, with a dominant zigzag configuration).

The local electronic structure of GNR edge is explored by STS, where dI/dV reflects the energy-resolved local density of states (LDOS). Two peaks rise up in the dI/dV spectrum at the edges, Fig. 1.11 (b). Their amplitude decreases exponentially far from the edge and oscillates parallel to the ribbon's edge with a periodicity of ~ 20 Å, corresponding to the 21 Å periodicity for a (8,1) edge.

Bilayer zGNRs

The band structure of bilayer zGNRs corresponds to two superimposed and somehow deformed band structures of individual monolayers zGNRs (Fig. 1.12). To understand this feature, we first assume that the two graphene layers are decoupled. The system is therefore expected to behave as two isolated monolayer GNRs with all bands in the dispersion relation being doubly degenerate. By turning on the

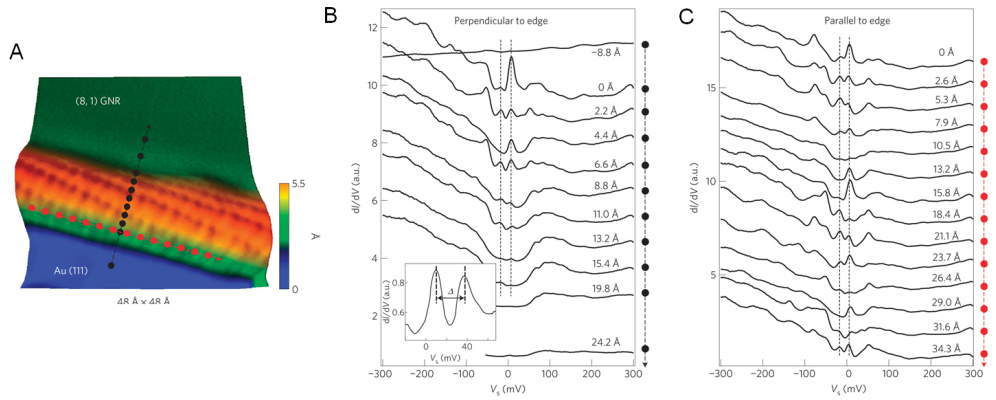

Figure 1.11: **A**, Atomically-resolved STM image of the edge of an GNR of width 19.5±0.4 nm. **B**, dI/dV spectra of the GNR edge shown in A, measured at different points along a line perpendicular to the GNR edge (black dots). Inset: higher resolution dI/dV spectrum for the edge. **C**, dI/dV spectra measured at different points along a line parallel to the GNR edge shown in A (red dots). Adapted from [Tao 2011].

coupling between the two layers the degeneracy of the states is lifted, with the degree of splitting depending on the coupling strength [Xu 2009].

Bilayer GNRs with zigzag edges (assuming Bernal stacking) come in two types depending on their edge alignment, denoted α and β alignment, insets in Fig. 1.12. For α-alignment, the second layer is shifted only in one direction (x direction) while, for β-alignment, the shift is in two directions (x and y). In Fig. 1.12 (a) is plotted the energy spectrum of the α-aligned zGNR of 1 nm width. A gapless structure with a flat band shifted away from $E = 0$ is clearly seen, it occurs roughly at one third the distance from the edge of the Brillouin zone.

The band structure for the β-aligned ribbon is shown in Fig. 1.12 (b), where we observe an almost flat band at the Fermi level, which is also seen in single-layer zGNR calculations.

1.2.2 Armchair graphene nanoribbons

The geometry of the armchair graphene nanoribbons (aGNRs) is illustrated in Fig. 1.7 (c). In this orientation, the width of the ribbon is related to the number of dimers between edges, N_a, by $W_a = (N_a - 1)\sqrt{3}a/2$. Contrary to the zigzag case, the main features of the aGNRs band structure can be deduced from cross-sections of the 2D graphene along the transverse direction, as we saw before.

The electronic states of armchair GNRs is calculated through the Dirac Hamiltonian [Brey 2006] using the appropriate border conditions. Here, the border consists of A-B dimers. As a consequence, the wave function amplitudes vanishes for both sublattices at both edges (Fig. 1.8 (a)):

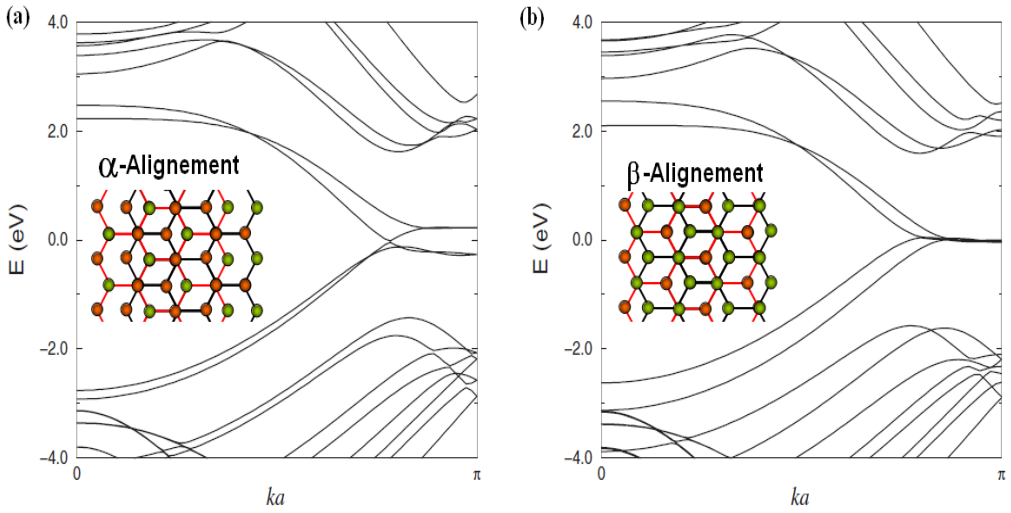

Figure 1.12: Band structure of bilayer ribbons with an α (a) and a β-alignment (b) calculated by a tight-binding model. The width of the ribbon is 1 nm and the Fermi level is set to zero. Insets: crystallographic structures of bilayer zGNRs with α and β-alignment. Adapted from [Sahu 2008].

$$\Psi_A(y=0) = \Psi_B(y=0) = \Psi_A(y=W) = \Psi_B(y=W) = 0\,. \tag{1.30}$$

The boundary conditions are satisfied for any y if

$$\phi_\mu(0) + \phi'_\mu(0) = 0 \quad \text{and} \quad e^{iKW}\phi_\mu(W) + e^{-iKW}\phi'_\mu(W) = 0\,, \tag{1.31}$$

with $\mu = A, B$. As before, after some algebra [Brey 2006, Castro-Neto 2009]. The solutions are:

$$\phi_B = Ae^{ik_n y} + Ce^{-ik_n y} \tag{1.32}$$

$$\phi'_B = De^{ik_n y} + Ee^{-ik_n y}\,. \tag{1.33}$$

By applying the boundary conditions, we deduce the allowed values of k_n given by:

$$k_n = \frac{\pi n}{W} - \frac{4\pi}{3\sqrt{3}a}\,, \tag{1.34}$$

with energies $\varepsilon^2 = k_n^2 + k_x^2$ and n an integer. Note that, in contrast to the results found for zGNRs, the allowed values of k_n do not depend on k_x. Thus, the nanoribbon electronic spectrum consists of a set of 1D branches labeled by the integer n. The boundary conditions couple the $\mathbf{K}$ and $\mathbf{K}'$ valleys: they merge in one single valley centered in the middle of the Brillouin zone, lifting the valley degeneracy present in 2D graphene (Fig. 1.13).

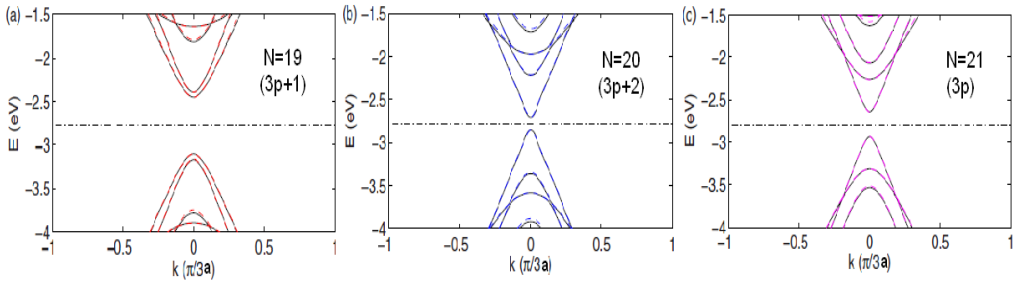

Figure 1.13: Energy dispersions obtained by First-principles (solid line) and third-nearest neighbor tight-binding (dashed line) for three GNRs, with N=19 (a), 20 (b) and 21 (c). Adapted from [Gunlycke 2008].

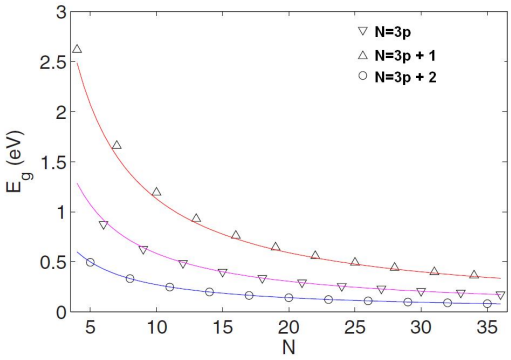

Figure 1.14: Band gaps for graphene nanoribbons with different widths (between 0.5 and 4.2 nm, corresponding to 5 and 35 dimmer chains, respectively). The open symbols and solid curves represent first-principle data and analytical expressions, respectively. Adapted from [Gunlycke 2008].

By using the expression (1.34), we study the energy of the system around $k_x = 0$, where the lower conduction band and upper valence band are closer. The energy gap depends on the ribbons width and comes in three families $N_a = 3p$, $3p+1$ and $3p+2$, where p is an integer. In this approach, there is a family of ribbons with states at zero energy. However, tight-binding calculations taking into account the third-nearest neighbor [A. Cresti 2008, Gunlycke 2008], ab initio [A. Cresti 2008] and first principle local-density functional calculations [Gunlycke 2008] reveal the existence of an energy gap for all aGNRs, as shown in Fig. 1.13.

We finally give the analytical expressions of the dependence of the energy gap, for the three families, with the width of the ribbon, the first and the third nearest neighbor hopping parameters (γ_{1NN} and γ_{3NN}) and the distortion parameter, $\Delta\gamma_1$ [Gunlycke 2008]:

$$E_{g(3p)} = -\frac{3(\gamma_3 + \Delta\gamma_1)a}{W}, \tag{1.35}$$

$$E_{g(3p+1)} = -\frac{\pi(\gamma_1 - 2\gamma_3)a}{\sqrt{3}W} - \frac{3(\gamma_3 + \Delta\gamma_1)a}{W}, \tag{1.36}$$

$$E_{g(3p+2)} = -\frac{\pi(\gamma_1 - 2\gamma_3)a}{\sqrt{3}W} + \frac{3(\gamma_3 + \Delta\gamma_1)a}{W}. \tag{1.37}$$

The gap hierarchy $E_{g(3p+1)} > E_{g(3p)} > E_{g(3p+2)}$, as it can be observed in Fig.

1.14. where the energy gap values are plotted for different ribbon widths, between 0.5 and 4.2 nm, corresponding to 5 and 35 dimmer chains, respectively. For the three families of ribbons, the dependence on the inverse of the ribbon width is preserved. From Fig. 1.14, we extract $E_g = \alpha/W(nm)$ where $\alpha \sim 0.2 - 1.5$ eV nm. These values are in good agreement with the gap deduced from transport experiments [Han 2007]. The experimental data were well fitted by $E_g = \alpha/(W - W^*)$, with $\alpha = 0.2$ eV nm and $(W - W^*)$ is interpreted as the active GNR width participating to the charge transport.

Bilayer aGNRs

As in the case of bilayer zGNRs, the electronic structure is strongly dependent on layer alignment (α or β-alignment), illustrated in inset of Fig. 1.15. The border conditions for the bilayer systems, respect to monolayer, do not change, only the coupling between layers is added.

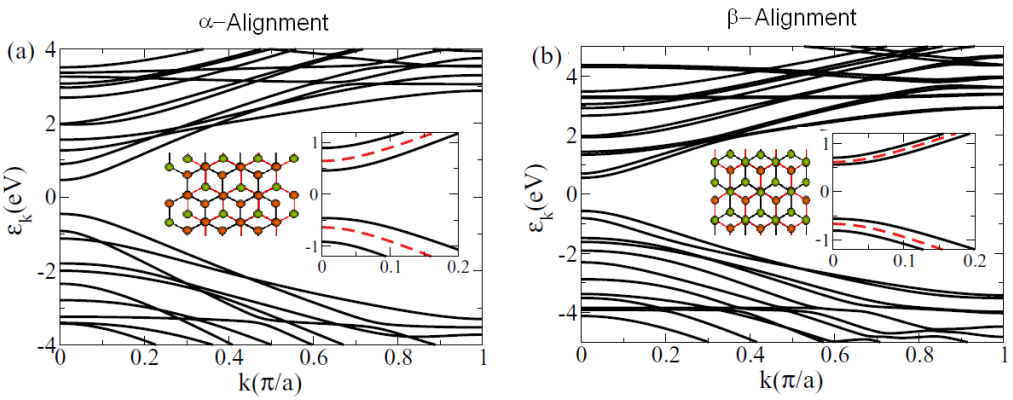

Figure 1.15: Band structure of (a) bilayer aGNR with α alignment and (b) β-alignment (N=11), obtained by the Pariser-Parr-Pople- Restricted Hartree-Fock approach. The right hand insets contains the magnified band structure near the Fermi energy for each band structure and, in dashed line (red), the band structure of a monolayer aGNR of the same width. Also in insets, the crystallographic structure for both alignments. Adapted from [Gundra 2011].

In Fig. 1.15, are presented the band structures for bilayer aGNRs with α and β alignments. When we compare with the monolayer (inset in red in the two figures) we see that in presence of the second layer, each band splits into two bands, thus reducing the energy gap.

One notes that the gap energy reduction is higher for the α case, suggesting that a larger perturbation introduced by the second layer in the α case. A geometrical explanation has been given by [Gundra 2011]. For the α-case, the difference with respect to the AA stacking (stacking with more layer interaction) is less because the layers are only displaced in one direction, while in the β-alignment, the layers are displaced in both directions, resulting in a larger misalignment. Therefore, in the

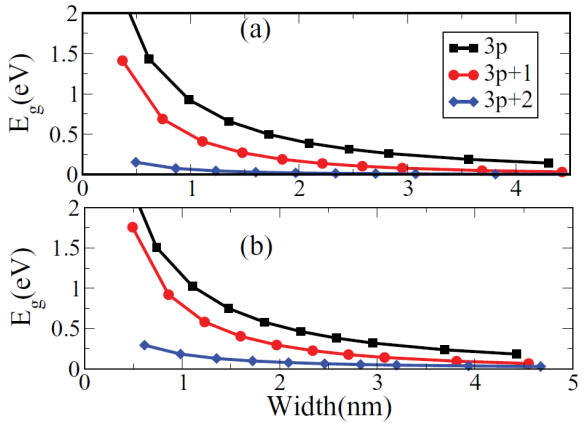

Figure 1.16: Variation of the energy gap with the width for bilayer aGNRs, obtained by the tight-binding method for (a) α and (b) β alignment. Adapted from [Gundra 2011].

α-alignment, the layers interact with each other more than those in β case, resulting in a smaller energy gap.

The energy gaps in bilayer are, in general, smaller than those of monolayer aGNRs due to the interlayer coupling [Gundra 2011] (Fig. 1.16). Three families of bilayer aGNR are also deduced with non of them metallic. The energy gap also follows an inverse dependence with the width of the .

1.2.3 Electronic transport in pristine GNRs

The electronic transport in ideal GNRs is directly related to the band structure since the conductance is determined by the number of propagating modes at the Fermi energy. Indeed, in the ballistic regime, the two-probe conductance of a 1D confined system (Fig. 1.17 a) is easily described by the Landauer formalism.

1.2.3.1 The electronic transport from the Landauer formalism

The current results from a flux difference (I^+ and I^-) between k^+ and k^- electrons, injected with two different electrochemical potentials $\mu_\pm = E_F \pm eV/2$ (Fig. 1.17 (b)) and is given by [Ferry 2009]:

$$\begin{aligned} I =& I^+ - I^- \\ =& \frac{e}{\pi}\left[\int_0^{\mu_+} f(k^+)v(k^+)T(E)\left(\frac{dk^+}{dE}\right)dE - \int_0^{\mu_-} f(k^-)v(k^-)T(E)\left(\frac{dk^-}{dE}\right)dE\right] \\ =& \frac{e}{\pi\hbar}\int_{\mu_-}^{\mu_+} T(E)dE\,, \end{aligned} \tag{1.38}$$

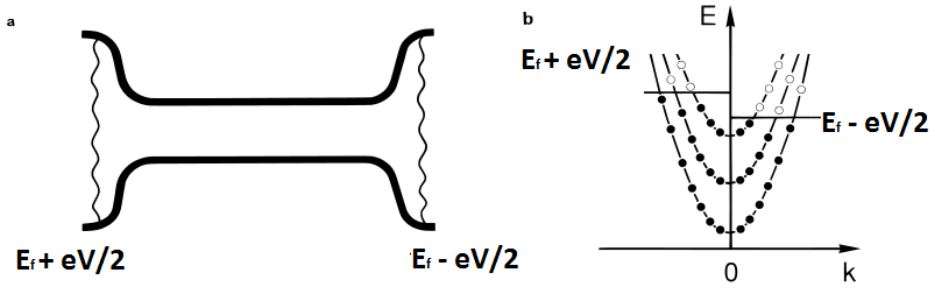

Figure 1.17: **(a)**, Narrow channel with a chemical potential difference between electrodes. **(b)**, Schematic representation of the dispersion relation in the narrow channel. $k > 0$ states are filled up to a chemical potential $E_F - eV/2$ and right-moving states up to $E_F + eV/2$. Occupied states are represented by solid dots and unoccupied states with open dots. Adapted from [Beenakker 1991].

where $T(E)$ is the transmission coefficient, $v(k^{\pm})$ are the velocities and $f(k^{\pm})$ are the reservoir distribution functions characterized by $\mu_{\pm}$. At $T = 0$ K, the conductance is equal to:

$$G = \frac{g_s g_v e^2}{h} \sum_{n=1}^{N} T_n = \frac{g_s g_v e^2}{h} N \,, \tag{1.39}$$

with N the number of conducting 1D bands at E_F. At T$\neq$ 0 K:

$$G(E_F, T) = \int_0^{\infty} G(E, 0) \frac{df}{dE_F} dE = \frac{g_s g_v e^2}{h} \sum_{n=1}^{\infty} f(E_n - E_F) \,. \tag{1.40}$$

Here, E_n denotes the energy of the bottom of the nth subband. The thermal smearing df/dE_F is about $4k_BT$. This means that the conductance steps should disappear when the subband splitting at the Fermi energy is $\Delta E \lesssim 4k_BT$.

As a consequence, the analytical expressions of the conductance in pristine zGNRs (G_z) and aGNRs (G_a) at T=0 K are simply expressed as follow, considering the degeneracies of each system [Onipko 2008]:

$$G_z = (2n + 1)G_0 \tag{1.41}$$

$$G_a = nG_0 \,, \tag{1.42}$$

where the integer $n = 0, 1, 2, ...$ is the number of conducting bands.

In zGNRs, the lower conduction band and the upper valence band touch each other at $E = 0$ and they are just spin degenerated, Fig. 1.18 (a), giving a conductance for zero energy equal to G_0. The rest of the bands are four fold degenerated (2 for spin and 2 for valley) generating steps of $2G_0$ each time a 1D band is added.

For aGNRs, the valley degeneracy is lifted and the opening of an energy gap is present for all the ribbon families. In the plot of the transmission as a function of

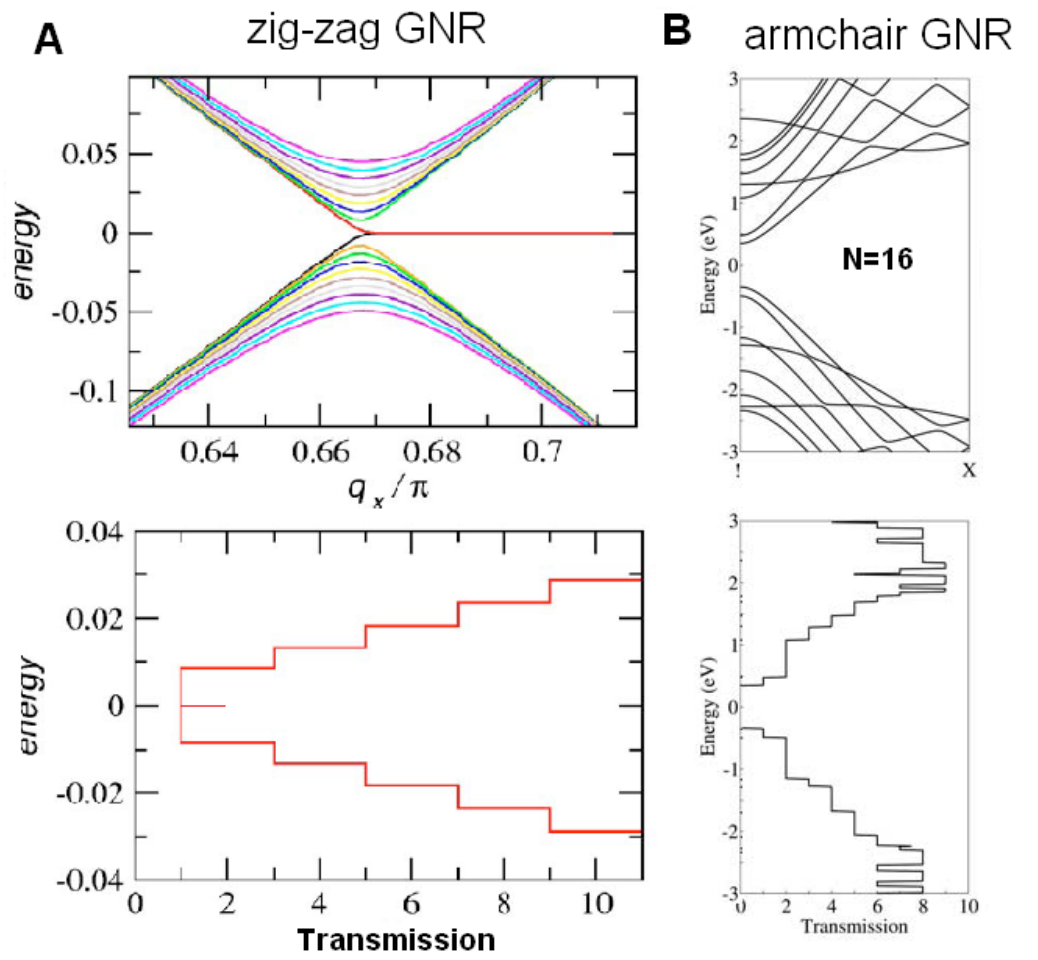

Figure 1.18: **(a)**, One dimensional energy bands (energy in units of t) associated with a zigzag GNR of $N_z = 300$. Lower panels: Transmission (in units of $2e^2/h$) as a function of energy. Adapted from [Peres 2006a]. **(b)**, Band structure and associated transmission (in units of $2e^2/h$) for aGNRs of $N_a = 16$. Adapted from [Dubois S. 2009].

energy, Fig. 1.18 (b), we see the appearance of this energy gap and the transmission in step of G_0, reflecting the valley degeneracy lifting.

In the bilayer case, the analytical expressions for the conductance in zGNRs (G_{bz}) and aGNR (G_{ba}) are given by [Xu 2009]:

$$G_{bz} = 2(n+1)G_0\,, \tag{1.43}$$

$$G_{ba} = nG_0\,. \tag{1.44}$$

1.2.4 Experimental evidence of the 1D electronic band structure of GNRs by electronic transport

During the last five years, tremendous experimental efforts have been devoted to give evidence of the 1D electronic subbands spectrum of GNRs. They mainly consist on conductance measurements on high quality GNR based transistors as a function of the gate voltage V_g. The pioneer and remarkable experimental results are summarized in Fig. 1.19.

In Fig. 1.19 (a), the conductance steps of a 31 nm wide GNR are associated to the gain of extra conducting channels with increasing E_F. In the same plot is presented the conductance simulation (continuous and dashed lines), using the Landauer approach for an aGNR of $N = 256$ ($W \approx 31$ nm), suggesting the validity of the band structure even if the $\mathbf{K}$ and $\mathbf{K}'$ valley degeneracy lifting is not evidenced [Lin 2008]. The steps of the conductance quantizations are of $2tG_0$ where $t = 0.016$ is the transmission coefficient. This extremely low transmission coefficient reveals a large contact resistance and/or strong scattering along the GNR. In this context, the robustness of the 1D subbands signature on the electronic transport is astonishing.

For narrower (11 nm) ribbons [Poumirol 2010], Fig. 1.19 (b), the conductance as a function of gate voltage unveils reproducible modulations superimposed to the overall increase of the conductance. These modulations can be favorably compared with the presence of van Hove singularities for an aGNR of $N = 90 \pm 3$. Here, in the diffusive regime, the divergence of the density of states at the bottom of the 1D subbands induces a drop of the conductance each time the E_F enters into a new subband.

Additionally, more recent experiments on high mobility suspended graphene nano-constrictions, with an estimated width of 200 nm, show a conductance quantization steps of $\sim 2e^2/h$ (Fig. 1.19 (c)). The appearance of plateaus at each G_0 for electrons and holes doping suggest valley degeneracy lifting induced by the confinement [Tombros 2011].

1.3 Summary

The goal of this chapter is to put together the main characteristics of the graphene nanoribbons band structure and electronic transport.

We gave evidence of some marked differences between the zigzag and armchair GNRs, concerning their energy spectra: for zigzag, the valley degeneracy is preserved while localized states develop, at zero energy, at the edges. In case of armchair, we stress the opening of an energy gap and the coupling of the valleys which give rise to a degeneracy lifting.

Pioneer experimental transport measurements already gave some evidence of 1D subbands driven by the confinement. At this stage, no clear signature of the atomic configuration at the edges has been observed. The disorder in real GNR certainly play a major role. In that respect, we propose, in the next chapter to study the influence of the main sources of disorder in aGNR and zGNR.

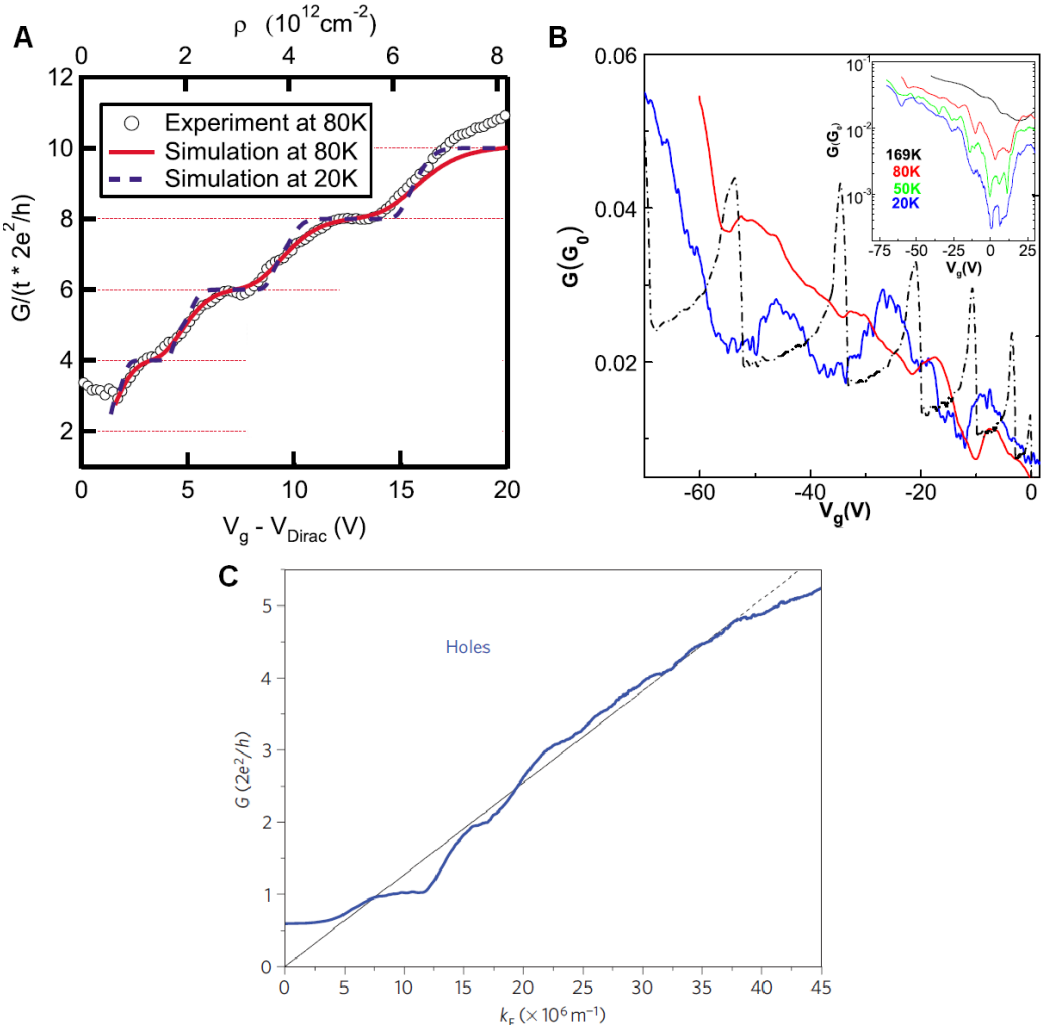

Figure 1.19: **(a)**, Measured conductance as a function of back-gate voltage (low axis) and carrier density (upper axis) for a GNR of $W = 31$ nm and numerical simulations for an aGNR with $N_a = 256$. Here, t is the transmission coefficient for each subband. Adapted from [Lin 2008]. **(b)**, Conductance versus back-gate voltage at 80 K measured on a 11 nm wide GNR for two V_b, 50 mV (red) and 1 mV (blue). The density of states for a $N = 90$ aGNR is superimposed (dashed line). Inset: $G(V_g)$ at several temperatures. Adapted from [Poumirol 2010]. **(c)**, Conductance as a function of the Fermi wave number for holes in a suspended graphene nanoconstriction at 4.2 K. Inset: conductance as a function of the Fermi wave number for electrons. Adapted from [Tombros 2011].

Chapter 2

Scattering and Electronic Transport in Disordered GNRs

Contents

In this chapter, we review the main effects of disorder on the electronic transport properties of GNRs: decrease of the conductance, drop of the carrier mobility and opening of a transport gap. The disorder also induces mesoscopic effects like quantum interference between electron wave functions, which manifested themselves by conductance fluctuations and weak (anti)localization. The specificities of graphene based devices will be briefly presented.

Graphene layer is known to have only few lattice defects, however, extrinsic disorder is regularly present in graphene based devices, limiting its carriers mobility. The most common sources of disorder are originate from the synthesis method, the graphene flakes' support (substrates) and the chemical contamination from the production of field effect devices (e. g. polymer resist, solvents and patterning process).

2.1 Electronic transport in disordered graphene

The Hamiltonian of pristine graphene, eq. (1.6), is invariant under translation, rotation, time reversal and chiral symmetry in the isospin space. When disorder is introduced, translation, rotation and other symmetries, depending on the nature of disorder, are broken (e.g. nonmagnetic disorder may break all the symmetries except the time-reversal) [Mucciolo 2010]. The effects of disorder in graphene can be distinguished according to the range of interaction and their effect on the conductance, depending on the carrier density.

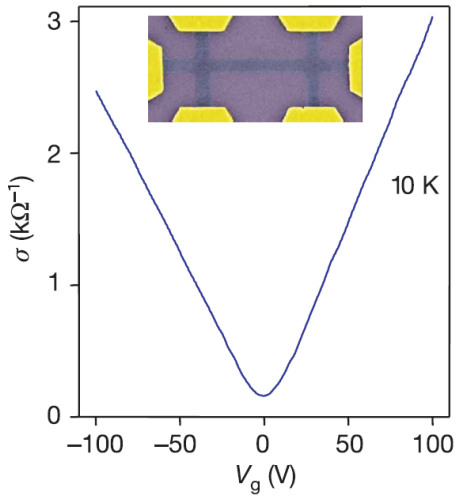

Figure 2.1: Conductivity as a function of back-gate voltage at T=10 K. Inset: optical micrography of the sample. Adapted from ref. [Novoselov 2005].

Transport at low carrier density

The electronic transport close to the charge neutrality point has some exceptional properties. When the disorder is sufficiently smooth, varying only over length scales larger than the lattice constant, it is called *long-range disorder*. It may come from: charge impurities located at (or not far from) the interface between the graphene layer and the oxide substrate. This local fluctuation of the electrostatic potential creates puddles of electron/holes in the graphene flake, with an average size of $\sim$ 30 nm [J. Martin 2008]. In this case, the two valleys present a little mixing, making localization due to quantum interference absent (inter-valley scattering and therefore backscattering is negligible). Since, in the presence of long-range potential fluctuations, carriers move across charge puddles (Klein tunneling, section 1.1.1).

In the case of non-chiral, *short-range* scattering (e.g. localized defects, neutral impurities or adsorbate at the atomic scale), the symmetry of the A-B sublattices is broken and the inter-valley mixing become significant. The neutral impurities or adsorbates can transfer enough momentum to carriers and makes the coupling between the two valleys possible. The most common effect of short-range disorder, at low carrier density, is the reduction, but not the complete suppression, of the conductivity and the presence of localization when the degree of disorder becomes important.

Transport at high carrier density

The effects of the *long-range* disorder in the electronic transport at high carrier density can be studied through the Boltzman model. Assuming a diffusive homogeneous system, we can describe the conductivity as [Das Sarma 2010]:

$$\sigma = \frac{e^2}{2} \int dE \left(-\frac{\partial f}{\partial E} \right) \rho(E) v_F^2 \tau(E) \,, \tag{2.1}$$

where $\rho(E) = g_s g_v E_F/(2\pi\hbar^2 v_F^2)$ is the density of states, $f(E)$ is the Fermi-Dirac distribution function and $\tau(E)$ is the relaxation time. The Fermi energy is calculated self-consistently to conserve the total number of electrons. At $T = 0$, we express the conductivity in a diffusive system as:

$$\sigma = \frac{e^2 v_F^2}{2} \rho(E_F) \tau(E_F) \,. \tag{2.2}$$

For a Coulomb potential (charged impurities), the relaxation time (for more details see [Castro-Neto 2009]) is expressed by:

$$\tau(E_F) = \frac{v_F}{u_0^2} k_F \,, \tag{2.3}$$

where u_0 is the strength of the scattering potential. Substituting the relaxation time, the density of states and the expression for the Fermi wave-vector $k_F = \sqrt{4\pi n/g_s g_v}$, in eq. (2.2), we obtain the conductivity:

$$\sigma = \frac{e^2 v_F^2}{\hbar u_0^2} n \tag{2.4}$$

This, explains very well the linear dependence of the conductivity with the carrier density (or gate voltage) observed experimentally (Fig. 2.1 (a)). In such a case, the mobility is charge density independent. It also explain the change from linear to sub-linear ($\propto \sqrt{V_g}$) dependence of the conductance with the gate voltage in suspended samples before and after electrical annealing (Fig. 1.6 (b)) [Bolotin 2008].

Let's see now the effects of *short-range* disorder, like vacancies, on the conductivity. The scattering with vacancies generates a change in phase space due to midgap states. The transition rate, τ_k, expressed as a function of the phase shift, δ_k, is given by [Stauber 2007]:

$$\frac{\hbar}{\tau_k} = \frac{8 n_i}{\pi \rho(E)} \sin^2(\delta_k) \,, \tag{2.5}$$

where n_i is the impurity density and the phase shift due to scattering with vacancies is:

$$\delta_k = -\frac{\pi}{2} \frac{1}{\ln(k R_0)} \,, \tag{2.6}$$

and R_0 is the radius of the vacancy. This means that for $R_0 k \ll 1$ and at large carrier density $\rho(E) \sim k$, the relaxation time is:

$$\tau_k = \frac{k}{v_F \pi^2 n_i} (\ln(k R_0))^2 \,. \tag{2.7}$$

This leads to a conductivity with a logarithmic density dependence of the form [Stauber 2007]:

$$\sigma = \frac{2e^2}{\pi h}\frac{n}{n_i}(\ln(R_0 k))^2 \,. \tag{2.8}$$

Note that, apart from the logarithmic correction, the conductance has the same behavior as in the case of long-range Coulomb scattering. This dependence has been experimentally observed by Chen et al. irradiating graphene with Ne and He ions to create atomic defects [Chen 2009]. The conductivity in these experiments is well described by this midgap theory.

2.2 Electronic transport in disordered graphene nanoribbons

In this section, we review the main theoretical and experimental results of the electronic transport in disordered GNRs. The conductance drop, with respect to an ideal ribbon, depends on the type of defects (edge defects and long- or short-range bulk defects). In Fig. 2.2 (a)-(c), we show the main numerical results for metallic armchair GNRs when different sources of disorder are introduced. In these simulations, made by [Ihnatsenka 2009], the strength and the concentration of disorder are fixed, as well as the ribbon width, W=30 nm. The conductance is plotted as a function of the energy for different lengths of the sample. As a general trend, when the length is increased, the quantized steps are gradually suppressed and the conductance drops when the localization length starts to be smaller than the sample length.

In case of *bulk vacancies* (Fig. 2.2 (a)), even at small concentrations, the impact on the conductance is very marked. The conductance depends strongly on the energy, the sample length and the vacancy location [Ihnatsenka 2009]. Intra-subbands scattering predominate and the conductance scales in a similar way for all subbands.

When we consider *edge disorder* (Fig. 2.2 (b)), the conductance scales non-uniformly for all the subbands. The edge defects scatter electrons into all subbands equally, giving rise to a strong suppression of the conductance at high energy, when more subbands are available. At the charge neutrality point, a strong suppression of the conductance is observed, which is not only dependent on the disorder concentration but also on the edge orientation [Mucciolo 2009]. In Fig. 2.2 bottom, we remark that the transport gap is less pronounced in case of zigzag GNRs. Indeed, close to the charge neutrality point, the transport is mostly carried by the bulk states making zigzag GNRs less sensitive to edge disorder at low energies [Mucciolo 2009]. The opening of a transport gap due to the edge disorder, for both edge orientations, has been demonstrated numerically to scale approximately with the inverse of ribbons width [Mucciolo 2009].

When *long-range potentials* are considered (Fig. 2.2 (c)), the potential inhomogeneities, due to charged impurities, electron and hole puddles in the GNRs, like in 2D graphene. In this case, the scattering with these impurities mixes the bands and smears conductance steps. As the energy increases, the inter-valley scattering

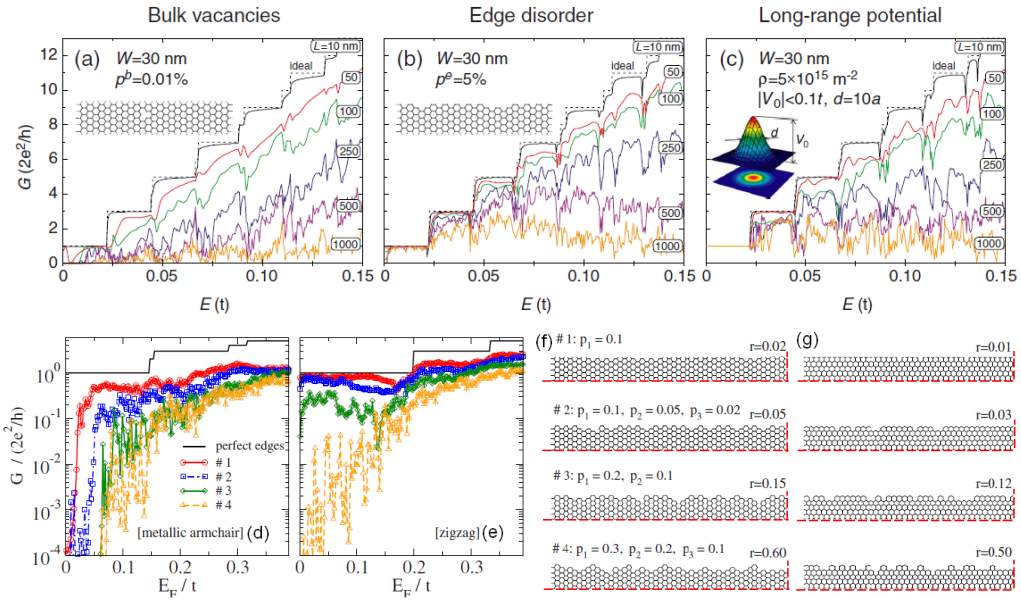

Figure 2.2: **Top**, conductance as a function of the energy for a GNR of width W=30 nm and different lengths L=10, 50, 100, 250, 500 and 1000 nm, with different types of disorder: (a) bulk vacancies, (b) edge disorder, and (c) long-range potential. The dotted lines in (a)-(c) show the conductance quantization for the ideal aGNR. Adapted from [Ihnatsenka 2009]. **Bottom**, conductance as a function of the energy for GNRs with different edge roughness. All GNRs have the same length, the width for armchair is 4.4 nm (d) and 4.7 nm for zigzag (e). Typical edge profile for armchair (f) and for a zigzag (g) (p is related to edge defect density and r is the roughness parameter). Adapted from [Mucciolo 2009].

becomes more efficient with a stronger backscattering for higher subbands in long GNRs. As in the case of edge disorder, when long-range potentials are introduced to the system, different responses are obtained depending on edge symmetry:

In case of zigzag GNRs, the partially flat band at $E = 0$ (edge states) is responsible for a single chiral mode in each valley. This induces a perfect conducting channel, which is preserved in presence of long-range disorder but, it is destroyed in presence of short-range disorder, leading to Anderson localization [Wakabayashi 2007]. The same perfectly conducting channel behavior has been predicted for metallic CNTs [McEuen 1999].

In armchair GNRs, spite the lack of a well separated valleys, a nearly perfect transmission is simulated in presence of long-range scattering at low energy. This is a consequence of the cancellation of scattering matrix terms as a manifestation of the internal phase structure of its wave function [Yamamoto 2009]. For the multichannel regime, the nearly-perfect transmission is not anymore valid.

A model combining edge disorder and potential fluctuations (hole/electron puddles) has been developed to explain the observation of well defined Coulomb di-

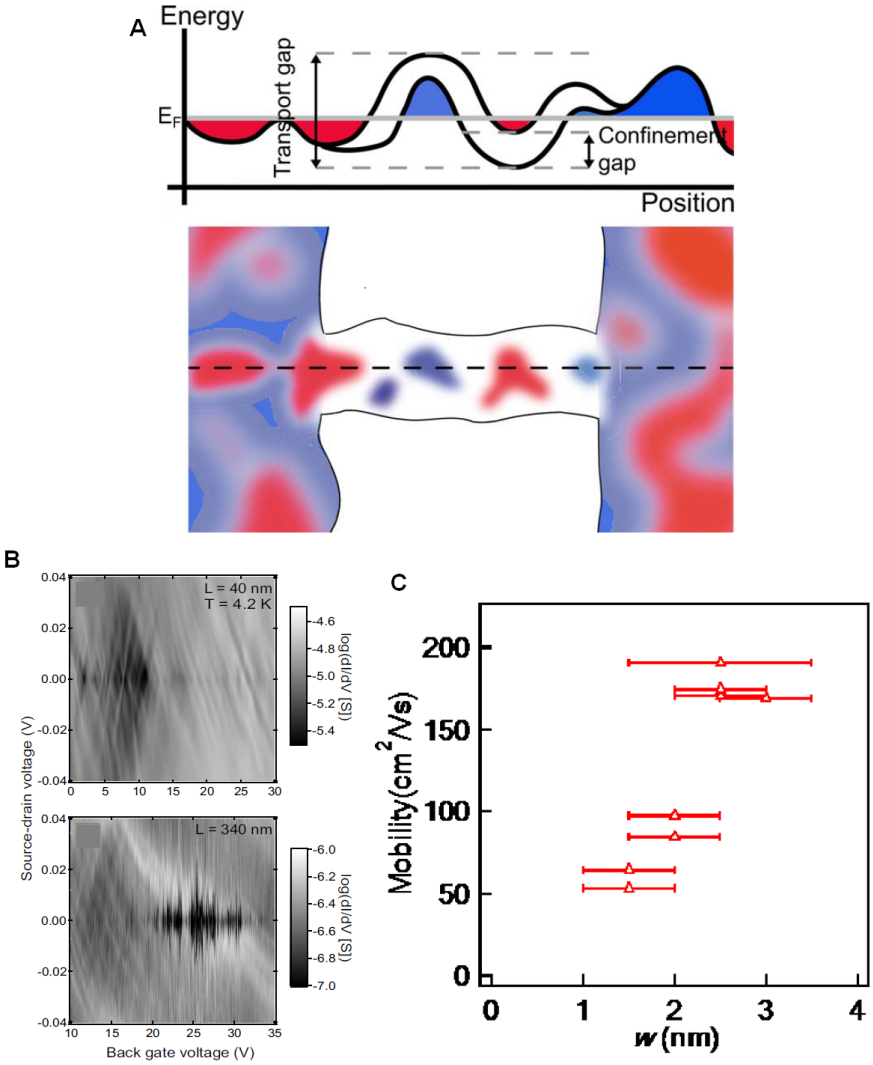

Figure 2.3: **(a)** Illustration of the quantum dots formation along the GNR due to potential inhomogeneities and confinement gap. Red (blue) zones represent electron (holes) puddles. **(b)** Differential conductance versus source-drain and gate voltage measured on GNRs with different lengths. Adapted from [Gallagher 2010]. **(c)**, Experimental field effect mobility as a function of the GNR width. Adapted from [Wang 2008].

amonds, resembling to quantum dots in series or parallel (Fig. 2.3 (a) and (b)). Electron and hole puddles are now isolated by the confinement gap. In the experiments of [Gallagher 2010], the study of GNRs before and after annealing shows a size reduction and a shift of the transport gap closer to zero gate voltage. The transport gap is therefore a consequence of charged impurities (that generate potential fluctuations) plus the confinement gap (Fig. 2.3 (a)).

Another important effect of the disorder is its direct impact on the carrier

mobility. The mobility for ultra-narrow GNRs with smooth edges reaches ~ 200 $\mathrm{cm^2V^{-1}s^{-1}}$ (Fig. 2.3 (c)). This represents a strong decrease of the mobility compare with larger GNRs, $\sim 1500\,\mathrm{cm^2V^{-1}s^{-1}}$ for a 60 nm width [Hettmansperger 2012] and a much higher drop with respect to 2D graphene on Si/SiO_2 substrates where mobilities of $\sim 5 \times 10^4$ $\mathrm{cm^2V^{-1}s^{-1}}$ has been achieved [Zhang 2006, Jiang 2007b].

When the phase coherence length is preserved over long distances, at low temperatures, the scattering by disorder is also responsible for quantum interference between electron wave functions. Those mesoscopic effects on the conductance are described in the following section.

2.3 Mesoscopic effects in presence of disorder

2.3.1 Weak localization

Weak localization (WL) can be understood in term of interference around a diffusive loop between two counter-propagating trajectories. There is a set of elastic scatterers, for which a particle experiences multiple scattering and returns to its original position. Since time-reversal symmetry is present, the particle may follow the original path or its time-reversed path (inset in Fig. 2.4). The interference between these paths is constructive, decreasing the probability of carriers to move forward.

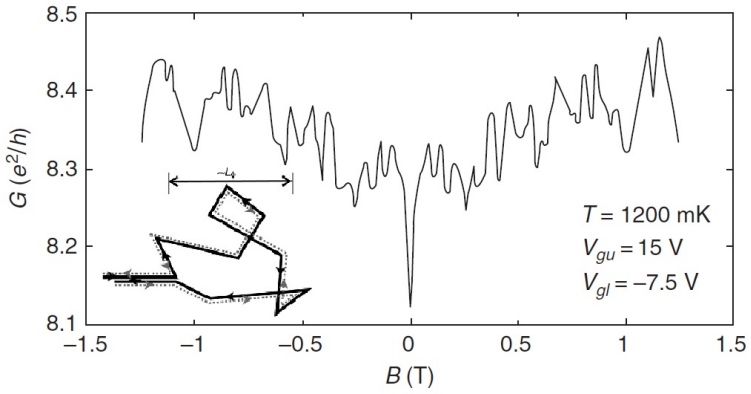

Figure 2.4: Magneto-conductance curve for a short quantum Si wire (V_{gu} and V_{gl} are the upper and lower gate voltages, respectively). The conductance minimum at $B = 0$ is due to the weak localization. Inset: Illustration of the close loop of scattering in which time-reversed paths interfere each other. Adapted from [de Graaf 1992].

In the case of a dirty metals, the weak localization correction to the conductance, in absence of magnetic field, is defined as [Ferry 2009]:

$$\Delta\sigma = -\frac{e^2}{\pi\hbar}\begin{cases} \frac{1}{2\pi}\ln\left(1+\tau_\phi\tau\right), & d=2 \\ l_\phi\left(1-\sqrt{\frac{\tau}{\tau+\tau_\phi}}\right), & d=1 \end{cases} \tag{2.9}$$

where d is the dimension of the system, τ represents the elastic relaxation time and l_ϕ is the phase coherence length defined as, $l_\phi = \sqrt{D\tau_\phi}$, where D is the diffusion coefficient and τ_ϕ is the phase coherence relaxation time.

When a magnetic field is applied, the time-reversal symmetry is broken due to the circulation of the vector potential. This induces a phase shift between the two trajectories and a suppression of the WL, resulting in an increase of the conductance (Fig. 2.4).

According to the relation between the different lengths (the mean free path $l_e = v_F\tau$, the phase coherence length $l_\phi = \sqrt{D\tau_\phi}$, the magnetic length $l_m = \sqrt{\hbar/eB}$, the width W and the length L of the system), we define the transport regime and estimate the critical field, B_c, and the magnetic "lifetime", τ_B, at which the WL contribution is reduced to the half, Table (2.1).

Regime	Length scales	τ_B	B_c
Quasi-2D	$l_e, l_\phi \ll W$	$\frac{l_m^2}{2D}$	$\frac{\hbar}{2el_\phi^2}$
Quasi-1D	$l_e \ll W \ll l_\phi$	$\frac{3l_m^4}{W^2D}$	$\frac{\sqrt{3}\hbar}{Wel_\phi}$
Quasi-Ballistic	$W \ll l_e, \quad Wl_e \ll l_m^2$	$\frac{C_1 l_m^4}{W^3 v_F}$	$\frac{\hbar}{We}\sqrt{\frac{C_1}{Wv_F\tau_\phi}}$
	$W \ll l_e, \quad W^2 \ll l_m^2 \ll Wl_e$	$\frac{C_2 l_m^2}{W^2 v_F}$	$\frac{\hbar}{We}\frac{C_1}{Wv_F\tau_\phi}$

Table 2.1: Expressions for the magnetic relaxation time, τ_B, and critical magnetic field, B_c, according to their transport regime, for weak localization in a channel. The constants depend upon the nature of the boundary scattering, for specular scattering $C_1 = 9.5$ and $C_2 = 4.8$, while for diffusive scattering $C_1 = 4\pi$ and $C_2 = 3$. Adapted from [Ferry 2009].

From Table (2.1) we deduce the WL conductance corrections in presence of a magnetic field. In the 2D case, we have [Ferry 2009]:

$$\Delta G_{WL}^{2D}(B) - \delta G_{WL}^{2D}(0) = \frac{W}{L}\frac{g_s g_v e^2}{4\pi^4\hbar}\left[\Psi\left(\frac{1}{2}+\frac{\tau_B}{2\tau_\phi}\right) - \Psi\left(\frac{1}{2}+\frac{\tau_B}{2\tau}\right) + \ln\left(1+\frac{\tau_\phi}{\tau}\right)\right], \tag{2.10}$$

where $\Psi(x)$ is the digamma function and $g_{s(v)}$ is the spin (valley) degeneracy factor. The weak localization is completely suppressed by the magnetic field when $\tau_B < \tau$. This field, in general, is much weaker than the usual quantum limit where Landau levels are formed.

In the one-dimensional case, $W \ll l_\phi$, the time-reversed trajectories are squeezed by the finite width of the wire. The full expression for the magnetic field dependence of the WL conductivity corrections is then given by [Ferry 2009]:

$$\delta G_{WL}^{1D}(B) = \frac{g_s g_v e^2}{hL}\left(\frac{1}{D\tau_\phi}+\frac{1}{D\tau_B}\right)^{-1/2}. \tag{2.11}$$

All these expressions suffer a series of modifications in case of graphene due to the chirality of its electrons.

Weak localization in graphene

When electrons in graphene perform a close loop without being scattered between valleys (absence of short-range disorder), a change in the relative weight of the two components of the wave function leads to a Berry's phase of π, changing the sign of the amplitude of one path with respect to its time-reversed path, making a destructive interference and suppressing backscattering [Castro-Neto 2009]. In absence of scattering between valleys, a negative magneto-conductance i.e. weak anti-localization (WAL), is therefore expected.

Taking into account intra- and inter-valley scattering (through τ_* and τ_i, the intra- and inter-valley scattering time, respectively) the conductance corrections in presence of a magnetic field is described by the following equation [McCann 2006a]:

$$\begin{aligned}\Delta G_{\text{Graphene}}(B) =& \frac{We^2}{\pi hL}\left[F\left(\frac{\tau_\phi}{\tau_B}\right) - F\left(\frac{1}{\tau_B(\tau_\phi^{-1}+2\tau_i^{-1})}\right)\right. \\ & \left. - 2F\left(\frac{1}{\tau_B(\tau_\phi^{-1}+\tau_i^{-1}+\tau_*^{-1})}\right)\right]\end{aligned} \tag{2.12}$$

where

$$F(z) = \ln(z) + \Psi\left(\frac{1}{2}+\frac{1}{z}\right).$$

In absence of intra and inter valley scattering, in a defect free graphene layer $\tau_{i,*} \to \infty$, the expression (2.12) is totally controlled by the third term, showing a negative magneto-conductance, characteristic of WAL. In the opposite case, where the intra- and inter-valley scattering are strong $\tau_{i,*} \to 0$, both negative terms are suppressed and the first term dominates, corresponding to electron localization.

A simplification of eq. (2.12), for small fields, has been derivate by [Tikhonenko 2009]. From this expression, we deduce that the favorable conditions for WAL are small $\tau_\phi/\tau_{i,*}$ ratios. This means that WAL is possible by decreasing the carrier density (increasing τ_i) or increasing the temperature (decreasing τ_ϕ).

Weak anti-localization has been already observed in high quality graphene samples (Fig. 2.5-Left). These results show a transition from localization to anti-localization, at 14 K and 27 K, when the carrier density is decreased (from region II to I). These means that intra- and inter-valley scattering times increase as the carrier density decreases. However, at 5 K, where the phase coherence length is expected to be larger, anti-localization is not observed because of the high $\tau_\phi/\tau_{i,*}$ ratio, as propose by [Tikhonenko 2009].

For graphene bilayer, anti-localization is not possible due to the non-suppression of backscattering given by a Berry phase of 2π. As a consequence, the third term of expression (2.12) is positive [Kechedzhi 2007]. In this case, the inter-valley scattering is given by $\tau_*^{-1} = 2\tau_z^{-1} + \tau_w^{-1}$ where τ_z is the time of chirality breaking and τ_w is the intra-valley warping time.

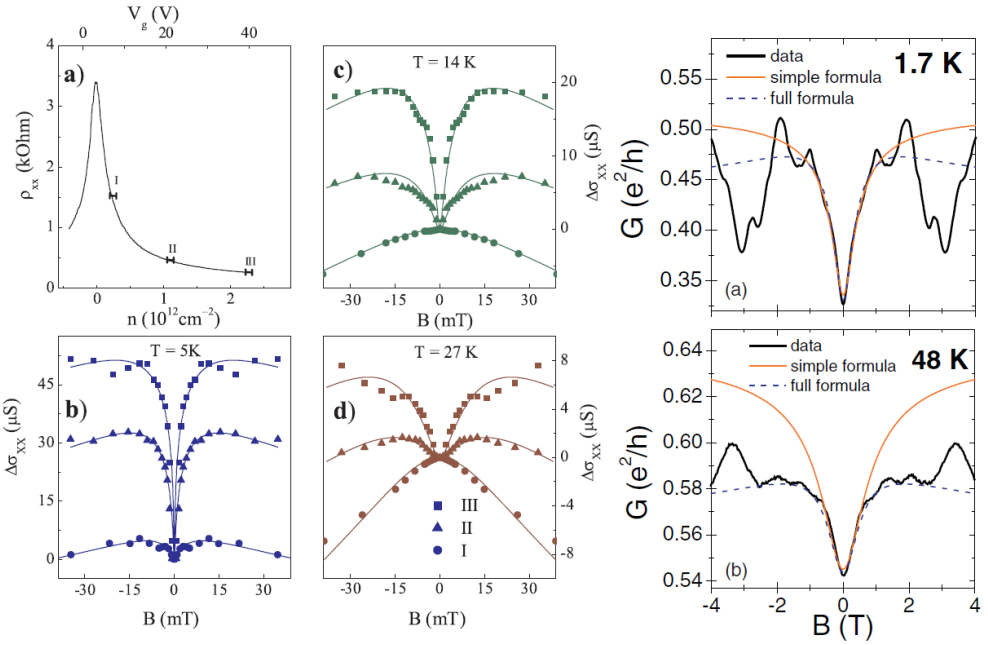

Figure 2.5: **Left**, (a) Resistivity as a function of the carrier density, with the three regions where the magneto-conductance is studied indicated by bars. (b)-(d) evolution of the magneto-conductance with decreasing the electron density at three temperatures: (b) T= 5 K, (c) T=14 K and (d) T=27 K. Adapted from [Tikhonenko 2009]. **Right**, Magneto-conductance for two different temperatures T=1.7 K (a) and 48 K (b). Experimental curves (black) are fitted using the 1D expression for weak localization in metals eq. (2.11) (orange) and the expression for GNRs eq. (2.13) (dashed blue). Adapted from [Minke 2012a].

In the case of GNRs, we can intuitively argue that unavoidable sharp defects at the edges restore the intra-valley scattering, then making the WL most probable. Recently, an expression for localization corrections in the presence of a magnetic field have been obtained for graphene nanoribbons [Minke 2012a]. This expression takes into account the intra- and inter-valley scattering times in a 1D system:

$$\Delta G_{\mathrm{GNR}}(B) = \frac{2e^2\sqrt{D}}{hL}\left[\left(\frac{1}{\tau_\phi}+\frac{1}{\tau_B}\right)^{-1/2} - \left(\frac{1}{\tau_\phi}+\frac{2}{\tau_i}+\frac{1}{\tau_B}\right)^{-1/2} - 2\left(\frac{1}{\tau_\phi}+\frac{1}{\tau_*}+\frac{1}{\tau_B}\right)^{-1/2}\right]. \tag{2.13}$$

In this equation, as for 2D graphene, when $\tau_{i,*} \to \infty$ WAL is present. In case of intra- and inter-valley scattering are present, WL is restored. Results of the fit of this expression in experimental data on GNRs can be observed in Fig. 2.5-Right. We can see that there is a good agreement for both fitting curves (1D in metal and

1D in graphene) but at higher temperatures it seems to be a better agreement with the recently proposed expression for GNRs [Minke 2012a].

2.3.2 Conductance fluctuations

Universal conductance fluctuations (UCF) occur when a coherent electron wave function scatters repeatedly with fixed scatterers while it travels through a disordered conductor (following all possible paths through the sample). The different paths interfere with each other, creating fluctuations in the conductance as a function of the disorder configuration. They are time independent but sample dependent they behave like a fingerprint of the microscopic configuration of the disorder in the sample [Lee 1987].

When the accumulated phases along these paths are changed by varying the Fermi energy, it induces a change of the interference pattern. The interference are also changed as a function of the magnetic field, because of the vector potential modifying the accumulated phase. This means that we can replace an average over samples with different disorder configurations by an average over conductance values versus field or energy on a given sample. This is called ergodic hypothesis [Lee 1987].

At zero-temperature, the amplitude of the conductance fluctuations is related to the quantum mechanical transmission probability from the incident reservoir to the outgoing reservoir (Landauer formula). The root mean square of the conductance fluctuations is independent of l_e and L and is expressed by [Lee 1987, Beenakker 1991]:

$$\delta G_{\mathrm{rms}} \equiv \frac{g_s g_v}{2} \beta^{-1/2} C \frac{e^2}{h}, \tag{2.14}$$

where the factors $g_{s(v)}$ assume a complete spin (valley) degeneracy, $\beta = 1$ when the time reversal symmetry holds and $\beta = 2$ when is broken. The constant C depends on the sample shape: $C \approx 0.73$ for a narrow channel (L≫W) and C is of the order of $\sqrt{W/L}$ for a wide and short channel (W≫L).

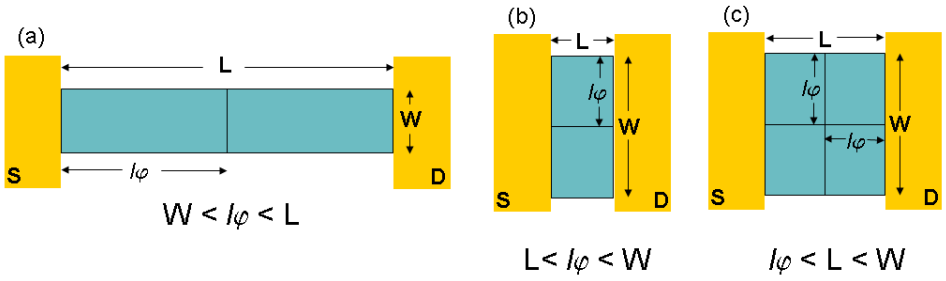

Figure 2.6: Representation of the uncorrelated and coherent segments that subdivide a mesoscopic sample when (a) $W < l_\phi < L$, the segments are in series, (b) $L < l_\phi < W$, in parallel and (c) $l_\phi < L, W$, in both series and parallel. S and D are the source and drain electrodes.

At finite temperature, the amplitude of the UCF is reduced because of the finite phase coherence length and because of the thermal averaging. For a narrow channel, $W < L$ (Fig. 2.6 (a)), if the phase coherence length is smaller than the thermal length ($l_\phi \ll l_T$, where $l_T \equiv \sqrt{\hbar D/k_B T}$), the thermal averaging is neglected and the system is equivalent to L/l_ϕ uncorrelated segments in series. Each one contributes in an incoherente way to conductance fluctuations of the order of e^2/h. Then, the amplitude of the fluctuations is given by [Lee 1987, Beenakker 1991, Gao 1989]:

$$\delta G_{\rm rms} = \sqrt{12}\frac{g_s g_v}{2}\beta^{-1/2}\left(\frac{l_\phi}{L}\right)^{3/2}\left(\frac{e^2}{h}\right), \quad \text{for} \quad W < l_\phi < L, l_T\,. \tag{2.15}$$

When the thermal smearing dominates ($l_T < l_\phi$), the system is still divided into uncorrelated segments and the fluctuations are expressed by:

$$\delta G_{\rm rms} = \left(\frac{8\pi}{3}\right)^{1/2}\frac{g_s g_v}{2}\beta^{-1/2}\frac{l_T l_\phi^{1/2}}{L^{3/2}}\left(\frac{e^2}{h}\right), \quad \text{for} \quad l_T < l_\phi < L\,. \tag{2.16}$$

In the intermediate regime ($l_\phi \approx l_T$), we use the interpolated formula [Beenakker 1991]:

$$\delta G_{\rm rms} = \frac{g_s g_v}{2}\beta^{-1/2}\sqrt{12}\left(\frac{l_\phi}{L}\right)^{3/2}\left[1+\frac{9}{2\pi}\left(\frac{l_\phi}{l_T}\right)^2\right]^{-1/2}\left(\frac{e^2}{h}\right). \tag{2.17}$$

We now generalize to the case where the conductor is divided in W/l_ϕ uncorrelated segments in parallel and L/l_ϕ uncorrelated segments in series, each of them presenting fluctuations of the order of e^2/h (Fig. 2.6 (c)). Neglecting the thermal averaging, the amplitude of the conductance fluctuations is given by [Lee 1987]:

$$\delta G_{\rm rms} \sim \frac{g_s g_v}{2}\beta^{-1/2}\left(\frac{W}{l_\phi}\right)^{1/2}\left(\frac{l_\phi}{L}\right)^{3/2}\left(\frac{e^2}{h}\right), \quad \text{for } l_\phi < L, W\,. \tag{2.18}$$

To calculate the energy scales of the system, we consider that two segments are uncorrelated if after a time t_1, the electrons acquire a phase difference of the order of the unit: $t_1\delta E/\hbar = 1$. During this time, the electrons diffuse over a distance $L_1 = (Dt_1)^{1/2}$. We define the correlation energy, E_c, as the energy necessary to change the phase of electrons, and it is given by [Beenakker 1991]:

$$E_c(L_1) = \frac{\hbar D}{L_1^2}\,, \tag{2.19}$$

where $L_1 = min(L, l_T, l_\phi)$ is the correlation length. In the same way, we deduce the magnetic field necessary to make a phase shift of $2\pi\Phi/\Phi_0 = 2\pi$, where $\Phi_0 = h/e$ is the magnetic quantum flux and Φ is the magnetic flux across the surfaces enclosed by the trajectories. The magnetic field necessary to decorrelate two magnetoconductance fluctuations is given by [Lee 1987]:

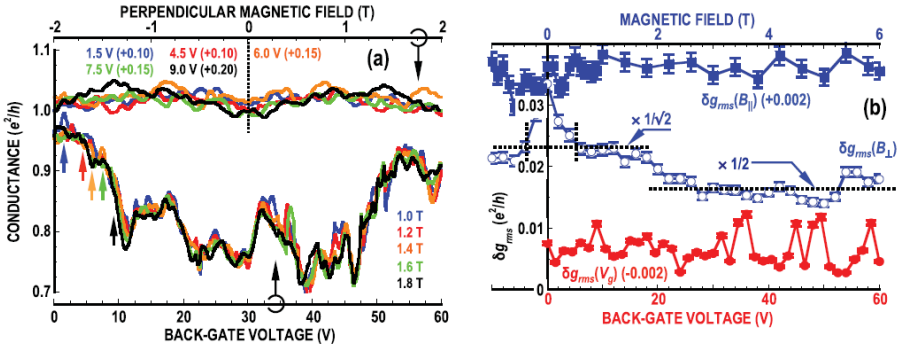

Figure 2.7: (a) Comparison of the conductance fluctuations obtained by sweeping the magnetic field (upper curves) and the gate voltage (lower curves) at 40 mK. Fixed gate voltages and magnetic fields are indicated in the plot. (b) Conductance fluctuations amplitude as a function of the magnetic field (blue curves) and the gate voltage (red curve). Adapted from [Bohra 2012a].

$$\Delta B_c \sim \frac{h}{eS}\,, \tag{2.20}$$

where S is the enclosed surface. According to the distribution of the uncorrelated segments, this surface is given by $S = L_{min}W_{min}$ where $L_{min} = min(L, l_T, l_\phi)$ and $W_{min} = min(W, l_T, l_\phi)$.

Conductance fluctuations in graphene

The theoretical work of [Kharitonov 2008] shows that, in presence of moderate long-range scattering, the amplitude of conductance fluctuations are two times larger than the conventional values for metals. When the concentration of disorder is increased and in case of a strong intra-valley scattering and/or in presence of trigonal warping, the amplitude of the conductance fluctuations is reduced, being $\sqrt{2}$ times greater than in a conventional metal. On the other hand, when inter-valley scattering is introduced, the amplitude of the fluctuations is the same as the one in metals [Kharitonov 2008]. Experimental confirmation of these predictions are still missing.

In Fig. 2.7, we present recent measurements of conductance fluctuations in graphene [Bohra 2012a]. In the (a) part are plotted the conductance fluctuations when the magnetic field and gate voltages are swept. The extracted $\delta G_{\rm rms}$ in the two configurations are quite different (Fig. 2.7 (b)) even when the time reversal symmetry is completely broken ($1/\sqrt{2}$ diminution factor) and the spin degeneracy is lifted (a second decrease of 1/2). This difference is assigned to a non-ergodicity of the conductance fluctuations in graphene [Bohra 2012a].

2.4 Summary

The symmetries of graphene's Halmitonian are responsible for some unique features concerning the electronic transport in presence of disorder.

The impact of different kinds of disorder like vacancies, edge disorder and potential fluctuations has been numerically studied. It shows, as a common characteristic, a drop of the conductance, the lack of quantized plateaus for moderated degree of disorder and a strong reduction of the carrier mobility. The combination of the edge disorder, the potential fluctuations and the energy confinement has been proposed to explain the opening of a transport gap and the formation of quantum dots in series and/or parallel observed in GNRs.

The mesoscopic effects of disorder, related to quantum interference, commonly observed in dirty metals, are also present in graphene. However, the existence of the chiral symmetry gives to graphene special features: the presence of weak anti-localization, when the inter- and intra-valley scattering times are increased and an enhancement of the amplitude of conductance fluctuations when inter-valley scattering is reduced.

Experimentally, weak anti-localization has only been observed in high quality samples but the enhancement of conductance fluctuation has not been measured yet.

In the experimental part of this thesis, the presence of weak localization and conductance fluctuations in GNRs will be analyzed to obtain the characteristic energies of the coherent transport at low temperatures.

Chapter 3

Landau States in GNRs

Contents

In this chapter, we review the effects of a magnetic field applied perpendicular to graphene systems (monolayer, bilayer and GNRs). The formation of Landau states reveal the presence of an anomalous quantum Hall effect intimately related to the band structure of graphene at zero magnetic field. In case of graphene nanoribbons, the electronic confinement and edge configuration influence the Landau spectrum. Such Landau signatures provide unique fingerprints for experimentalists to enlight the edge symmetry.

In a 2D electron gas, the application of a magnetic field may have a profound effect on the electronic band structure and the transport properties. It gives rise to a new fundamental behavior, not observed in a bulk system, the quantum Hall effect (QHE). This phenomenon is a consequence of the Landau level formation in a 2D system. In order to explain the effect of a magnetic field in GNRs, we first start start with the basic concepts of Landau states in 2D electron gas (2DEG) and in 1D waveguides.

3.1 A magnetic field applied perpendicular to a 2DEG: The quantum Hall regime

When a magnetic field, **B**, is applied perpendicular to a 2DEG, the electrons experience a Lorentz force:

$$\mathbf{F} = q\mathbf{v} \times \mathbf{B}\,, \tag{3.1}$$

where **v** is the carrier velocity and q its the charge. Since the Lorentz force is always perpendicular to the velocity, its motion in the absence of other forces is circular, with angular frequency given by the *cyclotron frequency*, ω_c, written as:

$$\omega_c = \frac{eB}{m_c}\,, \tag{3.2}$$

where e is electron's charge and m_c, the cyclotron mass as the electron performs circular orbits in k-space at constant energy. The cyclotron radius at the Fermi energy can be expressed as $r_c = \hbar k_F/eB$ [Beenakker 1991]. Quantum mechanically, the circular orbits associated must be quantized, in analogy with the orbital quantization occurring in the central potential of an atomic nucleus. In other words, the length of the circular orbit has to be a multiple of the de Broglie wave length. As a consequence, the kinetic energy of the electrons become quantized. The single-band effective mass Hamiltonian in presence of a perpendicular magnetic field can be written as [Ferry 2009]:

$$\left[-\frac{\hbar^2}{2m_z}\frac{\partial^2}{\partial z^2} + \frac{1}{2m^*}\left(\frac{\hbar}{i}\nabla_r + q\mathbf{A}\right)^2 + V_{\text{eff}}(z)\right]\psi(\mathbf{r},z) = E\psi(\mathbf{r},z)\,, \tag{3.3}$$

where $\mathrm{m}^*_{(z)}$ is the effective mass, **A** the vector potential and V_{eff}, the effective potential normal to the 2DEG. The solution can be separated as $\psi(\mathbf{r},z) = \varphi(z)\chi(x,y)$, where $\varphi(z)$ satisfies:

$$\left[\frac{\hbar^2}{2}\frac{\partial}{\partial z}\frac{1}{m_z}\frac{\partial}{\partial z} + V_{\text{eff}}(z)\right]\varphi_N(z) = E_N\varphi_N(z)\,, \tag{3.4}$$

and $\chi(x,y)$ satisfies:

$$\left[-\frac{\hbar^2}{2m^*}\frac{\partial^2}{\partial x^2} + \frac{m^*\omega_c^2}{2}(x-x_0)^2\right]\chi(x,y) = E_N\chi(x,y); \quad \text{with} \quad x_o = \frac{\hbar\partial}{ieB\partial y}\,, \tag{3.5}$$

where E_N is the energy associated with the transverse motion. Assuming a solution of the form $\chi(x,y) = \chi(x)e^{ik_y y}$, the center coordinate associated to the center of the circular orbits is $x_0 = \hbar k_y/eB$. The corresponding energy eigenvalues are given by the harmonic oscillator

$$E_N = \left[N + \frac{1}{2}\right]\hbar\omega_c, \qquad N = 0, 1, 2, ... \tag{3.6}$$

where N represents each Landau level associated with a magnetic subband. We calculate the cyclotron radius as a function of the Landau index and the magnetic field:

$$r_N = \left[\frac{2\hbar}{eB}\left(N + \frac{1}{2}\right)\right]^{1/2} . \tag{3.7}$$

From the cyclotron radius of the ground state, we recover the magnetic length $l_m = (\hbar/eB)^{1/2} \approx 25nm/\sqrt{B(T)}$.

The total number of states per unit area in each Landau level, also called the Landau degeneracy, corresponds to the number of quantum flux h/e threading the surface and is given by $D_0 = g_s g_v eB/h$, where $g_{s(v)}$ is the spin (valley) degeneracy factor.

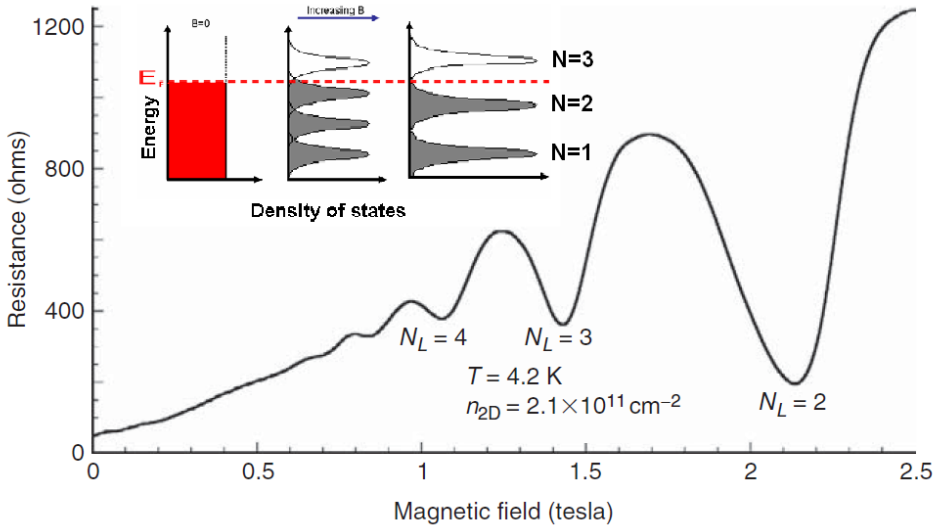

Figure 3.1: Shubnikov-de Haas oscillations in the longitudinal magneto-resistance of the 2DEG formed by a GaAs/AlGaAs heterojunction quantum well. Adapted from [Ferry 2009]. Inset: onset of the Landau levels in a 2DEG.

When we consider the effects of the Landau level formation in the electronic transport measurements, two scenarios are discussed:

Constant magnetic field, as the carrier density is increased, the Fermi energy, E_F, is pinned in the highest occupied magnetic subband until it is completely filled, then jumps to the next Landau level.

Constant carrier density, as the magnetic field increases, the density of states in lowest-lying subbands increases, and at a certain critical field, the highest occupied Landau level becomes depopulated and the Fermi level jumps to the next lower level.

Qualitatively, the crossing of the Fermi energy with a Landau level, shows-up in magneto-resistance measurements and results in an oscillatory behavior, known

as *Shubnikov-de Haas* (SdH) oscillations (Fig. 6.10). Such oscillations are observed only if distinct Landau levels exist, which implies that the broadening of the levels, $\hbar/\tau$, is less than the Landau level spacing, $\hbar\omega_c$. In other words $\omega_c\tau \geq 1$. These oscillations exhibit the well know $1/B$ periodicity given by:

$$\Delta\left(\frac{1}{B}\right) = \frac{g_s g_v e}{nh}, \tag{3.8}$$

where n is the carrier density. In contrast to the bulk SdH effect, there is no mass dependence, and the only variable is the 2DEG carrier density.

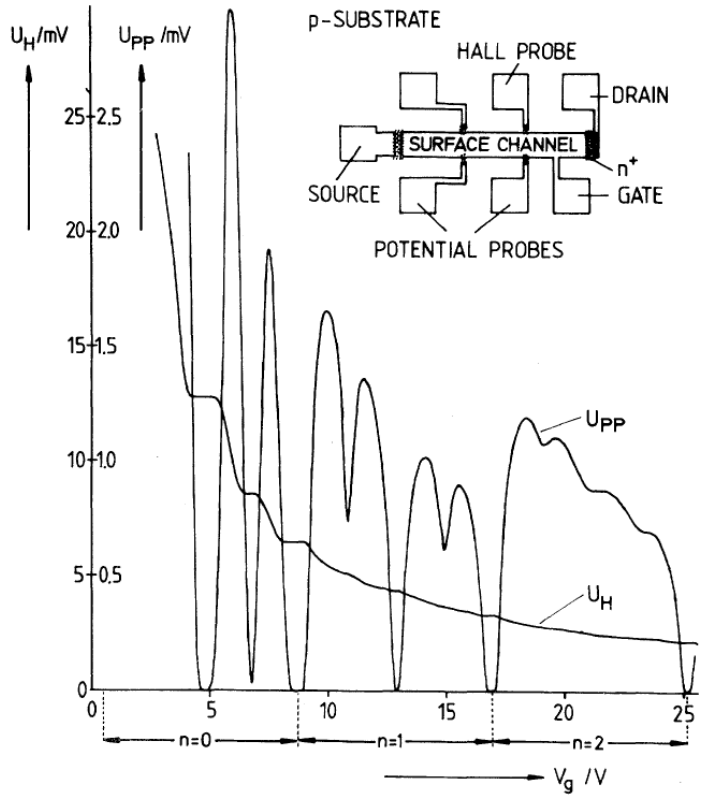

Figure 3.2: Hall voltage U_H, and voltage drop between the potential probes, U_{pp}, as a function of the gate voltage at $T = 1.5$ K and under 18 T. In inset, the device configuration. Adapted from [Klitzing 1980]

Another remarkable behavior is the Hall resistance: when the Landau levels are well defined the Hall resistance saturates at certain values over a wide range of magnetic field. This saturation happens at the same time as the SdH oscillations become distorted and the resistance drops to zero between two maxima, Fig. 3.2. The Hall plateaus resistance are universal, independent on the sample's quality and given by the simple relation [Klitzing 1980]:

$$R_H = \frac{h}{\nu e^2}, \qquad \nu = 1, 2, 3, ... \tag{3.9}$$

where the integer ν corresponds to the number of filled Landau levels (called the filling factor). The extremely high accuracy of these plateaus arises from the one-dimensional transport properties of the edge states that are formed at high magnetic field. In the bulk of these systems the conduction band is essentially flat, independent of position. The corresponding Landau level energies are similarly constant. However, at the boundaries of the sample, the conduction band rises well above the Fermi level and confine the electrons at the edges. They form two counter-propagating edge states spatially separated and acting as one-dimensional channels. The only way in which backscattering can occur is for electrons to be transferred across the entire width of the sample. However, electrons propagating in edge states cannot be easily scattered over distance larger than the magnetic length, $l_m \approx 8$ nm for $B = 10$ T. Therefore, the electrical current through the sample is carried by a fixed number of edge states (corresponding to the number of occupied Landau levels) which propagate as one-dimensional channels in a ballistic regime.

3.2 A magnetic field applied perpendicular to a 1D waveguide

We consider an electron gas confined in one dimension (x) infinite along the y direction and a magnetic field is applied along the z direction. The remaining equation depending on (x, y) has a similar form as before [Ferry 2009]:

$$\left[-\frac{\hbar^2}{2m^*}\frac{\partial^2}{\partial x^2} + \frac{m^*\omega_c^2}{2}(x - x_0)^2 + V(x)\right]\chi(x, y) = E_n\chi(x, y)\,, \tag{3.10}$$

where $V(x)$ is the potential due to lateral confinement and the center coordinate is again $x_0 = k_y l_m^2$. Assuming a parabolic confining potential of the form $V(x) = m^*\omega_0^2 x^2/2$, the energies of the 1D subbands become:

$$E = E_N(k_y) = \left[N + \frac{1}{2}\right]\hbar\omega_c + \frac{\hbar^2 k_y^2}{2M} \tag{3.11}$$

with

$$\frac{\hbar^2 k_y^2}{2M} = \frac{m^*\omega_c^2\omega_0^2}{2\omega^2}x_0^2 \qquad \text{and} \qquad M = m^*\frac{\omega^2}{\omega_0^2} = m^*\frac{\omega_0^2 + \omega_c^2}{\omega_0^2}\,. \tag{3.12}$$

The last term of eq. (3.11) removes the Landau degeneracy. We finally obtain 1D sub-bands, also called magneto-electric sub-bands, with a non-zero dispersion along the y-direction. The group velocity is $v = \hbar k_y/M$. For $\omega_c \gg \omega_0$, the mass M goes to infinity, giving the 2DEG case. For $\omega_c \ll \omega_0$, M goes to the effective mass, m^*, which is just the limit of a quantum wire with no magnetic field.

The wave functions associated with the harmonic-oscillator-type solutions are localized on one of the two sides of the wire, depending on the center coordinate, which in turn, depends on the sign of k_y. Therefore, the flux probability in one

direction is localized on one side of the wire, while states with a flux propagating in the opposite direction are localized on the opposite side.

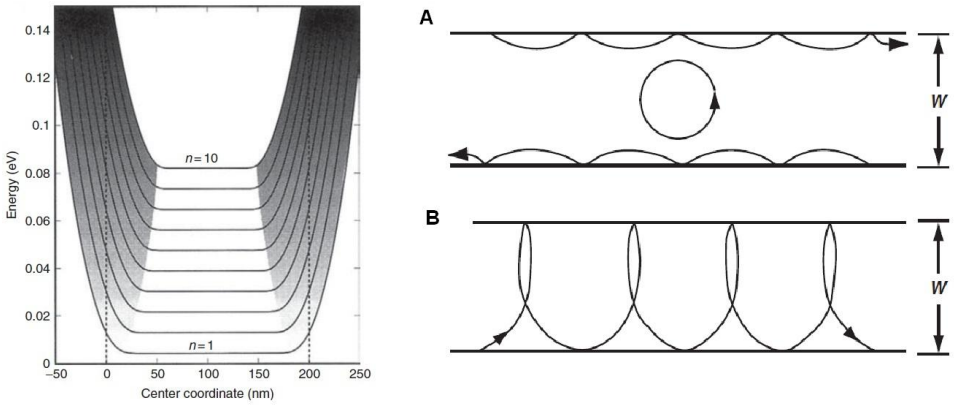

Figure 3.3: **Left**, calculated energy versus center coordinate for a 200-nm-wide wire under 5 T. The shaded regions correspond to skipping orbits. **Right**, three types of orbits in a confined structure: **A** cyclotron and skipping orbits and **B** traversing orbits. Adapted from [Ferry 2009].

We now consider a hard wall confinement in the transverse x-direction $V(x) = 0$ for $0 < x < W$ and $V(x) = \infty$ otherwise. The exact solution cannot be expressed analytically. In Fig. 3.3-left, we see that the dispersion relation, for a hard wall confinement, is almost flat in the middle of the waveguide and shows a strong dispersion close to the edges. This behavior can be interpreted from the classical motion of a particle in a waveguide, as shown in Fig. 3.3-right (a). Depending on the cyclotron radius at the Fermi energy, r_c, and the center coordinate, x_0, we can distinguish three types of trajectories: pure cyclotron orbits, skipping orbits and traversing orbits. In case of pure *cyclotron orbits*, the electronic states correspond to the flat regions of the dispersion curves shown in Fig. 3.3-left. If the distance from the center coordinate to a wall is less than the cyclotron radius the *skipping orbits*, refered as edge states, develop (Fig. 3.3-Right (a)). They corresponds to the shaded regions of the dispersion curves (Fig. 3.3-left). Finally, for a higher energy, the cyclotron radius sufficiently large, so that the electron perform *traversing orbits* (Fig. 3.3-Right (b)) and interact with both boundaries.

3.3 Integer quantum Hall effect in 2D graphene systems

In this section, we review the anomalous quantum Hall effect of 2D graphene monolayer and bilayer. We also briefly present the main experimental results in quantum Hall effect and degeneracy lifting on these systems.

3.3.1 QHE in graphene monolayer

The unique properties of the quantum Hall effect in graphene are among the most striking consequences of the Dirac nature of the massless low energy fermionic excitations in graphene. If the 2D Dirac equation is solved in presence of a magnetic field, the Landau level energies are given by:

$$E_N = \mathrm{sgn}\,(N)\sqrt{2e\hbar v_F^2 B|N|}, \tag{3.13}$$

where N represents an electron-like ($N > 0$) or a hole-like ($N < 0$) index (Fig. 3.4-top). In contrast to the 2DEG, there is a Landau level at zero energy. This level is shared by both electrons and holes. It is the responsible for the anomalous quantization rule of the Hall effect with a 1/2 shift:

$$R_H = \frac{h}{g_s g_v e^2(|N| + 1/2)}\,. \tag{3.14}$$

The zero energy Landau state is a direct consequence of the chiral nature of Dirac Fermions. For a given quasiparticle momentum $\mathbf{p} = (p\cos\varphi, p\sin\varphi)$, a general effective low energy Dirac Hamiltonian can be written as [McCann 2006b]:

$$H_J = \varepsilon(p)\boldsymbol{\sigma}\cdot\mathbf{n}(\varphi)\,, \tag{3.15}$$

where $\mathbf{n} = -(\cos(J\varphi), \sin(J\varphi))$ and the vector $\boldsymbol{\sigma}$ is made from the Pauli matrices. Using this notation, $J = 1$ for a monolayer and $J = 2$ for a bilayer. The eigenstates of H_J correspond to pseudospin polarized parallel (electrons) or anti-parallel (holes) to the 'quantization' axis $\mathbf{n}$. An adiabatic evolution of such a pseudospin state, which accompanies the rotation of momentum $\mathbf{p}$ by an angle φ, also corresponds to the rotation of axis $\mathbf{n}$ by an angle $J\varphi$. As a result, if quasiparticles encircle a closed contour in the momentum space (that is $\varphi = 2\pi$), a phase shift $\Phi = J\pi$ known as Berry's phase is gained by the quasiparticle's wavefunction. Berry's phase can be viewed as arising owing to the rotation of pseudospin, when a quasiparticle repetitively moves between different carbon sublattices (A and B for monolayer and A1 and B2 for bilayer)

For fermions completing cyclotron orbits, the Berry's phase contributes to the semiclassical quantization and affects the phase of Shubnikov-de Haas oscillations. For monolayer graphene, this results in a π-phase shift of the SdH oscillations and a related 1/2-shift in the sequence of QHE plateaus (Fig. 3.4-bottom, (b) for theoretical approach and (c) for experimental measurements), as compared with the conventional 2D system, Fig. 3.4-bottom (a), where the Berry's phase is zero.

There is another important experimental consequence of the Dirac nature of the fermion in graphene. Because graphene's Landau level energy scales as $\sqrt{NB}$, rather than linear as in a regular 2DEG, at low energies, the spacing between Landau levels, $\Delta_N \equiv E_{N+1} - E_N$, can be rather large ($\Delta_0 \approx 36meV\sqrt{B(T)}$), Fig. 3.4-Top. As the quantization of σ_{xy} relies on the condition $\Delta_N \gg k_B T$, the quantum Hall effect is observable at room temperature [Novoselov 2007].

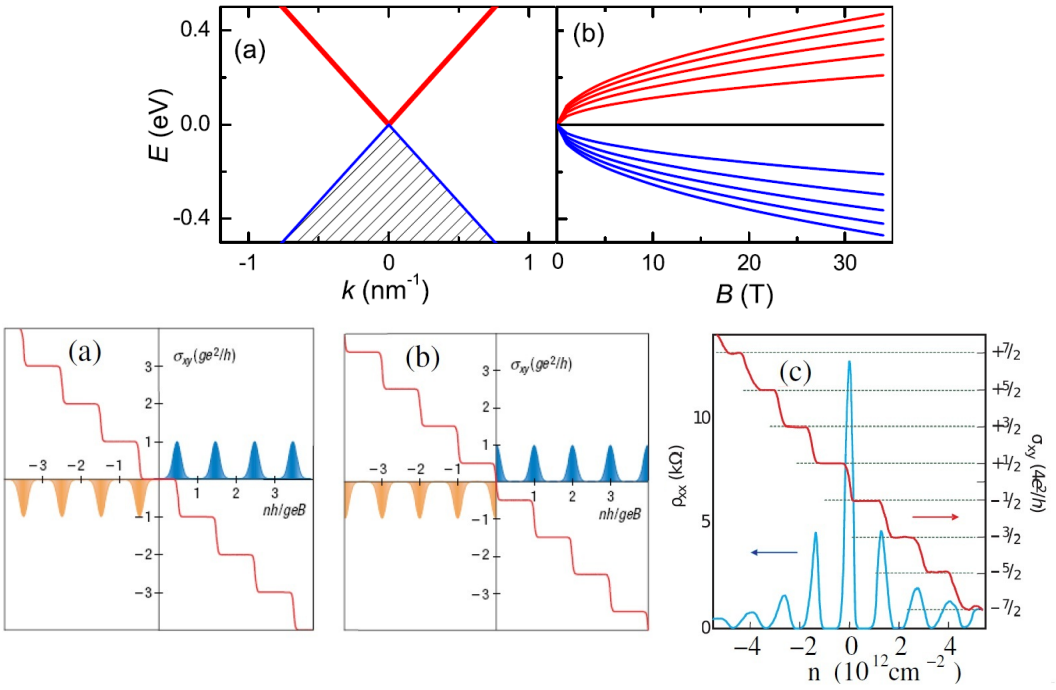

Figure 3.4: **Top**, (a) graphene energy dispersion at B=0 T, (b) Landau energy levels for monolayer graphene. **Bottom**, illustration of the integer QHE for (a) 2DEG and (b) monolayer graphene. The sequences of Landau levels as a function of carrier concentration n are shown as dark and light peaks for electrons and holes, respectively. (c) σ_{xy} (red) and ρ_{xx} (blue) for monolayer as a function of carrier density measured at $T = 4$ K and $B = 14$ T. Adapted from [Novoselov 2005].

Degeneracy lifting in graphene monolayer

The plateaus sequence for σ_{xy} described in eq. (3.14) refers to fully degenerated Landau levels including the spin and valley degeneracy. For these Landau levels, we have a filling factor of $\nu = 4(N + 1/2) = \pm 2, \pm 6, \pm 10, ...$ But spin and valley degeneracies can be lifted as a consequence of broken symmetries. These degeneracy lifting give place to intermediate filling factors $\nu = 0, \pm 1$ for the lowest Landau level and $\nu = \pm 3, \pm 4, \pm 5$ for $N = \pm 1$ Landau levels. The difficulty in observing theses intermediate quantum Hall plateaus is the lower value of the energy gap between successive split Landau levels, requiring very high quality samples (larger mobilities) and high magnetic fields.

Zhang et al. carried out magneto-transport measurements for several values of magnetic field between 9 and 45 T at 1.4 K on a graphene flake on Si/SiO_2 substrate with a mobility of $\sim 5 \times 10^4$ cm^2/Vs [Zhang 2006]. In Fig. 3.5 (a), the Hall conductivity, σ_{xy}, deduced from R_{xx} and R_{xy} is plotted as a function of back-gate voltage V_g. In addition to the $\pm 4(|N| + 1/2)$ expected plateaus observed at

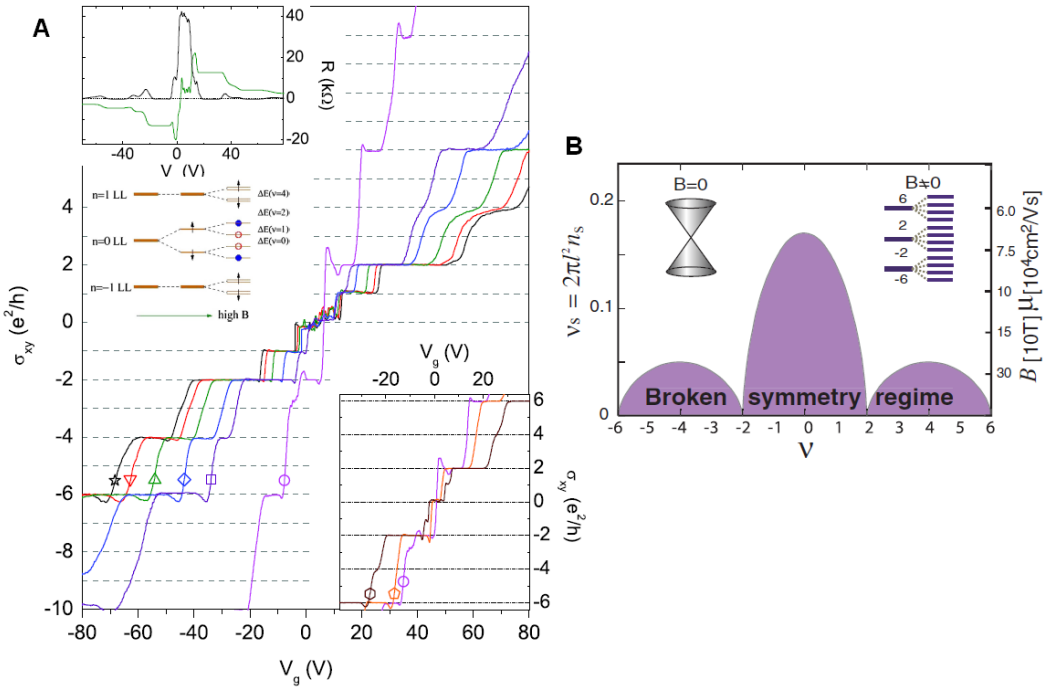

Figure 3.5: **A**, σ_{xy} measured on a graphene monolayer as a function of V_g at different magnetic fields: 9 T (circle), 25 T (square), 30 T (diamond), 37 T (up triangle), 42 T (down triangle), and 45 T (star). The data are taken at T=1.4 K, except for the B=9 T curve, which is taken at 300 mK. Left upper inset: R_{xx} and R_{xy} for the same device measured at 25 T. Left lower inset: a schematic drawing of the Landau levels in low (left) and high (right) magnetic fields. Right inset: detailed σ_{xy} data near the Dirac point for B =9 T (circle), 11.5 T (pentagon) and 17.5 T (hexagon) at T=30 mK. Adapted from [Zhang 2006]. **B**, Phase diagram for SU(4) quantum Hall ferromagnetism for the $N = 0$ and $N = 1$ Landau levels of graphene. Adapted from [Nomura 2006].

low magnetic field ($B < 9$ T), new QH plateaus appear at higher magnetic fields. Specifically, the $\nu = 0$ plateau is resolved at $B > 11$ T, and the $\nu = \pm 1, \pm 4$ plateaus appear at $B > 17$ T. The degeneracies of N=0 are fully lifted at high magnetic field. A close examination hints quantum Hall states developing at $\nu = \pm 3$, their weaker signatures indicate a hierarchy of the degeneracy lifting of the Landau levels.

Further measurements made by [Jiang 2007a], also in graphene samples deposited on Si/SiO_2 substrate with mobilities of the order of $\sim 2 \times 10^4$ cm^2/Vs, suggest that $\nu = \pm 1$ states are associated with valley splitting of the $N = 0$ Landau level. On the other hand, the quantum Hall state at $\nu = 0$ is related to the spin splitting of this Landau level, as well as the splitting of the level $N = 1$. The authors deduce a hierarchy of the degeneracy lifting as shown schematically in the lower left inset of the Fig. 3.5 (a). Here, up and down arrows are used to represent the spin

of the charge carriers, and solid (blue) and open (red) dots are the different valleys.

Another remarkable characteristic of the degeneracy lifting of the level $N = 0$ is the increase of the longitudinal resistance. Its origin remains without consensus and more work is needed to understand it. Later, higher quality samples also show the Hall plateaus for $\nu = \pm 3$ [Du X. 2009].

The phenomenon of interaction induced gaps and broken symmetries at integer filling factors is known as quantum Hall ferromagnetism. [Nomura 2006] derived a criterion for the occurrence of interaction-driven quantum Hall effect near intermediate values of e^2/h due to charge gaps in broken symmetry states. Fig. 3.5 (b) summarizes the estimated product of carriers mobility and magnetic field required to see quantum Hall ferromagnetism in graphene. In their model, the ordered region is bounded by a maximum value of the scattering filling factor, ν_s. This is inversely proportional to the product of the sample mobility and the external magnetic field strength and the order near integer filling factors requires the minimum values for this product indicated on the right-hand vertical axis of Fig. 3.5 (b). These theoretical predictions are in a good agreement with the experimental data shown above.

Also, in very high quality suspended graphene samples [Bolotin K. 2009, Du X. 2009] fractional quantum Hall effect has been observed for a filling factor $\nu = 1/3$. This effect appears at low temperatures in fields as low as 2 T and up to 20 K in a field of 12 T. It is significantly more robust than in the semiconductors-based 2D electron systems, reflecting the stronger Coulomb interaction and more the 2D nature of the electrons in graphene.

3.3.2 QHE in graphene bilayer

In graphene bilayer, the low energy fermionic excitations are massive (section 1.1.2). This fact would suggest that QHE in graphene bilayer might be similar to the one observed in regular 2DEG. However, two important differences subsiste for graphene bilayer, the band structure is gapless and fermions are chiral but with a Berry's phase equal to 2π. As a consequence, the energy levels have a different sequence from 2DEG and graphene monolayer, given by [McCann 2006b]:

$$E_N = \frac{\hbar e B}{m^*}\sqrt{N(N-1)} \quad \text{for} \quad N \geq 2 \tag{3.16}$$

where $m^* \approx 0.05 m_e$ is the effective mass (Fig. 3.6-top). Graphene bilayer, also has a Landau level at zero energy, however, because of the difference in the Berry's phase, the step between the plateaus of σ_{xy} across the CNP is twice as big as in monolayer graphene. it means that both Landau levels $N = 0$ and $N = 1$ merge at $E = 0$.

The origin of this energy level can be studied following the discussion of section 3.3.1. For graphene bilayer, $J = 2$, which means a phase shift of $\Phi = 2\pi$. One may expect that this 2π phase does not influence the QHE sequence. However, the exact analysis [Novoselov 2006] of the Landau level spectrum for the Hamiltonian,

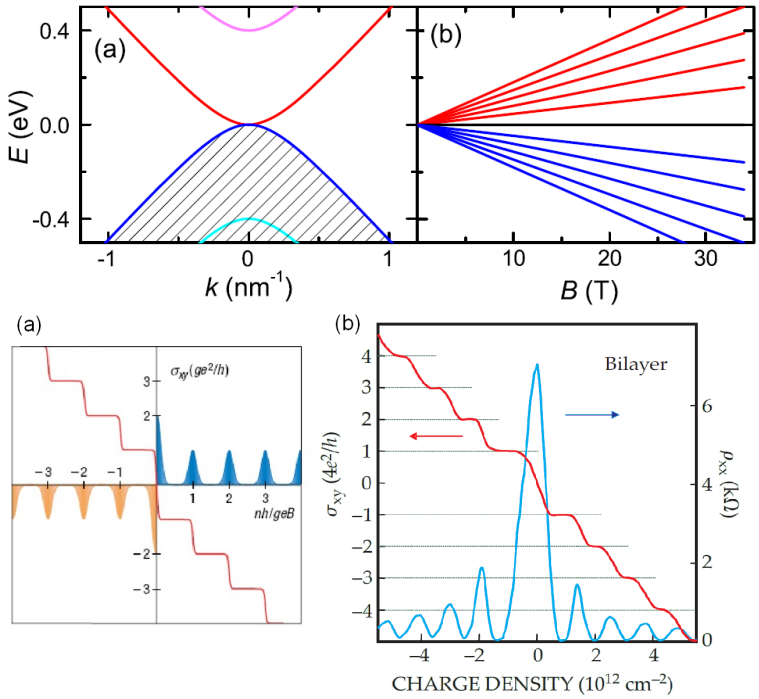

Figure 3.6: **Top**, (a) energy dispersion at B=0 T and (b) Landau energy levels for graphene bilayer. **Bottom**, (a) Illustration of the integer QHE for graphene bilayer. The sequences of Landau levels as a function of carrier concentration n are shown as dark and light peaks for electrons and holes, respectively. (b) σ_{xy} (red) and ρ_{xx} (blue) for graphene bilayer as a function of charge density measured at $T = 4$ K and $B = 12$ T. Adapted from [Novoselov 2006].

H_J, shows that the Berry's phase of $J\pi$ has an associated J-fold degeneracy of the zero-energy Landau level. For graphene monolayer ($J = 1, \Phi = \pi$), there is a single state ε_0 at zero energy. For graphene bilayer ($J = 2, \Phi = 2\pi$), the two lowest states $\varepsilon_0 = \varepsilon_1$ lie at zero energy (Fig. 3.6-bottom). The existence of such a Landau level implies that there must be a QH step across the neutrality point doublely degenerated, which takes twice the number of carriers to fill (an step in σ_{xy} of $8e^2/h$), as compared with all other Landau levels (an step in σ_{xy} of $4e^2/h$), Fig. 3.6-Bottom.

Degeneracy lifting in graphene bilayer

As discussed for graphene monolayer, we expect a degeneracy lifting by external perturbations and/or interactions. This has been observed in graphene bilayer deposed on Si/SiO_2 [Zhao 2010], BN [Dean 2012] and suspended [B. E. Feldman 2009]. We first remark is that the degeneracy lifting are seen in samples with mobilities of the order of $\sim 1 \times 10^4$ cm^2/Vs and in moderated magnetic fields (15 T). This contrasts with monolayer samples where 5 times higher mobilities and two timer

larger magnetic fields are required to observe the degeneracy lifting.

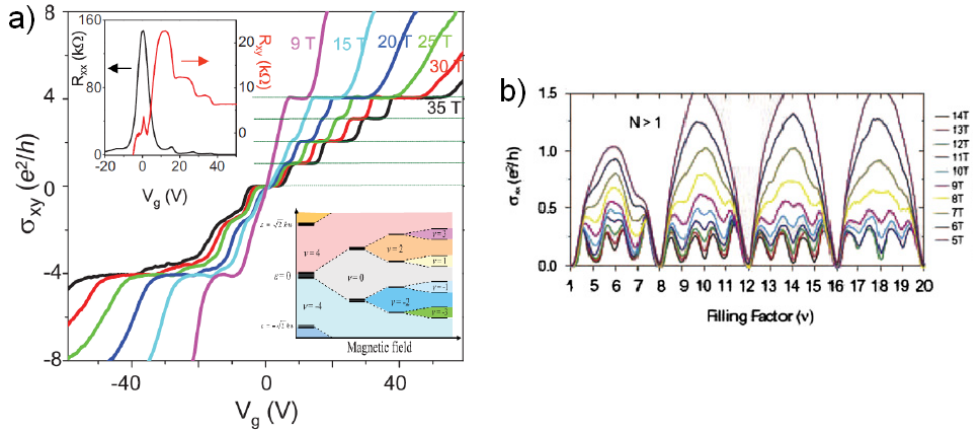

Figure 3.7: **a)** Hall conductivity σ_{xy} measured on a bilayer graphene as a function of back gate voltage V_g at $T = 1.4$ K for different magnetic fields: 9, 15, 20, 25, 30 and 35 T. Upper inset: R_{xx} (black) and R_{xy} (red) versus V_g at $B = 35$ T. Lower inset: the zero-energy Landau level hierarchy in bilayer graphene at high magnetic field. Adapted from [Zhao 2010]. **b)** σ_{xx} as a function of the filling factor for different magnetic fields measured on a bilayer graphene. Adapted from [Dean 2012].

In Fig. 3.7 (a),is plotted the calculated σ_{xy} with well quantized plateaus. For low magnetic fields ($B < 10$ T), QH states corresponding to $\nu = \pm 4$ are present and as B increases, new QH states emerge, as it is evidenced by additional QH plateaus at $\nu = 0$ and 2, and then, $\nu = 1$ and 3, at higher fields. For $B \geq 20$, the eightfold degeneracy of the zero-energy Landau level is fully lifted.

The new QH states are in accordance with the sequential symmetry breaking of the zero-energy Landau level as depicted in the inset of Fig. 3.7 (a). This suggests that different symmetry-breaking processes are relevant as B increases. Independent measurements of the longitudinal resistance as a function of a perpendicular field and temperature indicate that the degeneracy lifting for the $\nu = 1, 2$, and 3 has its origin in electron-electron interaction. This result is consistent with theoretical predictions of the formation of spin polarized QH ferromagnetism in bilayer graphene at high magnetic field [Barlas 2008]. The field dependence of the longitudinal resistance at the $\nu = 0$ reveals an insulating behavior similar to the one in single layer graphene [Zhao 2010].

Other experimental results in graphene based heterostructures (graphene bilayer on BN), Fig. 3.7 (b), show a fully degeneracy lifting of higher Landau levels ($N > 0$). Here, the symmetry breaking present a different hierarchy to the one observed for $N = 0$. The origin of this anomaly, where the odd filling factors are developed before the even ones, has not been established yet. It seems that the four degeneracies are lifted at the same time but the energy gap for the even states is smaller than the one for the odd states [Dean 2012].

For higher quality suspended bilayer graphene samples ($\mu \sim 27 \times 10^4$ cm^2/Vs),

a plateau at $\nu = 1/3$ has been observed (for a magnetic field between 15 and 28.5 T), characteristic of FQHE [Bao 2010].

3.4 Landau states in graphene nanoribbons

When we refer to the Landau levels formation in a GNR, two main effects have been considered: the electronic confinement and the edge symmetry.

3.4.1 Confinement effect: Anomalous Shubnikov-de Haas oscillations in GNRs

The confinement in graphene has been theoretically addressed by Peres et al., giving evidence of an anomalous Landau spectrum [Peres 2006b]. The Dirac fermions energy in presence of both a magnetic field and a confining potential is (in this section, we use units such that $c = \hbar = k_B = 1$):

$$E_{\varepsilon,\sigma} = \frac{\sigma v_F \sqrt{\varepsilon + \sigma}}{l_m}, \tag{3.17}$$

where $\sigma = \pm 1$ labels electrons and holes and ε a dimensionless term depending on the relative strength of the magnetic and the electronic confinement.

In presence of a large magnetic field, when $l_m \ll W$ (i.e. for a wide GNR), the dimensionless energy equals $2n+1$ and eq. (3.17) gives rise to an energy proportional to $\sqrt{B}$ like in graphene (eq. (3.13)). In such a case, the SdH oscillations are like in graphene with their maxima at $B = B_N$, defined by:

$$\frac{1}{B_N} = \frac{2 v_F^2 e N}{E_F^2}. \tag{3.18}$$

When the confining potential dominates, $l_m > W$, the dimensionless energy equals $(\pi N l_m / W)^2$. Then eq. (3.17) gives:

$$E_N = \sigma v_F \left[\frac{\pi N}{W} + \frac{\sigma W e B}{2\pi N} \right]. \tag{3.19}$$

The first term corresponds to the discrete transverse energies due to the confining potential and the second term, proportional to B, represents the diamagnetic effect on the energy sub-bands. This expression clearly demonstrates the contribution of both the transverse confinement and the magnetic field effects on the energies of the 1D sub-bands. One notes that the Landau level index N is, at zero field, the 1D sub-bands index. In this regime, the maxima of the SdH oscillations occur when $B = B_N$ defined by [Peres 2006b]:

$$\frac{1}{B_N} = \frac{W^2 e / 2\pi^2 N}{\left(\frac{E_F W}{\pi v_F} - N \right)}. \tag{3.20}$$

Interestingly, the spaced SdH oscillations are not anymore periodic in $1/B$, but the maxima become more at low magnetic field, i.e. at large Landau index. The $1/B$

dependence is supposed to diverge at a critical Landau level index $N_c = E_F W/\pi v_F$. This constitutes the major confinement effect on the Dirac Fermions.

The crossover from a linear magnetic field dependence to a $\sqrt{B}$ variation for a given subband of index N occurs when the corresponding Landau orbits fit into the width of the ribbon. Since each orbit encloses an integer number N of quantum flux Φ_0, we deduce a crossover that manifests itself when $B = B_c$ defined by [Peres 2006b]:

$$B_c = \frac{N\Phi_0}{W^2}\,. \tag{3.21}$$

The gradual change of the 1D sub-bands into magneto-electric sub-bands at higher fields is clearly illustrated in Fig. 3.8.

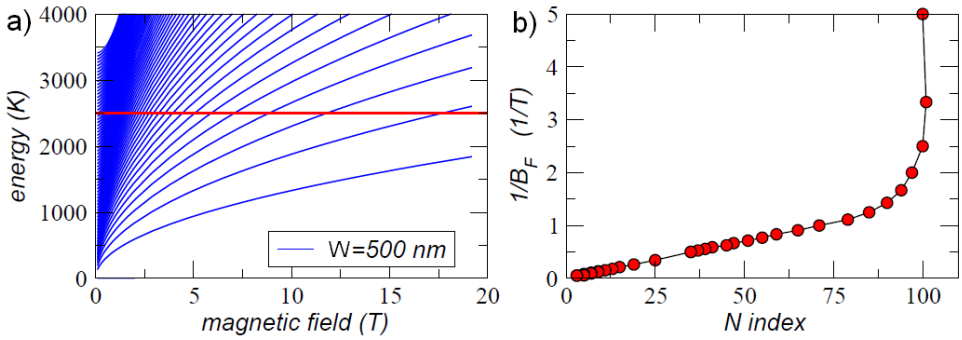

Figure 3.8: Magneto-electric subbands as a function of the magnetic field for a 500 nm wide aGNRs. The red line is the position of the Fermi energy. (b) The Landau plot for the given Fermi energy. Adapted from [Peres 2006b].

In Fig. 3.8 (a), is shown the energy spectrum as a function of the magnetic field for a GNRs of W=500 nm. For a certain Fermi energy (marked by a red line), we obtain the number of occupied Landau levels, N, as a function of the inverse of the magnetic field at which the Landau level crosses the Fermi energy (Landau plot).

In the Landau plot, Fig. 3.8 (b), we see that there is a linear dependence of the Landau level index with $1/B$ for high magnetic fields. For higher Landau levels, the spacing in $1/B$ becomes more pronounced and the linearity is not longer present, eq. (3.20). This corresponds to the low magnetic field regime where the cyclotron orbits do not fit inside the GNR.

3.4.2 The energy-momentum dispersion in the Landau regime for armchair and zigzag GNR

As we said before, when a magnetic field is applied perpendicular to a GNR the Landau levels start to develop and once they are formed (when $W > l_m$) their energies gradually evolve into a $\sqrt{B}$ dependence. However, we will show below that

the fine structure of the Landau spectrum of GNR contains reminiscence of the electronic band structure at zero field, with zigzag or armchair signatures.

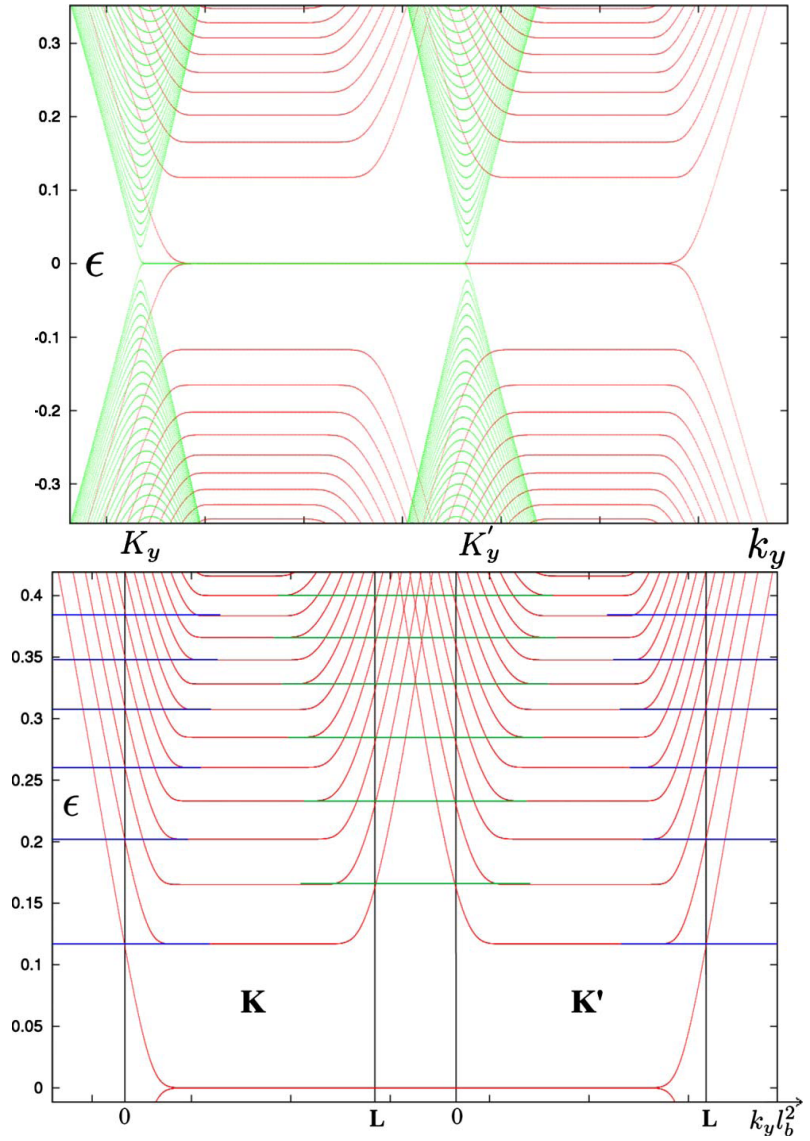

Figure 3.9: **Top**, Low energy tight-binding spectrum for a zigzag ribbon of width W= $199 \times 3a/2 \approx 41$ nm with (red) and without (green) magnetic field. **Bottom**, energy spectrum as a function of the position. Edges are represented by vertical black lines. Green and blue horizontal lines indicate the position of the bulk Landau level for comparison with the position of the level at the edge. The energy is given in unit of t and the magnetic flux is $\Phi = 0.00126\Phi_0$ ($\approx$ 51 T). Adapted from [Delplace 2010].

In case of *zigzag GNRs*, the Fig. 3.9-left, depicts the evolution of the band structure when a magnetic field is applied (green and red plots). The lowest Landau

level in this case support two types of edge states: *dispersionless* and *current caring*. The dispersionless states are the same as those studied in section 1.2.1, which are present at zero magnetic field (green curves) and do not contributed to the Hall conductance.

Concerning the current caring states, we see (Fig. 3.9-Right) that, for an electron in one valley, the edge states are asymmetric between the left and right edge. The situation is the same for the other valley but in the opposite edge. Therefore, a propagative edge state which forms a conduction channel is present at the two edges of the GNR, at the same energy, but belongs to different valleys. The valley degeneracy is preserved even if the electrons occupy different edges in function of their valley **K** or **K′**.

Standard magneto-transport measurements should not allow to distinguish this valley asymmetry. The challenge to evidence this could be to inject or photoexcite preferentially carriers in a chosen valley **K** or **K′**.

For the *armchair GNRs* case, Fig. 3.10, we observe that the lowest conduction band and the upper valence band move to form the $E = 0$ Landau level, closing the energy gap. At low k, the 1D subbands combine themselves to conform the standard dispersionless graphene Landau levels which are both spin and valley degenerated. At larger k, the Landau states are dispersive and each of them splits into 2 Landau subbands (except for $E = 0$), restoring the valley degeneracy lifting at the edge of the GNR.

The valley degeneracy lifting of the propagative states is a particular signature of the armchair symmetry. This effect is potentially observable by magneto-transport measurements. It will be the main objective of the experimental part of this thesis.

Electron-electron interaction effects in armchair GNRs

The effect of the electronic interaction on the charges tuned by a back-gate voltage and its impact on the GNR band structure have been theoretically considered in few articles within the Hartree approximation [Shylau 2010]. Self-consistent calculations show a non uniform distribution of the charge density across the width of the ribbon, with an enhancement of the density at the edges.

Under a perpendicular magnetic field, the electron interaction is responsible for a large pinning of the Fermi energy on the dispersionless states in the center of the GNR (Fig. **??**-right from (a) to (d)). In case of an aGNR, this induces a strong distortion of the $E(k)$ curves with a much larger valley degeneracy lifting between the Landau sub-levels, compared to the non interacting case (dashed lines Fig. **??**-left). The consequence on the magneto-conductance is quite severe: the quantized plateau of the conductance between two Landau levels are almost suppressed and it present bumplike features as a consequence of the pinning of the Fermi energy to the dispersionless states in the center of the GNR. Besides, the consistence of backward and forward currents on the same edge of the ribbon makes the magneto-conductance much more sensitive to the disorder. This arguments has been used by [Shylau 2010] to explain the absence of experimental evidence of quantized conductance in the

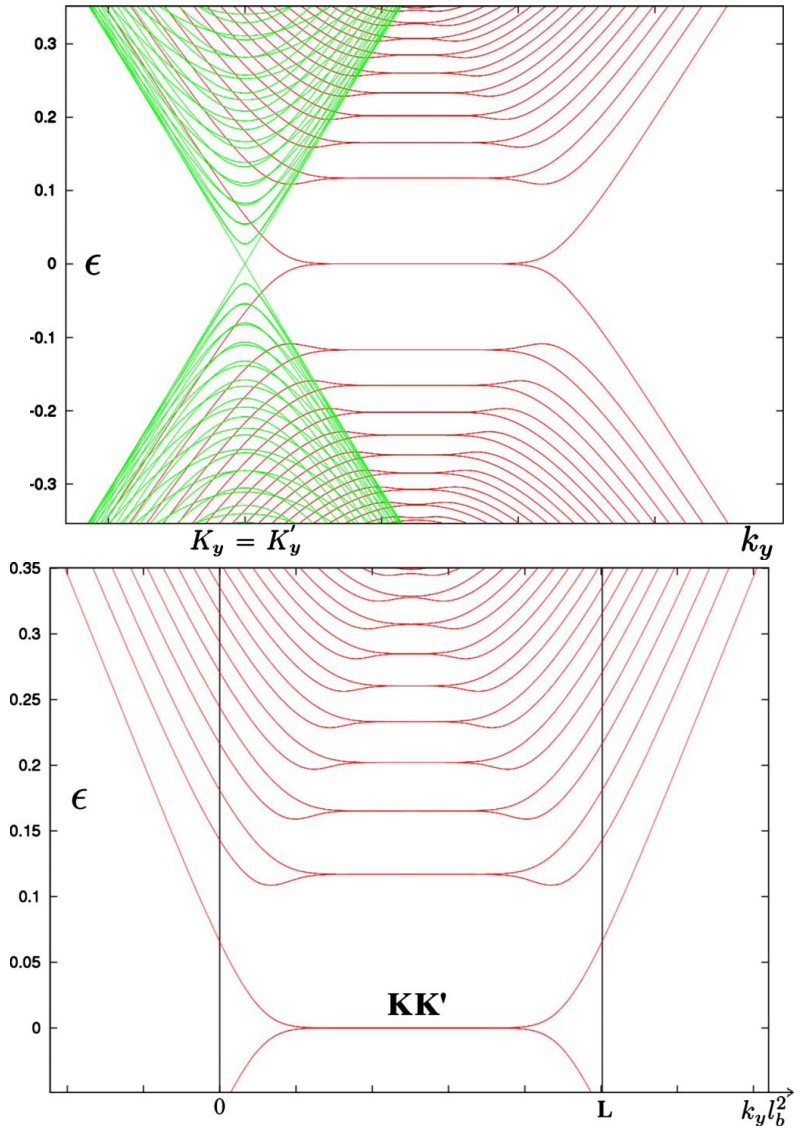

Figure 3.10: **Top**, low energy tight-binding spectrum for a armchair ribbon of width W= $199\sqrt{3}a/2 \approx 24$ nm with (red) and without (green) magnetic field. **Bottom**, energy spectrum as a function of the position. Edges are represented by vertical black lines. The energy is given in unit of t and the magnetic flux is $\Phi = 0.00126\Phi_0$ (≈ 51 T). Adapted from [Delplace 2010].

Landau regime in earlier measurements on GNRs.

We finally stress that, despite some theoretical calculations on the electron-electron interactions effects on the electronic density distribution and its impact on the band structure in GNR, there is no experimental evidence demonstrating that the single particle picture is no anymore valid. Indeed, recently Hettmansperger et al. gave evidence that the function of compressible and incompressible strips due to electrostatic interaction in quantum Hall regime, does not hold for the quantum

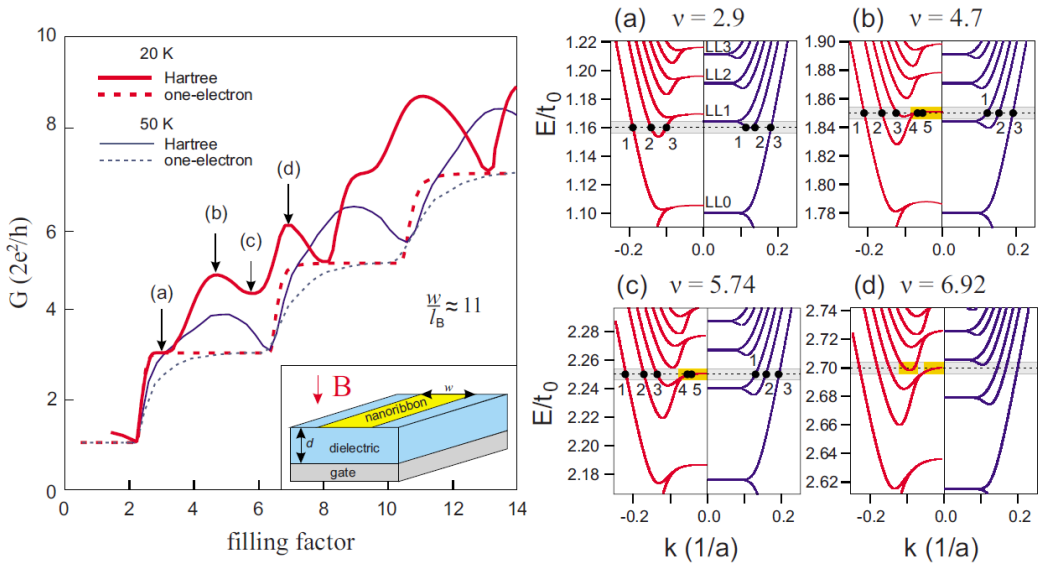

Figure 3.11: **Left**, simulated conductance of a 50 nm wide armchair GNR as a function of filling factor for interacting and noninteracting electrons at temperatures T=20 K (red) and 50 K (blue) in a magnetic field of B=30 T. **Right**, Evolution of the band structure of the GNR at different filling factors corresponding to arrows (a)-(d) in left figure. Left and right part of the panels corresponds to the interacting and noninteracting case, respectively. In order to align the noninteracting and the Hartree bands, the one electron dispersion has been shifted along the energy axis by averaging the Hartree energy. Adapted from [Shylau 2010].

Hall effect in GNR [Hettmansperger 2012]. The single-particle model remains more appropriate.

3.5 Landau spectrum in bilayer GNRs

Unfortunately, there are not many theoretical works on bilayer GNRs under magnetic field and some of them show contradictory results on the simulations of the band structure and its magnetic field dependence [Xu 2009, Li 2009, Chung 2010].

Zigzag bilayer GNRs: The two theoretical works concerning zigzag bilayer GNRs present different characteristics of the band structure under high magnetic field, summarized in Fig. 3.12. The results obtained by [Chung 2010] (Fig. 3.12 upper panel), show flat bands which represent the onset of the Landau levels. Each band for $N \neq 0$ is four times degenerated. The lowest landau level is composed of two doubly degenerated bands (spin degenerated). This level presents a strong asymmetry between electrons and holes and the appearance of an energy gap of $E_g \approx 6.5$ meV.

In the study of [Xu 2009] (Fig. 3.12 lower panel) a partially flat band at $E = 0$

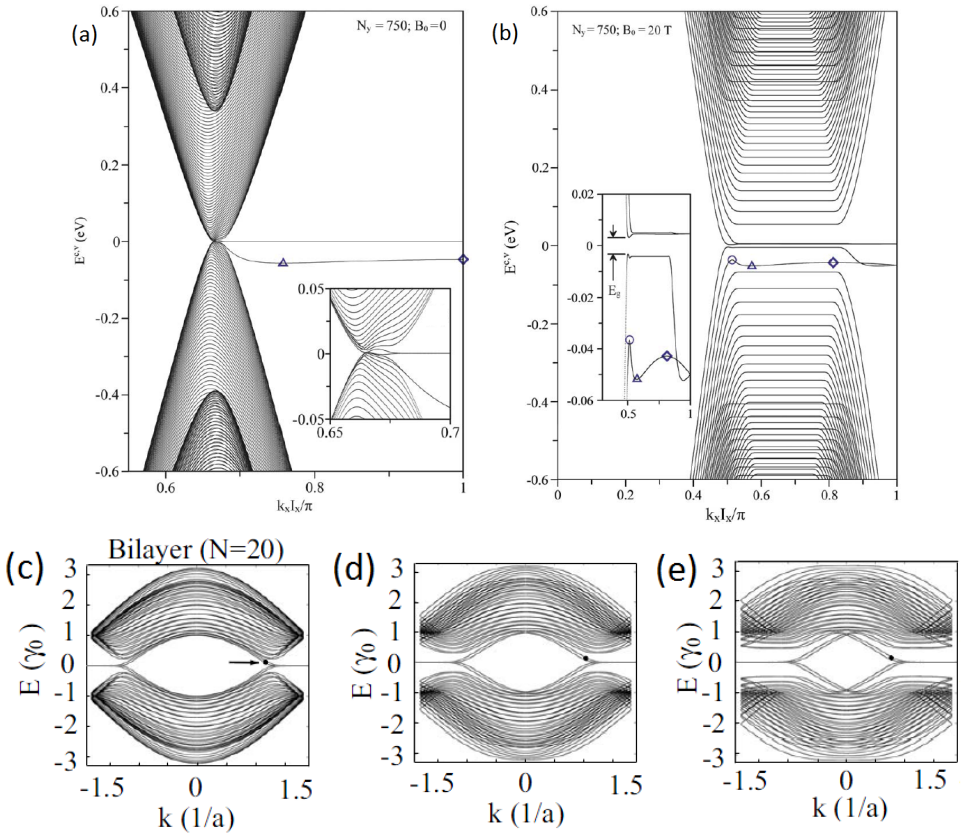

Figure 3.12: **(a)** Band structure of the AB-stacked bilayer zigzag nanoribbons of width W=159 nm at B=0 T. The Fermi energy is $E_F = 0$. Inset: Low energy region. **(b)**, band structure of the nanoribbon at $B = 20$ T. The inset shows the separated four bands. The band-edge state of the partial flat band are denoted by circle, triangle and diamond. Adapted from [Chung 2010]. **Lower panels** Energy band structure of zigzag bilayer nanoribbons with N=20 ($W \approx 20$ nm) for different magnetic flux through a hexagon (c) $\phi/\phi_0 = 0$ (B=0 T), (d) $\phi/\phi_0 = 1/100$ ($B \approx 400$ T) and (e) $\phi/\phi_0 = 1/50$ ($B \approx 800$ T). Adapted from [Xu 2009].

exists in the band structure and becomes flatter at higher magnetic field. Here, the spectrum remains symmetric between electrons and holes and no energy gap is reported.

Armchair bilayer GNRs: Following the procedure developed by [Xu 2009], the electronic structure of bilayer aGNR has been reproduced by Dr. Alessandro Cresti for several magnetic fields, preliminary results are shown in Fig. 3.13. In this figure, we see the onset of the Landau levels for low k, as for monolayer aGNRs. We remark that the only notable difference with respect to the monolayer case is the double band which forms the $N = 0$ Landau level.

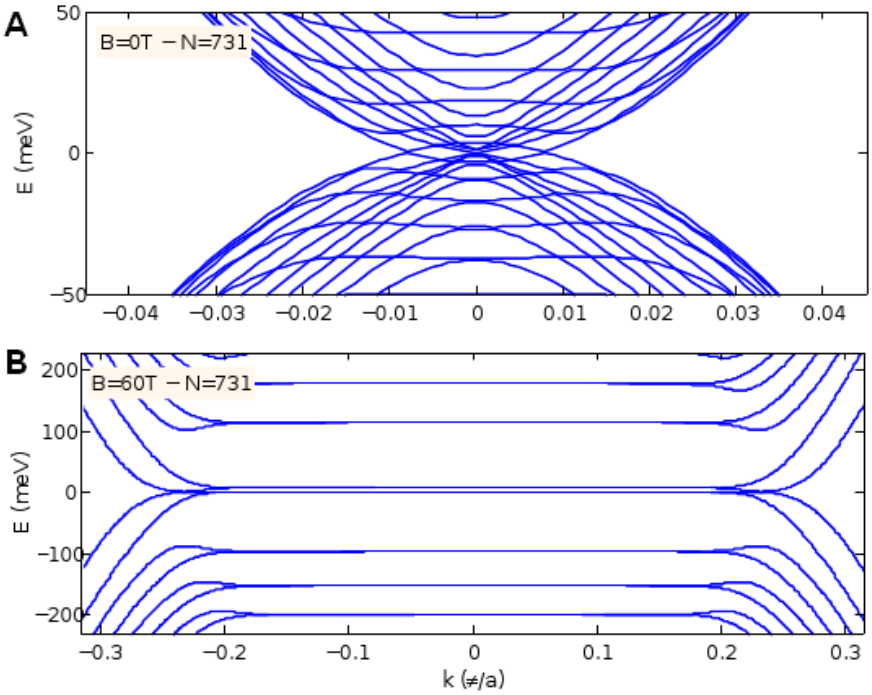

Figure 3.13: Energy band structure of a bilayer armchair GNR with N=731 ($W \approx 88$ nm) for different magnetic fields (a) $B = 0$ T and (b) $B = 60$ T. From [Cresti 2012].

3.6 Two-terminal magneto-conductance measurements in graphene

In a two terminal measurement the shape of the magneto-conductance strongly depends on the aspect ratio of the sample. In the simplest case of a square whit electrodes at opposite sides, the conductance is expressed as function of the longitudinal and Hall conductivity as follow:

$$G_{(\mathrm{L=W})} = \sqrt{\sigma_{xx}^2 + \sigma_{xy}^2} \tag{3.22}$$

An effective-medium approach has been developed to simulate the two probes magneto-conductance as a function of the carrier density for different sample shapes [Abanin 2008]. In this model, the local electric field and the current distribution are calculated in each point of the sample.

In Fig. 3.14 (a), is simulated the conductance as a function of the filling factor for several aspect rations. For a square configuration $L/W = 1$,the conductance exhibits a quantized step when a new Landau state is filled, like in the Landauer approach. When $L/W < 1$ the quantized plateaus (marked by arrows) are replaced by conductance minima preceded by a conductance maxima. For $L/W > 1$, the quantized values correspond to maxima of conductance preceded by minima. In Fig. 3.14 (b), we can see how the Landau level broadening affects the conductance

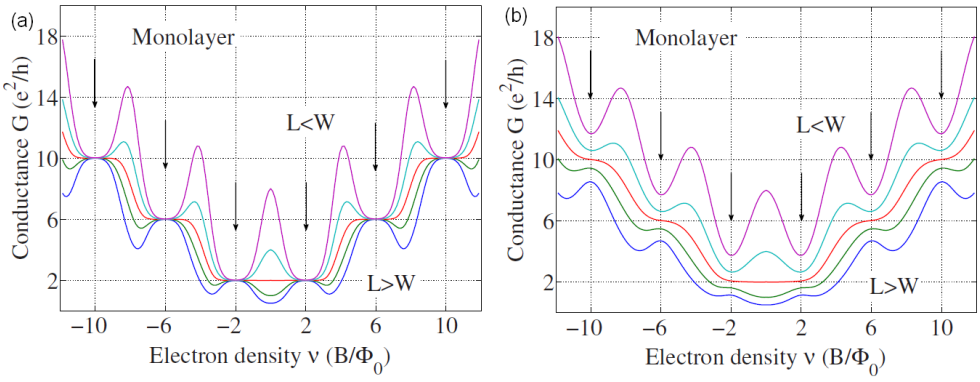

Figure 3.14: **(a)**, Two-terminal conductance as a function of the electron density for a rectangular graphene monolayer sample for aspect ratio $L/W = 0.25$, 0.5, 1, 2 and 4 (top to bottom) with a Landau level width of λ =1.7. **(b)**, Same as (a) for broader Landau levels with λ =0.5. Adapted from [Abanin 2008].

shape. The conductance for the electron densities at which we should found the quantized values is not recovered anymore because of the overlapping of the Landau levels, which brings extra conducting channels and as the edge currents are not well separated, it also allows the presence of backscattering because chiral currents are not well separated.

3.7 Experimental observations of Landau spectra in GNRs

The first studies of the electronic confinement in graphene ribbons under magnetic field has been made by [Berger 2006] at GeorgiaTech. They perform magnetoresistance and Hall-effect measurements on a Hall bar of 500 nm width made by e-beam lithography on epitaxial graphene, (Fig. 3.15 (a)). This structure presented a high mobility ($\mu \sim 2,7 \times 10^4$ cm^2/Vs). Even for this quite large width, the confinement effects in the SdH oscillations have been observed in form of a deviation of the linearity of the Landau index as a function of the inverse of the magnetic field, inset in Fig. 3.15 (a). They deduced an effective width of 270 nm. However, there were no possibility to adjust the doping level and despite the quite high mobility, there were no sign of Hall quantization on the ρ_{xy} measurements.

When the measurements are extended to much higher magnetic fields (up to 55 T) on ultra narrow ribbons W = 11 nm [Poumirol 2010] (Fig. 3.15 C), a large positive magneto-conductance has been also evidenced over a large range of back-gate voltages. Here, the magnetic length starts to fit entirely into the width of the ribbon for $B > 30$ T ($l_m < 5$ nm), and the mobility is of the order of $\mu \approx$80 cm^{2}V^{-1} s^{-1}.

The large gain of conductance in high field has been attributed to the gradual onset of the magneto-electric subbands. They go along with the onset of chiral conducting channels at the edge and a decrease of the backscattering probability as

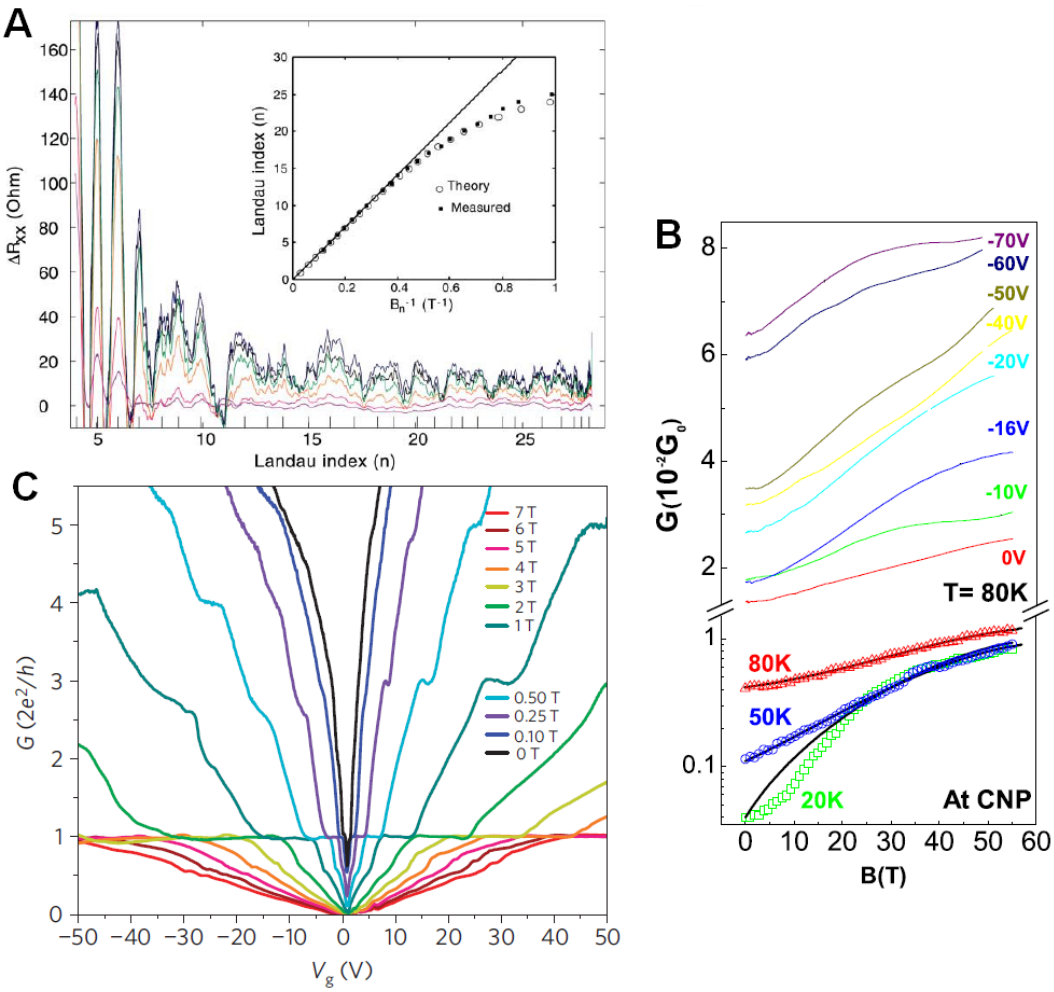

Figure 3.15: **(a)**, SdH oscillations as a function of the Landau index for several temperatures T =4, 6, 9, 15, 35 and 58 K. Inset: The experimental Landau plot and its simulation. Adapted from [Berger 2006]. **(b)**, Magneto-conductance at 80 K, for a 11 nm wide GNR, for several V_g (continuous lines) and at 80, 50 and 20 K at the charge neutrality point (open symbols). Adapted from [Poumirol 2010]. **(c)**, Conductance as a function of the back-gate voltage for different applied magnetic fields measured on a suspended graphene nanoconstriction. Adapted from [Tombros 2011].

the k^+ and k^- wave function start to be spatially separated. Conductance simulations in presence of disorder in a perpendicular magnetic field support this scenario. They also indicate that, the magnetic field induced reduction of backscattering occurs mainly when two types of disorder are present: a moderate short-range disorder at the edges with a long range potential disorder in the "bulk" of the ribbon.

Experimental observation of the Landau quantization in graphene nanoconstric-

tions has been performed by [Tombros 2011]. As shown in section 1.2.4, for a suspended nanoconstriction, of width $\approx$ 200 nm, a quantized plateau at $2e^2/h$ is observed at zero magnetic field. When a perpendicular magnetic field is applied, this plateau becomes more visible and a new plateaus at $6e^2/h$ and $10e^2/h$ develop.

3.8 Summary

In this chapter, we have briefly described the electronic band structure under a perpendicular magnetic field considering a 2DEG, a 1D wave-guide, a graphene mono and bilayer and finally graphene mono and bilayer nanostructures .

These theoretical works predict an unusual behavior of Dirac fermions on presence of both a magnetic and an electronic confinement. Quite spectacular is the different Landau spectra expected for GNR depending on the edge symmetry. However, such predictions suffer from a lack of experimental confirmation. Evidence of magneto fingerprints of the edge orientation motivates, for a large part, the experimental works of this thesis. At the beginning of this thesis, the electronic transport measurements on GNRs at zero or moderate magnetic field did not reveal yet the Dirac fermion confinement and the edge types of the ribbons. We therefore envisage to play with a much larger magnetic confinement, combined to optimized mobility devices on Si/SiO_2 to reveal the magneto conductance driven by the onset of magneto-electric subbands.

Chapter 4

Experimental Frame

Contents

In this chapter, we describe our sample fabrication methods, from Si/SiO_2 substrates to field effect graphene nanoribbons devices, the methods to improve device quality (electrical and thermal annealing) and the experimental techniques for the structural and electronic characterizations: micro-Raman spectroscopy, electronic transport at zero and under pulsed magnetic field and also photo-conductance under THz excitation.

The mastering of graphene based high quality devices is a central issue since the first fabrication of isolated graphene layers [Berger 2004, Novoselov 2004]. It becomes even more critical, when graphene layers are structured into ribbons: the reduction of the lateral size drastically degrades the mobility. In case of graphene nanoribbons (GNRs), many techniques have been developed with relative success to decrease the width and preserving the edge quality (i.e. atomically smooth edges). The first graphene ribbons were obtained by e-beam lithography and oxygen plasma on epitaxial graphene [Berger 2006]. They had a quite large width ~500 nm and a low edge quality because of the isotropic properties of the oxygen plasma etching. Despite this, some electronic confinement effects have been observed, as mentioned in the previous chapter.

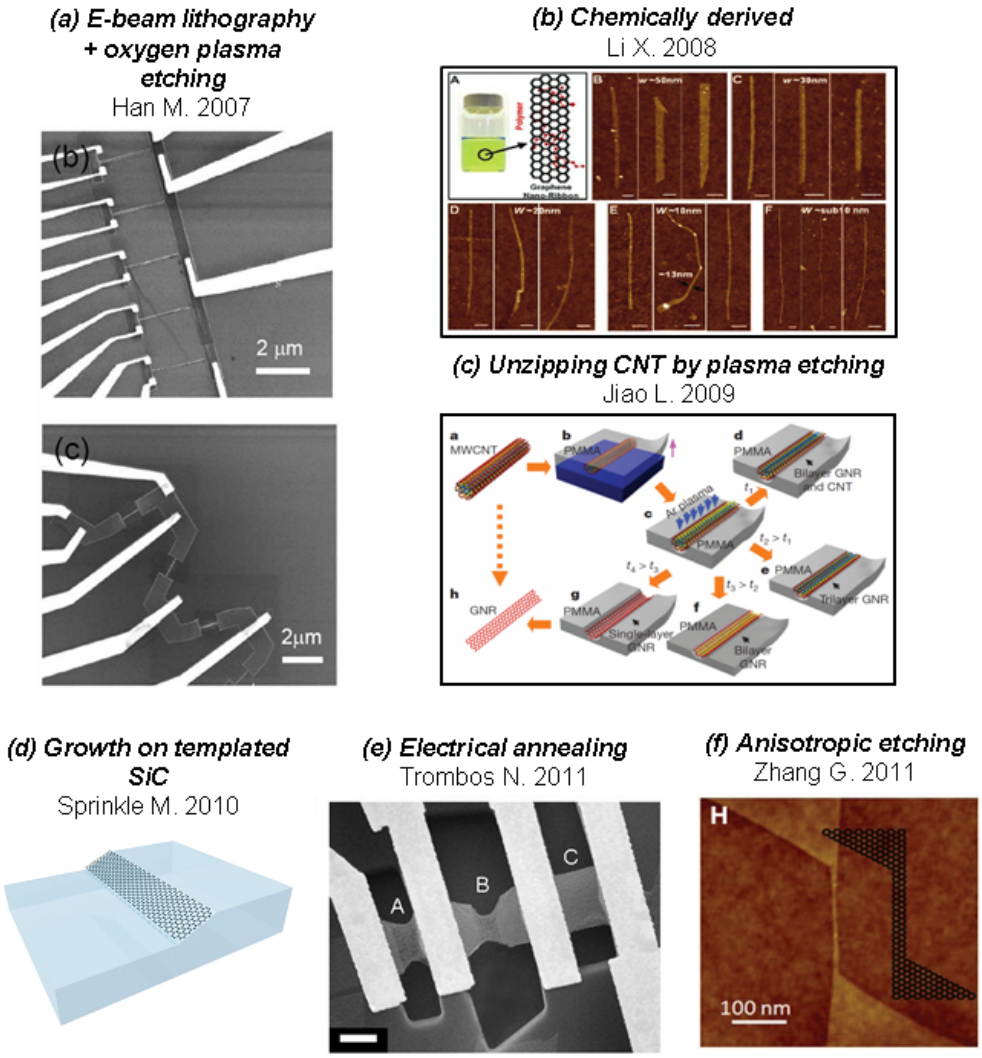

Figure 4.1: Selected GNR fabrication methods: (a) e-beam lithography plus oxygen plasma etching [Han 2007], (b) Chemically derived GNRs [Li 2008], (c) unzipped carbon nanotubes by plasma etching [Jiao 2009], (d) growth on template SiC substrates [M. Sprinkle 2010], (e) nano-constrictions made by electrical annealing [Tombros 2011] and (f) anisotropic etching [Shi 2011].

The technological efforts in the conception of narrow GNRs with smooth edges have been tremendous. Some of the related techniques can be summarized as follow (Fig. 4.1):

- **e-beam lithography and oxygen plasma etching**: This technique allows the patterning of GNRs on different substrates. It consists in creating an etching mask, using e-beam lithography to etch away the uncovered graphene by an oxygen plasma. This technique is limited by the resist and e-beam resolution and does not allow an accurate edge control due to the isotropic

nature of the oxygen plasma [Han 2007, Berger 2006].

- **Chemically derived GNRs**: sub-10 nm widths with ultra-smooth edges are obtained by chemical process where graphene is exfoliated at high temperatures and then dispersed in a 1,2-dichloroethane solution of PmPV by sonication [Li 2008].

- **Unzipping carbon nanotubes**: the first technique to unzip multi-walls-CNTs consisted in etching a non-covered part of the CNT with Ar plasma. This technique allows to obtain GNRs with widths between 10-20 nm [Jiao 2009]. A second technique based on the calcination and the sonication of multi-walls carbon nanotubes (MWCNTs) drastically improved the size reduction (less than 5 nm). This technique shows high quality GNRs with atomically smooth edges [Tao 2011].

- **Scalable templates growth of graphene on SiC**: this bottom-up approach provides a high quality GNRs from the decomposition of SiC, in etched steps on the substrate, allowing the control of the width. It also avoids the edge damage due to the post-processing [M. Sprinkle 2010].

- **Electrical annealing**: this technique is used to fabricate suspended nano-constrictions. It consists in a controlled rupture of a suspended graphene flake by the application of a large current. It results in the formation of a clean and ultra narrow constriction [Moser 2009, Tombros 2011].

- **Anisotropic etching** (hydrogen plasma): this top-down approach is based on a preferential etching of the hydrogen plasma along the zigzag axis of graphene. It allows an atomically smooth edges [Shi 2011]. This technique shows very good results in the conception of multilayer zigzag GNRs with nominal widths around 10 nm.

4.1 Samples Fabrication

In this section, we present in more details two techniques for the fabrication of field effect transistors from GNRs: (i) *lithographically patterned GNRs* using e-beam lithography and oxygen plasma etching and (ii) GNRs derived from *unzipping carbon nanotubes* [Tao 2011]. The entire fabrication process for the lithographically patterned GNRs and the connection process for the GNRs derived from CNTs are carried out in the clean room (class 10.000 and 100) of the Laboratory for Analysis and Architecture of Systems (LAAS) in Toulouse with the support of TEAM (Techniques et Equipements Appliqués à la Microélectronique).

During this thesis, other techniques were developed: *GNRs patterned using Hydrogen silsesquioxane (HSQ) resist and oxygen plasma etching*, with this technique the ribbons' width is reduced to ∼10 nm. Unfortunately, even when ribbons connection and its patterning were successful, the devices broken during the early stage

of the measurement. We also try to contact *ultra long natural GNRs* made by printing technique where silicon stamps are used to cleave graphite and to transfer it onto Si/SiO_2 substrates. Such "natural" GNRs were provided by the group that developed this technique [Moreno-Moreno 2009]. Unfortunately, the high ribbon density and the large amount of graphite surrounding the GNRs made impossible the connection of an isolated GNR.

4.1.1 Lithographically patterned GNRs

Here, we describe, step by step, the fabrication process to obtain GNRs by patterning exfoliated graphene with e-beam lithography and oxygen plasma, as reactive ion etching (RIE).

Substrates

The substrates are made in a heavily doped 6 inch Si n^{++} ($n\sim 10^{18}$ cm^{-3}) wafers with thermally grown 300 nm SiO_2 layer. The specific width of the SiO_2 layer allows a direct observation of the graphene flakes using an optical microscope [Novoselov 2004].

Marks on the substrates (alphanumeric and angle) are fabricated by optical lithography. The exposure of the optical resist (LOR plus LOFT) to ultraviolet light is made using a Canon mask aligner (stepper technique), FPA 3000i4. After this, metals are deposited by Joule evaporation, Ti/Au (10 nm/ 40 nm), and a conventional lift-off process with acetone is performed. This technique achieves a resolution of ∼500 nm. The substrate design is shown in Fig. 4.2.

The alphanumeric marks on the substrate are used to localize the graphene flakes deposited by mechanical exfoliation (the "scotch tape" technique) [Novoselov 2005]. This technique gives rise to the best graphene based devices quality and graphene flakes as large as ∼1 mm^2 have been achieved [Peres 2010]. In our case, we use natural graphite and we typically obtained flakes of ∼10 μm by side. The angle marks in the substrate are used for an automatic recognition of e-beam lithography which highly improves the accuracy. The minimal size of the working area is of 100x100 μm to get a high resolution lithography.

GNRs patterning

The different steps of the fabrication process are summarized in Fig. 4.3. Once the graphene flakes are deposited on the substrates and located by optical microscopy (step a), we proceed to the deposition of PMMA (Polymethyl Methacrylate) (step b) on the substrate, followed by an e-beam exposure made with a Raith 150 of ultra high resolution (step c) and finally a metal deposition of Ti/Pd/Au (1nm/10nm/40nm from Joule evaporation) (step d) for the conception of metallic electrodes.

A second deposition of PMMA and e-beam lithography are necessary to define the etching mask (step e). This step defines the shape of the ribbons, with a mini-

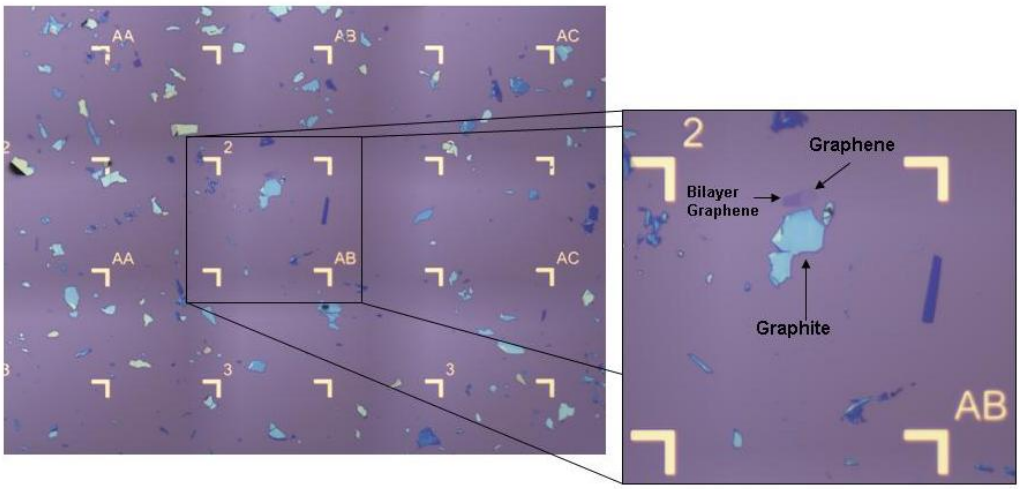

Figure 4.2: Optical observation of a Si/SiO_2 after a mechanical exfoliation and deposition of graphene. Zoom: minimum working area for e-beam lithography (100 μm by side). Marks and alpha-numeric symbols are used to localize the graphene flakes.

mum width of 50 nm. After this, the sample is exposed to an oxygen plasma (RF= 300 W, 40 sccm of Oxygen, 20 s) to remove the uncovered graphene by the etching mask (step f). In the right hand of Fig. 4.3, we see the AFM image of the resulting lithographically patterned GNR with a width of 60 nm and a length of 300 nm.

4.1.2 GNRs derived from unzipping CNTs by calcination

The samples are provided by two sources Prof. H. Dai's group at Stanford University, USA and Prof. X. Wang's group at Nanjing University, China. These GNRs present a very high quality, with smooth edges (as seen by STS and STM [Tao 2011]). The yield of GNRs is ~2 % of the starting raw CNTs soot material, which is an amount significantly higher than former methods based on MWCNTs.

MWCNTs are synthesized by arc discharge (Bucky tube, Aldrich). This raw soot material is first calcined in air at 500 °C to etch/oxidize MWCNTs at defect sites and ends without oxidizing the pristine sidewalls of the nanotubes. In the gas-phase oxidation step (Fig. 4.4), the oxygen reacts with pre-existing defects on nanotubes to form etch pits on the sidewalls. Then, CNTs are dispersed in a 1,2-dichloroethane (DCE) organic solution of poly(m-phenylenevinylene-co-2,5-dioctoxy-p-phenylenevinylene) (PmPV). Using sonication, the calcined nanotubes are found to unzip into nanoribbons. A last ultracentrifuge step is applied to remove the remaining nanotubes and graphitic carbon nanoparticles. The result is a high percentage (>60%) of nanoribbons in the supernatant (for more details see [Jiao 2010]).

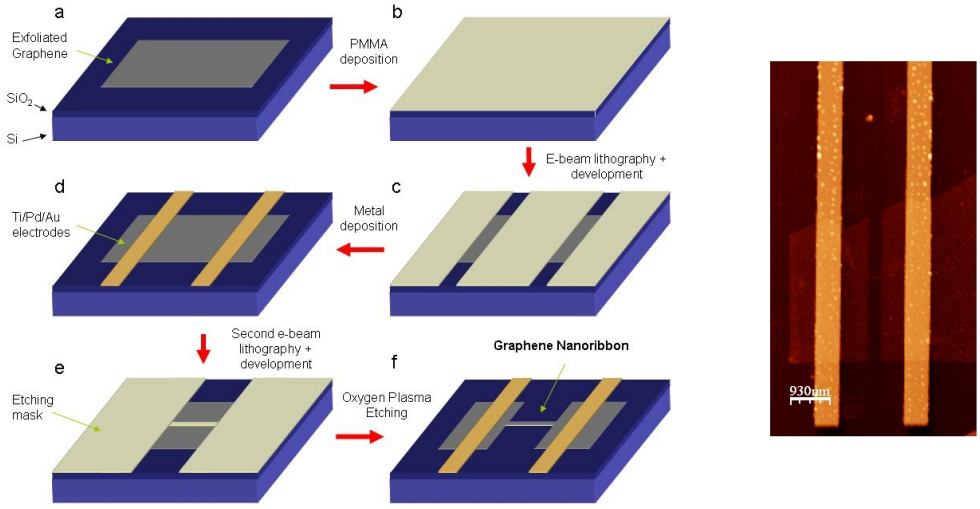

Figure 4.3: **Left**, fabrication process for lithographically patterned GNRs: a) Exfoliated graphene on top of a Si/SiO_2 substrate b) PMMA deposition c) e-beam exposure and development of electrodes d) metal deposition e) second PMMA deposition plus e-beam exposure and development f) GNR after the oxygen plasma etching to remove the non covered graphene. **Right**, atomic force microscopy of a 60 nm width and 300 nm length graphene nanoribbon made by e-beam lithography.

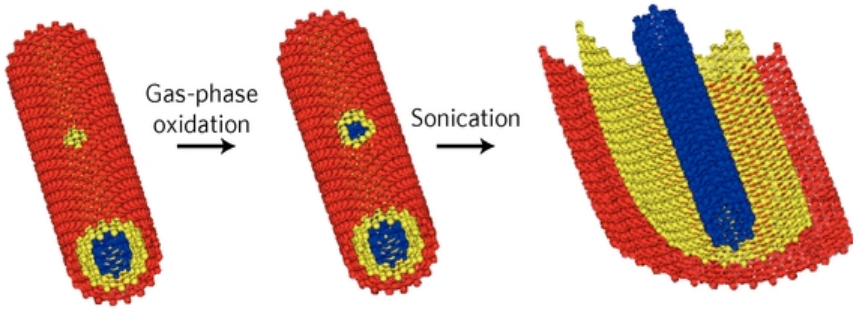

Figure 4.4: Schematic representation of the unzipping processes of MWCNT. Adapted from Ref. [Jiao 2010].

Substrates

The substrates on which are deposited the GNRs in liquid solutions are made from heavily doped Si, with 300 nm layer of SiO_2, wafers. Predefined macroelectrodes are made by optical lithography and metal deposition of Ti/Au (10 nm/ 40 nm) (Fig. 4.5 (a)). An extra layer of metal (50 nm Au) is deposited to have more robust electrodes for the wedge bonding.

The macroelectrodes delimit a central area for nano-objects connexion (Fig. 4.5

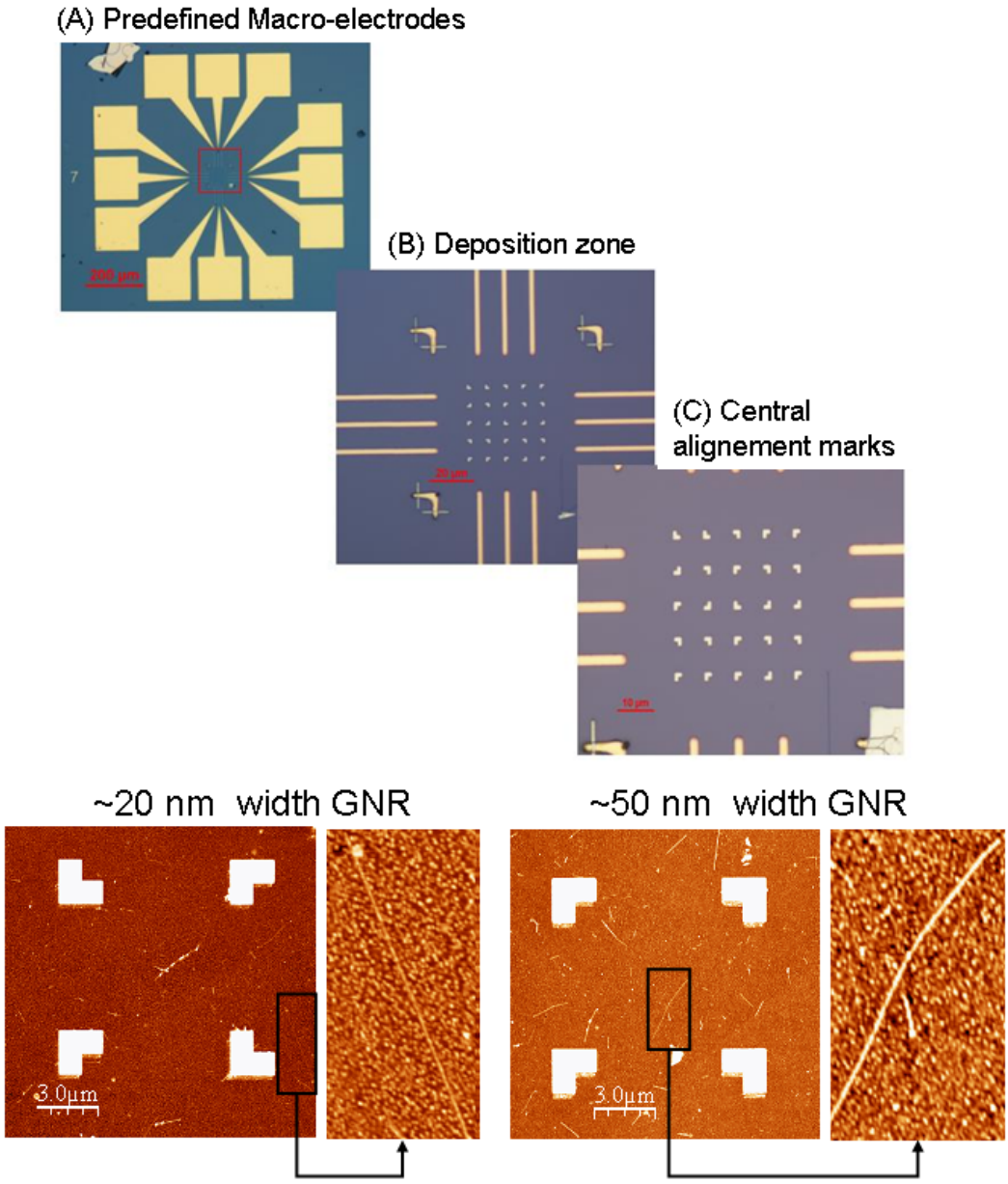

Figure 4.5: **Top**: Si/SiO_2 substrate with predefined macro-electrodes made by optical lithography: (a) Predefined macro-electrodes, (b) deposition zone and (c) marks made by e-beam lithography to align nano-objects. **Bottom**, AFM images of two micro-zone where GNRs of ~ 20 and ~ 50 nm width are located.

(b)). In this central area, 16 zones are designed by e-beam lithography to make easier the localization of nano-object by AFM imaging (Fig. 4.5 (b) and bottom).

Connection method

Many chemical products are involved in the synthesis of these GNRs. To eliminate most of the molecules absorbed around the GNRs, different annealing steps are needed. The two first steps consist in annealing the sample at 320 °C in air for 20 min and after, at 450 °C in Ar for 30 min, to calcine any surfactant or solvent surrounding the GNRs.

An accurate location of the GNRs is obtained by AFM (Fig. 4.5 bottom). After this, specially designed micro-electrodes are defined by e-beam lithography in order to electrically connect the GNRs to the macro-electrodes. These micro-electrodes are specially challenging because the total length of the ribbon is quite moderate, around 1 μm. To approach the ballistic regime, we first envisaged a rather short distance between the source and drain, less than 100 nm. For such a configuration, the electron dose of the e-beam lithography has to be increased by a factor of two. Increasing the electronic dose reinforces the proximity effect, decreasing the size of the unexposed resist between electrodes. After the metal deposition of Ti/Pd (1 nm/40 nm), an extra thermal annealing is made at 200 °C, under Ar, for 15 minutes to improve the electrodes and the contact resistance.

4.1.3 Graphene devices for THz detection

We used the same substrates as for the lithographically patterned GNRs (Si/SiO_2) to design the device for graphene's THz detection. The samples have an antenna, as the one described in [Mendis 2005], with the appropriate dimensions to be efficient up to ∼0.7 THz. This creates an asymmetry between contacts, responsible for a THz photoresponse in field effect transistors.

The final design is shown in Fig. 4.6, presenting a full image of the antenna and its internal parts. As for the previous samples, the antenna and the electrodes are performed with the Raith 150 ultra high definition e-beam writer. The distance between source and drain is L_{S-D}= 1 μm, the source and drain electrode width is W_{S-D}= 2 μm, and the Hall probes are separated by L_{H-H}= 0.93 μm.

4.2 Connection of the GNRs to the electrical measurement system

The connection step is critical since our devices are very sensitive to electrostatic discharge and difficult to handle. A specific procedure is adopted to ensure that the device, the experimentalist, and the equipment are always connected to the ground through 1 MΩ. Steps to connect the samples are the following:

Connection to the sample holder: once the samples fabrication is finished, the substrates are cut into 4x4 mm^2 and the devices are first tested by an home made probe station. Then the substrate is glued with silver paste to the sample holder (a circular ceramic with 8 serigraphied gold electrodes, which allow the connection of

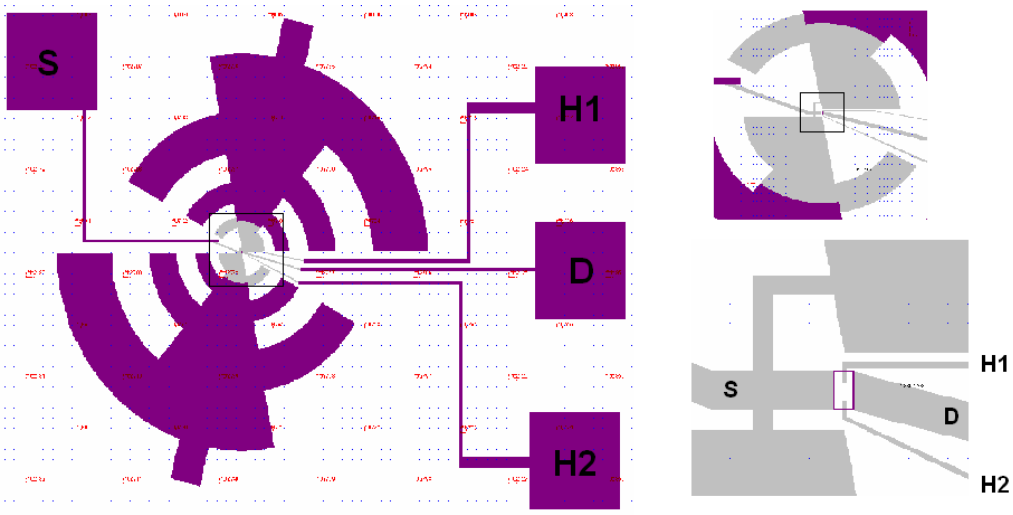

Figure 4.6: Design of graphene samples for THz detection. **Left**, the antenna used to create an asymmetry between electrodes. The device has four contacts: source **S**, drain **D** and two Hall probes **H1** and **H2**. **Right up**, central area of the antenna. **Right down**, The internal part where the electrodes connect the sample (represented by a purple square).

a maximum of 3 GNRs with the back-gate, Fig. 4.7-Top) to ensure a connection to the Si back-gate.

We connect the device by wedge bonding to the sample holder (Fig. 4.7-Top). The wedge bonding may be, in some cases, a dramatic step for the sample. If the bonding parameters are not well set, it may induce a break of the GNR or a damage of the SiO_2 layer between the electrodes and the gate. After the wedge bonding, the samples are tested again with the probe station as well as the gate effect.

Connection of the sample holder to the inset: the sample holder is connected to the inset using a gold wire of 50 μm of diameter and silver paste. This inset is specially designed for pulsed magnetic field environment and low temperatures (Fig. 4.7-Bottom). Its lower part is fabricated in glass fiber to avoid some heating effects during the pulse magnetic field. It has a pick-up coil (to measure the magnetic flux), a Si diode connected to a temperature controller, Lakeshore 332 (calibrated from 300 K to 1.2 K) and 12 connection pins to measure several devices at the same time. After the connection of the sample to the inset, a sock is used to hermetically close the inset, in order to control the atmosphere surrounding the device.

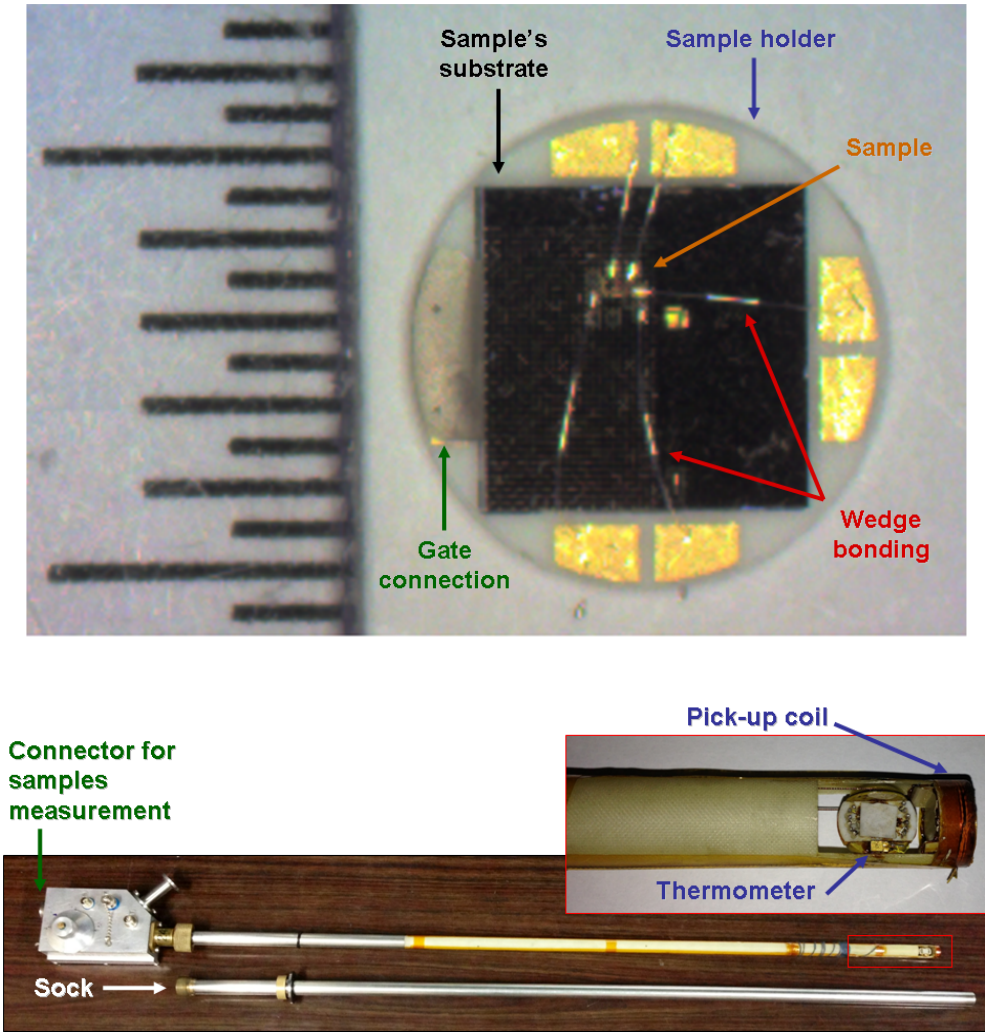

Figure 4.7: **Top**, GNRs sample connected to the sample holder through wedge bonding. Millimeter scale on the left. **Bottom**, photo of the magneto-transport insert specially designed for pulse magnetic field and cryogenic temperatures.

4.3 Samples annealing

Before the electronic transport measurements, an in-situ annealing of the devices is needed to remove contaminants (resist residues, water, etc) and to improve the electronic mobility. After this treatment, the device is not exposed anymore to the air. Depending on the device and its degree of contamination, we use two different types of annealing processes:

4.3.1 The thermal annealing

It consists in warming-up the sample up to 130 °C under moderate vacuum during 3 hours. This process mainly removes water molecules and residual solvents on the GNRs and SiO_2 surfaces.

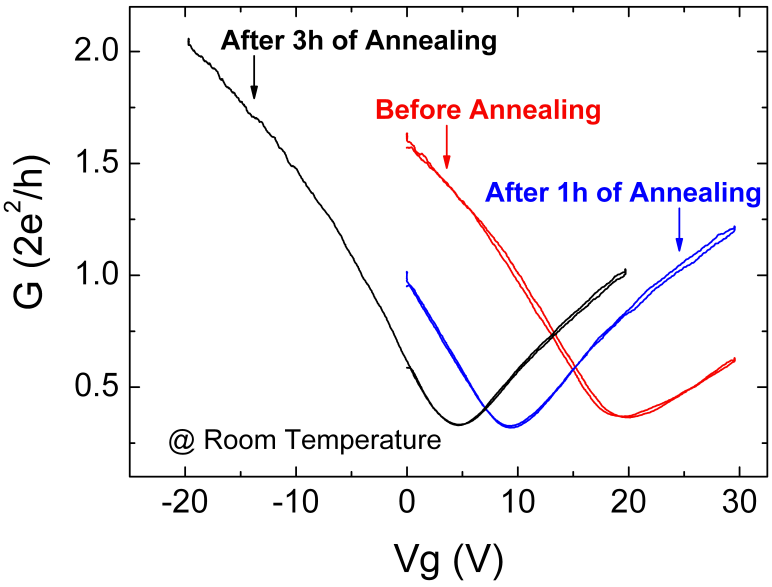

Figure 4.8: Conductance as a function of the back-gate voltage for a 100 nm wide GNR, before thermal treatment (red), after 1 hour (blue) and 3 hours (black) of thermal annealing at 130 °C, under vacuum.

The effect of the thermal annealing is illustrated in Fig. 4.8. A clear shift of the charge neutrality point from ∼20 V to ∼5 V is obtained after 3 hours of annealing. This is a clear signature that the unintentional doping of the sample has been considerably reduced.

4.3.2 The electrical annealing

In some cases, and this was specially the case of GNRs from unzipping CNTs, the thermal annealing treatment is not efficient enough to reveal the intrinsic properties of the GNRs. The main reasons are the chemical processes used to disperse the GNRs into the solution. In this case, the improvement of the conductance characteristic implies an electrical annealing.

The method is based on the application of a source-drain bias voltage of a few Volts which induces a large Joule heating. The limitation of this technique is that the sample's temperature is difficult to estimate [Moser 2007]. In practice, we apply

several sweeps of the bias voltage under vacuum ($\sim 1 \times 10^{-5}$ mbar). If the sweep shows hysteresis effects, the bias voltage has to be gradually increased. This hysteresis appears when the contamination is reduced: the charge neutrality point is closer to zero which increases the resistance of the GNR. In the same time, we are supposed to improve the contact resistance. We assume that the electrical annealing process is finished when the hysteresis is not anymore present .

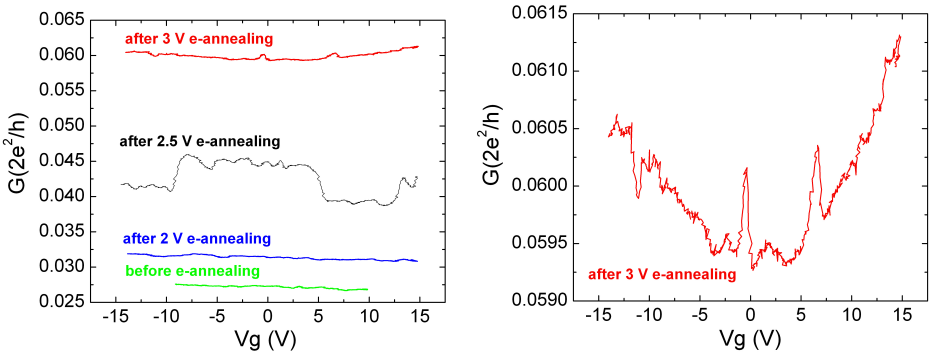

Figure 4.9: **Left**: Conductance as a function of the back-gate voltage for a 23 nm wide and 50 nm long GNR before (green) and after 2 V (blue), 2.5 V (black), and 3 V (red) of e-annealing. **Right**: Conductance as a function of back-gate voltage after 3 V of e-annealing.

The Fig. 4.9 present the conductance as a function of the back-gate voltage curves measured on a GNR derived from CNTs L= 50 nm and W= 23 nm, after different electrical annealing and an increase of the maximum bias voltage up to 3 V. Before the electrical annealing (green curve), the conductance is quite low, with almost no gate effect. After the different annealing processes the conductance is increased by a factor of ~ 3, and a moderate gate effect that starts to develop (right part of the Fig. 4.9). Here, we strongly suspect that the molecules used as surfactant (PmPV) and the solvents are responsible for the low conductance, the bad contacts and also of the screening of the back-gate voltage. The electrical annealing certainly allowed to remove part of the contaminants but both the conductance and its gate dependence remain far from the expected one for a clean GNR.

Despite several tentative on this source of GNR, with many ribbons burned during such a risky process, we did not succeed in reaching optimal electrical characteristics.

4.4 Samples Characterization

The experimental techniques used in this thesis are, the micro-Raman spectroscopy to characterize the number of graphene layers, and mostly the electrical transport measurements at zero field and in the pulsed magnetic field environment.

4.4.1 Micro-Raman spectroscopy

For some samples, the identification of the exact number of layers can not be deduced by optical observations. In such cases, the Raman spectroscopy is very helpful as its spectrum evolves with the number of layers (Fig. 4.10) [Ferrari 2006]. The micro-Raman spectroscopy measurements presented in this work were performed at Centre d'Elaboration de Materiaux et d'Etudes Structurales (CEMES) de Toulouse, with the help of Dr. Miguel Rubio Roy and at LNCMI-Toulouse with the collaboration of Dr. Paulina Plochocka's group.

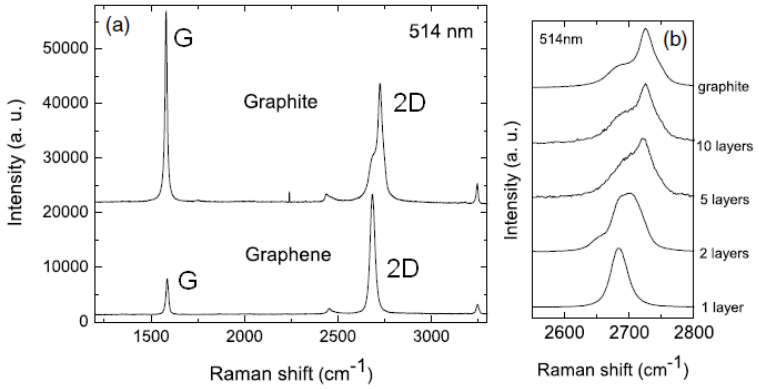

Figure 4.10: **(a)** Comparison of Raman spectra for graphite and graphene monolayer. the intensities have been scaled to have the similar height of the 2D peak. **(b)**, Evolution of the 2D peak with the number of layers. Adapted from [Ferrari 2006].

Raman spectra was performed in the reflexion mode at room temperature. For micro-Raman measurements, a Spectrometer 2950 was used with a vertical polarization and a 100x objective. A laser spot of few microns size was achieved. The laser excitation had a wave length of 532 nm. For each session, measurements on SiO_2, monolayer graphene and HOPG were performed for calibration.

4.4.2 Electronic transport measurements

The electronic transport measurements $G(V_g, V_b)$at zero magnetic field:

Consist in measuring the current that passes through the device as a function of the back-gate voltage (V_g), and at a given bias voltage (V_b). In practice, we apply a low AC voltage ($\sim$ 50 μV) to the device with an ultra low distortion function generator *Stanford Research Systems DS360*, this generator allow us to apply simultaneously an AC and a DC voltage (offset). We measure the AC current that

passes through the device with a Lock-in amplifier *Stanford Research System DSP SR830* while we sweep the back-gate voltage with a DC voltage source *Yokogawa model GS610*. Once the sweep of the back-gate voltage is complete the bias voltage of the sample (offset) is increased and we repeat measurement. We obtain a 2D map of the conductance as a function of the back-gate voltage and the bias voltage $G(V_g, V_b)$. This technique used to study energy dependence of the conductance (Fig. 4.11), the Coulomb blockage regime or the Fabry-Perot oscillations depending on the transparency of the contacts.

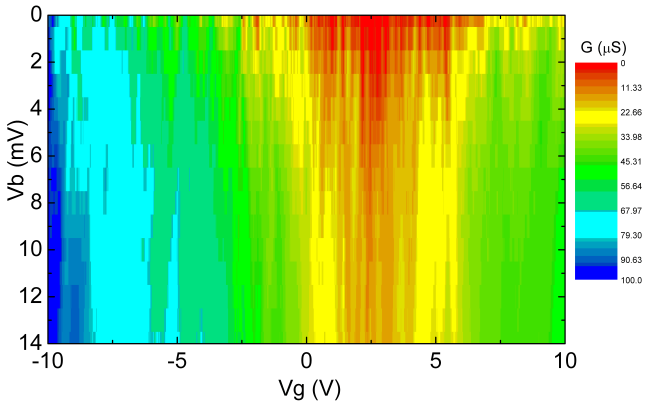

Figure 4.11: Conductance as a function of the back-gate voltage and the bias voltage $G(V_g, V_b)$ for a lithographically patterned GNR of L=350 nm and W=100nm at 2 K.

4.4.3 Electronic transport under pulsed magnetic field

The nondestructive pulsed magnetic field technique has been developed at LNCMI-Toulouse since the 60's. At the moment, we are able to reach 80 T in nondestructive pulsed magnetic fields. For this thesis, we mainly used magnetic fields up to 60 T.

The technique consists in the discharge of a capacitor bank (600 capacitor with a maximum energy of 14 MJ, Fig. 4.12 (a) in a resistive coil made of copper alloys and Zylon, with an internal diameter of 28 mm (Fig. 4.12 (b)). Wires used for the coils combine a very low electrical resistance, a high specific heat and held mechanical, up to 1 GPa. The total pulse duration is around 300 ms,with an increase of the field up to its maximum value during the first 50 ms and after, an exponential and rather slow decrease of the field (Fig. 4.12 (c)).

Our measurement inset and the sample holder are specially designed for the pulsed magnetic field environment. The precautions are twofold: the use of metals to fabricate the sample holder is forbidden to avoid heating effects coming from eddy currents during the pulse. The measuring wires are twister pairs to reduce the induce voltage, proportional to dB/dt.

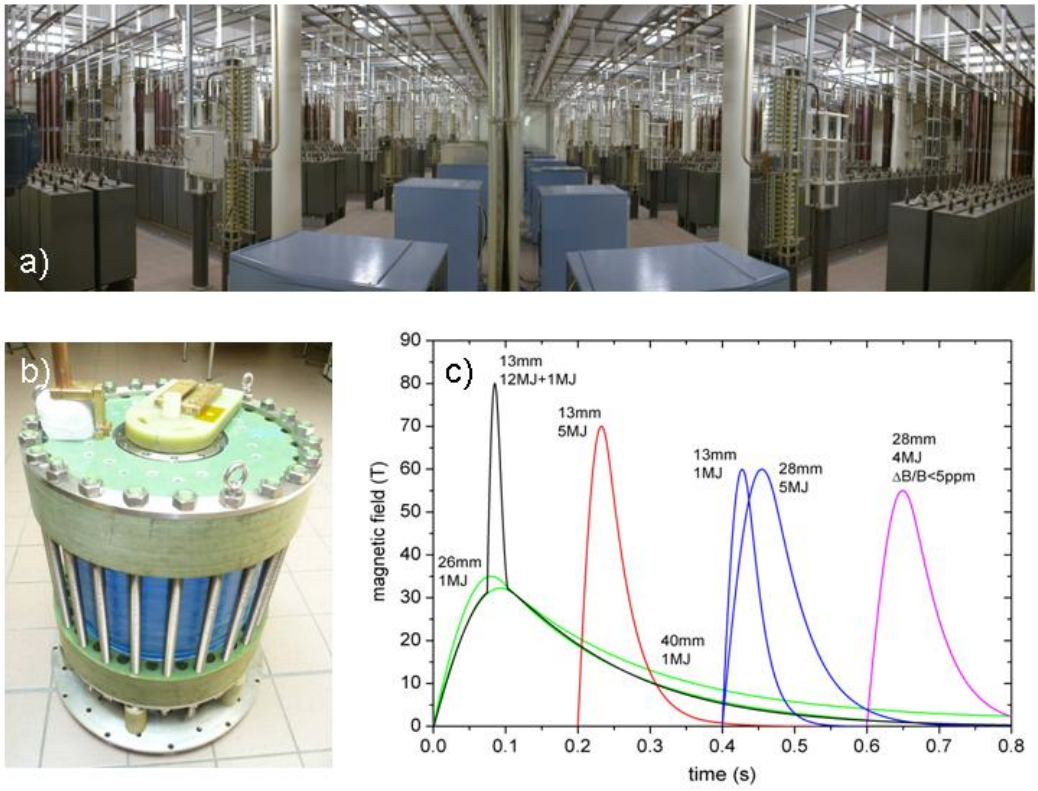

Figure 4.12: (a) 14 MJ capacitor bank at LNCMI-Toulouse (b) Standard 60 T resistive coil and (c) different available magnetic fields as a function of time obtained by different resistive coils, both the inner diameter and the required energy are indicated.

All the magneto-transport results presented in this thesis were performed in DC configuration by applying a voltage and measuring the current. Note that, despite the use of twister pairs, some loops where the induce voltage develops are inevitable. This contribution is numerically subtracted to our signal after the measurement.

4.4.4 THz detection

The idea of using FETs for emission and detection of THz radiation was put forward by [Dyakonov 1993]. The possibility of the detection is due to non-linear properties of the transistor, which lead to the rectification of an AC current induced by the incoming radiation. As a result, a photo-response appears in the form of DC voltage between the source and the drain, proportional to the radiation power (photo-voltaic effect). Obviously, some asymmetry between the source and drain is needed to induce such a voltage. To create this asymmetry, the samples are designed with specific electrodes shapes (section 4.1.3).

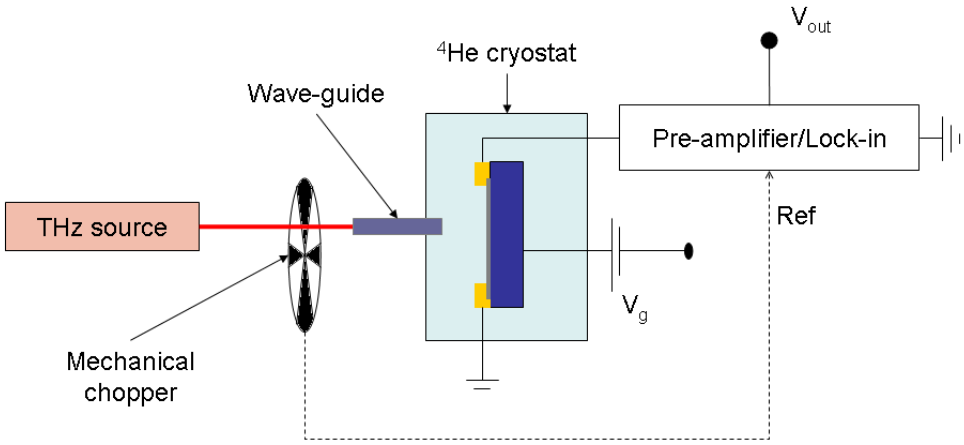

Figure 4.13: Schematic representation of the experimental setup for THz detection available at the Charles Coulomb Laboratory (Montpellier University-France).

An electronic 0.3 THz source based on a frequency multiplier has been used. The contact for the back-gate was outside from the beam spot, to avoid any coupling between the gate and the THz radiation. The incoming radiation intensity was mechanically chopped at 333 Hz and the source-drain voltage (photo-response) was measured with low noise amplifier followed by a lock-in amplifier detecting the DC rectified photo-response (Fig. 4.13). The photoresponse has been studied as a function of the back-gate voltage.

The measurements were conducted in a cryostat at 4.5 K. For the first and second harmonic conductance measurements, the samples were biased with ac current $I_0 \cos(\omega t)$, of frequency $\omega = 133$ Hz in a few ten of nanoampere range, and voltage was measured with a low noise amplifier followed by a lock-in amplifier detecting the first- and second-harmonic responses $V_1 \cos(\omega t)$ and $V_2 \cos(2\omega t)$.

The THz detection experiments were carried out during my stay in Laboratoire Charles Coulomb in the Université Montpellier II, with Prof. Dominique Coquillat.

4.5 Summary

In this chapter, the technological challenges to fabricate good quality GNR devices and the experimental techniques under extreme conditions of magnetic fields have been presented. The mastering of the lithography techniques to pattern and to connect the GNRs has required tremendous efforts in clean room to optimize the different parameters.

We fabricate a total of 168 lithographically patterned GNRs. From these, we measured successfully (electronic transport at zero and under magnetic field at various temperature) only 12 GNRs, 8 of them presented a high quality. Concerning GNRs derived from CNTs, we connected 120 ribbons and we measured completely 9

of them. Unfortunately, non of them show good electronic transport characteristics.

We conclude by saying that our best GNR devices have been finally obtained by e-beam lithography and oxygen plasma etching, with nominal widths between 70 and 100 nm. As we will see in the next chapter, these devices exhibit "good" mobilities, at least high enough to unveil new quantum phenomenon in the high magnetic field regime.

Chapter 5

Experimental Evidence of the Landau Spectrum in Monolayer Graphene Nanoribbons

Contents

In this chapter, we present the electronic transport and the magneto-transport (up to 55 T) results obtained on lithographically patterned monolayer GNRs of widths between 55 and 100 nm. The electronic transport characteristics demonstrate a good quality of the GNRs with a mobility of few thousands. The magneto-transport measurements unveil an anomalous Landau spectrum, which may be explained by an armchair contribution at the edges.

Samples have been prepared from exfoliated graphene and the GNRs have been patterned using e-beam lithography and oxygen plasma etching, following the procedure explained in section 4.1.1. Here, we focus on results obtained on two specific GNRs, called *sample A* with W=100 nm (width) and L=350 nm (length), and *sample B*, with W=70 nm and L=750 nm (see AFM image in Fig. 5.1 (a)). Along this chapter, we also compare these two main results with others obtained on GNRs with similar characteristics.

5.1 Electronic transport at zero magnetic field

Prior to the electronic characterization, the samples are subjected to a thermal annealing treatment in vacuum, as described in section 4.3.1. The conductance as a function of the back-gate voltage, $G(V_g)$, for several temperatures (Fig. 5.1 (b)-(c)) shows the typical ambipolar nature of graphene. A semiconducting behavior, given by the decrease of the conductance at low temperature, and the onset of conductance fluctuations at 4 K are observed. The charge neutrality point (CNP) is found for

back-gate voltages of $V_{CNP} \approx 2.5$ V and -0.5 V, respectively for *sample A* and *B* (Fig. 5.1 (d)). We conclude that the residual doping, after annealing, is low on the two samples.

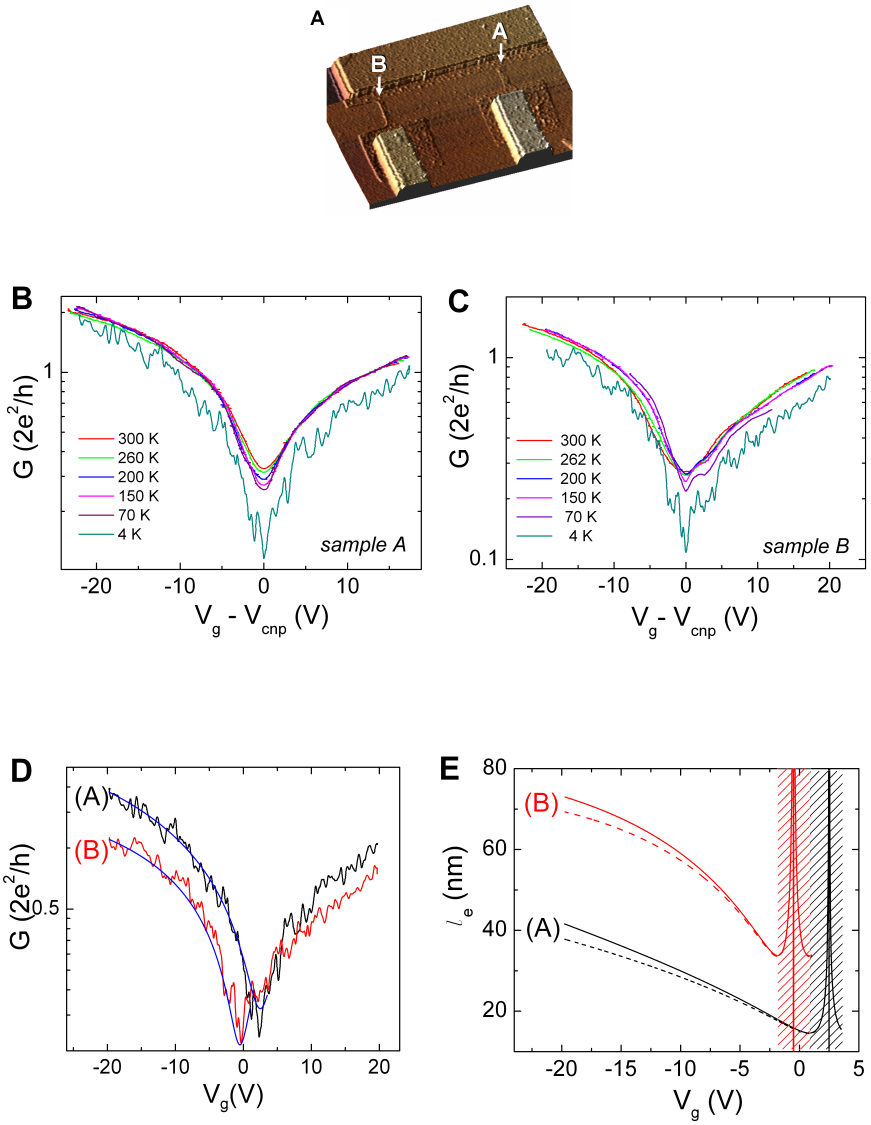

Figure 5.1: **(a)**, AFM image of the two GNRs named *sample A* and *B*. **(b) - (c)**, conductance as a function of back-gate voltage for *sample A* and *B* respectively, at several temperatures. **(d)**, conductance as a function of back-gate voltage for *sample A* (black) and *B* (red) at 4 K, blue lines represent the simulations using eq. (5.1). **(e)**, Extracted mean free path, l_e, as a function of the back-gate voltage for *sample A* (black) and *B* (red), for two contact resistance R_c=500 Ω (dashed line) and R_c=1 kΩ (solid line). The dashed areas represent the back-gate voltages regions where the mean free path calculation is not reliable.

The experimental $G(V_g)$ curves, shown in Fig. 5.1 (d), can be used to estimate the characteristic transport parameters. In a two terminals configuration, the total resistance of the device, R_T, is simply expressed by [Farmer 2009]:

$$R_T = R_c + R_s = R_c + \frac{L}{We\mu\sqrt{n_0^2 + n^2}}\,, \tag{5.1}$$

where R_s is the sample resistance, R_c is the contact resistance, n_0 is the residual carrier density, μ is the field effect carrier mobility, $n = \alpha(V_g - V_{CNP})$ is the carrier density[1], $\alpha = C_g/e$ is the capacitive efficiency and C_g is the electrostatic coupling.

The electrostatic coupling between the ribbons and the back-gate has been estimated, using the software Fast Field Solvers, $C_g \approx 2.4 \times 10^{-4}$ F/m^2. This value is two times larger than the value calculated for a plane capacitor, regularly used for graphene, $\sim 1.1 \times 10^{-4}$ F/m^2. The difference is a consequence of the size reduction. When the aspect ration of the GNR width and the oxide thickness d becomes smaller than 1, in our case $W/d \sim 0.33$, the electric field lines deviate from that of a plane capacitor [Lin 2008]and some fringing fields develop on the edges and onto the top of the GNR. This induces a more intimate coupling and an increase of the effective electrostatic coupling. The value of C_g has been confirmed by the Shubnikov-de Haas oscillation period, as described below.

The use of expression (5.1) to fit the experimental data is shown in Fig. 5.1 (d) (blue). The fitting parameter are: the carrier mobility of $\mu \approx 1200$ (3500) cm^2/Vs, the residual carrier density $n_0 \approx 32{\times}10^{10}$ ($48{\times}10^{10}$) cm^{-2} and the contact resistance $R_c \approx 800$ (950) Ω for *sample A (B)*.

Another way to express the sample resistance, in the frame of the Landauer formalism, in the diffusive regime and neglecting the coherence effects, is:

$$R_s = \frac{h}{2e^2}\frac{1}{\langle T\rangle} = \frac{h}{2e^2}\frac{L/l_e + 1}{N} \tag{5.2}$$

where T is the transmission coefficient, l_e is the mean free path and N is the number of conducting channels at the Fermi energy, E_F. Using expression (5.2), we calculate the total resistance and we deduce a useful relation between the conductance and the mean free path:

$$G = \left(\frac{N}{L/l_e + 1 + NR_c[h/2e^2]}\right)\left(\frac{2e^2}{h}\right)\,. \tag{5.3}$$

Note that the R_c is expressed in unit of $h/2e^2$. For wide ribbons, we express the number of channels by:

$$N = \frac{k_F W}{\pi} = \frac{E_F W}{\pi\hbar v_F} \approx 1.11 \times 10^{-3} E_F(meV) \times W(nm)\,. \tag{5.4}$$

[1] Taking into account the quantum capacitance in graphene, the change in the carrier density induced by an external gate voltage is given by $n = C_g V_g/e + n_Q(1 - \sqrt{1 + C_g V_g/en_Q})$ where $n_Q \equiv \frac{\pi}{2}(\frac{C_g \hbar v_F}{e^2})^2$. The last term in this expression is analogous to the quantum capacitance in 2DEG. For a dielectric constant $\kappa \sim 4$, a gate voltage larger than few millivolts and a thickness of the dielectric larger than few angstroms, the last term can be neglected [Das Sarma 2010].

We assume a contact resistance between R_c ~0.5 and 1 kΩ in consistency with the previous estimation from $G(V_g)$ and the magneto-transport measurements (see below). These estimations are not reliable close to the CNP (striped regions): the final expression for the mean free path is inversely proportional to the Fermi energy and $E_F \propto \sqrt{V_g - V_{\mathrm{CNP}}}$, therefore the expression diverge as we approach the CNP. The resulting mean free path is plotted in Fig. 5.1-(a) for *sample A* (black) and *B* (red). At $V_g = -20$ V, we infer $l_e \approx$ 37-41 (69-73) nm for *sample A (B)*. This rather low value of the mean free paths, compare to the one obtained in unstructured graphene [Peres 2010] is certainly a consequence of the edge disorder induced the oxygen plasma etching along with the bulk disorder characteristic of graphene on SiO_2 substrates. Nevertheless, if one compare with results obtained on GNRs by the same technique [Oostinga 2010, Minke 2012b, Hettmansperger 2012], we remark that the mobility we achieve belongs to the highest values. The electronic mean free path is of the order of the ribbons width, $l_e \sim W$, and $L/l_e \sim 9,5-8,5$ $(10,7-10,2)$, for sample A (B), signature of a weakly diffusive transport regime.

5.2 Electronic transport under high magnetic field

When a magnetic field is applied perpendicular to a GNR, electrons start to describe orbit. Once the magnetic field is high enough, full cyclotron orbits are formed in the bulk of the ribbon and skipping orbits (edge currents) are develop at the edges. When a complete spatial separation of the chiral currents is achieved, the two probe conductance exhibits the Landau quantization. This quantization is intimately related to the band structure of the system at zero magnetic field. The study of the Landau level formation is therefore a powerful tool to explore the electronic confinement effects on the energy dispersion of GNRs.

The magneto-transport measurements presented in this section are performed at 4 K and under a perpendicular magnetic field, up to 55 T. In Fig. 5.2, we plot the resistance as a function of magnetic field, for *sample A*, each curve represents a different carrier density tuned by the back-gate voltage. Remarkable characteristics are clearly visible. A quantized plateau of resistance at ~ 13 kΩ ($\sim (2e^2/h)^{-1}$) is observed for a large range of magnetic field and for different gate voltages. We would like to notice that this was the first reported observation of Landau quantization on GNRs deposited on SiO_2 [Ribeiro 2011]. This resistance plateau is also observed in narrower samples, down to $W = 80$ nm, as seen in inset Fig. 5.2. Interestingly, the quantized plateaus are preceded by a resistance maximum. In a two probes configuration and for device with an aspect ratio $W/L < 1$ [Abanin 2008], an increase of the resistance is actually expected when the Fermi energy crosses a Landau level (section 3.6). In our case, we clearly observe a broadening and a shift to higher magnetic field of the resistance maximum as the gate voltage is changed from -2,5 V to -20 V. The shift of the resistance maximum is a straight-forward consequence of the moving away of the Fermi energy from the CNP. However, the broadening of the maximum is enhanced when the Fermi energy is increased. This is certainly not

intuitive since we would have expected more defined Landau levels when they cross the Fermi energy at larger field.

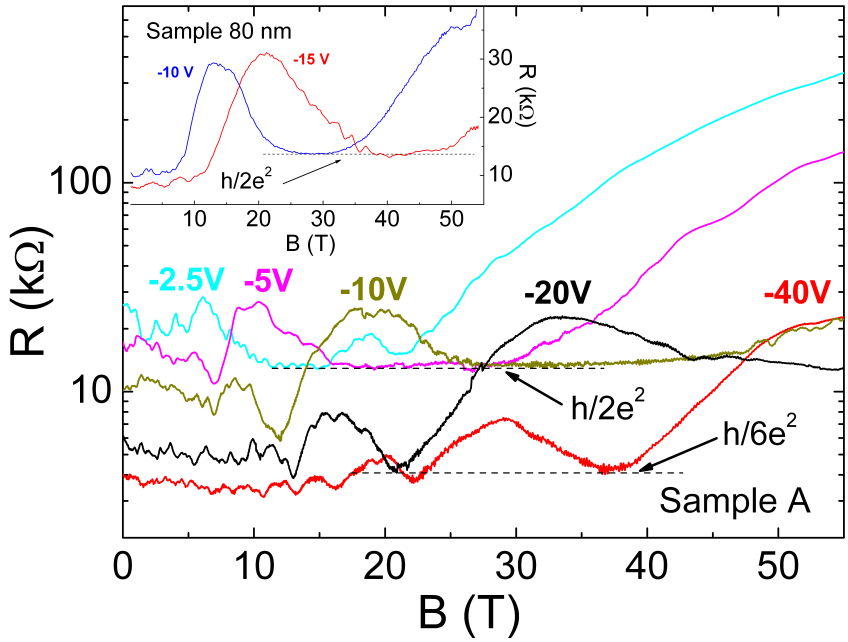

Figure 5.2: Two probe esistance of *sample A* as a function of the applied magnetic field at 4 K, for several back gate voltages V_g=-2.5, -5, -10, -20 and -40 V. Inset: magneto-resistance for another GNR device of width 80 nm at two different back-gate voltage V_g=-10 and -15V showing similar characteristics.

Another quantized value of the resistance, forming a minimum and not a plateau, at ∼4 kΩ (∼ $(6e^2/h)^{-1}$) is seen when the carrier density is increased (curves at -20 and -40 V, Fig. 5.2). These two values of the resistance quantization are the expected when the Fermi energy lies between the Landau levels N=0 and 1, in case of a monolayer graphene with a filling factor of $\nu = 2$ and 6. Note that the experimental values of the quantization plateaus and minima are slightly larger than $h/2e^2$ and $h/6e^2$. This is due to the non zero contact resistance still present in a two probes configuration. We extract a contact resistance between 0,5-1 kΩ, in consistency with the field effect mobility analysis. After the plateau at $\nu = 2$, we observe a large increase of the resistance in higher magnetic fields, this occurs when the Fermi energy starts to enter into the lowest Landau level at zero energy, as already observed in 2D graphene [Checkelsky 2009].

The first signatures of the electronic confinement appear at high doping levels ($V_g = -40$ V), where the Shubnikov-de Haas oscillations are observed, Fig. 5.3 (a). At first look, these oscillations seem standard $1/B$ SdH oscillations. However,

the location of the resistance maxima as a function of the inverse magnetic field shows a strong departure from the $1/B$ periodicity (Fig. 5.3 (b)). This deviation occurs at low fields when the electronic confinement overcomes the magnetic one (section 3.4). We analyze this departure from the linearity using the expression of the number of occupied subbands at the Fermi energy in a square-well potential of width W [Beenakker 1991]:

$$N = Int\left\{\frac{2E_F}{\hbar\omega_c}\left[Arcsin\left(\frac{W}{d_c}\right)+\frac{W}{d_c}\left(1-\left(\frac{W}{d_c}\right)^2\right)^{1/2}\right]\right\} \qquad for \;\; d_c > W \tag{5.5a}$$

$$N = Int\left\{\frac{1}{2}+\frac{E_F}{\hbar\omega_c}\right\} \qquad for \;\; d_c < W \tag{5.5b}$$

This expression was originally calculated for a confined 1D electron gas. We modify this formalism to account the Dirac fermions with their specific energy dependence of the Landau states. We finally obtain:

$$N = Int\left\{\frac{2\hbar n}{\pi eB}\left[Arcsin\left(\frac{W}{d_c}\right)+\frac{W}{d_c}\left(1-\left(\frac{W}{d_c}\right)^2\right)^{1/2}\right]\right\} \qquad for \;\; d_c > W \tag{5.6a}$$

$$N = Int\left\{\frac{\hbar n}{eB}\right\} \qquad for \;\; d_c < W \tag{5.6b}$$

By using the sample width as a fitting parameter, we reproduce the magnetic field dependence of the number of occupied Landau states (Fig. 5.6 (b)). We extract an effective width of $W_{\text{eff}} \approx 93$ nm, which is in good agreement with the nominal value of our ribbon width (≈ 100 nm, measured by AFM).

From the SdH oscillations at different carrier densities, we can also extract the electrostatic coupling between the GNR and Si back-gate. The relation between the oscillation frequency and the capacitive coupling is given by:

$$B_F = \frac{hn}{4e} = \frac{h\alpha(V_g - V_{\text{CNP}})}{4e} = \beta(V_g - V_{\text{CNP}})\,. \tag{5.7}$$

From the slop of the $B_F(V_g)$ curve (Fig. 5.2 (c), red line). We deduce $\beta = 1.55$ T/V, and by using the expression (5.7), we infer $\alpha \approx 1.48 \times 10^{15}$ m^{-2} V^{-1} and $C_g \approx 2.3 \times 10^{-4}$ F/m^2. This value is in a very good agreement with the numerical simulation presented in section 5.1. Note that recent results obtained on GNRs with a similar geometrical configuration show the same enhancement of the capacitive efficiency [Hettmansperger 2012].

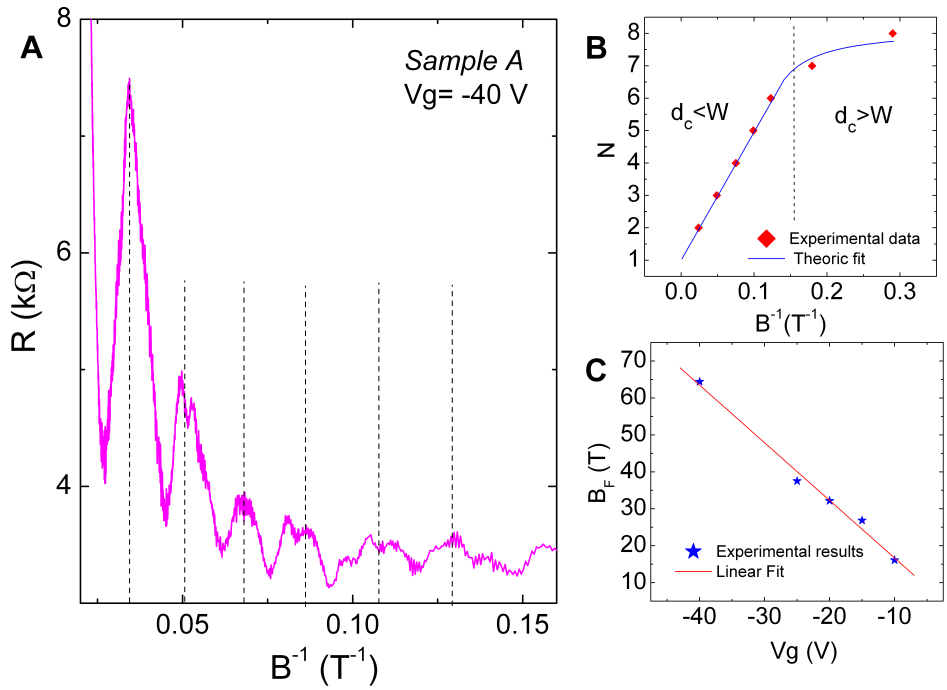

Figure 5.3: **Shubnikov-de Haas oscillations analysis.** **(a)** Resistance as a function of the inverse magnetic field for *sample A* at high doping level V_g=-40 V. The dashed lines indicate the resistance maxima. **(b)**, number of occupied Landau levels as a function of the inversed magnetic field extracted from the SdH oscillations (red diamonds) and its fit using eq. (5.6) (blue). The dashed vertical line represents the magnetic field where $d_c \approx$W. **(c)**, SdH oscillation period for different back-gate voltage (blue stars) and the linear fit (red).

Lets now turn our attention to *sample B*. The magneto-resistance measurements for high doping levels, V_g=-30, -40 and -50 V (inset of Fig. 5.4), also reveal the SdH oscillations and the presence of a quantized minimum of resistance at ~ 4 kΩ ($\sim (6e^2/h)^{-1}$), marked by a dashed line in the plot. These SdH oscillations also exhibit a departure from the $1/B$ dependence similar to the previous ribbon.

However, contrary to *sample A*, the magneto-resistance measurements at low doping levels (Fig. 5.4 main panel), present a clear double peak (marked by vertical arrows) before the expected plateau at $(h/2e^2)$ at larger fields. Only an unique and broad maximum of resistance was observed on sample A.

We also note that the twofold resistance maxima shifts to higher magnetic field when the carrier concentration is increased. If we plot the resistance as a function of the filling factor, $\nu = hn/eB$, (Fig. 5.5), we see that the resistance maxima occur

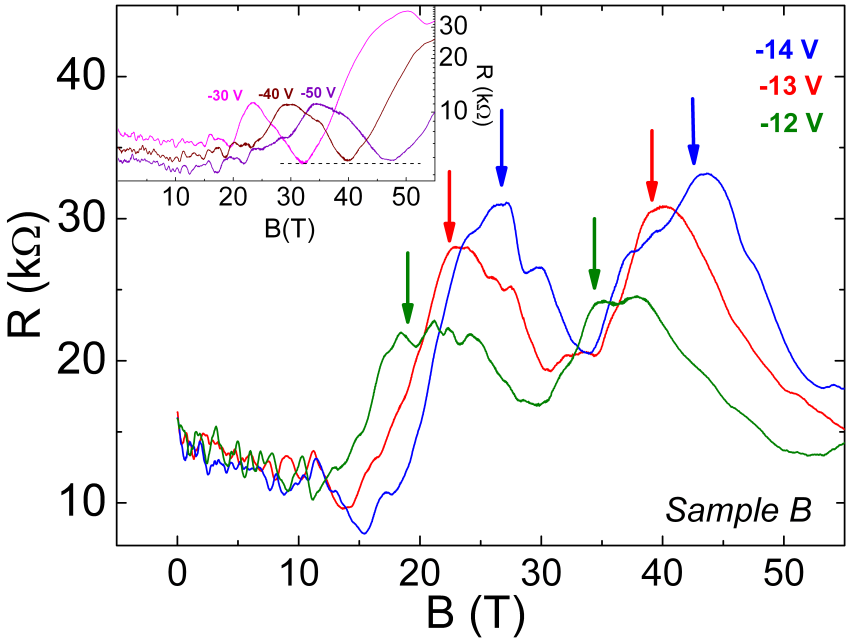

Figure 5.4: Magneto-resistance measurements of *sample B* for different back-gate voltages, V_g= -12 (green), -13 (red), -14 (blue) V. The arrows pintpoint the unexpected double peak. Inset: Magneto-resistance for *sample B* at high doping levels V_g= -30 (pink), -40 (wine), -50 V (violet). The dashed line indicates a resistance quantization of ($\sim h/6e^2$).

at identical values of ν. This is a proof that this feature is related to the electronic band structure and its magnetic field dependence.

In order to deeply understand the main characteristics of the magneto-resistance measurements, we present in the following section, numerical simulations of the electronic band structure of aGNR and its magnetic field dependence.

5.2.1 Evidence of magneto-electric subbands in GNRs

The simulations of the GNR band structure under a perpendicular magnetic field have been performed by Dr. Alessandro Cresti from the CEA-INAC-Grenoble. In this part, we bring evidence that the onset of the magneto-electric subbands and their crossing of the Fermi energy explain in details, the magneto-resistance we measure in high field, for different doping levels.

The electronic structure of an aGNR of 70 nm width at B=0 T is shown in Fig. 5.6 (a). As the ribbons used in our experiments are quite wide, their band structure is not dependent on the exact number of dimmers that compose the GNR. We note

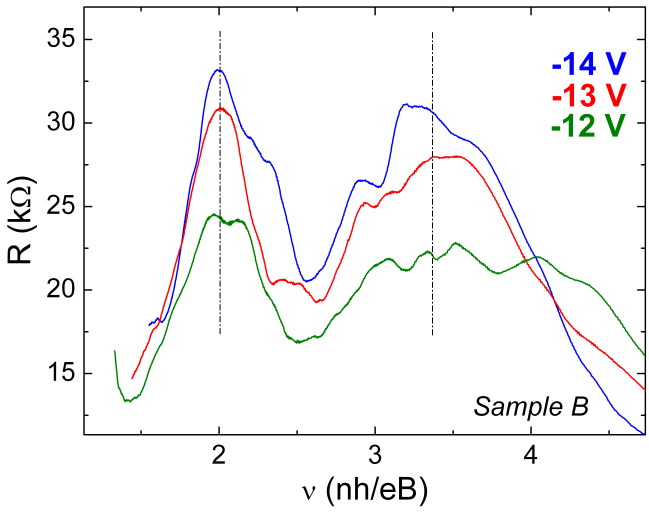

Figure 5.5: Resistance of *sample A* as a function of the filling factor at 4 K, for V_g= -12 (green), -13 (red), -14 (blue) V.

the direct gap at the center of the Brillouin zone as well as the valley degeneracy lifting of the 1D subbands (doted and solid line) due to the mixing of the two K and K' valley imposed by the boundary conditions of the aGNR.

Once a strong magnetic field is applied ($l_m \ll W$), Fig. 5.6 (b) (B=50 T, $l_m \approx 4$ nm), we see that the energy gap is closed forming the N=0 Landau level. The valley degeneracy lifting is preserved at the ribbons edges, where edge currents are formed and conduction takes place. However, at the center of the ribbon (for low k), the standard graphene Landau levels (bulk states) develop with the K and K' valley degeneracy. If one follows the minima of the 1D electronic bands as a function of the magnetic field, one obtains the magneto-electric subbands (Fig.5.6 (c)). In this figure, the dashed and solid lines represent the valley degeneracy lifted subbands. For moderate magnetic field (around 10 T), the magneto-electric subbands recover the $\sqrt{B}$ behavior expected for graphene. As the magnetic field increases, the propagating states become more confined along the armchair edge and the lift of the valley degeneracy is enhanced.

Additionally, from the energy bands, $E(k)$, we deduce the density of states and then the Fermi energy for a given doping level and also for a given magnetic field (blue and green curves at Fig. 5.6 (c)).

The Fermi energy, as expected, oscillates to keep constant the number of available states filled by the extra charge carriers $n(V_g)$ below E_F. As a consequence, the Fermi energy is pinned into the van Hove singularities, at the bottom of each subband. This pinning is specially large for the lowest levels where the corresponding flat bands are more extended.

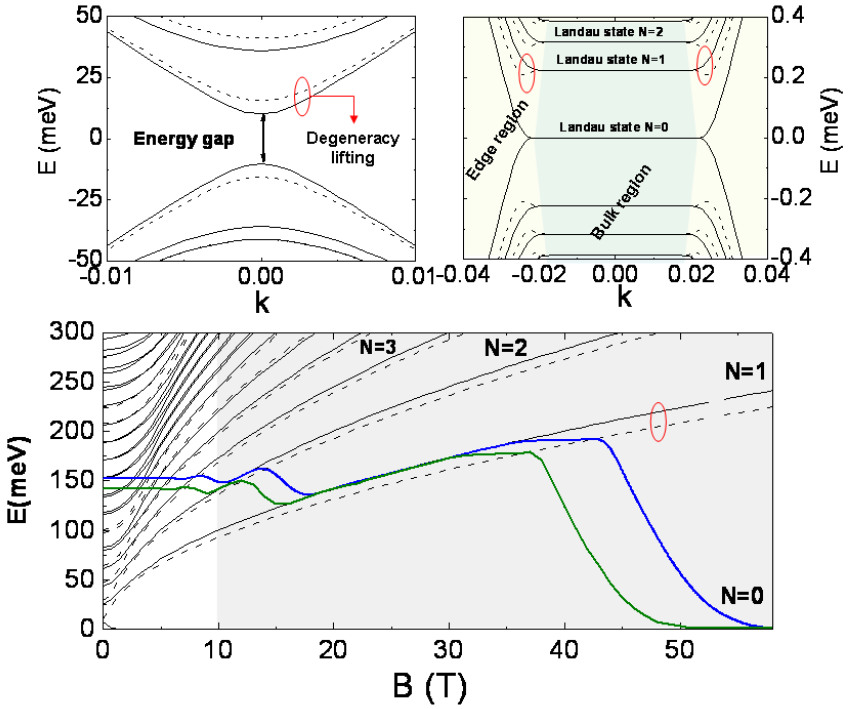

Figure 5.6: **(a)** Electronic structure of an aGNR of 70 nm wide. The red circle shows degeneracy lifting. **(b)** The same electronic structure under B= 50 T. The yellow region represents the edges of the ribbon, the blue region the bulk, and the red circle indicates the valley degeneracy lifting. **(c)** Evolution of the minima of the band structure in high magnetic field, the gray region represents the $\sqrt{B}$ behavior of the 1D subbands. Blue and green lines are the Fermi energy (see text). In all the figures, the dashed lines represent the 1D branches resulting from degeneracy lifting due to edge structure.

To correlate the magneto-transport with the magneto-electric subbands, it is necessary to calculate the Fermi level and its field variations for each gate voltage. At zero magnetic field, the carrier density and the Fermi energy are related by: $n = 4\pi E_F^2/(h^2 v_F^2)$. This expression holds for 2D graphene. Here, we assume that it remains valid since, at rather high doping levels where we focus our study, the number of 1D subbands is quite high. By using this expression, we also neglect the influence of electron and hole puddles, which is reasonable, considering we work quite far from the CNP. The Fermi energy versus the gate voltage is finally defined by $E_F(\text{meV}) \approx 40 \times \sqrt{(V_g - V_{\text{CNP}})}$. Once the Fermi energy, $E_F(B)$ for each magneto-resistance curve is calculated, we compare the location of the maxima of resistance with the magneto-electric subbands intercepting $E_F(B)$.

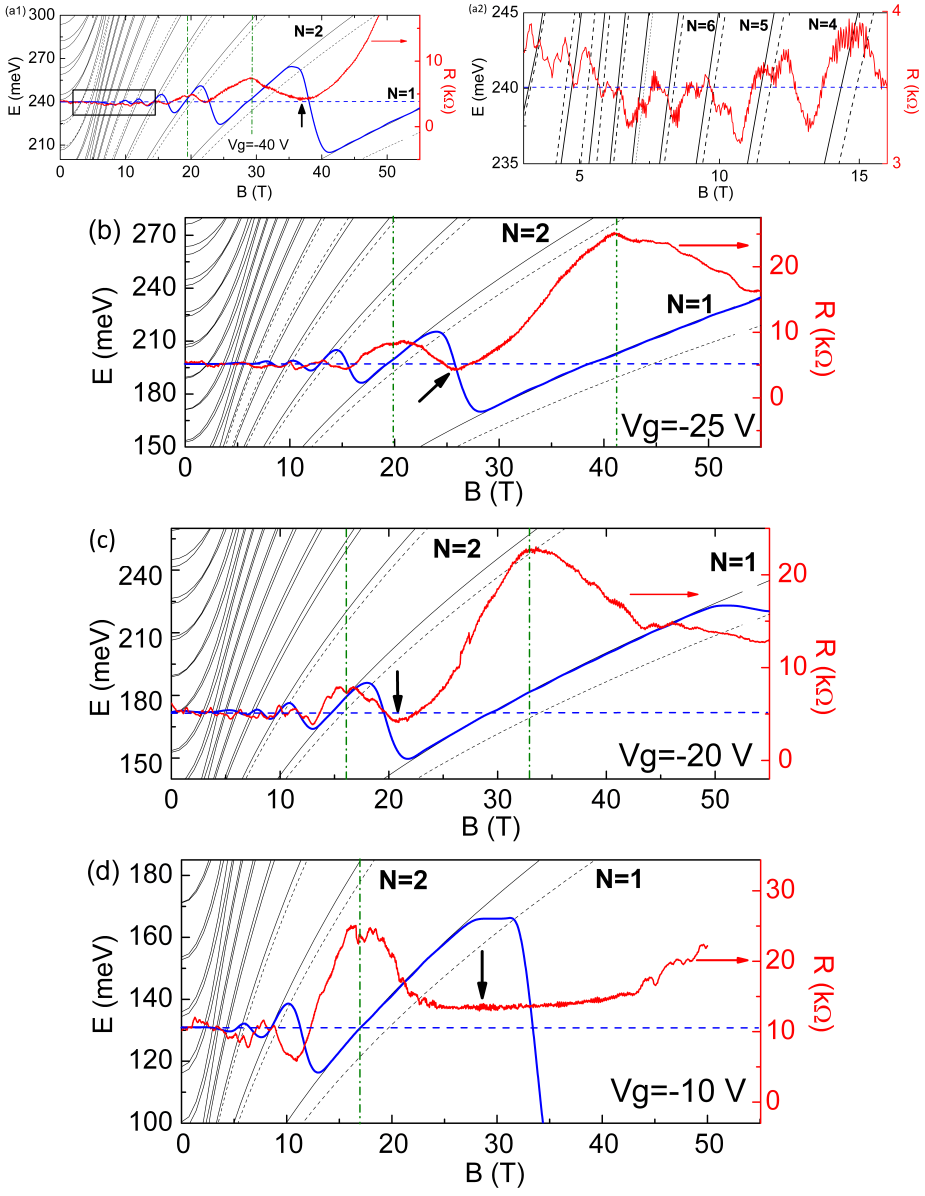

Figure 5.7: Magneto-electric subbands for a 100 nm wide aGNR and direct comparison with magneto-resistance measurements (red curves and right axis) for *sample A*. The blue curves are the calculated Fermi energy (see text) and the dashed blue line is the constant Fermi energy. (a-1), V_g =-40 V and (a-2) zoom on the low magnetic field. From top to bottom, V_g = -10 (b), -20 (c) and -25 V (d). The vertical dot dashed lines represent the maxima of magneto-resistance and the black arrows show the quantized values of theresistance. The index for the lowest Landau levels are given on the figures.

Analysis of sample A

In Fig. 5.7, we plot on a same graph the magneto-electric subbands (for a 100 nm wide aGNR) and the magneto-resistance curves of *sample A*.

For low magnetic fields, from 3 to 16 T, the Fermi energy pinning is negligible. A constant Fermi energy can reasonably be assumed (Fig. 5.7 (a) horizontal dashed line). We see that each time the Fermi energy crosses a Landau level, there is a maximum in the resistance due to the enhancement of the backscattering (zoom Fig. 5.7 (a2)). This is an additional confirmation of the SdH oscillations originating from the successive depopulation of the 1D magneto-electric subbands. At low magnetic field (below 5T), we can not distinguish between the SdH oscillations and the conductance fluctuations.

At higher magnetic field, we cannot neglect anymore the pinning of the Fermi energy on the lowest occupied subbands.

By comparing $E_F(B)$ (blue lines) and $R(B)$ (red curve) for different doping levels, we observe that the maxima of resistance roughly occur in the middle of the Fermi energy pinning (Fig. 5.7 (b), (c) and (d)). The minima that may correspond to quantized values develop when the Fermi energy is between two subbands. More important, we remark that the broadening of the resistance maximum scales with the strength of the Fermi energy pinning. This explains the enhanced broadening of the resistance maximum occurring at larger doping levels (i.e. at larger magnetic fields).

Analysis of sample B

The comparison of the calculated magneto-electric subbands for a 70 nm wide aGNR with the magneto-resistance of *sample B* show interesting features, (Fig. 5.8). As for sample A, a good agreement between the magneto-electric subbands crossing the Fermi energy and the quantum oscillations of the magneto resistance requires to consider the oscillatory behavior of the Fermi energy only when the lowest Landau states are occupied, Fig. 5.8 (a). Besides, as a consequence of the smaller width, the two sub-bands (dashed and solid lines) composing a Landau state are slightly more separated.

At 40 T, the energy separation of the Landau sub-levels forming the $N = 1$ Landau state is around 14 meV, instead of 11 meV for sample A. The calculated Fermi energy get pinned not only on the bulk states, at zero k, but also on the minimum of the sublevel that develops at larger k. This effective Fermi pinning on the second sublevel goes along with the experimental evidence of the splitting of the resistance maximum into two peaks (Fig. 5.8 (b) and (c)). When the doping level is increased, both the two fold resistance maximum as well as the twofold Fermi energy pinning are shifted to higher magnetic fields.

The very good agreement we observe between the pinning of the Fermi energy on the two levels and the double resistance maxima, for different doping levels, strongly support a direct signature of the valley degeneracy lifting of the Landau levels on the magneto-resistance curves. Such a behavior is only expected to occur on GNRs with armchair edges (section 3.4.2). So, the quantum oscillations we measure on sample B support an experimental evidence of an armchair type contribution at the edges, despite the rather aggressive patterning process we used (oxygen plasma

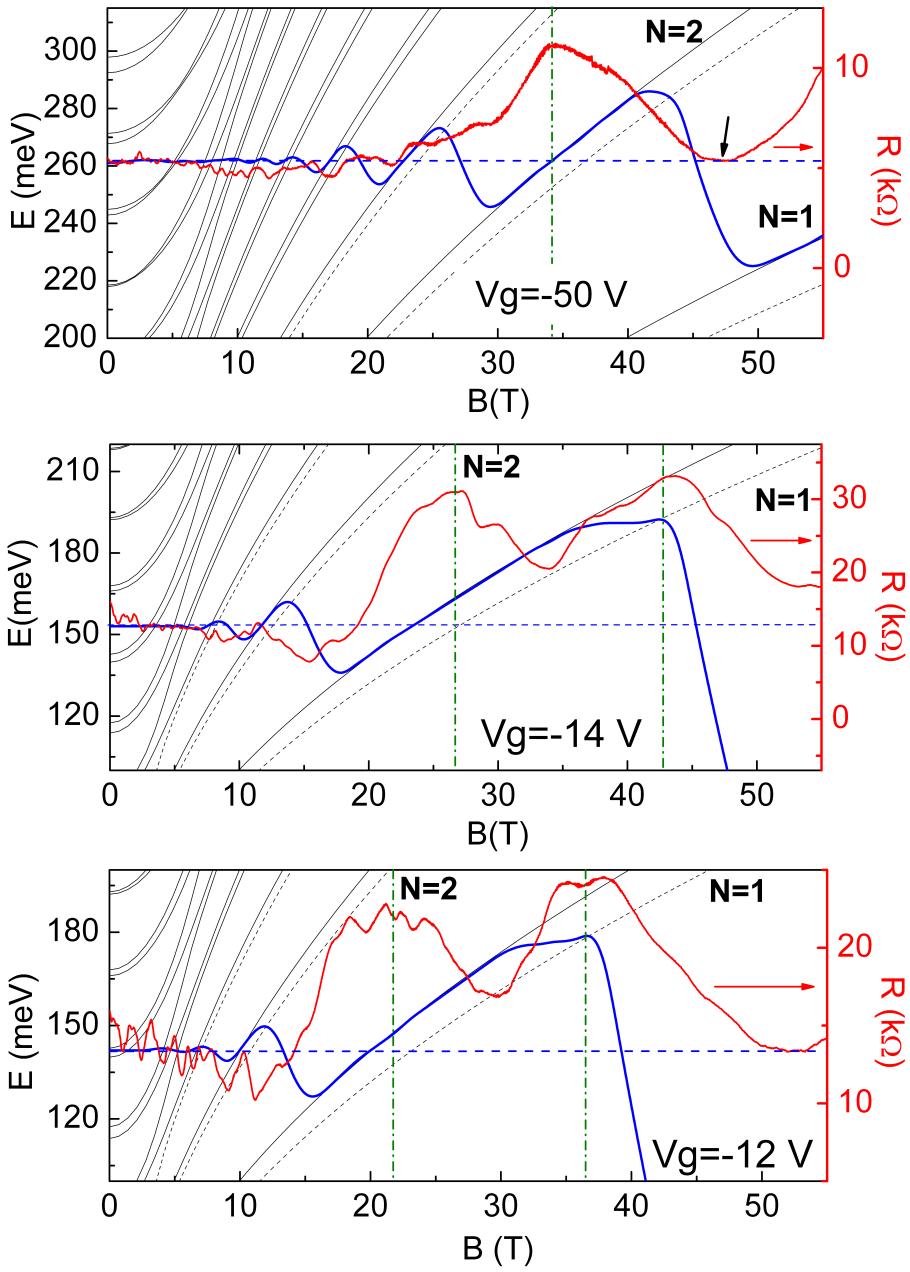

Figure 5.8: Magneto-electric subbands for a 70 nm wide aGNR and direct comparison with magneto-resistance measurements (red curves and right axis) of *sample B*. The blue curves are the calculated Fermi energy (see text) and the dashed blue line is the constant Fermi energy. From top to bottom, V_g = -12, -14 and -50 V. The vertical dot dashed lines represent the maxima of magneto-resistance and the black arrows indicate the quantized values of the resistance. The index for the lowest Landau levels are given on the figures.

etching).

As concluding remarks, we stress that a convincing agreement has been obtained between the magneto-electric subbands crossing the Fermi energy and the quantum oscillations we measured in pulsed magnetic field. Our analysis brings evidence of:

(i) Anomalous SdH oscillations, fingerprints of the conductance that reveals the well defined chiral edge currents on the two edge of the ribbon.

(ii) Specific magneto-electric sub-bands that are only supposed to develop for armchair edges.

The valley degeneracy lifting we suspect on sample B, signature of an armchair type contribution calls for the following remarks:

- The twofold resistance maxima, consequence of the twofold Fermi energy pinning on the Landau sublevels are not observed on sample A. As already mentioned, sample A is wider giving rise to a lower energy separation of the sub-levels and its mobility is reduced, implying a larger broadening of the Landau states.

- The valley degeneracy lifting of the $N = 1$ Landau level has been already reported on graphene Hall bar deposited on Si/SiO_2 [Zhang 2006] under $B > 25$ T. In such a case, the degeneracy lifting is not driven by the confinement but rather by the electronic interactions. We strongly believe that this bulk effect is not present in our devices since the electronic mobility of the GNR is definitively too low [Nomura 2006]. Additional measurements performed at the LNCMI on graphene flakes of similar mobilities than our GNRs do not reveal any degeneracy lifting under 60 T at 2 K.

- In terms of concept, it is interesting to emphasize the role of the magnetic confinement. On one hand, the magnetic confinement overcomes the electronic confinement, on the other hand, the magnetic confinement combined to a bias voltage pushed the conducting channels at the edges of the ribbon. Such a magnetic confinement at the edges makes the electronic transport more sensitive to the edge symmetry and it finally gives strong indication of the band structure at zero magnetic field.

5.2.2 The temperature effects on the Landau spectrum

As seen in Fig. 5.8, the energy spacing between the two sub-bands forming a Landau level (continuous and dashed lines) is relatively small, $\Delta_{SB} \sim 4$ meV at 25 T and ~ 5.5 meV at 45 T for N=1, in a 70 nm wide aGNR. It becomes larger at higher magnetic field. To observe these two subbands in magneto-transport measurements, the thermal broadening, k_BT, and the disorder induced broadening must be smaller than Δ_{SB}.

In Fig. 5.9, we plot the magneto-resistance measurements at two temperatures $T = 100$ (black) and 4 K (red), corresponding to a thermal broadening of $\Delta_{Th} \sim$ 8.6 and 0.34 meV, respectively. The (a) and (b) figures show the magneto-resistance curves for different back-gate voltages V_g = -14 and -20 V, respectively. We note that the temperature effects are very well marked in both cases: the broad maximum of resistance transforms into two well defined maxima.

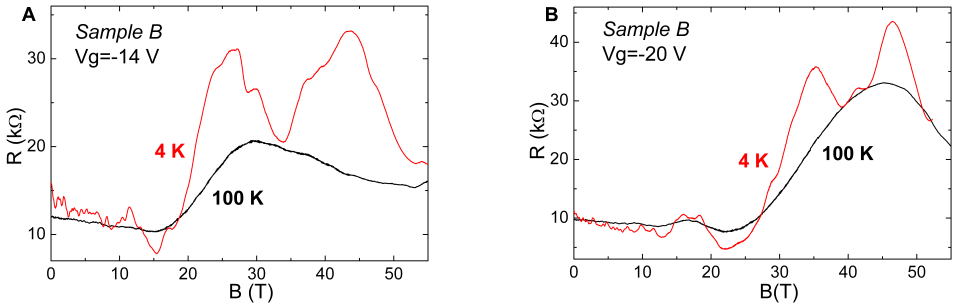

Figure 5.9: Magneto-resistance of *sample B* for two different temperatures 100 K (black) and 4 K (red) at different back gate voltages V_g = -14 (a) and -20 V (b).

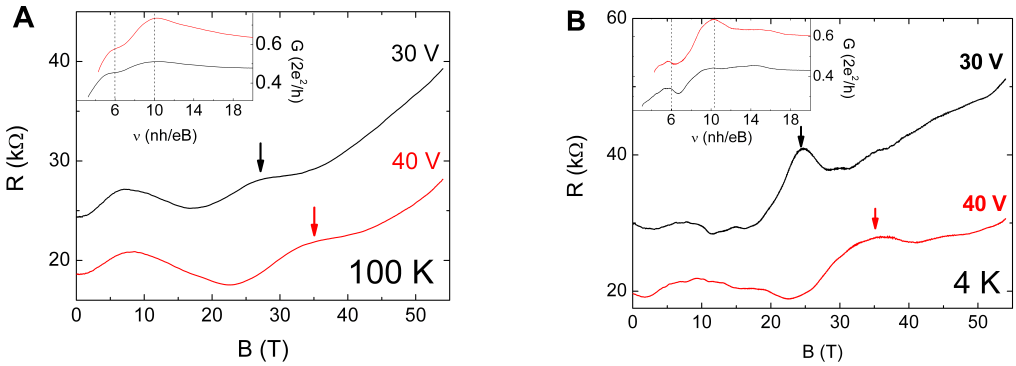

Figure 5.10: Magneto resistance of a 55 nm wide GNR with low mobility ($\mu \sim 600$ $cm^2V^{-1}s^{-1}$) for T= 100 (a) and 4 K (b). Measurements at two different back gate voltages V_g = 30 (black) and 40 V (red).

As an example, we show in Fig. 5.10, the magneto-resistance curves for a 55 nm wide GNR with a low mobility, $\mu \sim 600$ $cm^2V^{-1}s^{-1}$ at 4 K. We observe some structures (maxima or minima of resistance) that shift as a function of the back-gate voltage (marked by vertical arrows), signature of the onset of the Landau states. In the insets of the Fig. 5.10 are plotted the conductance as a function of the filling factor. Here, the maxima of conductance are present for ν ~6 and 10 as expected for a graphene monolayer. But the oscillatory behavior is poorly defined and there is not hint of quantization.

The device quality (i.e. its electronic mobility) remains a critical parameter even in high magnetic field.

5.2.3 Impact of the disorder on the Landau quantization

In Fig. 5.11 (a) and (b), we present the magneto conductance curves as a function of the filling factor, $\nu = nh/eB$, at 4.2 K for different charge densities, for sample A and B, respectively.

The shape of the conductance as function of the filling factor is not the step-like shape expected for the Hall conductance. Instead, this one is a mixture of the Hall and longitudinal conductance (section 3.4.2). In the case of a sample with an aspect ratio $L/W > 1$, a minimum of conductance between two quantized values is attended [Abanin 2008]. In Fig. 5.11 (a), we plot the numerical simulation of the conductance as a function of the filling factor for sample A in the frame of the Abanin's model [Abanin 2008]. We use the sample aspect ratio $\xi = L/W$ and the Landau broadening, λ, as fitting parameters. We obtain $\xi = 4.1$ as fitting parameter for the aspect ratio, in good agreement with the nominal of $\xi = 3.5$ and a Landau broadening of $\lambda = 0.84$ for $\nu = 2$ and $\lambda = 1.05$ for $\nu = 6$.

We now discuss the robustness of the conductance quantization at $\nu = 6$, for the two samples A and B, when the doping level is gradually reduced. We see that below a critical back-gate voltage, the conductance at $\nu = 6$ is not anymore quantized and its value start to decrease. Such a decrease has its origin in the backscattering between the chiral edge currents that are not anymore fully separated. From Figs. 5.11 (a) and (b), we extract the conductance values, at ν =6, and the corresponding magnetic field at which this filling factor is reached (Fig. 5.11 (c)). For *sample A*, a magnetic field of 25 T is required to completely separate the edge currents and, for *sample B*, this magnetic field is slightly higher, 32 T.

To visualize the width of the edge channels in pristine GNR, numerical simulations of the spatial distribution of the flowing current through the device has been performed by Dr. Alessandro Cresti. In Fig. 5.12 (a), is plotted the calculated current density mapping in a 70 nm armchair ribbon as a function of the magnetic field. The Fermi energy is varied accordingly to keep constant ν =6. In high magnetic field, the chiral channels are more and more pushed toward the edges, thus increasing their spatial separation. The possibility of backscattering is reduced and the conductance is quantized at $6e^2/h$.

From the transverse distribution of the current, we extract the current separation, Δl as a function of the magnetic field, Fig. 5.11 (d). The channel separation gradually increases from 0 to 60 (30) nm when the magnetic field increase from 4 (12) to 50 T, for sample A (B). We note that, at 25 T and 32 T, magnetic field values for which the quantization degrades, the separation between the edge channels are estimated in $\Delta l \sim 45$ nm and $\Delta l \sim 20$ nm for the two samples. Such large values, deduced in case of pristine GNR, does not allow any coupling between the k^+ and k^- currents. This result makes clear that some disorder must be introduced in the system to mixt the edge currents at 25 and 32 T.

For sample A, the chiral currents start to mix while they are supposed to be distanced by 45 nm. For sample B, this distance is reduced to 20 nm. This is consistent with a higher degree of disorder for sample A, showing a lower mobility.

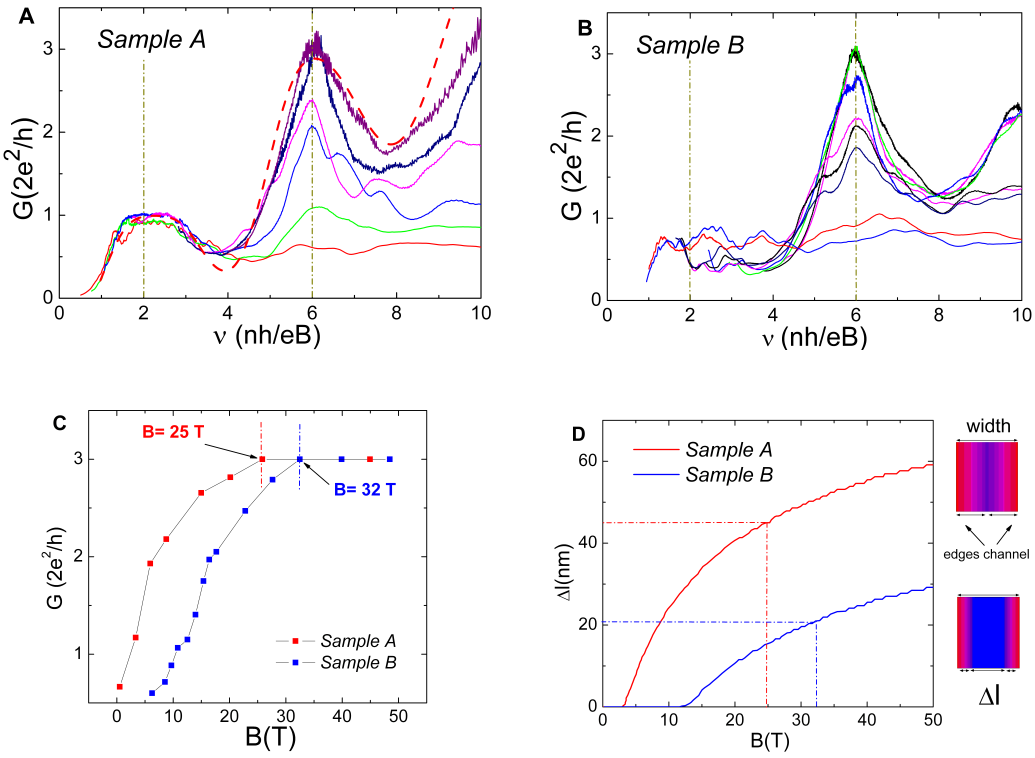

Figure 5.11: Conductance as a function of the filling factor for different gate voltages for *sample A* (**a**) and *sample B* (**b**). The red dashed line in the left figure is the simulation of $G(\nu)$ from the conformal mapping approach (see text). The green dash dot lines represent the filling factor where maxima of conductance are expected for monolayer graphene. **(c)** Conductance at ν =6 as a function of the magnetic field for *sample A* (red squares) and *sample B* (blue squares). **(d)** Numerical simulations of the edge current separation, Δl, as a function of the magnetic field for *sample A* (red) and *sample B* (blue).

To illustrate the impact of a single and long-range impurity on the spatial distribution of the edge current, simulations have been performed by Dr. A. Cresti, considering a Gaussian potential, which mimics a charged impurity on the substrate (Fig. 5.12). The maximum strength of the Gaussian potential is 1 eV and its spatial range is 1 nm. For different positions of the impurity, the edge channel turns out to be significantly deviated and pushed toward the center of the GNR. This may induce a non zero backscattering probability to the opposite edge state. We also mention that an increase of the gate voltage entails a stronger screening of the impurities, making them less diffusive. This effect also contributes to the conductance quantization at large back-gate voltage.

We conclude this part by mentioning that the conductance measurements in the Landau regime along with the simulation of the spacial distribution of the current

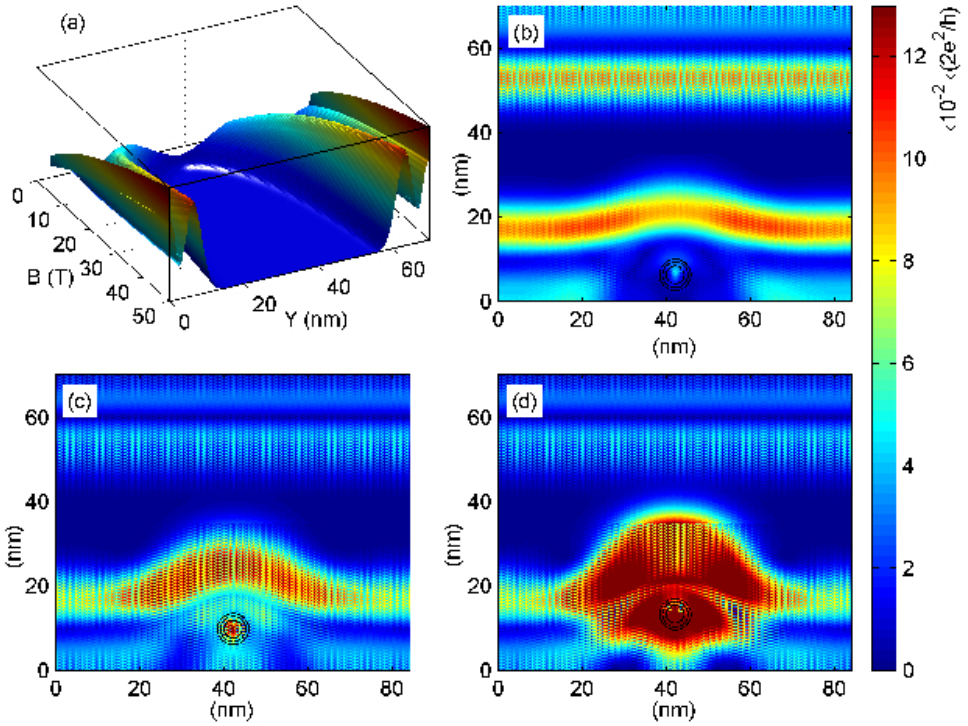

Figure 5.12: (a) Current density mapping of the edge channels at $\nu = 6$ calculated on a 70 nm wide aGNR, as a function of the magnetic field. (b-d) Mapping of the current density (E_F=119 meV and B=12 T) in presence of a charged impurity at different positions from the edge, indicated by the black circle. The impurity pushes the chiral edge current close together and enhances the backscattering probability. The red region around the impurity in d) indicates the presence of current forming closed loops.

give a qualitative indication of the impact of the disorder, mixing the edge channels.

5.3 Summary

Magneto-transport experiments (up to 55 T) at low temperatures on lithographically patterned monolayer graphene nanoribbons have been performed. The electronic transport study at zero field gives evidence of a weakly diffusive regime with a carrier mobility large enough to observe the Landau spectrum in high magnetic field.

We present results of the Landau quantization for a GNR of 100 nm wide where quantized values of the resistance correspond to filling factors of 2 and 6, as expected for a graphene monolayer. At high doping, we reveal the electronic confinement effects on the Shubnikov-de Hass oscillations, when the electronic confinement overcomes the magnetic one.

For a narrower GNR device, 70 nm, a new Landau spectrum is unveiled, giving

evidence of a degeneracy lifting which can not be related to the already observed degeneracy lifting in 2D graphene. By comparing the band structure of an armchair GNR in the presence of high magnetic field and the quantum oscillations, we found a good agreement between the maxima of resistance and the pinning of the Fermi energy on the two Landau sublevels. This agreement strongly support a contribution of an armchair symmetry at the edges of the GNR.

We also give a qualitative description of the impact of disorder in Landau regime. By comparing the distance between the chiral currents in pristine GNR and the magnetic field at which we observe the full quantization at $\nu = 6$. We conclude that some disorder, like long-range potential disorder, is necessarily present in our devices to couple the edge channels.

This study demonstrate the power of magneto-transport experiments at high magnetic field in rather clean devices. When these measurements were performed, we gave one of the first experimental evidences of the Landau quantization in GNR. The signature of a specific edge geometry on the Landau spectrum would require further experimental evidence with different sources of GNR. Also, a local probe, like STM, on the same device to directly address the edge structure could provide complementary confirmations.

Chapter 6

Experimental Evidence of the Landau Spectra in Multilayer Graphene and Nanoribbons

Contents

This chapter merges the magneto-transport results (up to 55 T) obtained on multilayer 2D graphene and GNRs. Measurements in multilayer graphene reveal the presence of complex magneto-electric subbands and possible crossing of the Landau levels. In case of multilayer GNRs, we perform measurements on samples obtained from different sources (e-beam lithography and unzipping CNTs). In both cases, we observe the signatures of Landau levels formation but without any sign of the Landau quantization.

Multilayer graphene systems present distinct physical properties compared to those observed in graphene monolayer. The electronic band structure of these systems is modified by the presence of the interlayer coupling which brings a series of new features, as the opening of an energy gap in biased graphene bilayer [Oostinga 2008, Ohta 2006] and the Landau level crossing in graphene trilayer [Taychatanapat 2011]. Here, we study the magneto-transport of multilayer 2D graphene and GNRs in order to observe how the extra layers modify the electronic structure in presence of a large magnetic field.

6.1 2D Multilayer Graphene

The samples presented in this part were fabricated during my stay in CEA Saclay, in the *Service de Physique de l'Etat Condensé* with the support of Dr. Michel Viret.

6.1.1 Structural characterization

When the number of graphene layers increases, the contrast in optical microscopy changes. In Fig. 6.1 (a), we observe the optical images of a monolayer (bottom) and of multilayer (top) graphene. A full recognition of the exact number of layers can not be made only with optical images. For this purpose, we use the Raman spectroscopy. The Raman spectroscopy presented in this section was performed at CEMES-Toulouse with the support of Dr. Miguel Rubio-Roy.

In the graphene's Raman spectrum, the 2D peak changes both in shape and in position as the number of layers is increased. This is a consequence of the differences in the electronic structure, which brings a double resonant Raman process [Ferrari 2006].

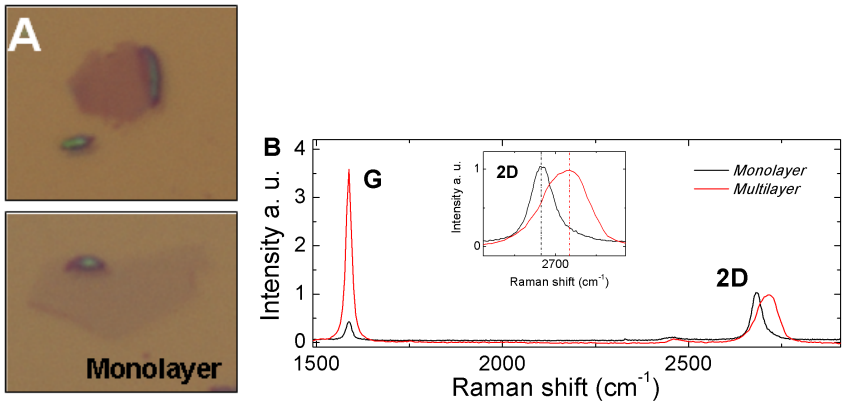

Figure 6.1: **(a)**, Optical image of the multilayer graphene (top) and the monolayer (bottom). **(b)**, Raman spectra for the multi (red) and monolayer (black) graphene shown in (a). The monolayer signal has been scaled to have the same height of the 2D peak. Inset: zoom of the 2D peak.

Let's start by analyzing the spectrum of the monolayer sample (Fig. 6.1 (b), black curve). The position of the single mode 2D peak at 2690 cm^{-1}, as well as the high integrated intensity ratio, I(2D)/I(G)=3.51, are the clear signatures of a single layer of graphene [Das 2009]. This confirms what we expect from the optical observations.

In case of the multilayer sample (Fig. 6.1 (b)-red curve), the 2D peak is much broader and up-shifted, as a consequence of a double resonant Raman process. In fact, the analysis of the Raman spectrum is quite complex and we can not establish the exact number of layers since other parameters like their coupling and their stacking affect the Raman spectrum. We limit our Raman study to say that this is

a multilayer system.

After the Raman characterization, the sample is electrically connected, in a two terminal configuration, with electrodes designed by e-beam lithography and metal deposition. The final dimensions of the sample are: W=5.2 μm and L= 1 μm.

6.1.2 Electronic transport characterization at zero magnetic field

The conductance as a function of the back-gate voltage, measured at 2 K and after thermal annealing is shown in Fig. 6.2 (red curve). The charge neutrality point is found at $V_g = -5$ V, indicating that the unintentional doping of the sample is quite low.

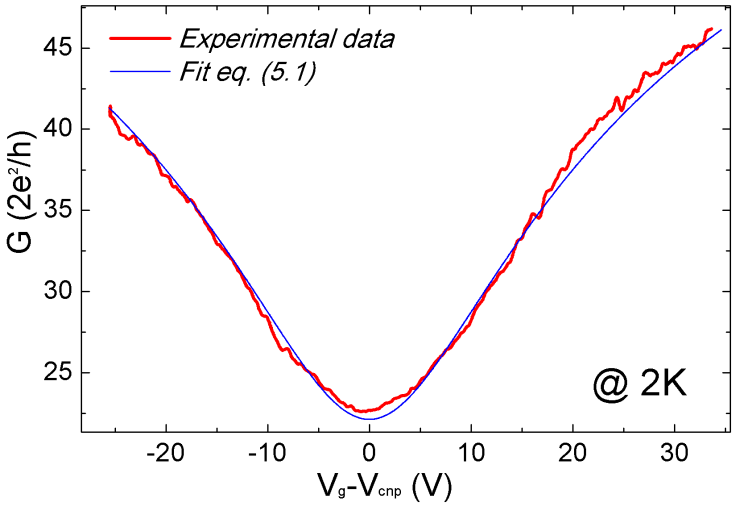

Figure 6.2: Experimental measurement of the conductance as a function of the back-gate voltage at 2 K (red) for the multilayer sample, and the comparison with the one calculated from eq. (5.1) (blue).

The carrier mobility is estimated using the procedure described in chapter 5. The fit of the experimental data is shown in Fig. 6.2 (blue curve). The capacitive efficiency we use, $\alpha = 7 \times 10^{10}$ cm^{-2}V^{-1}, is calculated from the planar capacitor equation and is in good agreement with the extracted value from the magneto-transport measurements (see below). We deduce a contact resistance of $R_c \approx 67$ Ω, a carrier mobility of $\mu \approx 2400$ cm^2 V^{-1} s^{-1} and a residual carrier density of $n_0 \approx 76 \times 10^{10}$ cm^{-2}. We notice that the carrier mobility calculated for this sample is slightly higher than the one previously reported for multilayer graphene (bilayer or trilayer) on Si/SiO_2 substrates [Zhu 2009, Kumar 2011].

Using the Einstein relation, $\sigma = \rho(E_F)e^2D$, where $\rho(E_F) = 2m/\pi\hbar^2$ is the density of states for graphene bilayer and trilayer [Zhu 2009], and D, the diffusion coefficient expression, $D = l_e v_F/2$, we obtain a relation between the mean free path and the conductance given by:

$$l_e = \frac{GL\pi\hbar^2}{Wm^*e^2v_F}. \tag{6.1}$$

Here, $m^* \approx 0.04m_e$. From this, we obtain a mean free path $l_e \approx 50$ nm in the highly doped regime, characteristic of a diffusive transport regime.

6.1.3 Electronic transport under high magnetic field

In this part we study the electronic transport in the presence of a high magnetic field at low temperatures (all measurements were performed at 2 K). For clarity, the magneto-transport measurements will be presented in two parts: high and low carrier density, these two parts present distinct characteristics and physical phenomena.

Magneto-transport at high carrier concentration

In Fig. 6.3-Top, we present the magneto-resistance measurements for three different back-gate voltages (V_g =-90, -60 and -40 V). These curves exhibit a magneto-resistance maximum that is shifted to higher magnetic fields as the carrier density is increased (black and gray arrows), a clear signature of a band structure effect depending on the doping level.

From the Shubnikov-de Hass oscillations (Fig. 6.3-bottom), we extract the $1/B$ values corresponding to maxima of resistance, $\Delta(1/B)$. From the expression (3.8), we deduce the capacitive efficiency, $\alpha \approx 6.8 \times 10^{10}$ cm^{-2} V^{-1}. In the inset of Fig. 6.3, we plot the Landau spectrum deduced from the SdH oscillations. To build this Landau plot in the absence of quantized values, we first calculate the filling factor, $\nu = nh/eB$, and the Landau index associated to each maximum. We see that the linearity of the Landau index as a function the inverse of magnetic field, as expected in 2D systems, is preserved. In the low Landau index regime, we remark the presence of a degeneracy lifting.

This degeneracy lifting is more obvious when we plot the conductance as a function of the filling factor (Fig. 6.4-bottom). However, the interpretation of these results requires some precautions. Previous calculations of the magneto-conductance in different two probes geometries [Abanin 2008] show that, for low aspect ratios ($L < W$, as in our case) the conductance present a minimum when the Fermi energy lies between two Landau levels. These predictions have also been experimentally confirmed [Williams 2009].

In Fig. 6.4-top, we plot the conductance as a function of the filling factor for different back-gate voltages. These curves present some notables features:

i) Three values of filling factors $\nu = 6$, 10 and 14, are robust and do not depend on the applied back-gate voltage. These values would be consistent with a monolayer or a trilayer signature. From the Raman spectrum of this sample, we exclude the monolayer graphene scenario.

ii) For the curve at V_g =-40 V, we observe that the Landau broadening is well pronounced, hiding the conductance minimum expected for $\nu = 14$. This minimum

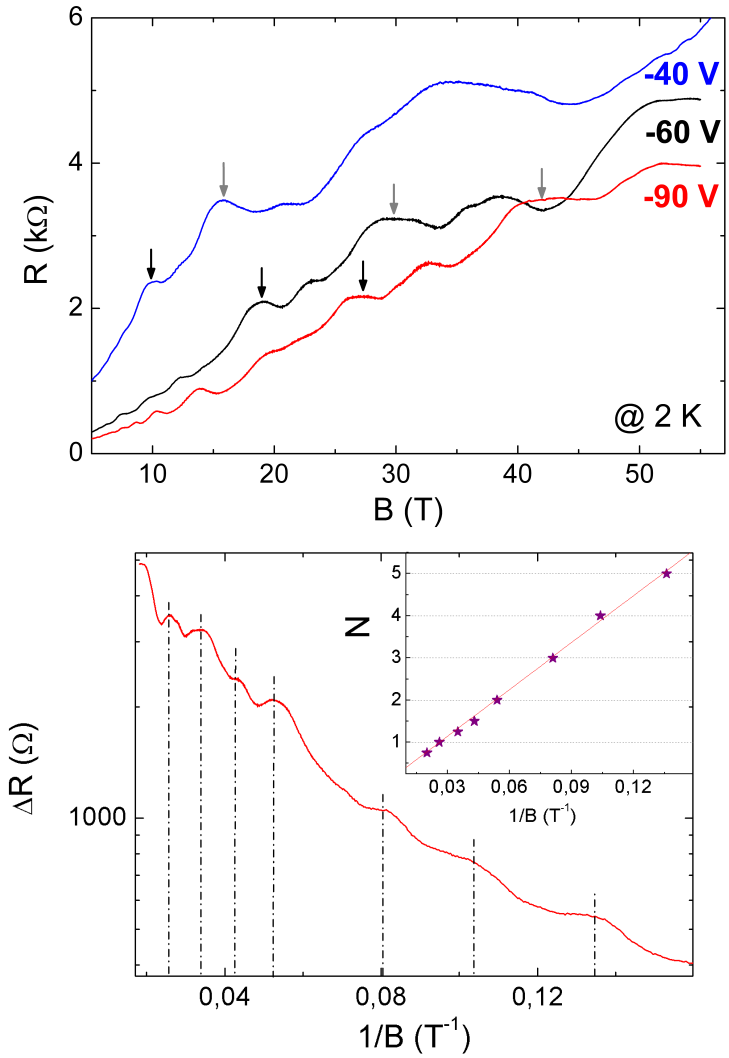

Figure 6.3: **Top**, magneto-resistance at V_g=-90, -60 and -40 V for the multilayer sample. The black and gray arrows show the structures that persist at different magnetic field as the carrier density changes. **Bottom**, Shubnikov-de Hass oscillations of the magneto-resistance at V_g =-60 V. Inset: Landau plot from experimental data (stars) and linear fit (line).

is recovered when the carrier density is increased. At V_g =-60 V, the conductance steps between the filling factor 10 and 14 is much higher than $4e^2/h$, this increase may also explained by the Landau level broadening which generates an overlap of the levels, giving as a result, a non quantized resistance and an increase of the number of conducting channels.

In Fig. 6.4-bottom, we plot the curve at $Vg = -90$ V. Here, the conductance steps as well as the $\Delta\nu$ have been expressed explicitly. For filling factors higher than 10, the conductance steps start to be larger than the one corresponding to $\Delta\nu$. This

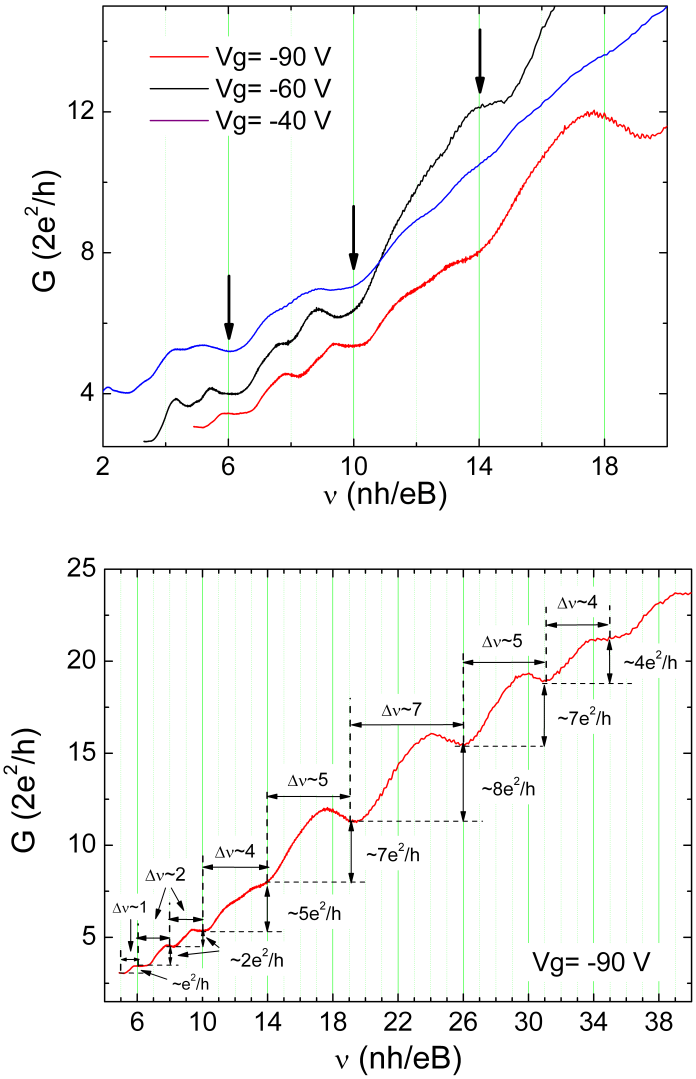

Figure 6.4: **Top**, conductance as a function of the filling factor at different V_g for the multilayer sample. The curves have been slightly shifted for clarity. The black arrows denote the reliable values of ν. **Bottom**, conductance as a function of the filling factor for $V_g = 90$ V.

behavior can be related to two phenomena:

a) The Landau level broadening starts to be important which increases the number of conducting channels at given charge density. For the conductance step between the filling factors 10 and 14, the number of conducting channels is increased by 5 instead of 4.

b) In case of trilayer graphene, the appearance of conductance steps higher than expected has been attributed to the crossing of the Landau levels coming from

different magneto-electric subbands [Taychatanapat 2011, Kumar 2011], as shown in Fig. 6.5. This is strongly dependent on the graphene stacking.

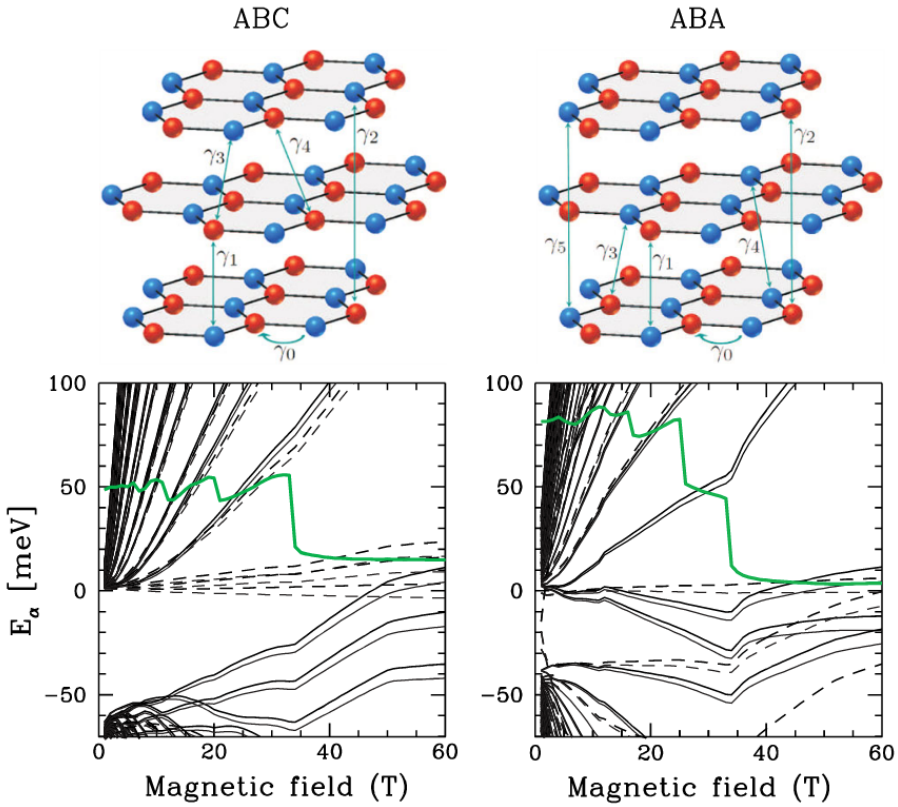

Figure 6.5: Magneto-electric subbands calculated for a graphene trilayer for different stacking (ABC left and ABA right). The solid and dashed lines stand for the Landau levels originating from valleys **K** and **K'**. Adapted from [Kumar 2011].

At lower filling factor $\nu < 10$, the steps of $2e^2/h$ on the conductance correspond very well with a change of $\Delta\nu = 2$. This behavior is also characteristic of trilayer graphene where the valley degeneracy is lifted (dashed and solid lines in Fig. 6.5). Interestingly, the last step in the conductance has a value of e^2/h this corresponds to a new degeneracy lifting, spin degeneracy, which from the best of our knowledge has not been observed before in trilayer graphene.

Magneto-transport at low carrier density

The low carrier density magneto-transport in this sample also shows some interesting features (Fig. 6.6). The first is the lack of resistance divergence for the curves close to the charge neutrality point (V_g=-6, -8 and -10 V). This has been already observed for single [Checkelsky 2009] and bilayer [B. E. Feldman 2009] graphene. In our case, the resistance rapidly increases by more than one order of magnitude, in the first 20 T. After this, an abrupt decrease down to a minimum around 37 T is

observed.

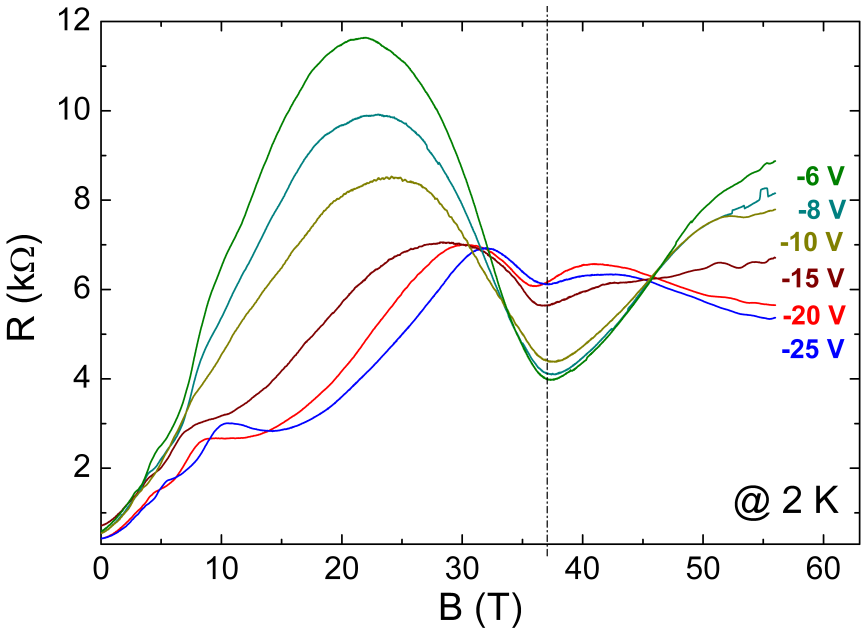

Figure 6.6: Magneto-resistance of the multilayer sample at low carrier density, measured at 2 K. Note the well defined minimum at 37 T that seems weakly dependent on the doping level.

The lack of resistance divergence is possibly related to the degeneracy lifting of the lowest Landau level. It would explain the fast increase of the resistance when the $N = 0$ Landau level starts to be depopulated. Then, for a larger magnetic field, the degeneracy is lifted, generating a change in the density of states, which manifests itself by a decrease of the resistance. The second increase would correspond to the depopulation of the remaining level. The origin of this degeneracy lifting as well as the origin of the pronounced minimum in the magneto-conductance remain unclear and need further studies,including the tilted magnetic field dependence at different temperatures.

6.2 Lithographically patterned bilayer GNRs

In the this section, we present results on a set of graphene samples (monolayer and bilayer) made from exfoliated graphene. These samples have been patterned by e-beam lithography and oxygen plasma etching (section 4.1.1). Here, we illustrate the differences in magneto-transport measurements on a monolayer and a bilayer GNR, originating from the same exfoliated flake (Fig. 6.7 (a)).

6.2.1 Structural characterization

The preliminary identification of the samples is made by optical microscopy. In Fig. 6.8 (a), we observe the optical image of the sample: a part of the sample has monolayer characteristics (*sample A*) and the other part, with a more pronounced contrast, is a multilayer graphene (*sample B*).The Raman spectra (Fig. 6.8) of the *sample A* (black curve) shows a mono-modal 2D peak center at ~ 2690 cm^{-1} with an intensity ratio $I(2D)/I(G) \sim 3.5$, characteristic of a monolayer graphene. The Raman spectroscopy for this sample was performed at LNCMI-Toulouse with the support of Dr. Paulina Plochocka's group.

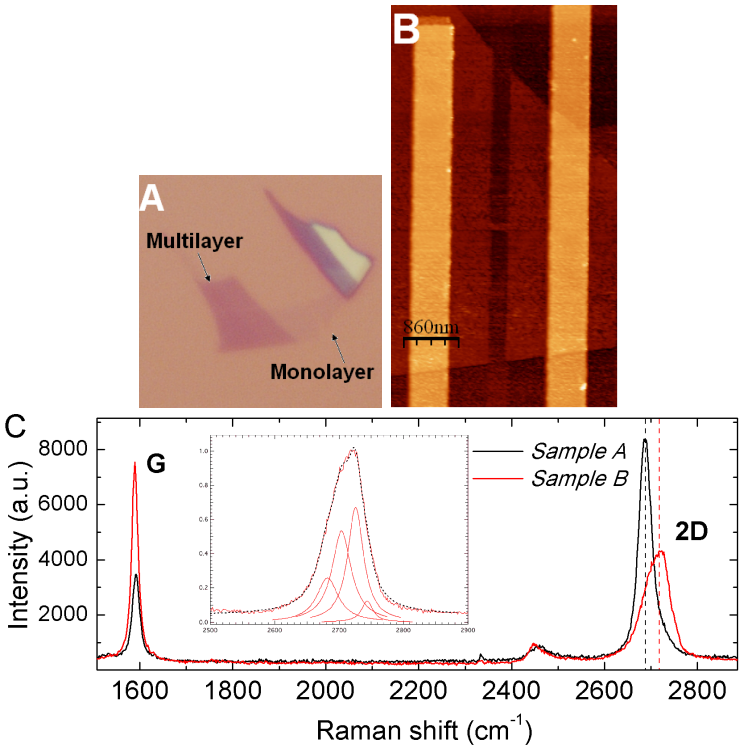

Figure 6.7: **(a)**, optical image of the graphene flake before contacting. **(b)**, AFM image of the *sample B*. **(c)**, Raman spectra for *sample A* (black) and *B* (red). Inset: Fit of the four modes that compose the peak 2D for *sample B*.

In contrast to this, the Raman spectrum of *sample B* (Fig. 6.7 (c) red curve), exhibits a 2D peak much broader and up-shifted. In the inset Fig. 6.7 (c), the 2D peak is reconstructed using four Lorentz functions which corresponds to the four modes expected for graphene bilayer. Besides, the integrated intensities is I(2D)/I(G)=0.85, in good agreement with the results of [Das 2009] for bilayer graphene .

After Raman spectrum, the graphene flake has been electrically connected by e-beam lithography and metal deposition. After the patterning the dimensions measured by AFM, are: for *sample A* (monolayer GNR) W= 80 nm and L= 295 nm

and for *sample B*, (multilayer GNR) W=90 nm and L= 280 nm (Fig. 6.8 (b)). In the following, we will focus on the results of *sample B* since the main characteristics of the monolayer GNR (sample A) are similar to those presented in the previous chapter.

6.2.2 Electronic transport characterization at zero magnetic field

The conductance as a function of the back-gate voltage, after thermal annealing, for both samples is shown in Fig. 6.8. We note that *sample A* shows a semiconducting behavior with a strong reduction of the conductance at the CNP at low temperature. This is the standard behavior of GNR, when the disorder and potential fluctuations combine to open a transport gap [Gallagher 2010, Han 2007]. On the other hand, *sample B* shows a much less pronounced minimum of conductance at the CNP and a slightly metallic regime in the n doped state. The CNP, after thermal annealing, is $V_g \approx -2$ V and ≈ -11 V for the *sample A* and *B*, respectively, suggesting a larger unintentional doping for *sample B*.

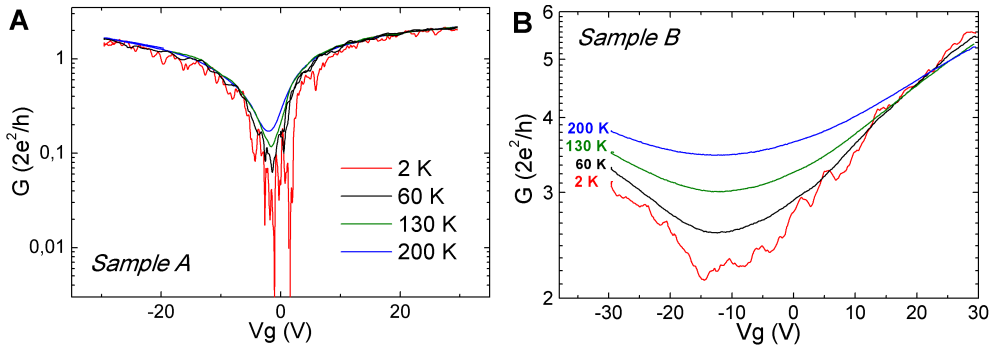

Figure 6.8: Conductance as a function of the back-gate voltage for *sample A* (a) and *B* (b) at different temperatures.

The carrier mobility, for both samples is deduced from the expression (5.1) and a capacitive efficiency of $\alpha = 1.3 \times 10^{10}$ cm^{-2}/V (calculated from magneto-transport measurements). We obtain a contact resistance of $R_c \approx$200 (900) Ω, a carrier mobility of $\mu \approx$ 2100 (1900) cm^2 V^{-1} s^{-1} and a residual carrier density of $n_0 \approx 15 \times 10^{10}$ (116×10^{10}) cm^{-2} for *sample A (B)*. The lower mobility for *sample B* is consistent with a higher doping in this sample and its higher residual carrier density, commonly observed in multilayer systems.

6.2.3 Electronic transport under high magnetic field

In Fig. 6.9 (a), are presented the magneto-resistance curves obtained on *sample B* for selected back-gate voltages, in the high doping regime (V_g =20, 30 and 40 V). The Landau level onset appears in the form of magneto-resistance modulations, that shift to higher (lower) magnetic field as the Fermi energy is increased (decreased), as indicated by arrows. This is quite clear in the low up to moderate magnetic field

($B < 30$ T) but becomes more complex at higher fields because of the appearance of new structures. Note that there is not quantized values of the resistance.

In the inset of Fig. 6.9 (a), we briefly illustrate the magneto-transport measurements of *sample A*. We see a clear quantized resistance plateau at $\sim h/2e^2$,like in the previous chapter. This confirms the monolayer structure in consistency with the Raman spectroscopy.

We now study the magneto-conductance as a function of the filling factor $\nu = nh/eB$ for *sample B* (Fig. 6.9 (b)). Most of the conductance maxima, which occur when the Fermi energy lies between two Landau levels [Abanin 2008], scale at the same filling factors. They correspond to the ones expected for a bilayer graphene, $\nu = 8$ and 12. Even so, the conductance values at these filling factors are lower than the expected ones. Indeed, we speculate that the Landau levels are not well spaced and there is some overlap between them. As a consequence, the edge currents are not completely separated and the backscattering between the chiral currents reduce the conductance.

In the inset of Fig. 6.9 (b), we zoom on the low filling factor regime between 2 and 6. The $G(\nu)$ curves are shifted for clarity. For the curve at 20 V, there is a broad maximum of the conductivity around $\nu \approx 4$. As the carrier density is increased, this maximum gradually splits into two more defined maxima. This experimental evidence may originate from a very beginning of a degeneracy lifting. A deeper study of the band structure of bilayer GNRs in high magnetic field is needed to clarify the origin of this splitting.

The comparison between the two samples put in evidence the different nature of the carriers in monolayer and bilayer GNRs. The distinct electronic structures give different relations of the Landau level energy as a function of the magnetic field (Fig. 6.10). For the graphene monolayer, the spacing for the lowest Landau level, $\Delta_0(meV) \approx 36.3\sqrt{B(T)}$, is larger than the one for bilayer, $\Delta_1(meV) \approx 3.2B(T)$. This may explain the lack of conductance quantization for the bilayer sample despite its quite decent mobility, comparable to monolayer one.

When we compare the results for high doping levels obtained on 2D bilayer graphene [Dean 2012] and our results for *sample B*, we note that, in the 2D case the presence of new Landau levels, due to degeneracy lifting, does not mask the expected filling factors for graphene bilayer (ν =4, 8 and 12). Iin case of the bilayer GNR (*sample B*) when the doping level increases, the degeneracy lifting starts to develop but conductance maximum for ν= 4 disappears. This may be the signature of a new Landau level spectrum where confinement effects mask the filling factors due to the presence of additional sub-bands, as revealed in the previous chapter for the monolayer case. Unfortunately, the lack of numerical simulations does not allow us to go further in the analysis.

The temperature and the carrier mobility effects on the Landau spectrum

The main panel of Fig. 6.11 (a) presents the magneto-resistance for two different back-gate voltages (V_g=20 and 40 V) at two temperatures 100 K (continuous line)

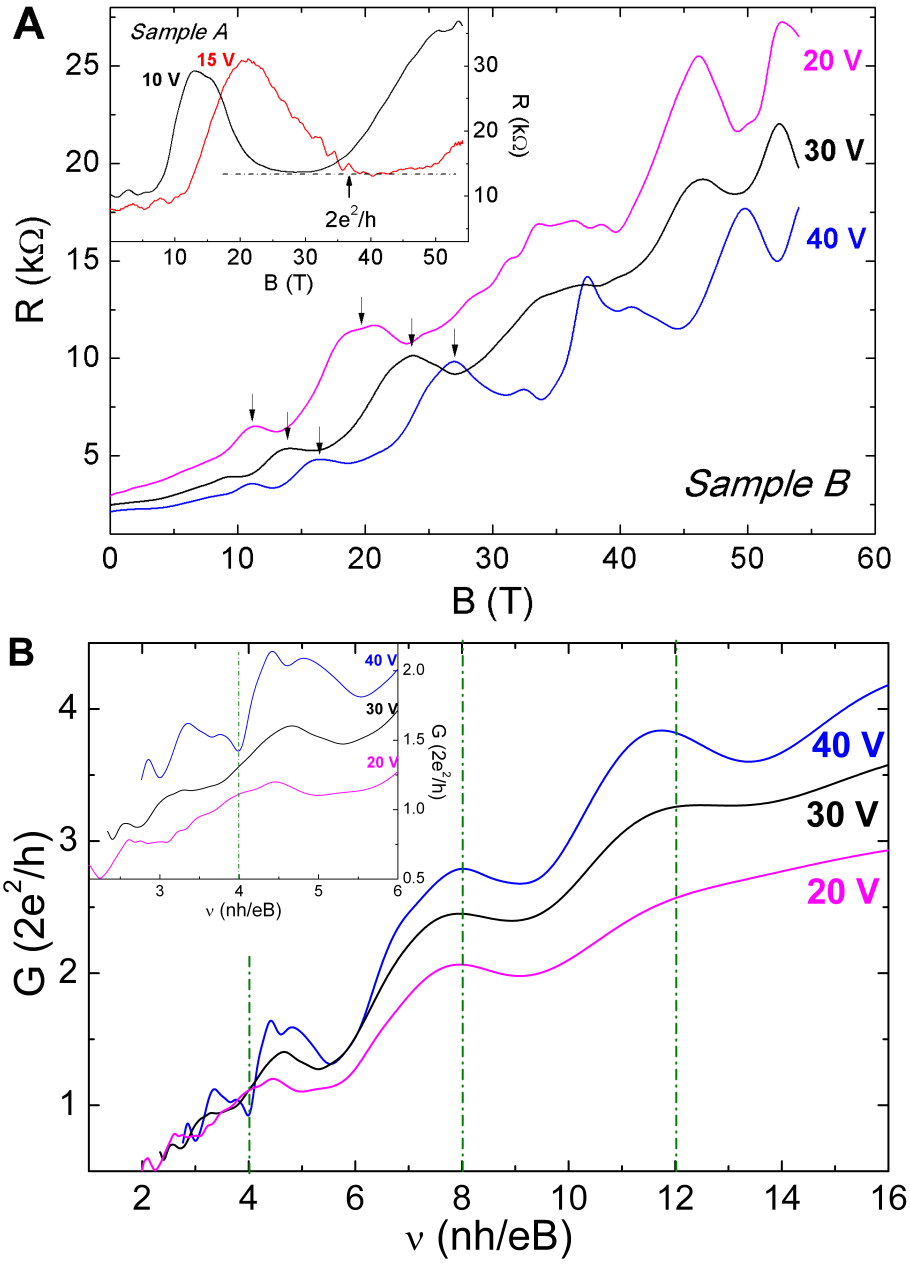

Figure 6.9: **(a)**, Resistance as a function of a perpendicular magnetic field and for different back-gate voltages for *sample B*. Inset, resistance as a function of the magnetic field for *sample A* at V_g =15 V and 10 V. The dashed line represents the quantized value of the resistance at $h/2e^2$. **B**, conductance as a function of the filling factor for *sample B* at V_g= 20 (magenta), 30 (black), and 40 V (blue). Inset: zoom at low filling factor. The curves at 30 and 40 V have been shifted for clarity. The dashed lines represent the filling factors expected for a bilayer graphene.

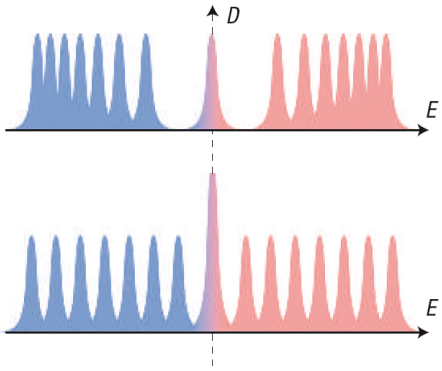

Figure 6.10: Sequence of Landau levels in density of states described by $E_N \propto \sqrt{NB}$ for massless Dirac fermions in single layer (**Top**), and by $E_N \propto \sqrt{N(N-1)}B$ for massive Dirac fermions in bilayer graphene (**Bottom**). Adapted from [Geim 2007].

and 2 K (dashed line) for *sample B*.

The temperature effects are obvious. At high temperature, the thermal broadening combined with an enhanced scattering, completely mask the onset of the Landau levels. In case of *sample A* (inset Fig. 6.11), we see the quantized plateau at $h/2e^2$ measured at 2 K transforms itself into a broad minimum of resistance at 100 K and its value is not anymore quantized. The increase of resistance may be assigned to an overlap of the Landau levels resulting in an increase of the backscattering probability.

Again, when we compare the two results, we remark that for *sample A*, the Landau level spacing, Δ_N, is larger than the thermal broadening ($4k_BT$), as a direct consequence of the $\sqrt{BN}$ scaling of the energy. At 20 T, we obtain $\Delta_0 = E_1 - E_0 \approx 1900$ K. In case of bilayer graphene, the Landau level spacing for the lowest Landau index is $\Delta_1 \approx 780$ K at 20 T.This is still a bit larger than $4k_BT$ at 100 K. This indicates that the disorder also play a crucial role in the edge current mixing which prevents the Landau level formation.

As an illustration of the disorder effect on the Landau level spectrum, we present (Fig. 6.11 (b)) the magneto-conductance obtained on another bilayer GNR of W=80 nm and L=50 nm at 2 K. This sample exhibits a rather low carrier mobility $\mu \sim 600$ cm^{2}V^{-1}s^{-1}. Only a broad maximum of the resistance, at moderated field, that shifts with the doping level is present on the magneto-conductance curves (marked by arrows). This is in strong contrast with the bilayer GNR sample with 1900 cm^{2}V^{-1}s^{-1} of mobility (Fig. 6.11 (a)) where, even if the quantization of the conductance is not observed, the Landau levels start to induce several conductance modulations in high fields.

6.3 Multilayer GNRs derived from unzipping CNTs

Here, we present the first experimental results on magneto-transport obtained in GNRs derived from unzipping carbon nanotubes (section 4.1.2). Unfortunately, despite a big technological and human effort to connect in the best way this kind of GNRs, the final results are still not optimum. We strongly suspect high contact resistance that can not be improved despite several treatments.

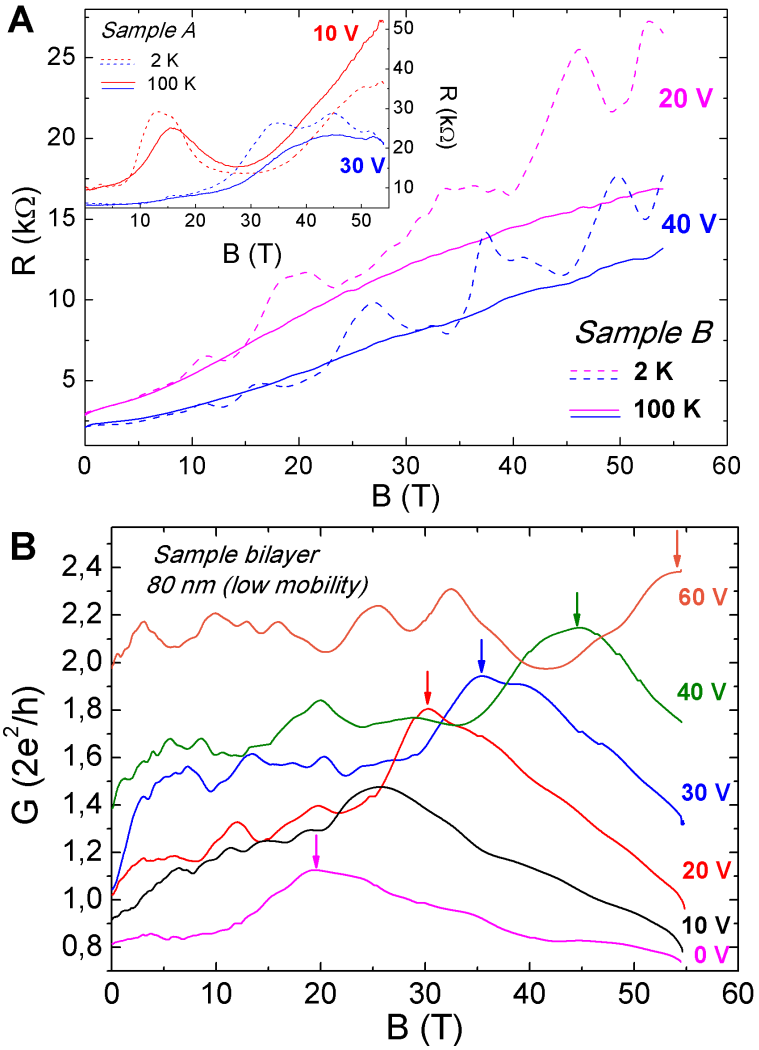

Figure 6.11: **(a)**, Resistance as a function of the magnetic field for *sample B* at V_g =20 and 40 V. Dashed and continuous lines represent the measurements at 2 K and 100 K, respectively. Inset: magneto-resistance for *sample A* for two different back-gate voltages V_g =10 and 30 V. **(b)** Conductance as a function of the magnetic field for a 80 nm wide bilayer GNR with a low carrier mobility ($\mu \sim 600$ cm^{2}V^{-1}s^{-1}), for selected back-gate voltages at 2 K.

The dimensions of the GNR sample we select in this section are: W=23 nm and L=50 nm. The resistance as a function of the back-gate voltage at 100 K (Fig. 6.12 inset), shows that the CNP remains above 20 V despite both, thermal and electrical annealing. This is the signature of a high doping of the sample. The high resistance of the sample is also an indication of a very high contact resistance or a strongly disorder sample. We nevertheless exclude this possibility, considering the already published date on GNR derived with the same technique [Tao 2011].

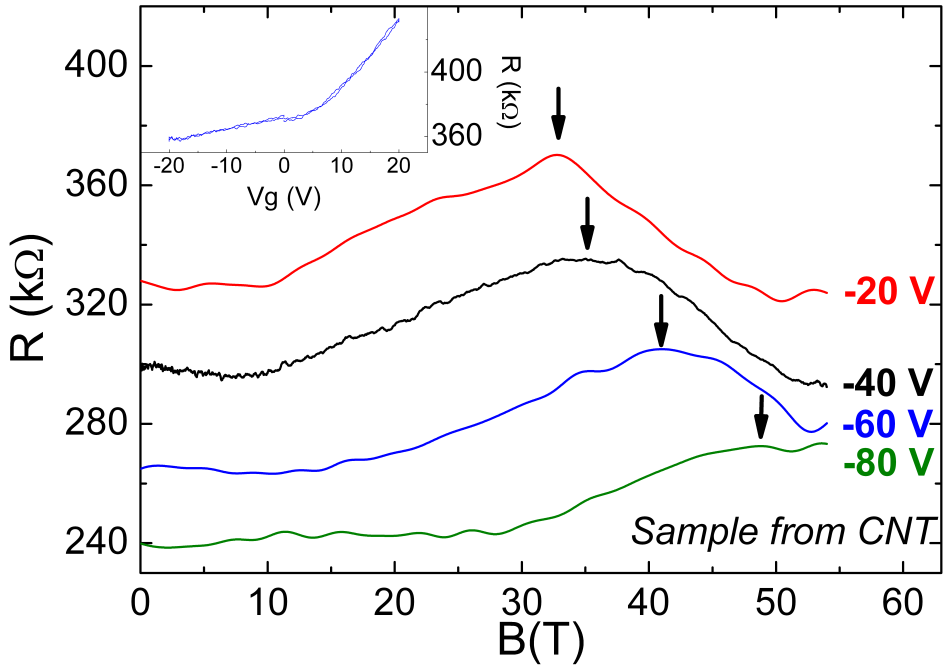

Figure 6.12: Resistance as a function of the magnetic field for a GNR derived from CNTs at several back-gate voltages V_g=-80, -60, -40 and -20 V. The curves have been shifted for clarity. Black arrows indicate possible signatures of a band structure effect. Inset: Resistance as a function of the back-gate voltage. All the measurements were taken at 100 K.

Concerning the magneto-transport measurements, we observe a large maximum of resistance, between 30 and 50 T, that shifts with the doping level. This broad maximum is certainly related to the onset of a Landau level and its crossing of the Fermi energy since $l_m \ll W$. However, the low mobility prevents any observation of SdH oscillations. Besides, this kind of samples turns out to be very fragile and frequently breaks during the cooling process down to 4.2 K. We would like to point out that the results obtained in this sample are representative of a large set of samples that were measured without any relevant magneto-resistance curves. More efforts are needed to prepare these samples in the right way e.g. with a more efficient annealing before the contacts deposition to get ride of possible adsorbate molecules that affect the mobility, the contact resistance and screen the back-gate effect.

6.4 Summary

In this chapter, we have presented experimental magneto-transport results obtained on multilayer 2D graphene and GNRs.

In case of trilayer graphene: the Raman spectroscopy shows the signature of a multilayer system and the magneto-transport measurements seem consistent with

the non-trivial Landau spectrum expected for a trilayer. For the lowest Landau levels, we also give evidence of a fully degeneracy lifting with a conductance step of e^2/h.

In case of bilayer GNR, we observe the presence of Landau levels for filling factors corresponding to $\nu = 8$ and 12 but with some unconventional characteristics at the lower filling factor, $\nu = 4$. The differences between the results obtained on 2D bilayer flake and those obtained on the bilayer GNR reveals a likely electronic confinement effect in the electronic structure. A comparison of the experimental results with the magneto-electric sub-bands for a bilayer GNRs is missing to fully establish this interpretation. Note that the different possibilities of stacking, the existence of an uncontrolled potential difference between the two layers and the different types of edge symmetry (armchair, zigzag or mix) necessarily imply a large variety of possible electronic band structures for a bilayer GNR. Once we add some disorder, the comparison with experimental data becomes very challenging.

The study of the multilayer GNRs derived from CNTs, unfortunately, was not as successful as we expected, mainly due to technological problems that we did not improve during this thesis. We hope that these problems can be fixed in the near future since the high edge quality of this type of GNR seems promising.

Chapter 7

Quantum Interference in GNRs

Contents

In this chapter, we show experimental results of quantum interference in GNRs. Weak localization and universal conductance fluctuations are studied in order to unveil the different characteristics of the coherent transport. Out-of-equilibrium conductance fluctuations reveal that electron-electron interaction is the main decoherence mechanism in this regime. Finally, as an additional part, we investigate graphene's response to a THz radiation. This generates conductance fluctuations strongly related to a non-linear quantum interference phenomenon.

7.1 Conductance Fluctuations in Bilayer GNRs

These results are obtained on a lithographically patterned bilayer GNR of $W =$ 80 nm and $L = 50$ nm. From the $G(V_g)$ curve at 2 K (Fig. 7.1 (a)) and using the eq. (5.1), with a capacitive efficiency of $\alpha \approx 4.2 \times 10^{10}$ cm^{-2} V^{-1} (from magneto-conductance measurements), we calculate the carrier mobility $\mu \approx 200$ cm^2 V^{-1}s^{-1}, the contact resistance $R_c \approx 850\ \Omega$ and the residual carrier density $n_0 \approx 60 \times 10^{10}$ cm^{-2}. The charge neutrality point, after thermal annealing, is around $V_{\mathrm{CNP}} \approx$ -22 V. The high value of V_{CNP} and the low mobility are a clear signature of a disordered GNR.

7.1.1 Temperature dependence of the conductance fluctuations

The conductance fluctuations are developed when the temperature decreases, due to an increase of the phase coherence length and a decrease of the thermal smearing. In inset Fig. 7.1 (c), the conductance fluctuations as a function of the back-gate voltage, at low bias voltage $V_b \approx 100\ \mu$V, are plotted for different temperatures. Here, the monotone variation of the conductance is subtracted. We remark

that the fluctuations are highly reproducible and their amplitude increases at low temperatures, which confirms its quantum interference origin.

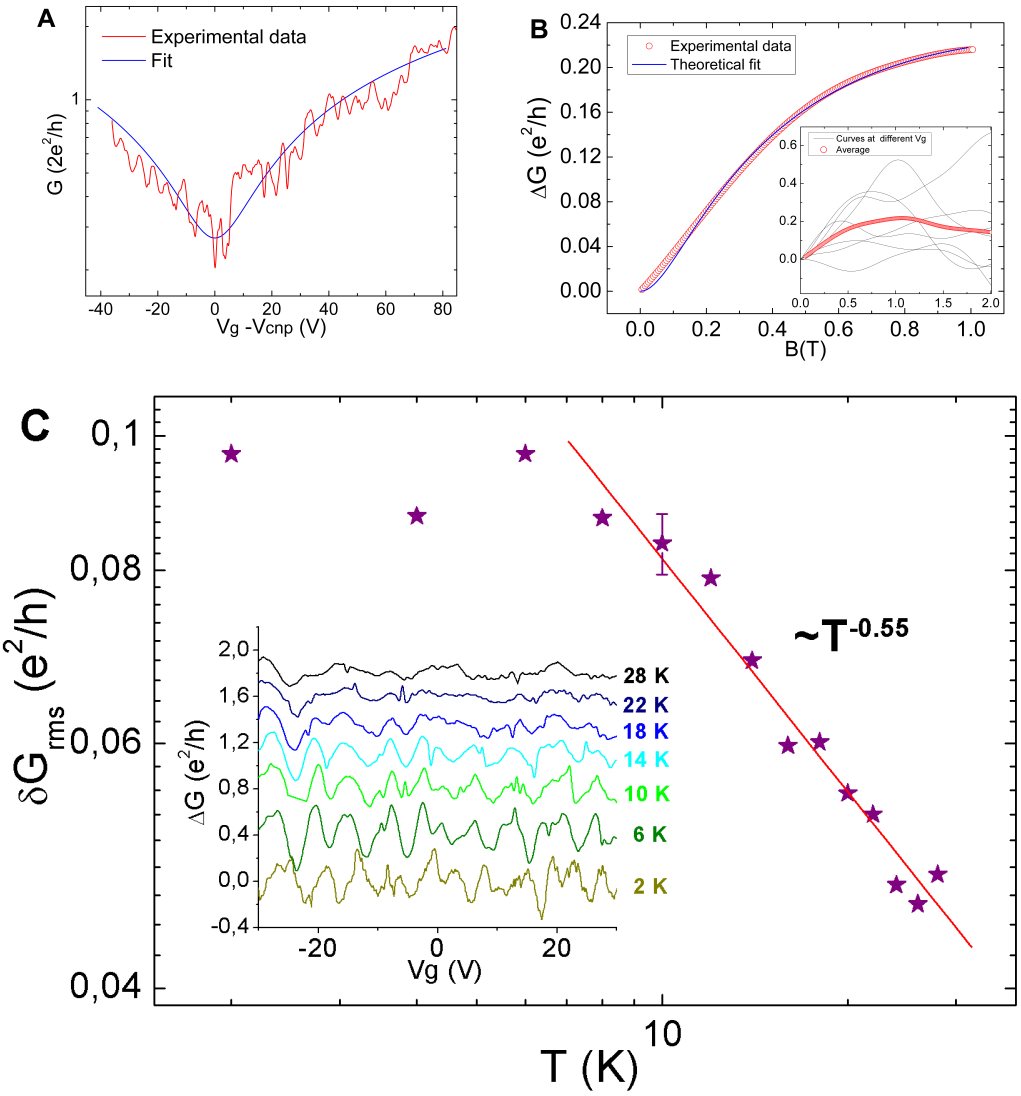

Figure 7.1: **(a)**, Conductance as a function of the back-gate voltage at 2 K (red) and its simulation using eq. (5.1) (blue), with the parameters described in the text. **(b)**, Variation of the magneto-conductance (red) and its simulation using the expressions (7.3) (blue) of the weak localization, see text. Measurements at 2 K. Inset: magneto-conductance at different back-gate voltages (black) and its average value (red). **(c)**, Root-mean-square value of the conductance fluctuations as a function of the temperature in log-log scale. The slope above 10 K suggests a $1/\sqrt{T}$ dependence. Inset: conductance fluctuations for several temperatures. The curves have been shifted for clarity.

We point out that previous works [Ojeda-Aristizabal 2010] show a dependence of the conductance fluctuations with the back-gate voltage, where the amplitude is enhanced close to the charge neutrality point. In our work, we do not observe such dependence.

In Fig. 7.1 (c), we show the amplitude of the conductance fluctuations, $\delta G_{\rm rms}$, as a function of the temperature. Above roughly 10 K (T>10 K) a decrease following a $1/\sqrt{T}$ behavior is observed. Intuitively, this regime may indicate a dephasing process driven by the thermal dephasing length, l_T. However, as we said before, the increase of the conductance fluctuations at low temperature may have two origins: an increase of the coherence length and a decrease of the thermal smearing.

We now consider the expressions of the conductance fluctuations when the thermal length or the phase coherence length is the correlation length that drives the dephasing [Lee 1987]:

$$\delta G_{\rm rms} = \left(\frac{8\pi}{3}\right)^{1/2} \frac{g_s g_v}{2} \beta^{-1/2} \frac{l_T W^{1/2}}{L^{3/2}} \left(\frac{e^2}{h}\right), \quad \text{for} \quad l_T < l_\phi < W, L \tag{7.1}$$

and

$$\delta G_{\rm rms} = \left(\frac{8\pi}{3}\right)^{1/2} \frac{g_s g_v}{2} \beta^{-1/2} \frac{l_\phi W^{1/2}}{L^{3/2}} \left(\frac{e^2}{h}\right), \quad \text{for} \quad l_\phi < l_T < W, L \tag{7.2}$$

For the expression (7.1), when the thermal length is the minimal length, as $l_T \equiv \sqrt{\hbar D/k_B T}$, the temperature dependence is $1/\sqrt{T}$. When the coherence length dominates the correlation, since $l_\phi = (D\tau_\phi)^{1/2}$ and τ_ϕ^{-1} is proportional to T [Lee 1987], the temperature dependence is the same. Both mechanisms seem to be consistent with our funding.

Below 10 K, the amplitude of the fluctuations varies much smoothly and almost saturates, suggesting that a different dephasing mechanism limits the quantum interference. Such a saturation of the amplitude at low temperatures is usually expected when the coherence length reaches the sample length (here 50 nm). To clarify this mechanism, we propose two complementary approaches:

i) We evaluate the phase coherence length through the weak localization contribution to the conductance: In the inset Fig. 7.1 (b), are plotted the low field magneto-conductance curves for different back-gate voltages (black) and its average (red) over a large back-gate voltage range to get ride of the magneto-conductance fluctuations. One notes that below 1 T, a well defined and monotone increase of the conductance is clearly visible suggesting an efficient averaging of the fluctuations. This curve has been fitted with the expression of weak localization for graphene bilayer (blue) given by [Kechedzhi 2007]:

$$\Delta G(B) = \frac{We^2}{\pi h L}\left[F\left(\frac{4eBl_\phi^2}{\hbar}\right) - F\left(\frac{4eB}{\hbar(l_\phi^{-2}+l_i^{-2})}\right) + 2F\left(\frac{4eB}{\hbar(l_\phi^{-2}+l_i^{-2}+l_*^{-2})}\right)\right] \tag{7.3}$$

where

$$F(z) = \ln(z) + \Psi\left(\frac{1}{2} + \frac{1}{z}\right),$$

l_i is the inter-valley scattering length and l_* is the intra-valley scattering length, given by $l_*^{-2} = 2l_z^{-2} + l_w^{-2}$ with l_z, the chirality breaking length and l_w, the intra-valley warping length. From the fitting procedure, we finally obtaine a good agreement between the average magneto-conductance and eq. (7.3), considering $l_\phi \approx 47 \pm 5$ nm, an inter-valley scattering $l_i \approx 75$ nm, a chirality breaking length $l_z \approx 5$ nm and an intra-valley warping length $l_w \approx 39$ nm. We notice the presence of an inefficient inter-valley scattering and a dominante intra-valley scattering. This is expected in graphene devices on SiO_2 substrates because of the long range potential variations due to charge impurities.

ii) As a second approach, we study the correlation voltage of the conductance fluctuations, V_c, directly related to the correlation energy, E_c, through the expression $E_c = \hbar^2\pi\alpha V_c/2m^*$ for graphene bilayer [Ojeda-Aristizabal 2010]. Here, α is the capacitive efficiency and $m^* \approx 0.04m_e$ is the effective mass. The correlation voltage is usually obtained from the half width at half maximum of the autocorrelation function:

$$F(\Delta V) = \langle \Delta G(V + \Delta V)\Delta G(V) \rangle . \tag{7.4}$$

At 2 K, we find $V_c \approx 0.98$ V and $E_c \approx 2$ meV (Fig. 7.2). The correlation energy is also defined from the correlation length $E_c = \hbar D/L_{min}^2$, where D is the diffusion coefficient and $L_{\min} = min(l_\phi, l_T, L)$. The diffusion coefficient is approximated from the Einstein relation, $D = G(2e^2/h)\hbar L/m^*W$, we obtain $D \approx 22$ cm^2/s below 10 K. We deduce at 2 K, a correlation length $L_{min} \approx 45$ nm, which is very close to the length of the device and in agreement with the calculated phase coherence length obtained from the weak localization.

The two approaches support a phase coherence length at low temperature limited by the device length. The system is therefore coherent over its length. The conductance fluctuations are dominated by uncorrelated and coherent segments in parallel, since $W > L$.

In such a configuration, the amplitude of the fluctuations, according to the ratio $\sqrt{W/L}$ [Rycerz 2007]:

$$\delta G_{\rm rms} = \sqrt{C\frac{W}{L}}\frac{g_s g_v}{2}\beta^{-1/2}\left(\frac{e^2}{h}\right), \quad \text{for} \quad l_\phi \sim L \ \text{ and } \ W > L \tag{7.5}$$

where C ia a constant equal to 0.116. In our case, it means conductance fluctuations of about $\sim 0.83e^2/h$, much larger than the measured ones (Fig. 7.1 (c), at 2 K) around $\sim 0.1e^2/h$. This large difference remains unexplained. We note that, as a general comment, the extraction of the characteristic lengths from a two probe configuration is unfortunately dependent on the transmission at the contacts. As a consequence, the use of eq. (7.5) would need an additional pre-factor, smaller than

1 to account for non perfect contacts. This may explain, partially, the different observed between the measured and the expected magnitude of the conductance fluctuations.

Additionally, we study the dependence of the correlation voltage with the temperature (inset Fig. 7.2), where a clear increase of the correlation voltage as the temperature increases is observed. We deduce the correlation length as a function of the temperature (Fig. 7.2). For $T > 10$ K, the correlation length matches with the thermal length meaning that, the electron dephasing mechanism is driven mainly by the thermal decoherence.

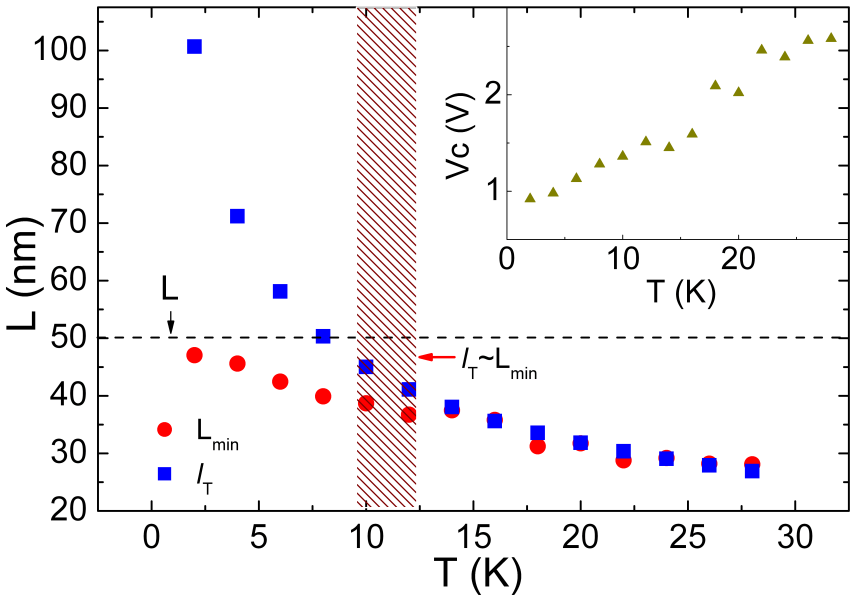

Figure 7.2: Calculated correlation length (red) and the thermal length (blue) as a function of the temperature. The striped region represents the temperature crossover when the correlation and thermal lengths start to have very similar values. The dashed line represents the GNR length. Inset: the correlation voltage as a function of the temperature.

To summarize, we give evidence that the magnitude of the conductance fluctuations follows a $\propto 1/\sqrt{T}$ dependence above 10 K, characteristic of dirty metals [Lee 1987, Holweg 1993]. From the best of our knowledge, this behavior has not been observed before for graphene bilayer. In previous works, a $1/T$ behavior has been reported [Bohra 2012b], but this dependence remains unexplained. Below 10 K, a much smaller temperature dependence is measured suggesting a kind of low temperature saturation of the fluctuations. In this regime, the phase coherence length is expected to be driven by the coherence of the system, with $l_\phi < l_T$. The

phase coherence length we deduce at 2 K, by two different methods, coincides with the sample length. An additional study of the correlation voltage as a function of the temperature reinforces our analysis. The correlation length of the system deduced from $V_c(T)$ equals to the thermal length $l_T(T)$ above 10 K, showing a possible thermal dephasing of the electronic trajectories.

7.1.2 Magneto-conductance fluctuations out-of-equilibrium

The magneto-conductance fluctuations are observed when a magnetic field is varied at a constant back-gate voltage. The magnetic field range for this study goes from zero to 10 T. The SdH contribution is not expected until ~ 20 T (when $B\mu > 1$). The magneto-conductance fluctuations are shown in inset Fig. 7.3 (a). The monotonous contribution has been subtracted.

Let's start with the analysis of their amplitudes (Fig. 7.3 (a)). We compare the amplitude obtained from the back-gate sweeping $\delta G_{\rm rms} \approx 0.1e^2/h$ and the one obtained from the magneto-conductance, $\delta G_{\rm rms} \approx 0.04e^2/h$, measured at 2 K, and in the equilibrium regime $eV \ll E_c$. The ratio between these two values is $\approx 0.35 \approx 1/2\sqrt{2}$. This is the expected ratio when the time-reversal symmetry is broken ($\beta = 2$) and the spin degeneracy is lifted [Bohra 2012a]. This is a confirmation of the ergodicity of the conductance fluctuations in graphene bilayer. The ergodicity has been considered for monolayer both experimentally and theoretically [Bohra 2012a, Rycerz 2007].

The Fig. 7.3 (a) shows an evident damping of the fluctuations above a certain bias voltage $V_b > 2$ mV, corresponding to a crossover from quasi-equilibrium ($eV < E_c$) to the out-of-equilibrium regime. The decrease of the magneto-conductance fluctuations follows a $1/V_b$ dependence. This has been already observed in graphene bilayer, by studying the conductance fluctuations as a function of the gate voltage [Liao 2010]. Despite this, a clear explanation of the $1/V_b$ decrease has not been found and the origin of this behavior remains puzzling.

We also extract the correlation field, B_c, from the width at the half maximum of the autocorrelation function. We observe that the correlation field (around 0.45 T) is poorly dependent on V_b (Fig. 7.3 (b)). We deduce the correlation length through [Beenakker 1991]:

$$B_c = C\frac{h}{eW_{\rm min}L_{\rm min}}\,, \tag{7.6}$$

where C=0.42 since $l_\phi < l_T$ (from previous results), $L_{\rm min} = min(L, l_T, l_\phi)$ and $W_{\rm min} = min(W, l_T, l_\phi)$. From the characteristic lengths calculated before, we know that $L \sim l_\phi < W \sim l_T$. We finally extract a weakly dependent correlation length as a function of V_b, of the order of ≈ 63 nm, in consistency with the coherence length values we previously deduced.

The bias voltage dependence of the fluctuations strongly contrasts with the correlation length deduced from B_c which is not affected by a large V_b dependence. In such a case, the decrease of the conductance fluctuations at large V_b seems not to

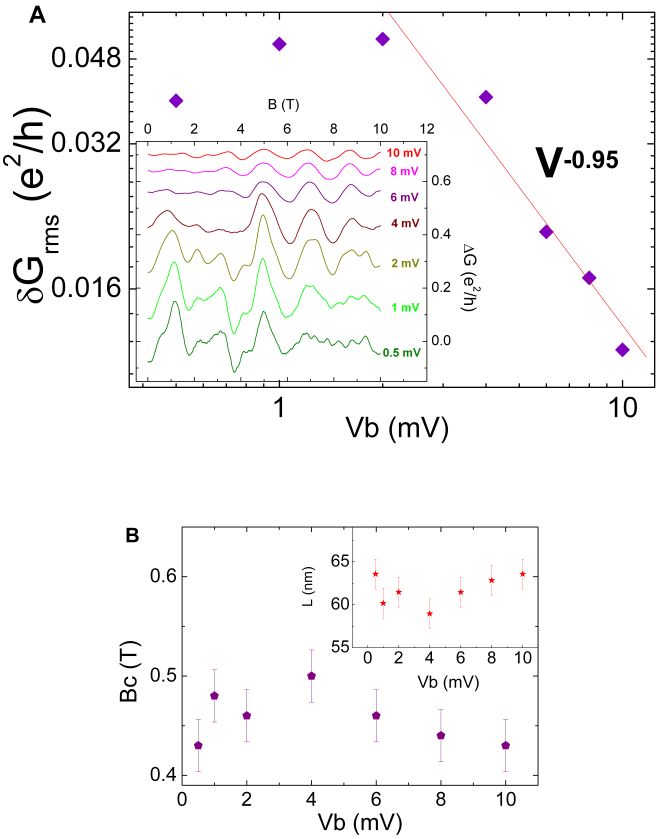

Figure 7.3: **(a)**, Root-mean-square velues of the magneto-conductance fluctuations as a function of the bias voltage, V_b, in log-log scale with a clear decrease of the amplitude for $V_b > 2$ mV. Inset, magneto-conductance measurements where the monotonous curves have been subtracted, for selected bias voltage values. **(b)**, correlation field as a function of the bias voltage and the calculated coherence length (inset). All the measurements are performed at 2 K.

be directly related to a change of the correlation length. A deeper understanding would require some theoretical support which has not been addressed yet.

7.2 Out-of-equilibrium conductance fluctuations in monolayer GNRs

In this section, we study the conductance fluctuations in the out-of-equilibrium regime. The energy dependence of the conductance fluctuations driven by the bias voltage gives an original insigth onto the coherent transport in mesoscopic systems. Indeed, a non-monotonous behavior of $\delta G_{\rm rms}(V_b)$ has been predicted, depending on the strengh of the inelastic scattering [Terrier 2002, Ludwig 2004]. If inelastic

process can be neglected, the conductance fluctuations are expected to be strongly increased by the bias voltage. This can be simply understood by considering a subdivision of the energy range for the transport into uncorrelated energy intervals, each participating to the fluctuations. This results into an enhancement of the conductance fluctuations as a function of V_b. On the other hand, above a critical voltage, the bias voltage induced inelastic scattering is predicted to gradually destroy quantum interference as a consequence of the reinforcement of the electron-electron correlations.

Below, we address the out of equilibrium conductance fluctuations in GNR. Note that, this topic remains poorly studied in mesoscopic systems and no specific theoretical approach has been developped for graphene.

The results we present here are obtained on a lithographically patterned monolayer GNR of $W = 100$ nm and L=350 nm. The $G(V_g)$ curves have been already analyzed in section 5.1. We extracted a mean free path $l_e \approx 25$ - 29 nm for the low doping regime (-5 V > V_g > -10 V). The carrier mobility is around 1200 cm^2 V^{-1} s^{-1}. Using the Einstein relation, $\sigma = \rho(E)e^2D$, where $\rho(E) = g_s g_v k_F/(hv_F)$ is the density of states, we deduce a diffusion coefficient of $D \approx 81 - 68$ cm^2 s^{-1}.

We start the analysis studying the conductance fluctuations on the $G(V_g)$ curve (Fig. 7.4 (a)) measured at low bias voltage ($V_b = 100\ \mu$V) and at 2 K. The amplitude of the conductance fluctuations is reduced close to the CNP due to the opening of a transport gap. Away from the CNP (e.g. $V_g < -2$ V), the amplitude of the conductance fluctuations is independent of the gate voltage. The dashed square in Fig. 7.4 (a) represents the back-gate voltage range of our study.

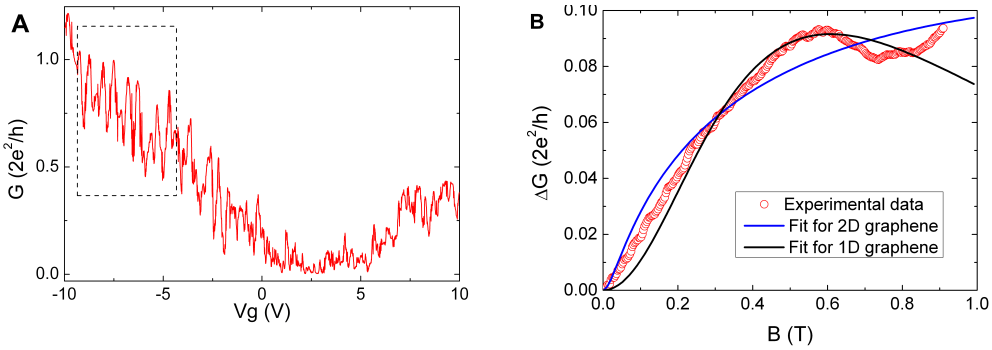

Figure 7.4: **(a)**, Conductance as a function of the back-gate voltage at 2 K for a GNR of W=100 nm and L= 350 nm. The dashed square represents the back-gate voltage range where the study takes place. **(b)**, Average of the magneto-conductance curves for different V_g (red) and its simulationnumerical fit for 2D (blue) and 1D (black) weak localization in graphene systems.

To define the correlation length, $L_{min} = min(L, l_\phi, l_T)$, we first estimate the thermal length, $l_T \approx$210 nm and we extract the phase coherence length from the weak localization contribution of the $G(B)$ curves (Fig. 7.4 (b)). In this figure

is plotted the average of magneto-conductance curves obtained at different V_g and the theoretical curves from the expressions (2.12) (blue) and (2.13) (black), for the weak localization correction in 2D and 1D graphene systems, respectively. The fitting parameters are $l_\phi = 113$ (170) nm, $l_i = 20$ (12) nm and $l_* = 79$ (120) nm for the 2D (1D) expression. Assuming a 2D system, we found $l_\phi \approx 113$ nm which is not consistent, since the coherence length must be smaller than the width ($l_\phi < W$). In case of a 1D system, the obtained value seems consistent with the 1D requirement. These results, as well as the rather poor agreement between the expressions (2.12) and (2.13) and the experimental data, seems to indicate that the system which is likely in the limit between 2D and 1D (quasi-1D).

We obtain the correlation energy $\mathrm{E}_c = D\hbar/l_\phi^2 \approx 0.4$ (0.3) meV calculated with the value extracted for 2D (1D) system. We finally conclude that, at equilibrium, $eV_b \ll E_c$, the device is in the diffusive regime defined by $l_e < W \lesssim l_\phi < l_T < L$.

The amplitude of the fluctuations, for a vanishing bias voltage, is $\delta G_{\mathrm{rms}} \approx 0.25e^2/h$ (Fig. 7.5 (b)). We compare this value with the one calculated with expression (2.17) using the thermal and phase coherence lengths calculated above. We obtain $\delta G_{\mathrm{rms}} \approx 0.77e^2/h$. We find that experimentally the conductance fluctuations are 3 times smaller than the one calculated. Here, we face the same problem as before with the dimensionality of the system. The dimensionality strongly changes the dependence of the conductance fluctuations and the coherence length. This may explain, the difference between the calculated and the experimental value of the fluctuations.

We now analyze the effects of an applied bias voltage larger than the correlation energy, $eV \gg E_c$. In this case, the system is in the *out-of-equilibrium* regime. In this regime, the inelastic scattering leads to an effective temperature of the electrons depending on the position, x, between the contacts [Ludwig 2004]:

$$T_{\mathrm{eff}}(x) = eV_b \frac{x}{L}(1 - \frac{x}{L})\,. \tag{7.7}$$

It takes its maximum value in the middle of the channel and decreases, approaching the contacts. The direct consequence of this effective temperature is a position-dependent dephasing length. The conductance fluctuations are therefore dominated by the coherent segments adjacent to the electrodes.

In Fig. 7.5 (b), we see a clear decrease of the fluctuations as a function of the bias voltage. When δG_{rms} is plotted in a log-log scale, we deduce that the damping of the fluctuations follows a $\delta G_{\mathrm{rms}} \propto V_b^{-0.5}$ dependence. This behavior is consistent with a dephasing originating from electron-electron scattering under high bias voltage, as proposed by [Ludwig 2004]

Note that, our experiment does not reveal a first increase of the conductance fluctuations as a function of the bias voltage, as mentioned in the introduction. In our case, the phase coherence length is already smaller than the length of the device at low bias voltage. The inelastic scattering, even at low bias, can not be neglected.

We also extract, from the $\Delta G(\mathrm{V}_g)$ curves, the correlation voltage $V_c(V_b)$. We obtain V_c from the width at the half maximum of the autocorrelation function.

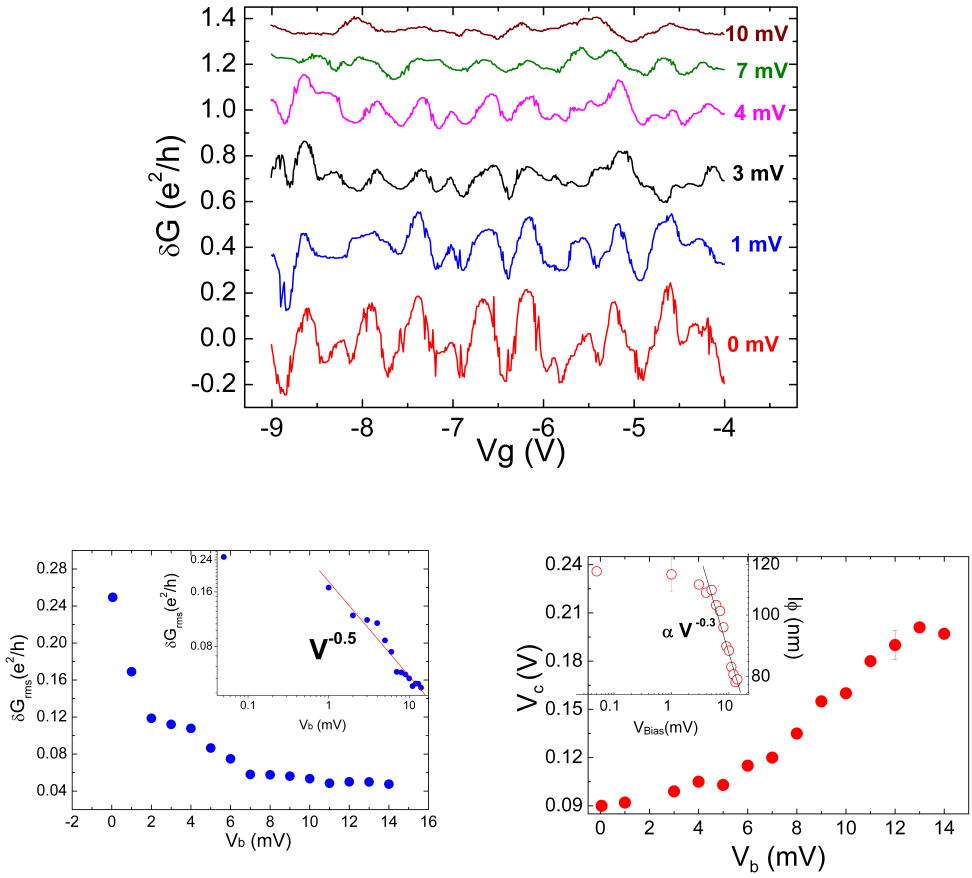

Figure 7.5: **Top**, conductance fluctuations as a function of the back-gate voltage for the low doping regime with selected applied bias voltages, measured at 2 K. All the curves, except for the curve at 0 mV, have been shifted. **Bottom left**, $\delta G_{\rm rms}$ calculated from the $\Delta G(V_g)$ curves, for different bias voltages. Inset: the same data in log-log scale revealing a $V^{-0.5}$ dependence above 1mV. **Bottom right**, correlation voltage as a function of the bias voltage. Inset: the coherence length calculated from correlation voltage (see text) in a log-log scale with a $V^{-0.3}$ dependence at large bias voltages.

An increase of V_b is observed at high bias voltage (Fig. 7.5 (c)). From the V_c values we obtain the correlation energy, given by $E_c = V_c \hbar v_F \sqrt{\pi C_g / 4eV_g}$ for graphene monolayer. At low bias voltage, we estimate $E_c \approx 0.5$ meV, for $V_g \approx 5$ V. This is in good agreement with the correlation energy previously deduced from the phase coherence length.

The dependence of the correlation voltage with the applied bias voltage is an indication that the decrease of $\delta G_{\rm rms}(\mathrm{V}_b)$ goes along with a decrease of the phase coherence length. We use the correlation energy expression for a graphene monolayer

and eq. (2.19) (assuming that this expression holds in a non-equilibrium regime) to determine the correlation length and its dependence with the bias voltage (Fig. 7.5 (c) inset). The value at equilibrium (zero bias voltage) of $L_{min} \approx 117$ nm is in the range of the one deduced from the weak localization. In inset, we plot $L_{\min}(V_b)$. The dependence of the correlation length with the bias voltage follows a $V^{-0.3}$ power law, as proposed by Ludwig et al. [Ludwig 2004], the $V^{-1/3}$ dependence with the bias voltage is a consequence of the $T^{-1/3}$ dependence with the effective temperature of the system.

This agreement with the Ludwig et al. model support that in GNRs, as in metals, the main decoherence mechanism in the out-of-equilibrium regime, is the electron-electron scattering.

7.3 Graphene's response to THz radiation

The interest in the applications of FETs for THz detection started with the pioneering theoretical work of Dyakonov and Shur [Dyakonov 1993], in this work, they predicted that a steady current flow in a FET channel can become unstable against the generation of plasma waves. This leads to the emission of electromagnetic radiation at the plasma wave frequency. The authors have shown that the nonlinear properties of the 2D plasma in the transistor channel can be used for detection and mixing of THz radiation [Knap 2009]. The experimental realization of this predictions by Knap and al. [Knap 2004], are at the heart of the research in the field of detection and emission of THz radiations.

The detection is due to nonlinear properties of the transistor, where the incident Terahertz radiation modulates simultaneously the carrier density and the carrier drift velocity at one side of the channel, this leads to the rectification of an AC current induced by the incoming radiation [Dyakonov 1993]. As a result, a photoresponse appears in the form of DC voltage between source and drain, it is proportional to the radiation power. Moreover, the possibility of high carrier mobility and long momentum relaxation times, presage amplification of plasma resonances in the FET channel at cryogenic temperatures. These plasma resonances can lead to resonant and electrically tunable Terahertz detectors for chip-based Terahertz spectroscopy [Ryzhii 2009, Videlier 2011, Knap 2009].

In this context, graphene is an attractive material for optoelectronics [Geim 2007, Bonaccorso 2010] as it offers a combination of unique electronic properties, such as high carrier mobility and long mean free path [Castro-Neto 2009], and excellent optical properties: optical absorption from ultraviolet wavelengths to terahertz frequencies with nearly equal strength, ultrafast optical response, and remarkable optical nonlinear behavior [Geim 2007, Bonaccorso 2010, Ryzhii 2009].

Recently a graphene terahertz modulator, based on intraband transitions and terahertz detectors based on FET [Vicarelli 2012], have been demonstrated, which is probably the first terahertz applications of graphene.

Beyond the motivation of future applications, the response of a 2DEG submitted

to a THz excitation might provide important advances in the understanding of fundamental phenomena of semiconductor devices. For instance, it was demonstrated in InGaAs/InAlAs FETs, in quantizing magnetic field, that there is a strong reduction of the Terahertz photoresponse when the magnetic field goes through the cyclotron resonance (plasma waves cannot propagate below the cyclotron frequency). This is probably the most spectacular manifestation of the importance of plasma waves in terahertz detection by FETs.

This section is dedicated to probe the effects of a THz radiation in graphene monolayer. These experiments were carried out during my stay in the Laboratoire Charles Coulomb of Montpellier II University with Dr. Dominique Coquillat.

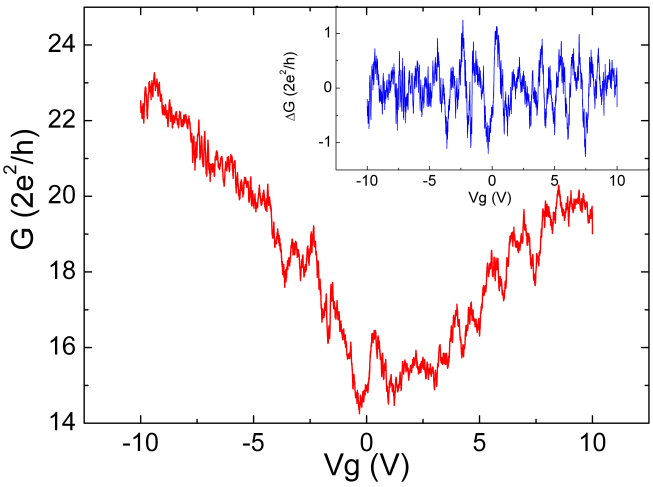

Figure 7.6: DC measurement of the conductance as a function of the back-gate voltage at 4 K with an applied bias voltage of V=100 μV. Inset: Conductance fluctuations in the DC measurements.

Sample's used in this section are fabricated as described in section 4.1.3. The sample's dimensions are L=390 nm and W=580 nm. In Fig. 7.6, we present the DC conductance as a function of the back-gate voltage. From this curve and the expression $\mu = \frac{dG}{dV_g}\frac{L}{\alpha e W}$, using the capacitive efficiency of a planar capacitor regularly used for graphene $\alpha = 7 \times 10^{10}$ cm^{-2}V^{-1}, we estimate a carrier mobility ~3300 cm^2 V^{-1} s^{-1}. Using the Einstein relation and the relation of the diffusion coefficient with mean free path we obtain $l_e = 2D/v_F \approx 20$ nm.

The experimental setup for THz detection is explained in section 4.4.4.

When we study the conductance as a function of a back-gate voltage at low temperatures, Fig. 7.6, we observe the development of conductance fluctuations, signature of quantum interference. The same phenomenon happens when we irradiate a graphene flake with THz radiation, a series of conductance fluctuations are developed as a function of the back-gate voltage (Fig. 7.7). Also in figure 7.7, we

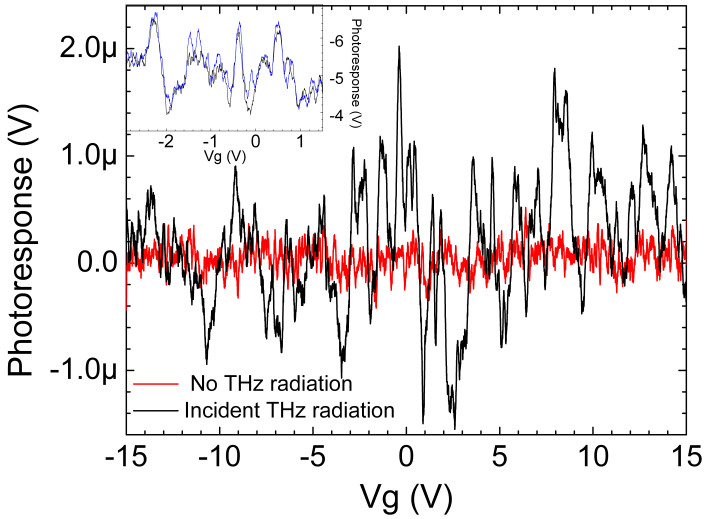

Figure 7.7: Photo-response as a function of the back-gate voltage (black) and voltage variations as a function of the gate voltage, at zero bias voltage, without THz excitation (red). Inset: Photo-response taken in different gate sweeps where a highly reproducible character is observed.

see the voltage variation without THz radiation and applied bias voltage (red). The difference between both cases is clear. In the case that a THz radiation excite the system the voltage fluctuations are much more important contrary to the case without THz radiation, where the response is just noise. Another very interesting feature of these photo-response fluctuations is their reproducibility, in the inset of the Fig. 7.7 we see two photo-response measurements taken at different moments which show that the fluctuations are highly reproducible, showing its quantum interference origin. The cross correlation of two independent photo-response measurement at the same temperature is usually larger than $> 85\%$.

At first look photo-response fluctuations are not directly related to the ones obtained in DC electronic transport. To elucidate the origin of these fluctuations we decide to study the first and second harmonics of the voltage. We know that the current that circulates through the system is given, in a general manner, as:

$$I = G_1 V + G_2 V^2 + ... \tag{7.8}$$

where G_1 is the first-order conductance and G_2 is the second-order conductance, which are respectively related to the first and second order terms of the voltage. These two values can be experimentally measured in an independent way by the first- and second- harmonic of the AC voltage V_1 and V_2, respectively, related to the conductance terms through:

$$G_1 = \frac{I_0}{V_1} \quad \text{and} \quad G_2 = \frac{2V_2 I_0}{V_1^3}\,. \tag{7.9}$$

The physical origin of this second-order conductance, G_2, is attributed to potential fluctuations. When a bias voltage is applied it induces potential changes in sample's landscape through charge accumulation around impurities and edges inducing a change in electrostatic density [Ojeda-Aristizabal 2010].

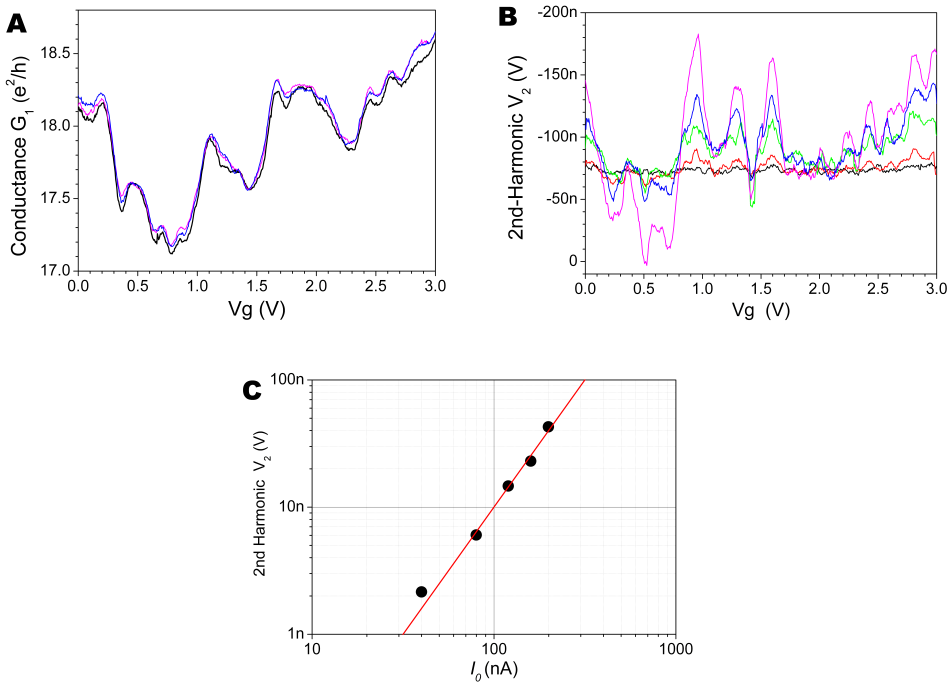

Figure 7.8: **(a)**, AC measurements of the first-order conductance as a function of the back-gate voltage for different applied currents from 20 to 200 nA. **(b)**, second-harmonic of the voltage drop as a function of the back-gate voltage for different applied currents from 20 to 200 nA. **(c)**, amplitude of the second-harmonic fluctuations as a function of the applied current in log-log scale where a slop of 2 is clearly seen.

In Fig. 7.8 (a) and (b), we plotted the first-order conductance and the 2nd harmonic of the AC voltage for different applied currents. We see that the first-order conductance do not show a strong change in the fluctuation amplitude as the current is increased from 20 to 200 nA. Contrary, in the case of the 2nd-harmonic voltage there is a clear increase of the conductance fluctuations amplitude as the applied current is increased. In the Fig. 7.8 (c), we see the amplitude of the second harmonic as a function of the applied current in a log-log scale which allow us to verify the quadratic dependence of these fluctuations amplitude with the applied current.

We now compare the 1st and 2nd harmonic of the voltage obtained in electronic transport with the photo-response Fig. 7.9. Even when a better agreement between the 2nd Harmonic and the photo-response can be seen by eye, a better understanding

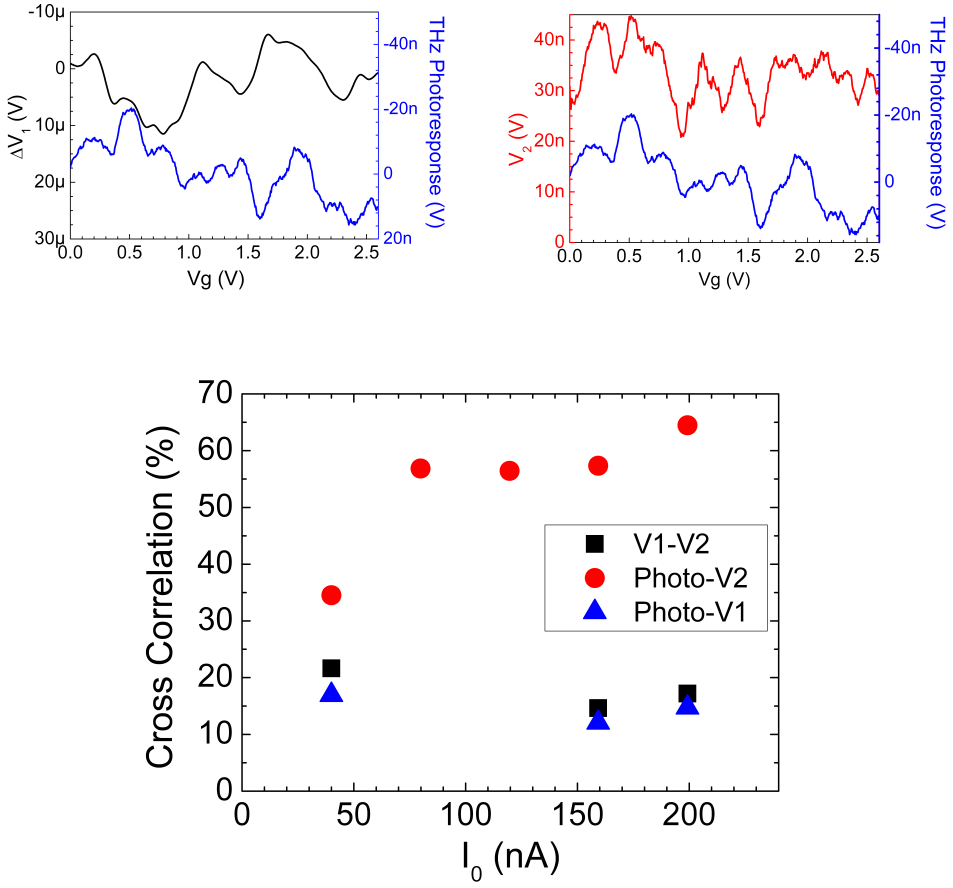

Figure 7.9: **Top left (right)** Photo-response (blue) and 1st (2nd) harmonic (black/red) as a function of the back-gate voltage for a excitations current of $I_0 = 200$ nA. Monotone curve has been subtracted for the first harmonic in order to have only conductance fluctuations. **Bottom** Cross correlation of Photo-response with 1st harmonic (black) and 2nd harmonic (red) and 1st and 2nd harmonic (blue) at different excitation currents.

is achieve when we look the cross correlation. For the 1st harmonic and the photo-response as well as the 1st and 2nd harmonics it is very low $< 25\%$ for all the applied currents (blue triangles and black squares). On the other hand, the correlation between the photo-response and the 2nd harmonic of the voltage turns our to be relatively high $> 55\%$ (red circles). This study reveals a good agreement between both experiments and allow us to say that voltage fluctuations observed when a THz radiation incide in a graphene sample are strongly related to the second Harmonics of the voltage.

To understand the physical phenomenon that lies behind this observations we study the origin of the photoresponse. The current density in the channel, j, and

the continuity equation for the voltage [Sakowiz 2011] can be expressed as:

$$j = -\sigma \frac{\partial V g}{\partial x}\,, \tag{7.10}$$

$$\frac{\partial n}{\partial t} + \frac{\partial j}{\partial x} = 0\,, \tag{7.11}$$

where $n = \alpha V_g$ is the charge density as we express earlier. Combining both equations we find the solutions of the differential equation as a expansion of powers of the amplitude:

$$V_g = U_0 + U_1 + U_2\,. \tag{7.12}$$

For this expansion U_1 is the AC component proportional to the modulation of the source-gate voltage, U_a, and U_2 is the DC component proportional to U_a^2. For the first order, after boundary conditions ($U_1(x = 0, t) = U_a \cos(\omega t)$, $U_1(x = L_g, t) = 0$, where d is the gate length), we obtain:

$$U_1 = U_a e^{-\kappa x} \cos\left(\omega t - \kappa x\right), \tag{7.13}$$

where $\kappa^2 = \frac{\omega\alpha}{2\sigma_0}$. For the second-order, for more details [Sakowiz 2011], we obtain:

$$U_2 = \frac{U_a^2}{4}\left[\frac{1}{\sigma}\frac{d\sigma}{dV g}\right]\left(1 - \exp\left(-2\kappa x\right)\right), \tag{7.14}$$

the photo-response of the system can be written as:

$$\Delta U = U_2(\infty) - U_2(0) = \frac{U_a^2}{4}\frac{d(\ln\sigma)}{dV g}\,. \tag{7.15}$$

We can evaluate this expression with the experimental results of the conductance as a function of the gate voltage, Fig. 7.9 right (blue) and we can compare directly with the experimental photo-response (black). Even to the naked eye is easy to realize that this two photo-responses are not highly correlated. This is an indication that the coupling of the system and the photo-response variation is not made through the gate.

We could expect an efficient coupling between the gate and the THz radiation because the back-gate pad is outside of the beam spot and it can not play the role of an antenna. Additionally, the distance between the gate and the antenna is relatively large ($\sim$ 300 nm, see before).

Following [Knap 2009] and using the product of the frequency, ω, and the electron momentum relaxation time, τ, we can distinguish the operation regimen of the FET. In our case the electron relaxation time has been estimated, using conductance measurements, in $\tau \approx 20$ fs, and the used frequency in $\omega = 1.8$ THz. The product of these two parameters $\omega\tau < 1$ which means that we are working in a low frequency regime. For this regime the photo-response is expected to be given by [Dyakonov 1993, Sakowiz 2011]:

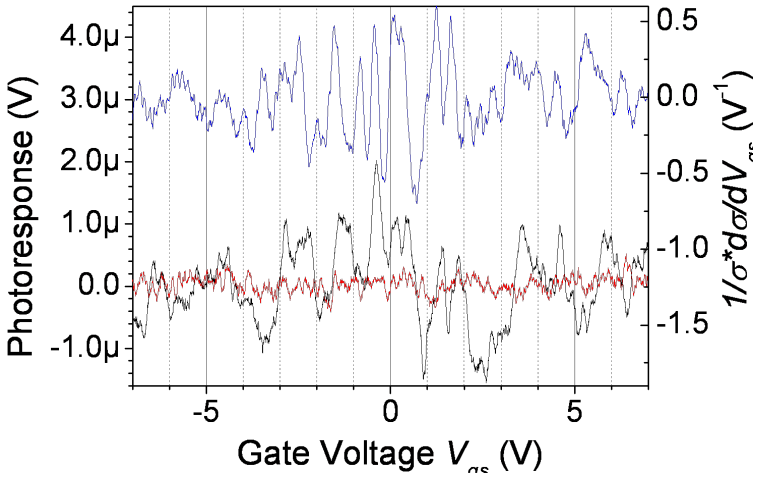

Figure 7.10: Calculated photo-response with eq. (7.15) (blue) compare with the photo-response.

$$\Delta U = \frac{U_a^2}{4U_0}\,. \tag{7.16}$$

As we see, photo-response is also a second-order effect and it explains very well why the second-harmonic of the voltage (which is also related to second order mechanism) is highly correlated to the photo-response of the system to THz radiations.

Now, the physical phenomenon is clear and that it has been probed that the conductance fluctuations present in graphene when a THz radiation is applied are related to second-order conductance fluctuations or what is the same to potential flutuations in the graphene flake. It shows that THz radiation can be used to explore non-linear quantum phenomenon, opening a new opportunity to study this phenomena where most of the physics of graphene remains unexplored and need of a deeper research and understanding.

7.4 Summary

In this chapter, we studied quantum interference through conductance fluctuations and weak localization to better understand the decoherence in grahene systems. Our study have different approaches to study the decoherence mechanism in GNRs.

We start studying the conductance fluctuations in a bilayer GNR when the temperature of the system is increased, these amplitudes follow a $\propto 1/\sqrt{T}$ behavior related to a thermal dephasing where the coherence length and the thermal length decrease as the temperature increase. Also we show through the study of the correlation voltage that after certain temperature ($T > 10$ K) the correlation length of the system follow the same behavior and has a magnitude very close to the thermal length.

When we compare the amplitude of the conductance and magneto-conductance fluctuations we found that the difference between these two is equal to $1/2\sqrt{2}$, this is the expected difference in the amplitudes when time reversal symmetry breaking and spin degeneracy is lifted.

Another important study is the amplitude of the conductance fluctuations in the out-of equilibrium regime, when a high bias voltage is applied to the sample. In this regime the amplitude of the fluctuations decrease following $1/\sqrt{V_b}$ characteristic of a dephasing driven by electron-electron interaction according to the model of [Ludwig 2004]. Contrary to the result found in magneto-conductance fluctuation for a bilayer GNR, where the dependence of the amplitude with the bias voltage follow a 1/V behavior and the correlation length do not depend of the bias voltage, the correlation length of the system varies indicating that the decrease of the fluctuations is due to the decrease of the coherence length.

As a final part, we study the response of graphene to a THz radiation. In this case we found fluctuation of the photo-response as a function of the back-gate voltage that are highly correlated to the fluctuations in the second harmonic of the voltage. This opens the opportunity to use THz radiation to study non-linear quantum phenomenon.

Conclusion

In this PhD thesis, we studied the electronic structure of graphene nanoribbons through their response to a pulse magnetic field. The main motivation was to reveal the characteristics of their Landau spectrum, as a magneto-fingerprint of the electronic confinement and edge symmetry. For this purpose, we first developed the technological processes to fabricate our own GNR based devices with widths between 50 and 100 nm. Different experimental techniques have been explored: GNR from e-beam lithography and oxygen plasma etching; GNRs from unzipping CNT; GNR from anisotropic etching; natural GNR from mechanical cleavage. We finally obtained interesting electronic transport characteristics, suitable for pulse field experiments for GNR derived by e-beam lithography and oxygen plasma etching.

We performed magneto-transport experiments (up to 55 T) at low temperatures (2 K) on monolayer and bilayer graphene nanoribbons (GNRs). The electronic transport study at zero field gives evidence of carrier mobilities larger than 1200 $cm^2V^{-1}s^{-1}$, large enough to induce a Landau redistribution of the electronic energies under high magnetic field.

For the *monolayer GNR devices*, we obtained the first experimental observation of the Landau quantization for GNR on SiO_2 substrates, with quantized values of the resistance at $h/2e^2$ and $h/6e^2$, corresponding to filling factors of $\nu = 2$ and 6, respectively. In the highly doped regime, the presence of anomalous Shubnikov-de Haas oscillations reveal the electronic confinement for widths smaller than 100 nm.

For the narrowest devices of 70 nm width, a new Landau spectrum is unveiled, giving evidence of a degeneracy lifting of the lowest Landau levels, which can not be related to the previously observed degeneracy lifting in 2D graphene. By comparing the theoretical expected band structure of an armchair GNR of similar width in the presence of high magnetic field and the quantum oscillations we measured, we found a convincing agreement between the maxima of resistance and the pinning of the Fermi energy on the two Landau sublevels, characteristic of the armchair edge symmetry. This evidence strongly supports a contribution of an armchair configuration at the edges of the GNR.

In case of *bilayer GNRs*, the experimental results are less convincing due to the limited mobility but they nevertheless unveil the presence of Landau levels for filling factors corresponding to graphene bilayer ($\nu = 8$ and 12) but without sign of resistance quantization. For the lowers filling factors ($\nu = 4$) new structures are reveal as the doping level is increased. These structures may be related to the beginning of a degeneracy lifting related to the confinement and the edge symmetry. To confirm this origin, numerical simulations of bilayer GNRs in presence of a high magnetic field and additional experiments are needed. Note that, these simulations handle a large number of parameters (stacking of the layers, potential difference between layers, edge symmetry) which makes the comparison challenging.

These studies also demonstrate the power of magneto-transport experiments at

high magnetic field in rather clean devices. An uncontroversial signature of a specific edge geometry on the Landau spectrum would require further experimental efforts with different sources of GNRs. Also, a local probe, like STM (Scanning Tunneling Microscope), on the same device to directly address the edge structure would provide complementary confirmations.

Another confirmation of this study will be to focus on high quality narrower GNRs. Unfortunately, our efforts on GNR derived from CNT did not allow to achieve the expected GNR devices quality, most probably due to large contact resistance. Ultimate GNR are certainly those obtained by th bottom-up approach, on metallic substrates using surface-assisted coupling of molecular precursors. Further works are needed to transfer these ribbons on non conducting substrates for a full electronic characterization and under a large magnetic field environment.

Additionally, we studied the quantum interference through conductance fluctuations and weak localization on GNRs to reveal the decoherence mechanism when different parameters are varied (e.g. temperature and bias voltage). This studies reveal a dominant thermal dephasing when the temperature is increased and the signature of electron-electron interactions when a high bias voltage is applied. We also study the conductance fluctuations produced when a THz radiation incide on a graphene flake, this are highly correlated to second order conductance fluctuations. This experimental founding opens a new possibility to study non-linear quantum phenomenon trough THz detection.

Nomenclature

$\rho(E_F)$	Density of states at the Fermi energy
G_0	Quantum of condutance $G_0 = 2e^2/h \approx 77.48\ \mu$S
$g_{s(v)}$	Spin (valley) degeneracy factor $g_{s(v)} = 2$
α	Capacitive efficiency $\alpha = C_g/e$.
Δ_{Th}	Thermal broadening
γ_1	hopping energy between atom A_1 and A_2
γ_3	hopping energy between atom B_1 and B_2
γ_4	hopping energy between atom A_1 (A_2) and B_2 (B_1)
$\mathbf{B}$	Magnetic field
μ	Field effect carier mobility
ω_c	Cyclotron frequency given by $\omega_c = \frac{eB}{m_c}$
Φ_0	Magnetic quantum flux $\Phi_0 = h/e$
τ_*	Intravalley scattering time
τ_i	Intervalley scattering time
a	Carbon-carbon distance $a = 0.142$ nm
E_c	Correlation energy
E_c	Correlation energy
E_F	Fermi energy
g_s	Spin degeneracy
g_v	Valley degeneracy
l_ϕ	Phase coherence Length
l_e	Elastic mean free path
l_m	Magnetic length $l_m = (\hbar/eB)^{1/2}$
l_T	Thermal length
m^*	Effective mass

m_e	Electron mass
N_a	Number of armchair dimers between GNR edges.
N_z	Number of zigzag chains between GNR edges.
r_N	Cyclotron radius $r_N = \left[\frac{2\hbar}{eB}\left(N + \frac{1}{2}\right)\right]^{1/2}$
t	In-plane hopping energy
$t_\perp$	the effective interlayer hopping energy
V_c	Correlation voltage
v_F	Fermi velocity, for graphene $v_F \simeq 1 \times 10^6$ m/s
C_g	Capacitive coupling
CNP	Charge neutrality point
CNT	Carbon Nanotube
D	diffusion coefficient
GNR	Graphene Nanoribbon
L	Sample's length
N	Landau level index
n	Carrier density
n_0	Residual carrier density
R_c	Contact resistance
R_T	Total resistance
V_g	Back-gate voltage
V_{CNP}	Charge Neutrality point gate voltage
W	Sample's width
W_a	Zigzag GNRs width $W_a = (N_a - 1)\sqrt{3}a/2$
W_z	Zigzag GNRs width $W_z = (N_z - 1)3a/2$
zGNR	Zigzag graphene nanoribbon

Bibliography

[A. Cresti 2008] B. Biel G. Niebler F. Triozon-G. Cuniberti A. Cresti N. Nemec et S Roche. *Charge Transport in Disordered Graphene-Based Low Dimensional Materials.* Nano Research, vol. 1, page 361, 2008. (Cited in pages 23 and 28.)

[Abanin 2008] Dmitry A. Abanin et Leonid S. Levitov. *Conformal invariance and shape-dependent conductance of graphene samples.* Phys. Rev. B, vol. 78, page 035416, Jul 2008. (Cited in pages 68, 69, 94, 106, 114 and 121.)

[B. E. Feldman 2009] J. Martin B. E. Feldman et A. Jacoby. *Broken-symmetry states and divergent resistance in suspended bilayer graphene.* Nature Physics, vol. 5, page 889, 2009. (Cited in pages 59 and 117.)

[Bao 2010] Wenzhong Bao, Zeng Zhao, Hang Zhang, Gang Liu, Philip Kratz, Lei Jing, Jairo Velasco, Dmitry Smirnov et Chun Ning Lau. *Magnetoconductance Oscillations and Evidence for Fractional Quantum Hall States in Suspended Bilayer and Trilayer Graphene.* Phys. Rev. Lett., vol. 105, page 246601, Dec 2010. (Cited in page 61.)

[Barlas 2008] Yafis Barlas, R. Côté, K. Nomura et A. H. MacDonald. *Intra-Landau-Level Cyclotron Resonance in Bilayer Graphene.* Phys. Rev. Lett., vol. 101, page 097601, Aug 2008. (Cited in page 60.)

[Beenakker 1991] C. W. J. Beenakker et H; van Houten. *Quantum Transport in Semiconductor Nanostructures.* Solid state physics, vol. 44, pages 1–228, 1991. (Cited in pages 31, 45, 46, 50, 96 and 132.)

[Berger 2004] C. Berger, Z. Song, T. Li, X. Li, A. Ogbazghi, R. Feng, Z. Dai, A. N. Marchenkov, E. H. Conrad, P. N. First et W. A. de Heer. *Ultrathin Epitaxial Graphite: 2D Electron Gas Properties and a Route toward Graphene-based Nanoelectronics.* The Journal of Physical Chemistry, vol. 108, no. 52, page 19912, 2004. (Cited in page 73.)

[Berger 2006] C. Berger, Z. Song, X. Li, X. Wu, N. Brown, C. Naud, D. Mayou, T. Li, J. Hass, A. N. Marchenkov, E. H. Conrad, P. N. First et W. A. de Heer. *Electronic Confinement and Coherence in Patterned Epitaxial Graphene.* Science, vol. 312, no. 5777, page 1191, 2006. (Cited in pages 69, 70, 73 and 75.)

[Bohra 2012a] G. Bohra, R. Somphonsane, N. Aoki, Y. Ochiai, R. Akis, D. K. Ferry et J. P. Bird. *Nonergodicity and microscopic symmetry breaking of the conductance fluctuations in disordered mesoscopic graphene.* Phys. Rev. B, vol. 86, page 161405, Oct 2012. (Cited in pages 47 and 132.)

[Bohra 2012b] G. Bohra, R. Somphonsane, N. Aoki, Y. Ochiai, D. K. Ferry et J. P. Bird. *Robust mesoscopic fluctuations in disordered graphene.* Applied Physics Letters, vol. 101, page 101, 2012. (Cited in page 131.)

[Bolotin K. 2009] Shulman M.D; Stormer H. L. Bolotin K. Ghahari F; et Kim P. *Observation of the fractional quantum Hall effect in graphene.* Nature, vol. 462, page 196, Nov 2009. (Cited in page 58.)

[Bolotin 2008] K. I. Bolotin, K. J. Sikes, J. Hone, H. L. Stormer et P. Kim. *Temperature-Dependent Transport in Suspended Graphene.* Phys. Rev. Lett., vol. 101, page 096802, Aug 2008. (Cited in pages 20 and 37.)

[Bonaccorso 2010] F. Bonaccorso, T. Sun Z. Hasan et A.C. Ferrari. *Graphene photonics and optoelectronics.* Nature Photonics, vol. 4, page 611, August 2010. (Cited in page 137.)

[Brey 2006] L. Brey et H. A. Fertig. *Electronic states of graphene nanoribbons studied with the Dirac equation.* Phys. Rev. B, vol. 73, page 235411, Jun 2006. (Cited in pages 23, 24, 25, 26 and 27.)

[Castro-Neto 2009] A.H. Castro-Neto, F. Guinea, N. M. R. Peres, K. S. Novoselov et A. K. Geim. *The electronic properties of graphene.* Reviews of Modern Physics, vol. 81, no. 1, page 109, 2009. (Cited in pages 13, 14, 15, 16, 23, 24, 27, 37, 43 and 137.)

[Checkelsky 2009] J. G. Checkelsky, L. Li et N. P. Ong. *Divergent resistance at the Dirac point in graphene: Evidence for a transition in a high magnetic field.* Phys. Rev. B, vol. 79, page 115434, Mar 2009. (Cited in pages 95 and 117.)

[Chen 2009] Jian-Hao Chen, W. G. Cullen, C. Jang, M. S. Fuhrer et E. D. Williams. *Defect Scattering in Graphene.* Phys. Rev. Lett., vol. 102, page 236805, Jun 2009. (Cited in page 38.)

[Chung 2010] H.C. Chung, Y.C. Huang, M.H.. Lee, C.C. Chang et M.F. Lin. *Quasi-Landau levels in bilayer zigzag graphene nanoribbons.* Physica E, vol. 42, page 711, 2010. (Cited in pages 66 and 67.)

[Cresti 2012] A. Cresti. *private communication.* 2012. (Cited in page 68.)

[Cserti 2007] József Cserti, András Csordás et Gyula Dávid. *Role of the Trigonal Warping on the Minimal Conductivity of Bilayer Graphene.* Phys. Rev. Lett., vol. 99, page 066802, Aug 2007. (Cited in page 19.)

[Das Sarma 2010] E.H. Hwang Das Sarma S. Shaffique A. et E. Rossi. *Electronic Transport in two dimensional graphene.* ArXiv, Nov 2010. (Cited in pages 19, 36 and 93.)

[Das 2009] A. Das, B. Chakraborty, S. Piscanec, S. Pisana, A. K. Sood et A. C. Ferrari. *Phonon renormalization in doped bilayer graphene.* Phys. Rev. B, vol. 79, page 155417, Apr 2009. (Cited in pages 112 and 119.)

[de Graaf 1992] C. de Graaf, J. Caro et S. Radelaar. *Weak localization in short one-dimensional channels contacted by two-dimensional probes.* Phys. Rev. B, vol. 46, pages 12814–12817, Nov 1992. (Cited in page 41.)

[Dean 2012] C Dean, A.F. Young, L. Wang, I. Meric, G.-H. Lee, Watanabe K., T Taniguchi, K. Shepard, P. Kim et J. Hone. *Graphene based heterostructures.* solid state communications, vol. 152, pages 1275–1282, May 2012. (Cited in pages 59, 60 and 121.)

[Delplace 2010] Pierre Delplace et Gilles Montambaux. *WKB analysis of edge states in graphene in a strong magnetic field.* Phys. Rev. B, vol. 82, page 205412, Nov 2010. (Cited in pages 22, 63 and 65.)

[Deretzis 2011] I. Deretzis et La Magna A. *Coherent electron transport in quasi one-dimensional carbon-based systems.* Eur. Phys. J. B, vol. 81, page 15, 2011. (Cited in page 23.)

[Du X. 2009] Duerr F. Luican A. Du X. Skachkoi I. et Andrei E. *Fractional quantum Hall effect and insulating phase of Dirac electrons in graphene.* Nature, vol. 462, page 192, Nov 2009. (Cited in page 58.)

[Dubois S. 2009] Declerck X. Dubois S. Zanolli Z. et Charlier J-C. *Electronic properties and quantum transport in Graphene-based nanostructures.* The European Physical journal B, vol. 72, page 1, Oct 2009. (Cited in page 32.)

[Dyakonov 1993] Michael Dyakonov et Michael Shur. *Shallow water analogy for a ballistic field effect transistor: New mechanism of plasma wave generation by dc current.* Phys. Rev. Lett., vol. 71, pages 2465–2468, Oct 1993. (Cited in pages 87, 137 and 142.)

[F. Miao 2007] Y. Zhang U.C. Coskun W. Bao-C.N. Lau F. Miao S. Wijeratne. *Phase-Coherent Transport in Graphene Quantum Billiards.* Science, vol. 317, page 1530, Septembre 2007. (Cited in pages 19 and 20.)

[Farmer 2009] D. B. Farmer, H-Y Chiu, Y-M. Lin, K. A. Jenkins, F. Xia et P. Avouris. *Utilization of a Buffered Dielectric to Achieve High Field-Effect Carrier Mobility in Graphene Transistors.* Nano Letters, vol. 9, no. 12, page 4474, 2009. (Cited in page 93.)

[Ferrari 2006] A. C. Ferrari, J. C. Meyer, V. Scardaci, C. Casiraghi, M. Lazzeri, F. Mauri, S. Piscanec, D. Jiang, K. S. Novoselov, S. Roth et A. K. Geim. *Raman Spectrum of Graphene and Graphene Layers.* Phys. Rev. Lett., vol. 97, page 187401, Oct 2006. (Cited in pages 85 and 112.)

[Ferry 2009] D. K. Ferry, S. M. Goodnick et J. Bird. *Transport in Nanoestructures.* 2009. (Cited in pages 30, 41, 42, 50, 51, 53 and 54.)

[Fujita 1996] M. Fujita, K. Wakabayashi, K. Nakada et K. Kusakabe. *Peculiar localized states at zigzag graphite edge*. Journal of the physical society Japan, vol. 65, page 1920, July 1996. (Cited in page 23.)

[Gallagher 2010] Patrick Gallagher, Kathryn Todd et David Goldhaber-Gordon. *Disorder-induced gap behavior in graphene nanoribbons*. Phys. Rev. B, vol. 81, page 115409, Mar 2010. (Cited in pages 40 and 120.)

[Gao 1989] J. R. Gao, J. Caro, A. H. Verbruggen, S. Radelaar et J. Middelhoek. *Temperature dependence of universal conductance fluctuations in narrow mesoscopic Si inversion layers*. Phys. Rev. B, vol. 40, pages 11676–11682, Dec 1989. (Cited in page 46.)

[Geim 2007] A. K. Geim et K. S. Novoselov. *The rise of graphene*. Nature Materials, vol. 6, page 183, 2007. (Cited in pages 123 and 137.)

[Gundra 2011] Kondayya Gundra et Alok Shukla. *Band structure and optical absorption in multilayer armchair graphene nanoribbons: A Pariser-Parr-Pople model study*. Phys. Rev. B, vol. 84, page 075442, Aug 2011. (Cited in pages 29 and 30.)

[Gunlycke 2008] D. Gunlycke et C. T. White. *Tight-binding energy dispersions of armchair-edge graphene nanostrips*. Phys. Rev. B, vol. 77, page 115116, Mar 2008. (Cited in page 28.)

[Han 2007] M. Y. Han, B. Özyilmaz, Y. Zhang et P. Kim. *Energy Band-Gap Engineering of Graphene Nanoribbons*. Phys. Rev. Lett., vol. 98, page 206805, May 2007. (Cited in pages 29, 74, 75 and 120.)

[Hettmansperger 2012] H. Hettmansperger, F. Duerr, J. B. Oostinga, C. Gould, B. Trauzettel et L. W. Molenkamp. *Quantum Hall effect in narrow graphene ribbons*. Phys. Rev. B, vol. 86, page 195417, Nov 2012. (Cited in pages 41, 66, 94 and 96.)

[Holweg 1993] P. A. M. Holweg, J. Caro, A. H. Verbruggen et S. Radelaar. *Correlation energy of conductance fluctuations in ballistic silver point contacts*. Phys. Rev. B, vol. 48, pages 2479–2485, Jul 1993. (Cited in page 131.)

[Ihnatsenka 2009] S. Ihnatsenka et G. Kirczenow. *Conductance quantization in strongly disordered graphene ribbons*. Phys. Rev. B, vol. 80, page 201407, Nov 2009. (Cited in pages 38 and 39.)

[J. Martin 2008] G. Ulbricht T. Lohmann J. H. Smet K. von Klitzing J. Martin N. Akerman et A. Yacoby. *Observation of electron-hole puddles in graphene using a scanning single-electron transistor*. Nature Physics, vol. 4, pages 144–148, Feb 2008. (Cited in page 36.)

[Jiang 2007a] Z. Jiang, Y. Zhang, H. L. Stormer et P. Kim. *Quantum Hall States near the Charge-Neutral Dirac Point in Graphene.* Phys. Rev. Lett., vol. 99, page 106802, Sep 2007. (Cited in page 57.)

[Jiang 2007b] Z. Jiang, Y. Zhang, H.L. Tan, H. L. Stormer et P. Kim. *Quantum Hall Effect in Graphene.* Solid State Communications, vol. 143, page 14, April 2007. (Cited in page 41.)

[Jiao 2009] L. Jiao, L. Zhang, X. Wang, G. Diankov et H. Dai. *Narrow graphene nanoribbons from carbon nanotubes.* Nature, vol. 458, no. 0, page 877, 2009. (Cited in pages 74 and 75.)

[Jiao 2010] L. Jiao, X. Wang, G. Diankov, H. Wang et H. Dai. *Facile synthesis of high-quality graphene nanoribbons.* Nature Nanotechnology, vol. 5, no. 0, page 321, 2010. (Cited in pages 77 and 78.)

[Katsnelson 2006a] M.I. Katsnelson. *Minimal conductivity in bilayer graphene.* Eur. Phys. J. B, vol. 52, page 151, 2006. (Cited in page 19.)

[Katsnelson 2006b] M.I. Katsnelson. *Zitterbewegung, chirality, and minimal conductivity in graphene.* Eur. Phys. J. B, vol. 51, page 157, 2006. (Cited in page 19.)

[Kechedzhi 2007] K. Kechedzhi, Vladimir I. Fal'ko, E. McCann et B. L. Altshuler. *Influence of Trigonal Warping on Interference Effects in Bilayer Graphene.* Phys. Rev. Lett., vol. 98, page 176806, Apr 2007. (Cited in pages 43 and 129.)

[Kharitonov 2008] Maxim Yu. Kharitonov et Konstantin B. Efetov. *Universal conductance fluctuations in graphene.* Phys. Rev. B, vol. 78, page 033404, Jul 2008. (Cited in page 47.)

[Klitzing 1980] K. v. Klitzing, G. Dorda et M. Pepper. *New Method for High-Accuracy Determination of the Fine-Structure Constant Based on Quantized Hall Resistance.* Phys. Rev. Lett., vol. 45, pages 494–497, Aug 1980. (Cited in page 52.)

[Knap 2004] W. Knap, J. Lusakowski, T. Parenty, S. Bollaert, A. Cappy, V.V. Popov et M.S. Shur. *Terahertz emission by plasma waves in 60 nm gate high electron mobility transistors.* Applied Physics Letters, vol. 84, page 2331, 2004. (Cited in page 137.)

[Knap 2009] W. Knap, M. Dyakonow, D. Coquillat, F. Teppe, N. Dyakonova, J. Lusakowski, K. Karpierz, M. Sakowicz, G. Valusis, D. Seliuta, I. Kasalynas, A. El Fatimy, Y.M. Meziani et T. Otsuji. *Field effect transistors for Terahertz Detection: Physics and First Imaging Applications.* J infrared Milli Terahz Waves, vol. 30, pages 1319–1337, 2009. (Cited in pages 137 and 142.)

[Kumar 2011] A. Kumar, W. Escoffier, J. M. Poumirol, C. Faugeras, D. P. Arovas, M. M. Fogler, F. Guinea, S. Roche, M. Goiran et B. Raquet. *Integer Quantum Hall Effect in Trilayer Graphene.* Phys. Rev. Lett., vol. 107, page 126806, Sep 2011. (Cited in pages 113 and 117.)

[Lee 1987] P. A. Lee, A. Douglas Stone et H. Fukuyama. *Universal conductance fluctuations in metals: Effects of finite temperature, interactions, and magnetic field.* Phys. Rev. B, vol. 35, pages 1039–1070, Jan 1987. (Cited in pages 45, 46, 129 and 131.)

[Li 2008] X. Li, X. Wang, L. Zhang, S. Lee et H. Dai. *Chemically derived, ultrasmooth graphene nanoribbon semiconductors.* Science, vol. 319, page 1229, Feb 2008. (Cited in pages 74 and 75.)

[Li 2009] T.S. Li, Y.C. Huang, S.C. Chang, C.P. Chang et M.F. Lin. *Magnetoconductance of graphene nanoribbons.* Philosophical Magazine, vol. 89, page 697, March 2009. (Cited in page 66.)

[Liao 2010] Z-M. Liao, B-H. Han, H-Z. Zhang, Y-B. Zhou, Q. Zhao et D-P Yu. *Current regulation of universal conductance fluctuations in bilayer graphene.* New journal of Physics, vol. 12, page 083016, August 2010. (Cited in page 132.)

[Lin 2008] Yu-Ming Lin, Vasili Perebeinos, Zhihong Chen et Phaedon Avouris. *Electrical observation of subband formation in graphene nanoribbons.* Phys. Rev. B, vol. 78, page 161409, Oct 2008. (Cited in pages 33, 34 and 93.)

[Ludwig 2004] T. Ludwig, Ya. M. Blanter et A. D. Mirlin. *Nonequilibrium mesoscopic conductance fluctuations.* Phys. Rev. B, vol. 70, page 235315, Dec 2004. (Cited in pages 133, 135, 137 and 144.)

[M. Sprinkle 2010] Y. Hu J Hankinson M. Rubio-Roy B. Zhang X. Wu C. Berger M. Sprinkle M. Ruan et W. A. de Heer. *Scalable templated growth of graphene nanoribbons on SiC.* Nature Nanotechnology, vol. 5, page 727, Octobre 2010. (Cited in pages 74 and 75.)

[McCann 2006a] E. McCann, K. Kechedzhi, Vladimir I. Fal'ko, H. Suzuura, T. Ando et B. L. Altshuler. *Weak-Localization Magnetoresistance and Valley Symmetry in Graphene.* Phys. Rev. Lett., vol. 97, page 146805, Oct 2006. (Cited in page 43.)

[McCann 2006b] Edward McCann et Vladimir I. Fal'ko. *Landau-Level Degeneracy and Quantum Hall Effect in a Graphite Bilayer.* Phys. Rev. Lett., vol. 96, page 086805, Mar 2006. (Cited in pages 55 and 58.)

[McEuen 1999] Paul L. McEuen, Marc Bockrath, David H. Cobden, Young-Gui Yoon et Steven G. Louie. *Disorder, Pseudospins, and Backscattering in Carbon Nanotubes.* Phys. Rev. Lett., vol. 83, pages 5098–5101, Dec 1999. (Cited in page 39.)

[Mendis 2005] R. Mendis, C. Sydlo, J. Sigmund, M. Feiginov et P. Meissner. *Spectral characterization of broadband THz antennas by photoconductive mixing: toward optimal antenna design.* Antennas and Wireless propagation letters, vol. 4, page 85, 2005. (Cited in page 80.)

[Min 2007] Hongki Min, Bhagawan Sahu, Sanjay K. Banerjee et A. H. MacDonald. *Ab initio theory of gate induced gaps in graphene bilayers.* Phys. Rev. B, vol. 75, page 155115, Apr 2007. (Cited in page 16.)

[Minke 2012a] S. Minke, J. Bundesmann, D. Weiss et J. Eroms. *Phase coherent transport in graphene nanoribbons and graphene nanoribbon arrays.* Phys. Rev. B, vol. 86, page 155403, Oct 2012. (Cited in pages 44 and 45.)

[Minke 2012b] S. Minke, S. H. Jhang, J. Wurm, Y. Skourski, J. Wosnitza, C. Strunk, D. Weiss, K. Richter et J. Eroms. *Magnetotransport through graphene nanoribbons at high magnetic fields.* Phys. Rev. B, vol. 85, page 195432, May 2012. (Cited in page 94.)

[Moreno-Moreno 2009] M. Moreno-Moreno, A. Castellanos-Gomez, G. Rubio-Bollinger, J. Gomez-Herrero et N. Agrait. *Ultralong Natural Graphene Nanoribbons and Their Electrical Conductivity.* Small, vol. 5, no. 4, pages 924–927, 2009. (Cited in page 76.)

[Moser 2007] J. Moser, A; Barreiro et A; Bachtold. *Current-induced cleaning of graphene.* Applied Physics Leters, vol. 91, page 163513, 2007. (Cited in page 83.)

[Moser 2009] J. Moser et A. Bachtold. *Fabrication of large addition energy quantum dots in graphene.* Applied Physics Leters, vol. 95, page 173506, 2009. (Cited in page 75.)

[Mucciolo 2009] E. R. Mucciolo, A. H. Castro Neto et C. H. Lewenkopf. *Conductance quantization and transport gaps in disordered graphene nanoribbons.* Phys. Rev. B, vol. 79, page 075407, Feb 2009. (Cited in pages 38 and 39.)

[Mucciolo 2010] E.R. Mucciolo et C.H. Lewenkopf. *Disorder and electronic transport in graphene.* Journal of physics: Condensed Matter, vol. 22, page 273201, 2010. (Cited in pages 16 and 35.)

[Nakada 1996] Kyoko Nakada, Mitsutaka Fujita, Gene Dresselhaus et Mildred S. Dresselhaus. *Edge state in graphene ribbons: Nanometer size effect and edge shape dependence.* Phys. Rev. B, vol. 54, pages 17954–17961, Dec 1996. (Cited in page 25.)

[Nomura 2006] Kentaro Nomura et Allan H. MacDonald. *Quantum Hall Ferromagnetism in Graphene.* Phys. Rev. Lett., vol. 96, page 256602, Jun 2006. (Cited in pages 57, 58 and 104.)

[Novoselov 2004] K.S. Novoselov, A. K. Geim, S. V. Morozov, D. Jiang, Y. Zhang, S. V. Dubonos, I. V. Grigorieva et A. A. Firsov. *Electric Field Effect in Atomically Thin Carbon Films.* Science, vol. 306, no. 0, page 666, 2004. (Cited in pages 12, 73 and 76.)

[Novoselov 2005] K.S. Novoselov, A. K. Geim, S. V. Morozov, D. Jiang, M. I. Katsnelson, I. V. Grigorieva, S. V. Dubonos et A. A. Firsov. *Two-dimensional gas of massless Dirac fermions in grephene.* Nature, vol. 438, no. 0, page 197, 2005. (Cited in pages 36, 56 and 76.)

[Novoselov 2006] K.S. Novoselov, E. McCann, S. V. Morozov, V. I. Falḱo, M. I. Katsnelson, U. Zeitler, D. Jiang, F. Schedin, et A. K. Geim. *Unconventional quantum Hall effect and Berrys phase of 2π in bilayer graphene.* Nature Physics, vol. 2, no. 0, page 177, 2006. (Cited in pages 58 and 59.)

[Novoselov 2007] K.S. Novoselov, Z. Jiang, Y. Zhang, S. V. Morozov, H. L. Stormer, U. Zeitler, J.C. Maan, G.S. Boebinger, P. Kim et K. Geim. *Room-temperature Quantum Hall Effect in Graphene.* Science, vol. 315, page 1379, 2007. (Cited in page 55.)

[Ohta 2006] T. Ohta, A. Bostwick, T. Seyller, K. Horn et E. Rotenberg. *Controlling the electronic structure of bilayer graphene.* Science, vol. 313, page 951, August 2006. (Cited in pages 18 and 111.)

[Ojeda-Aristizabal 2010] C. Ojeda-Aristizabal, M. Monteverde, R. Weil, M. Ferrier, S. Guéron et H. Bouchiat. *Conductance Fluctuations and Field Asymmetry of Rectification in Graphene.* Phys. Rev. Lett., vol. 104, page 186802, May 2010. (Cited in pages 129, 130 and 140.)

[Onipko 2008] Alexander Onipko. *Spectrum of π electrons in graphene as an alternant macromolecule and its specific features in quantum conductance.* Phys. Rev. B, vol. 78, page 245412, Dec 2008. (Cited in page 31.)

[Oostinga 2008] Jeroen B. Oostinga, Hubert B. Heersche, Xinglan Liu, Alberto F. Morpurgo et Lieven M. K. Vandersypen. *Gate-induced insulating state in bilayer graphene devices.* Nature Materials, vol. 7, page 151, Feb 2008. (Cited in pages 18 and 111.)

[Oostinga 2010] Jeroen B. Oostinga, Benjamin Sacépé, Monica F. Craciun et Alberto F. Morpurgo. *Magnetotransport through graphene nanoribbons.* Phys. Rev. B, vol. 81, page 193408, May 2010. (Cited in page 94.)

[Peres 2006a] N. M. R. Peres, A. H. Castro Neto et F. Guinea. *Conductance quantization in mesoscopic graphene.* Phys. Rev. B, vol. 73, page 195411, May 2006. (Cited in page 32.)

[Peres 2006b] N. M. R. Peres, A. H. Castro Neto et F. Guinea. *Dirac fermion confinement in graphene.* Phys. Rev. B, vol. 73, page 241403, Jun 2006. (Cited in pages 61 and 62.)

[Peres 2010] N. M. R. Peres. *Colloquium: The transport properties of graphene: An introduction.* Rev. Mod. Phys., vol. 82, pages 2673–2700, Sep 2010. (Cited in pages 15, 76 and 94.)

[Poumirol 2010] Jean-Marie Poumirol, Alessandro Cresti, Stephan Roche, Walter Escoffier, Michel Goiran, Xinran Wang, Xiaolin Li, Hongjie Dai et Bertrand Raquet. *Edge magnetotransport fingerprints in disordered graphene nanoribbons.* Phys. Rev. B, vol. 82, page 041413, Jul 2010. (Cited in pages 33, 34, 69 and 70.)

[Ribeiro 2011] Rebeca Ribeiro, Jean-Marie Poumirol, Alessandro Cresti, Walter Escoffier, Michel Goiran, Jean-Marc Broto, Stephan Roche et Bertrand Raquet. *Unveiling the Magnetic Structure of Graphene Nanoribbons.* Phys. Rev. Lett., vol. 107, page 086601, Aug 2011. (Cited in page 94.)

[Rycerz 2007] A. Rycerz, J. Tworzydlo et C.W.J. Beenakker. *Anomalously large conductance fluctuations in weakly disorder graphene.* EPL, vol. 79, page 57003, September 2007. (Cited in pages 130 and 132.)

[Ryzhii 2009] V. Ryzhii et M. Ryzhii. *Graphene bilayer field-effect phototransistor for terahertz and infrared detection.* Phys. Rev. B, vol. 79, page 245311, Jun 2009. (Cited in page 137.)

[Sahu 2008] Bhagawan Sahu, Hongki Min, A. H. MacDonald et Sanjay K. Banerjee. *Energy gaps, magnetism, and electric-field effects in bilayer graphene nanoribbons.* Phys. Rev. B, vol. 78, page 045404, Jul 2008. (Cited in page 27.)

[Sakowiz 2011] M Sakowiz, M.B. lifshits, O. A. Klimenko, F. Schuster, D. Coquillat, F. Teppe et W. Knap. *Terahertz responsivity of field effect transistors versus their static channel conductivity and loading effect.* journal of applied physics, vol. 110, page 054512, 2011. (Cited in page 142.)

[Shi 2011] Z. Shi, R. Yang, L. Zhang, Y. Wang, D. Liu, D. Shi, E. Wang et G. Zhang. *Patterning Graphene with Zigzag edges by self-aligned Anisotropic Etching.* Advanced Materials, vol. 23, no. 27, page 3061, 2011. (Cited in pages 74 and 75.)

[Shylau 2010] A. A. Shylau, I. V. Zozoulenko, H. Xu et T. Heinzel. *Generic suppression of conductance quantization of interacting electrons in graphene nanoribbons in a perpendicular magnetic field.* Phys. Rev. B, vol. 82, page 121410, Sep 2010. (Cited in pages 64 and 66.)

[Stauber 2007] T. Stauber, N. M. R. Peres et F. Guinea. *Electronic transport in graphene: A semiclassical approach including midgap states.* Phys. Rev. B, vol. 76, page 205423, Nov 2007. (Cited in page 37.)

[Tao 2011] Chenggang Tao, Liying Jiao, Oleg V. Yazyev, Yen-Chia Chen, Juanjuan Feng, Xiaowei Zhang, Rodrigo B. Capaz, James M. Tour, Alex Zettl, Steven G.and Dai Hongjie Louie et Michael F. Crommie. *Spatially resolving edge states of chiral graphene nanoribbons.* Nature Physics, vol. 7, page 616, August 2011. (Cited in pages 25, 26, 75, 77 and 124.)

[Taychatanapat 2011] T. Taychatanapat, K. Watanabe, T. Taniguchi et Jarillo-Herrero P. *Quantum Hall effect and Landau-level crossing of Dirac fermions in trilayer graphene.* Nature Physics, vol. 7, page 621, February 2011. (Cited in pages 111 and 117.)

[Terrier 2002] C. Terrier, D. Babi, T. Nussbaumer C.Strunk et C. Schonenberger. *The amplitude of non-equilibrium quantum interference in metallic mesoscopic systems.* Europhys Lett, vol. 59, page 437, 2002. (Cited in page 133.)

[Tikhonenko 2009] F. V. Tikhonenko, A. A. Kozikov, A. K. Savchenko et R. V. Gorbachev. *Transition between Electron Localization and Antilocalization in Graphene.* Phys. Rev. Lett., vol. 103, page 226801, Nov 2009. (Cited in pages 43 and 44.)

[Tombros 2011] N. Tombros, A. Veligura, J. Junesch, M.H.D. Guimaraes, Vera-Marun I.J., H.T. Jonkman et B.J. van Ween. *Quantized conductance of a suspended graphene nanoconstriction.* Nature Physics, vol. 7, page 697, Septembre 2011. (Cited in pages 33, 34, 70, 71, 74 and 75.)

[Vicarelli 2012] L. Vicarelli, M. S. Vitiello, D. Coquillat, A. Lombardo, A. C. Ferrari, W. Knap, V. Polini M. Pellegrini et Tredicucci A. *Graphene field-effect transistors as room-temperature terahertz detectors.* Nature Materials, vol. 11, page 865, August 2012. (Cited in page 137.)

[Videlier 2011] H. Videlier, N. Dyakonova, F. Teppe, C. Consejo, W. Knap, J. Lusakowski, D. Tomaszewski, J. Marczewski et Grabiec P. *Spin Related Effect in Terahertz Photovoltaic Response of Si-MOSFETs.* PIERS Proceedings, vol. Morocco 2011, pages 1272–12740, March 2011. (Cited in page 137.)

[Wakabayashi 2007] Katsunori Wakabayashi, Yositake Takane et Manfred Sigrist. *Perfectly Conducting Channel and Universality Crossover in Disordered Graphene Nanoribbons.* Phys. Rev. Lett., vol. 99, page 036601, Jul 2007. (Cited in page 39.)

[Wallace 1947] P. R. Wallace. *The Band Theory of Graphite.* Phys. Rev., vol. 71, pages 622–634, May 1947. (Cited in pages 12 and 13.)

[Wang 2008] Xinran Wang, Yijian Ouyang, Xiaolin Li, Hailiang Wang, Jing Guo et Hongjie Dai. *Room-Temperature All-Semiconducting Sub-10-nm Graphene Nanoribbon Field-Effect Transistors*. Phys. Rev. Lett., vol. 100, page 206803, May 2008. (Cited in page 40.)

[Williams 2009] J. R. Williams, D. A. Abanin, L. DiCarlo, L. S. Levitov et C. M. Marcus. *Quantum Hall conductance of two-terminal graphene devices*. Phys. Rev. B, vol. 80, page 045408, Jul 2009. (Cited in page 114.)

[Xu 2009] Hengyi Xu, T. Heinzel et I. V. Zozoulenko. *Edge disorder and localization regimes in bilayer graphene nanoribbons*. Phys. Rev. B, vol. 80, page 045308, Jul 2009. (Cited in pages 26, 32, 66 and 67.)

[Yamamoto 2009] Masayuki Yamamoto, Yositake Takane et Katsunori Wakabayashi. *Nearly perfect single-channel conduction in disordered armchair nanoribbons*. Phys. Rev. B, vol. 79, page 125421, Mar 2009. (Cited in page 39.)

[Zhang 2006] Y. Zhang, Z. Jiang, J. P. Small, M. S. Purewal, Y.-W. Tan, M. Fazlollahi, J. D. Chudow, J. A. Jaszczak, H. L. Stormer et P. Kim. *Landau-Level Splitting in Graphene in High Magnetic Fields*. Phys. Rev. Lett., vol. 96, page 136806, Apr 2006. (Cited in pages 41, 56, 57 and 104.)

[Zhao 2010] Y. Zhao, P. Cadden-Zimansky, Z. Jiang et P. Kim. *Symmetry Breaking in the Zero-Energy Landau Level in Bilayer Graphene*. Phys. Rev. Lett., vol. 104, page 066801, Feb 2010. (Cited in pages 59 and 60.)

[Zhu 2009] Wenjuan Zhu, Vasili Perebeinos, Marcus Freitag et Phaedon Avouris. *Carrier scattering, mobilities, and electrostatic potential in monolayer, bilayer, and trilayer graphene*. Phys. Rev. B, vol. 80, page 235402, Dec 2009. (Cited in page 113.)

Author: Rebeca RIBEIRO
Title: Magneto-transport in graphene nanoribbons.
Supervisors: Bertrand RAQUET and Jean-Marc BROTO
Speciality: Nanophysics

Laboratory: Laboratoire National des Champs Magnétiques Intenses (LNCMI-T), CNRS-UPR 3228, 143 avenue de Rangueil, 31400 Toulouse, France.

Abstract:

In the present PhD thesis, we study the electronic transport properties of graphene nanoribbons under a large magnetic field (up to 55 T) to unveil the electronic confinement effects on the band structure of graphene.
Graphene nanoribbons (GNRs) are promising materials to promote graphene for all carbon based nanoelectronics, including electronic wave guides and digital logic or radiofrequency devices. When graphene is structured at a nano-scale, with an accurate control of the edge symmetry, it is possible to open an energy gap in the band structure and to tune the number of conducting channels by a local electrostatic gate. Unfortunately, such a gap engineering goes along with a poor control of the edges' quality and, as a consequence, a drastic drop of the electronic mobility. Most of the confining potential effects on the band structure are masked by the presence of disorder and the experimental evidence of the intrinsic electronic band structure of GNR remains challenging.
Here, we demonstrate that, by playing with a large magnetic confinement, we bring experimental evidence of anomalous Landau spectra, signature of the confining potential in GNRs.
The magneto-transport experiments are mainly obtained on monolayer GNRs on Si/SiO_2 substrates patterned by e-beam lithography and reactive ion etching, with nominal widths between 55 and 100 nm. The carrier mobility varies from 600 to 3500 $cm^2\ V^{-1}\ s^{-1}$. For the largest GNR ($\sim$100 nm), presenting a weakly diffusive regime, we give evidence, at high doping levels, of anomalous Shubnikov-de Haas oscillations, fingerprint of the electronic confinement. At lower doping levels, we observe Landau quantization of the two probes conductance, for filling factor values expected for graphene. In narrower GNRs, new quantum oscillations develop in the quantum regime. This singular Landau spectrum, directly compared to magneto-electric subbands calculations, is assigned to a possible valley degeneracy lifting driven by the confining potential in presence of armchair symmetry at the edges.
Additionally, we present high magnetic field transport results obtained on bilayer graphene nanoribbons and we compare them to magneto-transport performed on un-structured graphene bilayer. The comparison unveils new magneto-signatures in bilayer GNRs, originating from the electronic confining effects.
As a complementary part, we finally study the phase coherence in our GNR devices that manifests itself by magnetic field and back-gate voltage induced conductance

fluctuations. We mainly focus on conductance fluctuations in the out-of-equilibrium regime. The analysis of the amplitude of the fluctuations and of the correlation voltage unveils the phase coherence length and its bias voltage dependence, signature of electron-electron interaction as the main mechanism responsible for the decoherence. Additionally, we investigate the response of graphene to a THz radiation. The experiments show a high cross correlation between the photo-response and the second harmonic conductance fluctuations of the electronic transport. This opens a new possibility to study non-linear mesoscopic effects using THz radiation.

Keywords: Graphene Nanoribbon, Magneto-transport, High Magnetic Field, Landau Levels, Universal Conductance Fluctuations.

Auteur: Rebeca RIBEIRO
Titre: Magnéto-transport dans les nanorubans de graphène.
Directeurs de théses: Bertrand RAQUET et Jean-Marc BROTO
Spécialité: Nanophysique

Laboratoire: Laboratoire National des Champs Magnétiques Intenses (LNCMI-T), CNRS-UPR 3228, 143 avenue de Rangueil, 31400 Toulouse, France.

Résumé:

Les progrès actuels et futurs dans les applications électroniques nécessitent une réduction de la taille et l'amélioration des performances des dispositifs. Ces deuxobjectifs sont centraux dans la conception de nouveaux equipements electroniques, en particulier depuis que les limites des transistors silicium deviennent imminentes.

Dans la quête de nouvelles technologies, l'électronique à base de carbone est devenue prometteuse. Au coeur de cette thématique, le graphène a attiré beaucoup d' attention au cours des dernières années en raison de sa mobilité électronique élevée (plus de 200.000 $cm^2\ V^{-1}\ s^{-1}$) de sa haute densité de courant supportable (~ 2 mA/μm) et de sa flexibilité mécanique. Cependant, l' inconvénient majeur pour les futures applications du graphène dans l'électronique logique est sa semi-métallicité, c'est a dire l'absence d'un gap d'énergie pour garantir un rapport de courant ON/OFF suffisant.

Dans la recherche d'une meilleure façon de concevoir un gap d'énergie, le confinement électronique semble l'approche la plus prometteuse. Si l'on considère l'image simple d'une particule dans une boîte, lorsqu'un électron est confiné dans une dimension, les conditions de bord imposent une quantification des vecteur k transver. Cette quantification conduit à l'apparition d'une structure de bande électronique 1D et l'ouverture d'un gap d'énergie entre la plus haute bande de valence et la plus basse bande de conduction. Le même mécanisme se produit dans le graphène quand il est coupé en nanorubans (GNR). Sauf que, ici, le confinement électronique est également dependent de la symétrie de bord, par exemple, zigzag ou armchair, ce qui entraînent les conditions aux limites spécifiques de la fonction d'onde électronique. Ceci conduit à une structure de bande électronique 1D dependant des configurations de bord. Pour des nanorubans avec un bord zigzag (zGNR), des états localisés sur les bords induisent une bande d'énergie plate à énergie zéro. À plus haute énergie, une sous-bande parfaitement conductrice, robuste au désordre, est appelée à se développer et la dégénérescence de vallée est préservée comme dans le graphène 2D. Dans le cas des nanorubans de graphène avec des bords armchair (aGNR), un gap d'énergie directe, de l'ordre de $[0,2-1,5]eV/W(nm)$ apparait (soit W, la largeur du ruban), et la dégénéracence de vallée est entièrement levée.

La configuration de bord offre donc un nouveau degré de liberté pour ajuster les propriétés électroniques des GNRs, en forte analogie avec le vecteur d'enroulement dans les nanotubes de carbone.

Malheureusement, les méthodes actuelles pour concevoir les nanorubans ne permettent pas un contrôle précis de la symétrie des bords. La plupart des méthodes introduisent un degré élevé de défauts, ce qui induit une réduction drastique de la mobilité des porteurs et la formation d'un gap de transport au le voisinage du point de neutralité de charge. Finalement, les propriétés électroniques de la matière première, le graphène, ne sont plus présentes dans les structures confinées et les spécificités de la symétrie de bord ne restent qu'à un stade de prédictions théoriques. Cela demande des efforts expérimentaux supplémentaires pour optimiser la qualité des nanorubans de graphène et développer des techniques originales pour obtenir des signatures de la structure de bande des GNRs.

Une manière appropriée détudier la structure electronique intrinsèque des nanorubans de graphène est l'expérience de magnéto-transport dans le régime des champ magnétiques élevśe. Pour certains des électrons, à proximité des bords, les trajectoires ne sont pas des orbites fermées, mais cycloides formant des nouveaux canaux conducteurs beaucoup moins sensibles au desordre. Dans le même temps sous champ magnétique, la structure de bande électronique évolue progressivement vers un spectre quantifié de niveaux de Landau possédant une certaine réminiscence du confinement électronique qui domine à champ magnétique nul. Une mesure du transport électronique dans un tel régime révele les propriétes intrinsèques du confinement électronique.

Dans cette thèse, nous proposons l'étude de nanorubans de graphène sous champ magnétique intense (jusqu'à 55 T) pour dévoiler leurs propriétés électroniques qui sont en partie masqués par la présence de desordre.

Ce manuscrit est divisé en deux parties. Dans la première partie (les trois premiers chapitres), nous passons en revue les principaux concepts des propriétés de transport électronique du graphène et des nanorubans de graphène. Nous nous concentrons principalement sur les effets de réduction de taille sur la structure de bande, l'impact du desordre et l'influence d'un champ magnétique intense. Dans cette partie, nous présentons également l'état de l'art expérimental sur ce sujet.

La seconde partie (du chapitre quatre à sept) est consacrée à la présentation des travaux réalisés au cours de cette thèse: la fabrication des échantillons et les résultats expérimentaux de magnéto-transport. Nous commençons d'abord par présenter les methodes de fabrication des échantillons (GNRs lithographiés et dérivés de nanotubes de carbone par calcilation et ultrasons) ainsi que les principales techniques de mesure utilisées dans ce travail.

Le coeur de ce travail repose sur des expériences de magnéto-transport effectuées sur nanorubans de graphène monocouche réalisés par lithographie électronique. Nous observons la signature d'un confinement électronique à travers des oscillations Shubnikov-de Haas anormales et un nouveau spectre de Landau qui peut être lié à la présence de bords armchair sur les nanorubans.

Dans le cas des nanorubans de graphène bicouche, nous observons certaines signatures de la formation de niveaux de Landau par la présence d'oscillations quantiques dans la magnéto-résistance. Cependant, le régime quantifié n'est pas atteint. Certaines anomalies dans le spectre Landau sont observées, possiblement liées au confinement électronique.

Enfin, nous présentons une étude des interférences quantiques dans des nanorubbans de graphène. Nous mettons en évidence les effets de la température et des tensions de polarisation en tant que sources de décohérence et nous apportons la preuve d'ergodicité dans des nanorubans de graphène bicouches. Comme partie supplémentaire, nous présentons brièvement une étude préliminaire du graphène sous radiations THz. Un bon accord entre les fluctuations de la photoréponse et le second harmonique de la fluctuations de conductance montre la possibilité d'utiliser des radiations THz pour sonder des phénomènes quantiques non linéaires.

Dans ce qui suit, nous présentons un résumé de la bibliographie et des principaux résultats obtenus dans ce travail de thèse.

Chapitre 1: Structure et transport électronique dans un nanoruban de graphène parfait.

Le but de ce chapitre est de présenter les principales caractéristiques de la structure de bande d'un nanoruban graphène, associées à ses propriétés de transport électronique.

Nous avons donné des preuves de certaines différences marquées entre les nanorubans de graphène avec bord zigzag et armchair, concernant leurs spectres d'énergie, figure 7.11: pour le bord zigzag, la dégénérescence de vallée est préservée tandis que des états localisés se développent, à énergie nulle, sur les bords. Dans le cas de bord armchair, nous insistons sur l'ouverture d'une gap d'energie et le couplage des vallées qui donne lieu à une levée de la dégénérescence de vallée.

Des premières mesures expérimentales de transport electronique ont donné des preuves de sous-bandes 1D, concequence du confinement électronique. A ce stade, aucune signature claire de la configuration atomique des bords a été observée. Le désordre dans le nanoruban de graphène joue certainement un rôle majeur. Pour cela, nous étudierons, dans le chapitre suivant, l'influence des principales sources de

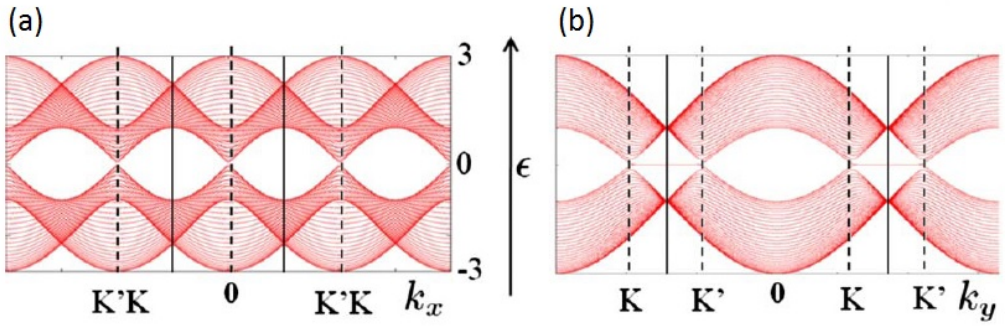

Figure 7.11: Structure de bande electronique pour les nanorubans de graphène avec de bord armchair **(a)** et zigzag **(b)**. Adapté de Delplace et al. PRB (2010).

désordre dans les nanorubans de type zigzag et armchair.

Chapitre 2: Transport électronique dans les nanorubans de graphène désordonnés

Les symétries de l'Halmitonian du graphène sont responsables de certaines caractéristiques uniques concernant le transport électronique en présence de desordre.

L'impact des différents types de desordre comme les lacunes, le desordre de bord et les fluctuations du potentiel a été étudiée numériquement. L'etude montre, comme caractéristique commune, une baisse de la conductance, l'absence de plateaux quantifié pour un degré modéré de désordre et une forte réduction de la mobilité des porteurs. La combinaison du desordre de bord, des fluctuations de potentiel et le confinement électronique a été proposée pour expliquer l'ouverture d'un gap de transport et la formation de boîtes quantiques en série et/ou parallèle observés dans les nanorubans de graphène.

Les effets mésoscopiques du désordre, comme les interférences quantiques, couramment observé dans les métaux desordonnés, sont également présents dans le graphène. Cependant, l'existence de la symétrie chirale donne des particularités au graphène: la présence de l'anti-localisation faible, lorsque le temps de diffusion inter- et intra-vallée augmente et une augmentation de l'amplitude des fluctuations de conductance lorsque le temp de diffusion inter-vallée est réduit.

Expérimentalement, l'anti-localisation faible n'a été observée que dans des échantillons de haute qualité, et le renforcement des fluctuations de conductance n'a pas encore été mesuré.

Dans la partie expérimentale de la présent thése, la présence de localisation faible et

des fluctuations de conductance dans les nanorubans de graphène sera analysée afin d'obtenir les énergies caractéristiques du transport cohérent à basse température.

Chapitre 3: Niveaux de Landau dans les nanorubans de graphène

Dans ce chapitre, nous décrivons brièvement la structure de bande électronique sous un champ magnétique perpendiculaire appliqué à: un gaz d'électrons bidimensionnel, un guide d'onde 1D, un monocouche de graphène et finalement à des nanorubans monocouches et bicouches.

Ces travaux théoriques prédisent un comportement inhabituel de fermions de Dirac en présence à la fois d'un champ magnétique et d'un confinement électronique. Très spectaculaire est le spectre de Landau prévu pour les nanorubans de graphène en fonction de la symétrie de bord, figure 7.12. Dans le cas de zGNR, nous voyons la présence des niveaux de Landau à l'interieur du ruban combiné à une asymétrie de vallée dans les états dispersifs. Pour les nanorubans de bord armchair, on observe également la présence des niveaux de Landau à l'interieur du ruban, où la dégénérescence vallée est préservée. Par contre, sur les bords du ruban, la dégénérescence de vallé est levée, caractéristique de la structure de bande du nanoruban armchair à champ magnetic nul.

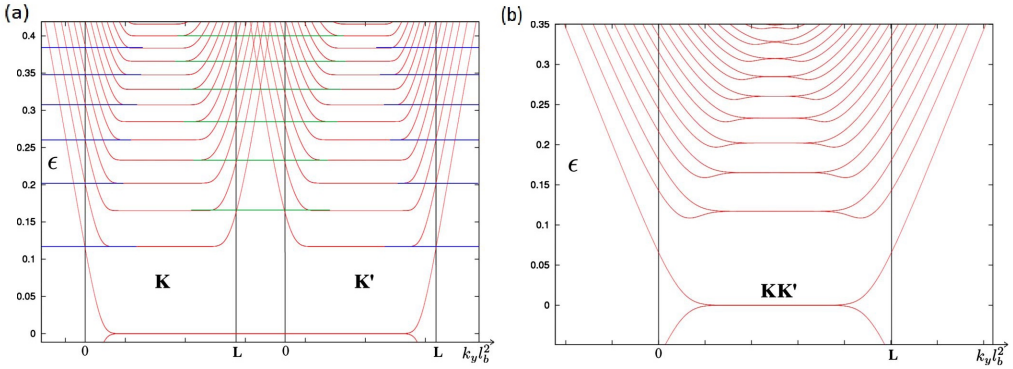

Figure 7.12: **(a)**, Structure de bande électronique d'un nanoruban de graphene de 24 nm de large avec des bords de type zigzag sous un champ magnetique appliqué de 51 T. **(b)**, Structure électronique d'un nanoruban de graphène de 41 nm de largeur avec des bords de type armchair soumiss à 51 T. Adaptee de Delplace et al. PRB (2010).

Toutefois, ces prévisions theorique souffrent d'un manque de confirmation expérimentale. Ce qui motive, pour une large part, les travaux expérimentaux de cette thèse. Au début de cette thèse, les mesures de transport électronique sur GNRs à champ magnétique nul ou modérée n'ont pas révélé le confinement des fermions de Dirac et les types de bords des rubans. Nous envisageons donc de jouer avec un

confinement magnétique beaucoup plus large, combinée à des dispositifs de mobilité optimisée sur Si/SiO_2 pour révéler les sous-bandes magnéto-électriques.

Chapitre 4: Techniques Experimentals

Dans ce chapitre, nous présentons les défis technologiques de fabrication des dispositifs de nanorubans de graphène de bonne qualité et les techniques expérimentales de mesures sous des conditions extrêmes de champs magnétiques. La maîtrise des techniques de lithographie optique et electronique pour dessiner et connecter les nanorubans a exigé des efforts considérables en salle blanche afin d'optimiser les différents paramètres.

Nous fabriquons un total de 168 nanorubans de graphène lithographiés, figure 7.13. De ceux-ci, nous avons mesuré avec succès (transport électronique à zéro et sous champ magnétique à différentes températures) seulement 12 GNRs, 8 d'entre eux ont présenté une bonne qualité. Concernant les nanorubans dérivés de nanotubes de carbone, nous avons connecté 120 rubans et nous avons mesuré complètement 9 d'entre eux. Malheureusement, aucun d'entre eux ne montre de bonnes caractéristiques de transport électronique.

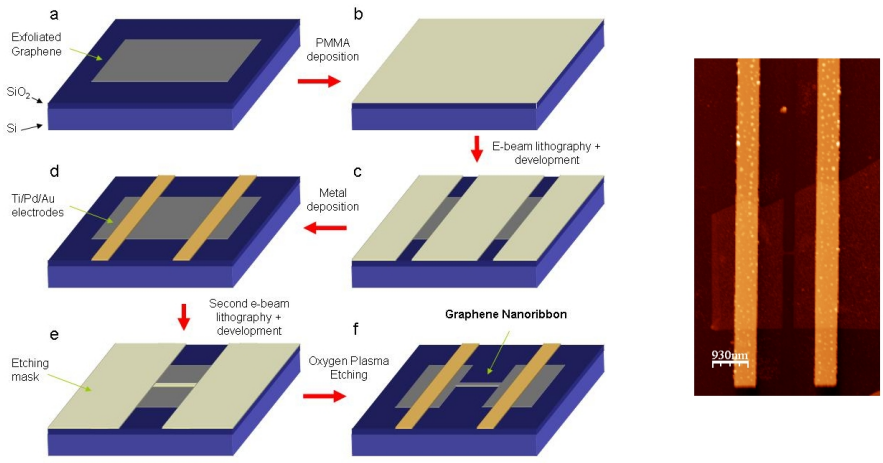

Figure 7.13: **Gauche**, Processus de fabrication des nanorubans lithographiés: a) Exfoliation du graphène sur un substrat de Si/SiO_2 b) dépôt du PMMA c) insolation avec un e-beam et révélation des electrode d) dépôt de metal e) deuxieme dépôt de PMMA plus insolation avec l'e-beam et révélation f) nanorubans de graphène après la gravure avec du plasma d'oxygène. **Droit**, Microscopie à force atomique pour un nanoruban de 60 nm de largeur et 300 nm de long fait avec la technique du lithographie electronique.

Nous concluons en disant que nos meilleurs dispositifs de nanorubans de graphène ont été finalement obtenus par lithographie electronique et gravure par plasma

d'oxygène, avec des largeurs nominales comprises entre 70 et 100 nm. Comme nous le verrons dans le chapitre suivant, ces dispositifs présentent une "bonne" mobilité, au moins suffisamment élevée pour dévoiler de nouveaux phénomènes quantiques dans le régime des champs magnétiques élevés.

Chapitre 5: Evidence experimentale du spectre de Landau dans les nanorubans de graphène monocouches

Les expériences (jusqu'à 55 T) à basse température sur des nanorubans lithographiés de graphène monocouche de magnéto-transport ont été effectuées sur deux GNRs avec par dimensions: échantillon A, $W = 100$ nm et $L = 350$ nm et échantillon B avec $W = 70$ nm et $L = 750$ nm. L'étude du transport électronique à champ nul donne la preuve d'un régime faiblement diffusif avec une mobilité des porteurs ($\approx$ 1,200 cm^2 V^{-1} s^{-1} pour échantillon A et 3500 cm^2 V^{-1} s^{-1} pour échantillon B) assez grande pour observer le spectre de Landau sans champ magnétique élevé.

Dans les résultats de magnéto-transport, nous observons la présence de la quantification de Landau pour échantillon A, 100 nm de large, où les valeurs quantifiées de la résistance correspondent à des facteurs de remplissage de 2 et 6, comme prévu pour une monocouche de graphène, figure 7.14. Ces résultats ont été trouvés aussi pour les petits rubans, figure 7.14-insert. Il s'agit de la première observation de quantification de Landau dans les nanorubans de graphène sur Si / SiO_2.

Á haut niveau de dopage (V_g = -40 V), la présence d'anomalies dans les oscillations Shubnikov-de Hass révéle des effets de confinement électroniques, figure 7.15 (a). Lorsque le confinement électronique commence à etre plus forte que le confinement magnétique, il est observé une déviation de la linéarité du spectre de Landau, figure 7.15-(b). Cela se produit lorsque le diamètre cyclotron devient plus grande que la largeur des rubans. Cette déviation de la linéarité peut être ajustée a l'aide de la règle de quantification Borh-Sommerfeld en utilisant comme paramètre la largeur du ruban. Dans ce cas (ligne bleu figure 7.15-b) on a obtenu W$\approx$94 nm, en bon accord avec la valeur nominale de 100 nm mesurée par l'AFM.

En utilisant les mesures de magnéto-transport dans le regime fortement dopées, il est possible de calculer le couplage capacitif entre l'échantillon et la grille; dans ce cas, on obtaine $\alpha = 1,5 \times 10^{11}$ cm $^{-2}$ V^{-1}. Cette augmentation comparée à la valeur calculée pour le graphène 2D est attendue par la largeur réduite du ruban par rapport à l'épaisseur d'oxyde.

Pour un nanoruban de graphène plus étroit, 70 nm (échantillon B), un nouveau spectre de Landau est observé, témoignant d'une levée de dégénérescence qui ne peut pas être liée à la levée de dégénérescence déjà observée dans le graphène 2D. En comparant les sous-bandes magnéto-électriques d'une largeur de 70 nm avec des

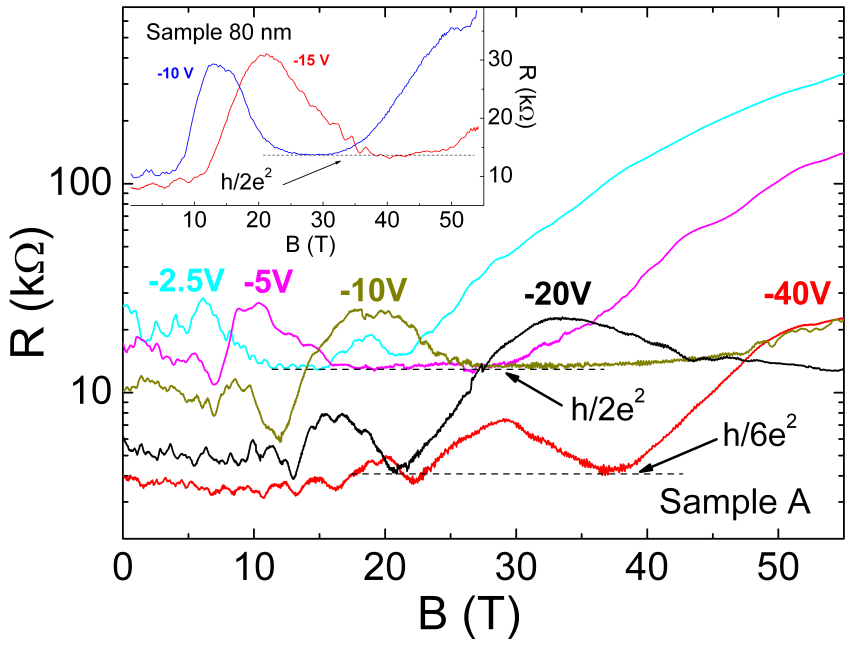

Figure 7.14: Resistance a deux points sur *échantillon A* en fonction du champ magnetic appliqué à 4 K, pour des differentes valeures de la tension de grille V_g=-2.5, -5, -10, -20 et -40 V. Insert: magnéto-resistance d'un nanoruban de graphène plus étroit, de 80 nm de large, pour des tensions de grille de V_g=-10 et -15 V.

bord armchair et les oscillations quantiques, nous avons trouvé un bon accord entre le champ magnétique au cours du que les maxima de résistance sont présents et le pinning de l'énergie de Fermi sur les deux sous-niveaux de Landau, figure 7.16. Cet accord tend à montrer que le double maximum observé dans les mesures de magnéto-résistance est un concequence du pinning de l'énergie de Fermi dans les deux sous-bandes 1D qui existent aussi en raison de la levée de dégénérescence de vallée caractéristique d'un bord armchair. Cela montre qu'il pourrait y avoir une contribution plus importante de la symétrie armchair sur les bords du nanoruban.

Nous donnons aussi une description qualitative de l'impact des defauts dans le régime de Landau. Pour cela, on compare la distance entre les courants chiraux, obtenus par des simulations numériques, sur un nanoruban parfait, figure 7.17-(d), et le champ magnétique pour lequel on observe la pleine quantification à $\nu = 6$, figure 7.17-(c), obtenue à partir de la conductance en fonction du fateur de remplissage, figure 7.17 (a)-(b). Nous concluons que certains defauts, comme des defauts à longue portée sont nécessairement présents dans nos dispositifs pour coupler les canaux de bord.

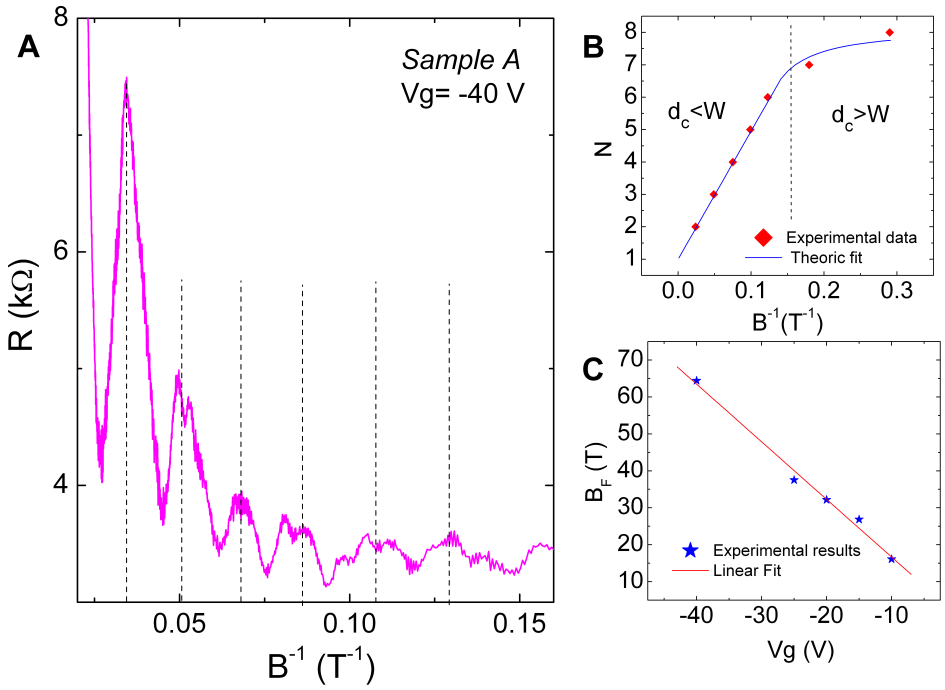

Figure 7.15: **Oscillations Shubnikov-de Haas.** **(a)** La résistance en fonction de l'inverse du champ magnétique de *échantillon A* à haut niveau de dopage V_g=-40 V. Les lignes pointillées indiquent les maxima de résistance. **(b)**, le nombre de niveaux de Landau occupés en fonction de l'inversé du champ magnétique extrait des oscillations (diamants rouges) et la prediction de Bohr-Sommerfeld (bleu). La ligne verticale en pointillée représente le champ magnétique où $d_c \approx$W. **(c)**, période d'oscillations SdH pour différentes tensions de grille (étoiles bleues) et l'ajustement linèaire (rouge).

Cette étude démontre la puissance des expériences de magnéto-transport sous champ magnétique élevé dans les dispositifs plutôt propres. Lorsque ces mesures ont été effectuées, nous avons donné la première preuve expérimentale de la quantification de Landau dans des nanorubans de graphène. La signature d'une géométrie de bord spécifique sur le spectre Landau aurait besoin d'autres preuves expérimentales avec différentes sources de nanorubans. En outre, une sonde locale, comme la STM, sur le même dispositive pourrait adresser directement la structure de bord et fournir des confirmations complémentaires.

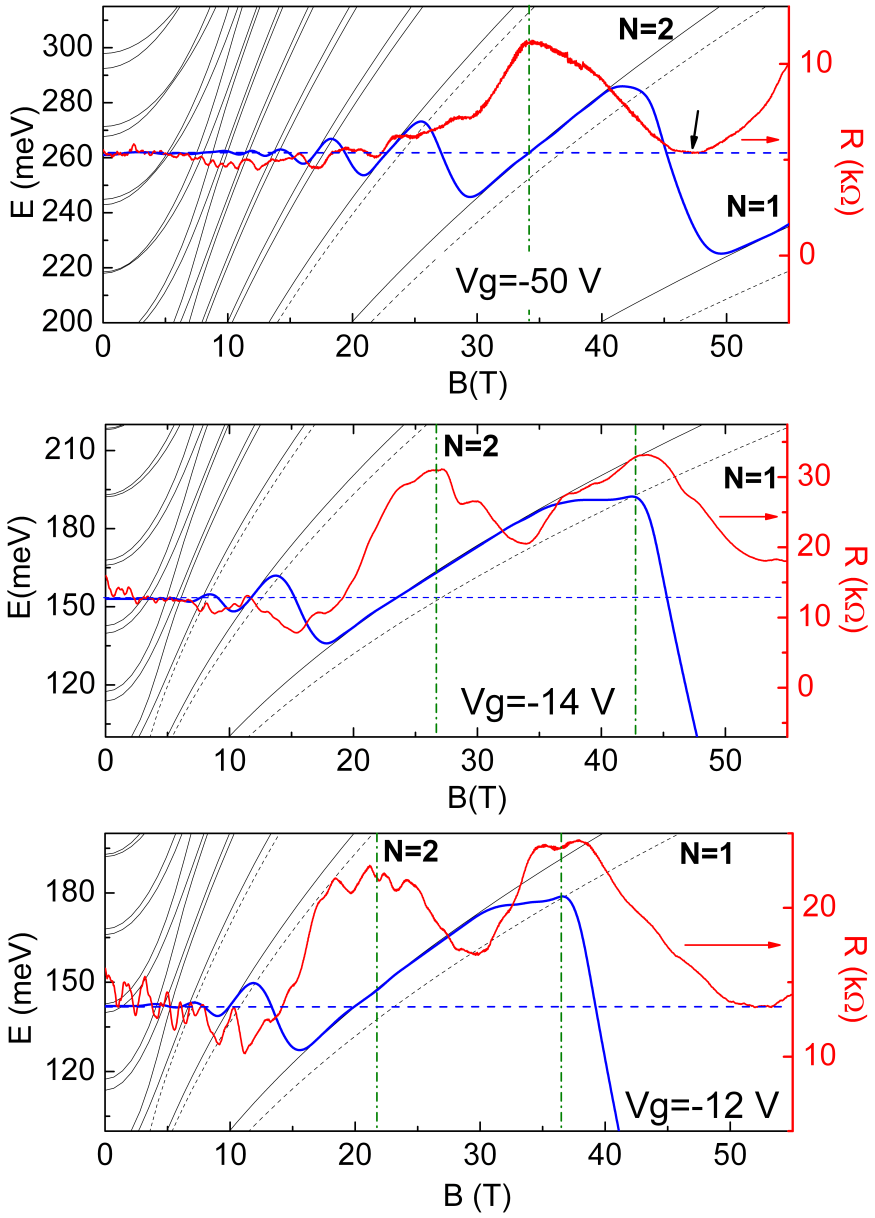

Figure 7.16: Sous-bandes magnéto-électriques d'un nanoruban de graphène de 70 nm de largeur en comparaison directe avec les mesures de magnéto-résistance (courbes rouges et axe droite) de *échantillon B*. Les courbes bleues sont l'énergie de Fermi calculée et la ligne bleue pointillée représente l'énergie de Fermi constante. De haut en bas, $V_g = -12$, -14 et -50 V. Les lignes verticales en pointillée représentent les maxima de magnéto-résistance et les fléches noires indiquent les valeurs quantifiées de la résistance. Les indice pour des niveaux de Landau sont donnés sur les figures.

Chapitre 6: Evidence experimentale du spectre de Landau dans le graphène bidimensionel et les nanorubans multi-couches

Dans ce chapitre, nous présentons les résultats expérimentaux de magnéto-transport obtenus sur le graphène 2D multicouche et les nanorubans de graphène, également

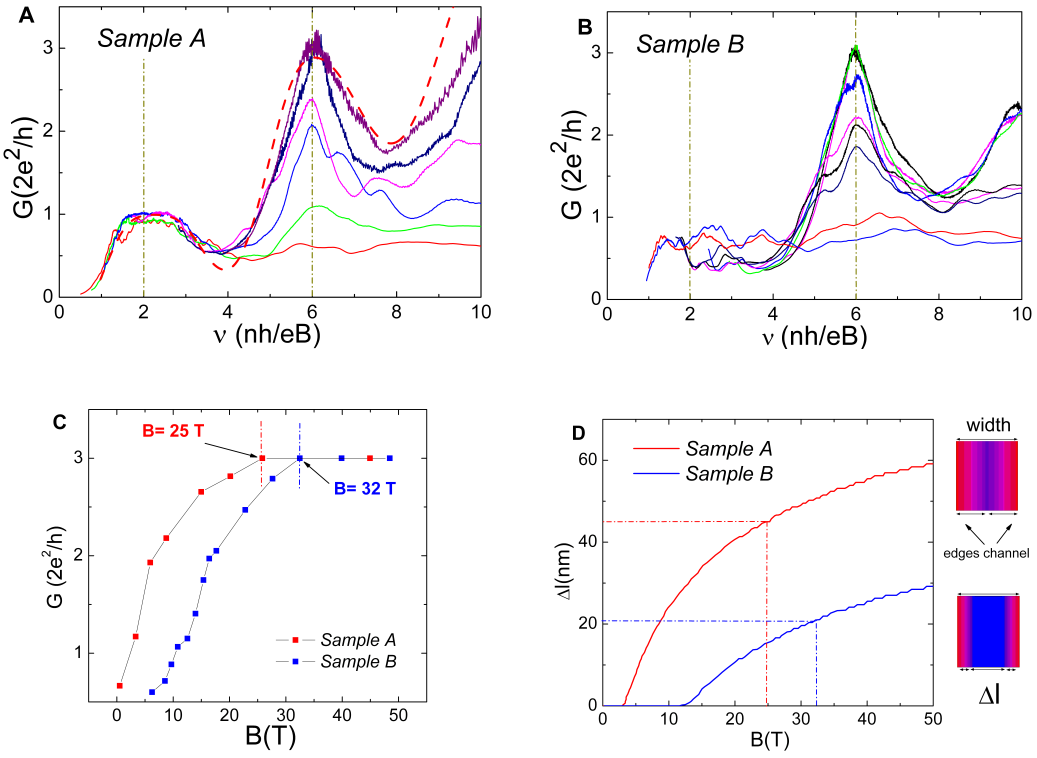

Figure 7.17: Conductance en fonction du facteur de remplissage pour différentes tensions de grille pour *échantillon A* (**a**) et *échantillon B* (**b**). La ligne pointillée rouge dans la figure de gauche est la simulation numerique de $G(\nu)$. Les lignes en points vert représentent le facteur de remplissage où les maxima de conductance sont attendus pour le graphène monocouche. **(c)** conductance à $\nu = 6$ en fonction du champ magnétique pour *échantillon A* (carrés rouges) et *échantillon B* (carrés bleus). **(d)** Des simulations numériques de la séparation des canaux de bord, Δl, en fonction du champ magnétique pour *échantillon A* (rouge) et *échantillon B* (bleu).

multicouches.

Dans le cas du graphène 2D multicouches la spectroscopie Raman montre la signature claire d'un système multicouche et les mesures de transport électronique montrent la présence de la structure dans la magnéto-résistance, qui peut être suivie en champ magnétique quand la tension de grille est modifiée, figure 7.18-Haut. Ces caractéristiques semblent compatibles avec le spectre de Landau non-trivial attendu pour un graphène tricouche. Pour le niveau de Landau le plus bas, nous donnons également preuve d'une levée de dégénérescence complet avec une pas de conductance de e^2/h, pas observée avant pour une tricouche graphène, figure 7.18-Bas.

Pour une nanoruban de graphène bicouche, de $W = 90$ nm et $L = 280$ nm, avec une

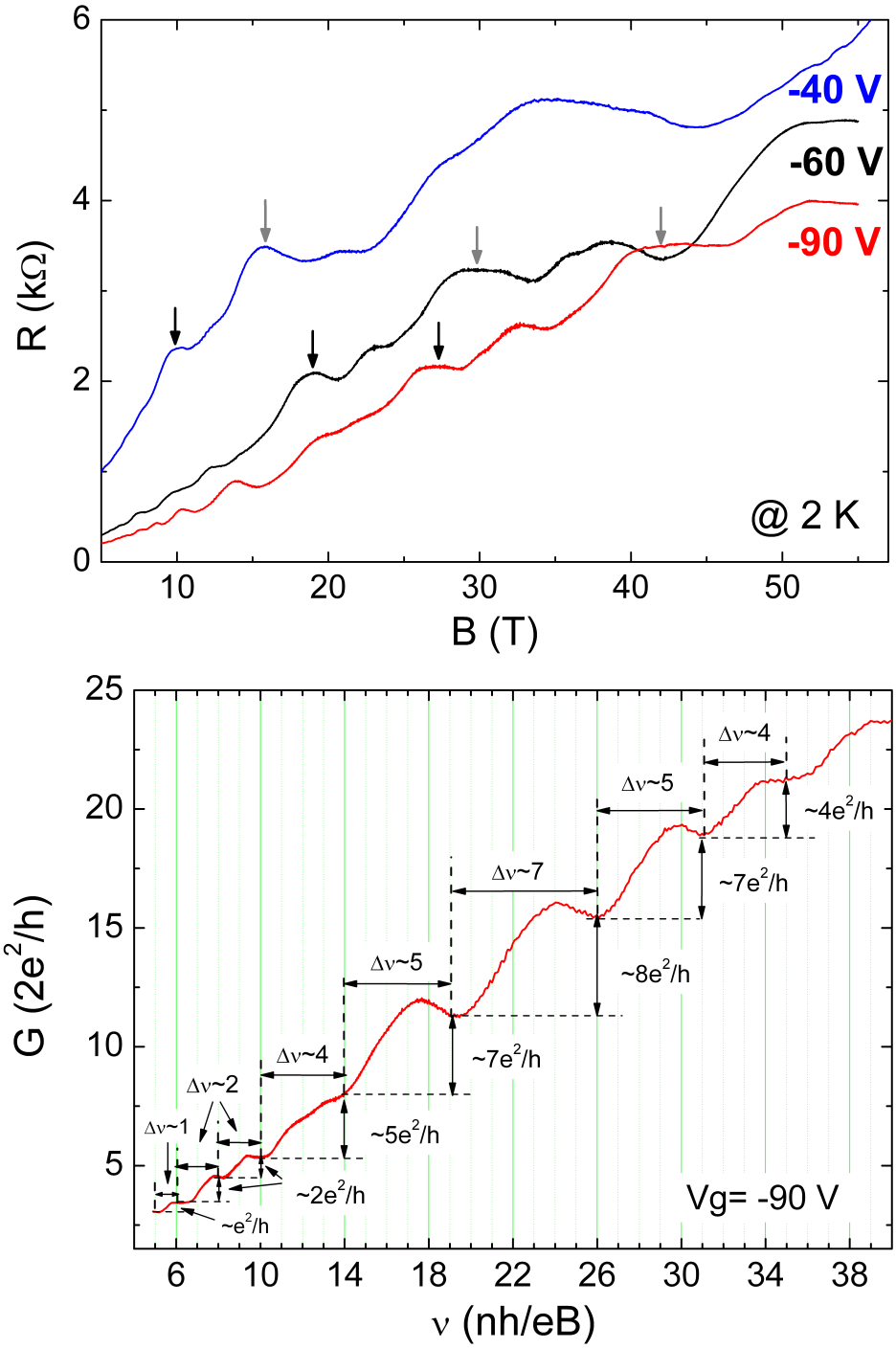

Figure 7.18: **Haut**, magnéto-résistance à V_g = -90, -60 et -40 V pour l'èchantillon multicouche. Les flèches noires et grises montrent les structures qui persistent à différents champs magnétiques quand la densité de porteurs change. **Bas**, la conductance en fonction du taux de remplissage de $V_g = 90$ V.

mobilité des porteurs de ≈ 1900 cm^2 V^{-1} s^{-1}, la mesure de magneto-résistance montrent la présence claire de structures correspondant au niveau de Landau, mais aucun signe de quantification de la résistance, figure 7.19-(a). Contrairement à cela, un échantillon monocouche mesurée en même temps et avec des propriétés de transport électronique très similaires au nanoruban bicouche, montre une résistance entièrement quantifiée pour des champs magnétiques autour de 25 T, figure 7.19-(a)-insert.

La présence de niveaux de Landau est observée pour les facteurs de remplissage correspondant à $\nu = 8$ et 12, identiques à ceux attendus pour le graphène bicouche, mais avec quelques caractéristiques non conventionnelles. Pour les facteurs de remplissage inférieur, $\nu = 4$, le maxima de conductance observé pour une tension de 20 V de grille est "divisé" en deux maxima quand la tension de grille est augmentée, figure 7.19-(b). Les différences entre les résultats obtenus sur graphène bicouche 2D et ceux obtenus sur les nanorubans bicouche révèle un effet de confinement électronique probable dans la structure électronique. Une comparaison des résultats expérimentaux avec les sous-bandes magnéto-électriques pour une nanoruban bicouche manque pour établir pleinement cette interprétation. Notez que les différentes possibilités d'empilament, l'existence d'une différence de potentiel incontrôlée entre les deux couches et les différents types de symétrie de bord (armchair, zigzag ou mélange) impliquent nécessairement une grande variété de structures de bandes électroniques possibles pour un nanoruban bicouche. La comparaison avec les données expérimentales devient très difficile.

Chapitre 7: Interference quantique dans les nanorubans de graphène

Nous commençons à étudier les fluctuations de conductance dans un nanoruban bicouche de $W = 80$ nm et $L = 50$ nm. Lorsque la température du système est augmentée, les amplitudes des fluctuations de conductance suivent un comportement $\propto 1/\sqrt{T}$, figure 7.20-bas, lié à un déphasage thermique où la longueur de cohérence et la diminution de la longueur thermique que l'augmentation de la température. Aussi, à travers l'étude de la tension de corrélation est possible estime la longueur minimale qui que controle la corrélation du système, après une certaine température ($T > 10$ K) cette longueur suivre le même comportement et dispose d'un valeur très proche de la longueur thermique, figure 7.20-bas.

En comparant l'amplitude des fluctuations de conductance et la magnéto-conductance, nous avons constaté que la différence entre les deux est égale à $1/2\sqrt{2}$, c'est la différence attendue dans les amplitudes lorsque la symétrie d'inversion temporelle est brisée et que la dégénérescence de spin est levée. C'est la preuve de l'ergodicité des fluctuations de conductance dans un nanoruban bicouche.

Une autre étude importante est l'amplitude des fluctuations de conductance dans

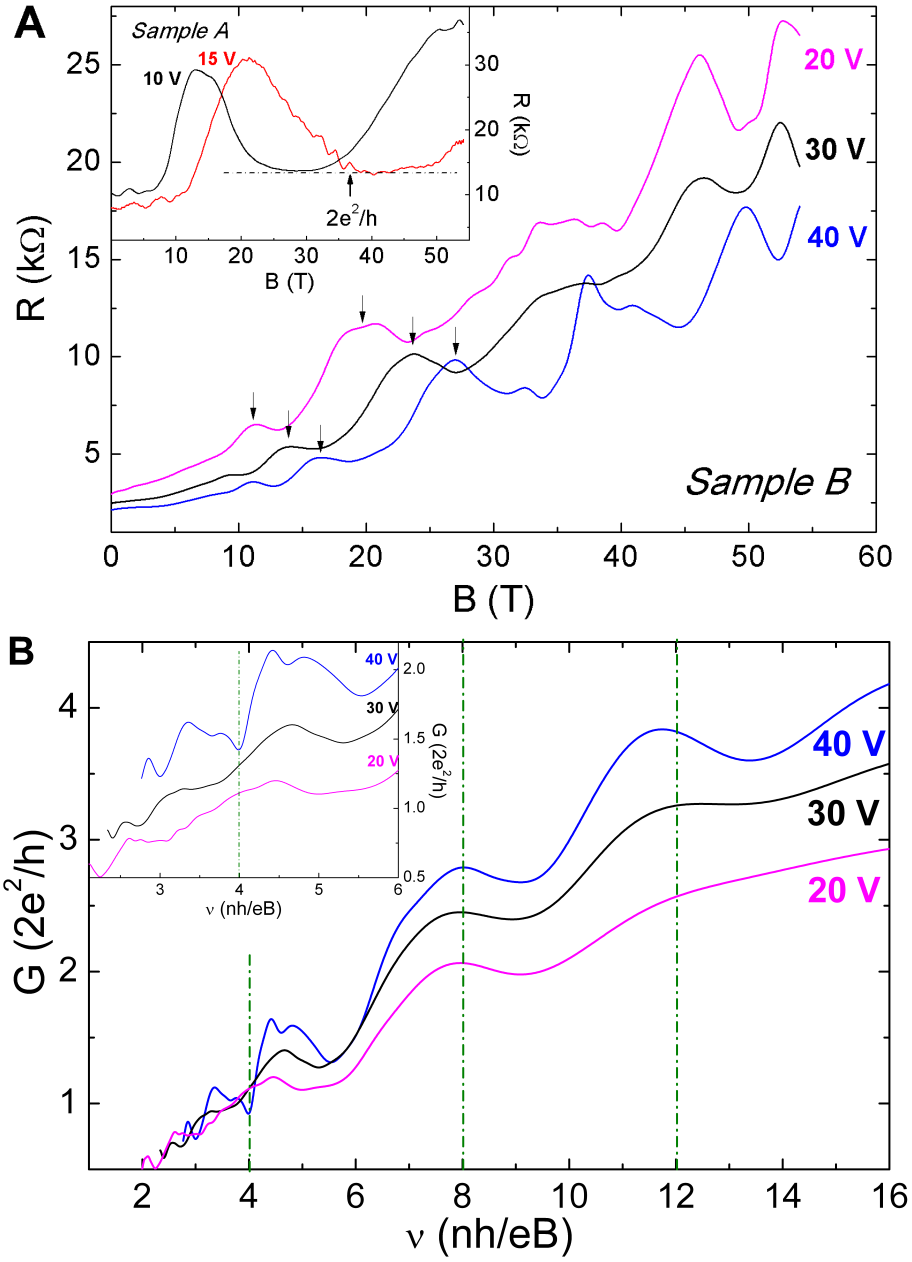

Figure 7.19: **(a)**, Résistance en fonction du champ magnétique perpendiculaire pour différentes tensions de grille pour *échantillon B* (bicouche). En insert, la résistance en fonction du champ magnétique pour *échantillon A* (monocouche) à $V_g = 15$ V et 10 V. La ligne en pointillée représente la valeur quantifiée de la résistance à $h/2e^2$. **B**, Conductance en fonction du facteur de remplissage de *échantillon B* à $V_g = 20$ (magenta) et 30 (noir) et 40 V (bleu). Insert: zoom à facteur de remplissage faible. Les courbes à 30 et 40 V ont été décalés pour plus de clarté. Les lignes pointillées représentent les facteurs de remplissage attendus pour un graphène bicouche.

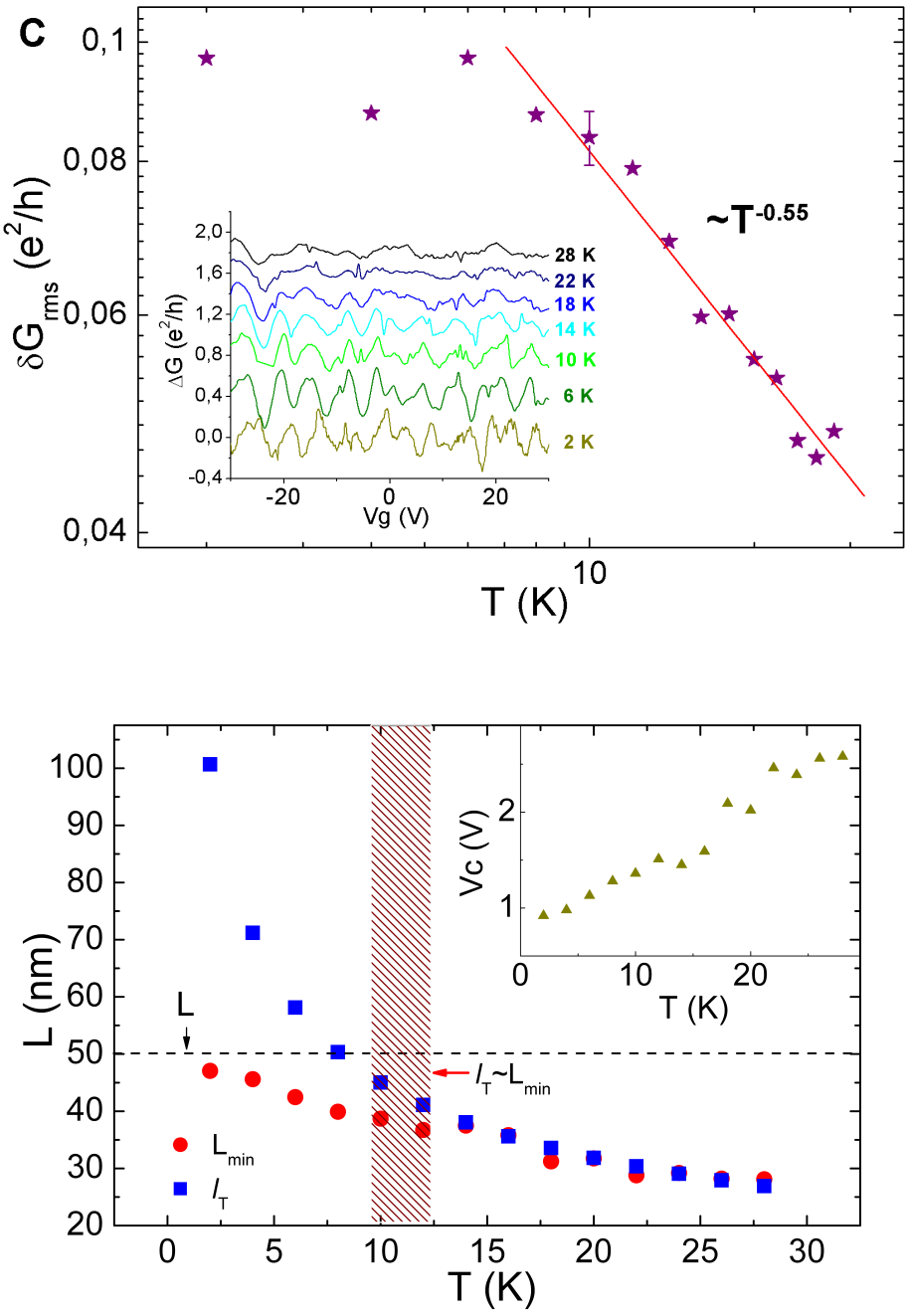

Figure 7.20: **Haut**, Ecart-type des fluctuations de conductance en fonction de la température en l'échelle log-log. La pente au-dessus de 10 K suggère une dépendance $1/\sqrt{T}$. Insert: fluctuations de conductance pour plusieurs températures. Les courbes ont été décalées pour plus de clarté. **Bas**, Longueur minimale calculée à partir de la tension de corrélation (insert) et comparée à la longueur thermique.

le régime hors-equilibre, quand une forte tension de polarisation est appliquée à l'échantillon, figure 7.21-bas. Dans ce régime, l'amplitude des fluctuations diminue comme $1/\sqrt{V_B}$, caractéristique d'un déphasage controlé par l'interaction électron-électron selon le modèle proposé par Ludwig et al., figure 7.21-bas à gauche. Contrairement aux résultats de fluctuation magnéto-conductance pour un nanoruban bicouche, où la dépendance de l'amplitude de la tension de polarisation suit un comportement 1/V et où la longueur de corrélation ne dépend pas de la tension de polarisation, la longueur de corrélation du système varie, indiquant que la diminution des fluctuations est due à la diminution de la longueur de cohérence.

Le modèle d'interaction électron-électron comme une source principale de déphasage est également confirmé par l'étude de la tension de corrélation des fluctuations et l'utilisation de celui-ci pour calculer la longueur de cohérence. Dans ce cas, cette longueur a un dépendance $\propto V^{-0,3}$, avec la tension de polarisation également en accord avec le modèle proposé par Ludwing et al., figure 7.21 en bas à droite.

Conclusion

Dans cette thèse, nous avons étudié la structure électronique des nanorubans de graphène par leur réponse à un champ magnétique intense. La motivation principale était de révéler les caractéristiques de leur spectre de Landau, comme une magnéto-empreinte du confinement électronique de la symétrie de bord. À cette fin, nous avons d'abord développé les procédés technologiques pour fabriquer nos propres dispositifs basés sur des nanorubans de graphène avec des largeurs comprises entre 50 et 100 nm. Différentes techniques expérimentales ont été explorées: nanorubans faits par lithographie électronique et gravure par plasma d'oxygène; nanorubans obtenus à partir de CNT; nanorubans de gravure anisotrope; nanorubans naturels faits par clivage mécanique. Nous avons finalement obtenu des caractéristiques de transport électroniques intéressantes, adaptées à des expériences de champs magnetiques pulsées pour des nanorubans de graphène dérivés par lithographie électronique et gravure par plasma d'oxygène.

Nous avons effectué des expériences de magnéto-transport (jusqu'à 55 T) à basse température (2 K) sur des nanorubans de graphène monocouche et double couche (GNR). L'étude du transport électronique à champ nul donne la preuve de mobilités de porteurs supérieures à 1200 $\mathrm{cm}^2\ \mathrm{V}^{-1}\ \mathrm{s}^{-1}$, assez grande pour induire une redistribution des etat éelectroniques dans des niveau de Landau sous champ magnétique élevé.

Pour les *dispositifs de nanorubans monocouche sur* SiO_2, nous avons obtenu la première observation expérimentale de la quantification de Landau, avec des valeurs quantifiées de la résistance à $h/2e^2$ et $h/6e^2$, ce qui correspond à des facteurs de remplissage $\nu = 2$ et 6, respectivement. Dans le régime fortement dopé, la présence

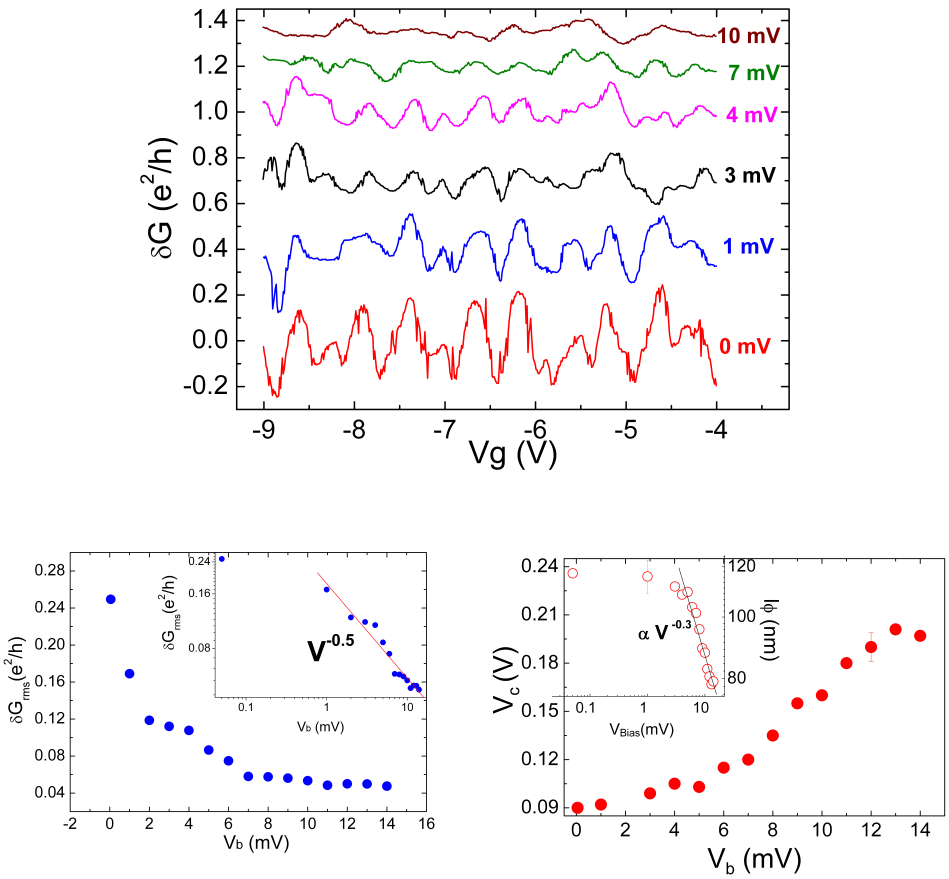

Figure 7.21: **Haut**, les fluctuations de conductance en fonction de la tension de grille pour le régime à faible dopage avec des tensions de polarisation appliquées séectionnés, mesurées à 2 K. Toutes les courbes, à l'exception de la courbe à 0 mV, ont été décalées. **En bas à gauche**, δG_{eff} calculé à partir de $\Delta G(V_g)$, pour différentes tensions de polarisation. Insert: les mêmes données en échelle logarithmique qui révèlent une dépendance en $V^{-0.5}$, au-dessus de 1 mV. **En bas à droite**, la tension de corrélation en fonction de la tension de polarisation. Insert: la longueur de cohérence calculée à partir de la tension de corrélation, dans une échelle logarithmique avec une dépendance $V^{-0.3}$ par les fortes tensions de polarisation.

d'anomalies sur les oscillations Shubnikov-de Haas révéle le confinement électronique pour des largeurs inférieures à 100 nm.

Pour les rubans les plus étroits de 70 nm de large, un nouveau spectre de Landau est dévoilé, témoignant d'une levée de dégénérescence des niveaux de Landau N=1, qui ne peut être lié à la levée de dégénérescence observée précédemment dans le graphène 2D. En comparant la structure de bande attendue théorique d'un nanoruban armchair de largeur similaire en présence de champ magnétique élevé avec les oscillations

quantiques mesurées, nous avons trouvé un accord convaincant entre les maxima de la résistance et le pinning de l'énergie de Fermi sur les deux sous-niveaux de Landau, caractéristique de la symétrie de bord armchair. Ces données soutienent fortement une contribution d'une configuration armchair sur les bords du nanoruban.

Dans le cas des *nanorubans bicouche*, les résultats expérimentaux sont moins convaincants en raison de la mobilité limitée, mais néanmoins ils dévoilent la présence de niveaux de Landau aux facteurs de remplisage correspondant aux bicouche graphène ($\nu = 8$ et 12), mais sans signe de quantification de la résistance. Pour le facteur de remplissage ($\nu = 4$), de nouvelles structures se révèlent lorsque le niveau de dopage est augmenté. Ces structures peuvent être liées au début d'une levée de dégénérescence liée à la symétrie de bord. Pour confirmer cette origine, des simulations numériques de nanorubans bicouche en présence d'un champ magnétique élevé et des expériences supplémentaires sont nécessaires. Notez que ces simulations gérent un grand nombre de paramètres (empilement des couches, différence de potentiel entre les couches, la symétrie de bord) ce qui rend la comparaison difficile.

Ces études démontrent aussi la puissance d'expériences de magnéto-transport à champ magnétique élevé dans les dispositifs plutôt propres. Une signature confirmée d'une géométrie de bord spécifique sur le spectre Landau exigerait des efforts supplementaires avec différentes sources de nanorubans. En outre, une sonde locale, comme le STM (Microscope a éffet tunnel), sur le même rubans permetrait d'adresser directement la structure de bord et fournirait des confirmations complémentaires.

Une poursuite de cette étude sera de mettre l'accent sur la qualité des nanorubans étroits. Nos efforts sur les nanorubans provenant de nanotubes de carbone n'ont pas permis d'atteindre le qualité des dispositifs prévue, probablement due à la grande résistance de contact. Les nanorubans ultime sont certainement ceux obtenus par les approche bottom-up, sur des substrats métalliques à partir de précurseurs moléculaires. D'autres travaux sont nécessaires pour transférer ces rubans sur des substrats non conducteurs pour une caractérisation entièrement électronique et sous un environnement de très fort champ magnétique.

Nous avons finalement étudié les interférences quantiques à travers les fluctuations de conductance et la localisation faible sur les nanorubans pour révéler les mécanismes de décohérence. Ces études révèlent un déphasage thermique dominant lorsque la température est augmentée et la signature d'interactions entre électrons lorsqu'une tension de polarisation élevée est appliquée. Nous avons aussi étudié les fluctuations de conductance produites quand un rayonnement THz est appliqué sur un feuille de graphène, fortement corrélés à des fluctuations de conductance de deuxieme ordre. Cette évidence expérimentale ouvre une nouvelle possibilité d'étudier les phénomène quantiques non-linéaire avec radiation THz.